Report Title: AOI [3] High-Temperature Nano-Derived Micro-H_2 and -H_2S Sensors

Type of Report: Final Scientific/Technical

Reporting Period Start Date: July 8, 2010

Reporting Period End Date: May 15, 2014

Principal Author: Edward M. Sabolsky
Associate Professor, West Virginia University

Date Report Issued: August 2014

DOE Award Number: DE-FE0003872

Name and Address of Submitting Organization:

Prime Organization:
Dr. Edward M. Sabolsky
Associate Professor
Energy Materials Program
Mechanical and Aerospace Engineering
West Virginia University
Phone: (304) 293-3272
Fax: (304) 293-6689
ed.sabolsky@mail.wvu.edu

Participating Organization:
NexTech Materials, Ltd.
Point of Contact: Dr. Lora Thrun
404 Enterprise Drive
Lewis Center, OH 43035
Phone: (614) 842-6606 x129
Fax: (614) 842-6607
l.thrun@nextechmaterials.com

DISCLAIMER:

ABSTRACT:

The emissions from coal-fired power plants remain a significant concern for air quality. This environmental challenge must be overcome by controlling the emission of sulfur dioxide (SO_2) and hydrogen sulfide (H_2S) throughout the entire coal combustion process. One of the processes which could specifically benefit from robust, low cost, and high temperature compatible gas sensors is the coal gasification process which converts coal and/or biomass into syngas. Hydrogen (H_2), carbon monoxide (CO) and sulfur compounds make up 33%, 43% and 2% of syngas, respectively. Therefore, development of a high temperature (>500°C) chemical sensor for in-situ monitoring of H_2, H_2S and SO_2 levels during coal gasification is strongly desired. The selective detection of SO_2/H_2S in the presence of H_2, is a formidable task for a sensor designer. In order to ensure effective operation of these chemical sensors, the sensor system must inexpensively function within harsh temperature and chemical environment. Currently available sensing approaches, which are based on gas chromatography, electrochemistry, and IR-spectroscopy, do not satisfy the required cost and performance targets. This work focused on the development microsensors that can be applied to this application. In order to develop the high-temperature compatible microsensor, this work addressed various issues related to sensor stability, selectivity, and miniaturization.

In the research project entitled "High-Temperature Nano-Derived Micro-H_2 and -H_2S Sensors", the team worked to develop micro-scale, chemical sensors and sensor arrays composed of nano-derived, metal-oxide composite materials to detect gases like H_2, SO_2, and H_2S within high-temperature environments (>500°C). The research was completed in collaboration with NexTech Materials, Ltd. (Lewis Center, Ohio). NexTech assisted in the testing of the sensors in syngas with contaminate levels of H_2S. The idea of including nanomaterials as the sensing material within resistive-type chemical sensor platforms was to increase the sensitivity (as shown for room temperature applications). Unfortunately, nanomaterials are not stable at high temperatures due to sintering and coarsening processes that are driven by their high surface to volume ratio. Therefore, new hydrogen and sulfur selective nanomaterial systems with high selectivity and stability properties in the proposed harsh environment were investigated. Different nano-morphologies of zirconate, molybdate, and tungstate compounds were investigated. The fabrication of the microsensors consisted of the deposition of the selective nanomaterial systems over metal based interconnects on an inert substrate. This work utilized the chemi-resistive (resistive-type) microsensor architecture where the chemically and structurally stable, high temperature compatible electrodes were sputtered onto a ceramic substrate. The nanomaterial sensing systems were deposited over the electrodes using a lost mold method patterned by conventional optical lithography. The microsensor configuration with optimized nanomaterial system was tested and compared to a millimeter-size sensor platform in terms of sensitivity and accuracy. The outcomes of this research will contribute to the economical application of sensor arrays for simultaneous sensing of H_2, H_2S, and SO_2.

TABLE OF CONTENTS:

EXECUTIVE SUMMARY:

The long-term goal of this program was to demonstrate sensor materials and processing strategies that can also be used on sensor arrays that monitor other chemicals (besides H_2 and H_2S), such as carbon dioxide, carbon monoxide, methane, and nitrogen oxides levels within a similar environment. The impact of this work will enable the inexpensive implementation of sensor arrays within broad sensor nets. These sensor nets will allow for *in situ* gas testing for three-dimensional fuel and emission maps within various industrial energy applications, such as current coal-fired power plants, and future Integrated Combined Cycle Gasification (IGCC) systems and direct-coal fuel cell generator systems. In order for these smart chemical sensor systems to effectively operate, they must efficiently and inexpensively function within the proposed harsh temperature and chemical environment. Current chemical sensors based on chromatography, electrochemistry, and spectroscopy are not available to suit the desired cost and performance targets. In order to achieve this goal, the work will concurrently address issues relating to sensor stability, selectivity, and miniaturization. These three issues are the main factors limiting the implementation of nano/micro-ceramic gas sensors for high-temperature operational conditions.

The specific project objectives were as follows:

- Investigate methods for stabilizing the microstructure of nanomaterials for H_2, SO_2, and H_2S selective electrodes for high-temperature, chemi-resistive sensing applications using refractory electrolyte nanoparticles to enhance and stabilize the performance of known metal-oxide sensing semiconducting oxides.
- Investigate the effect of sensor electrode poisoning due to typical impurities in coal syngas at high-temperature.
- Define a lost-mold, microcasting process to produce micron-scale, three-dimensional sensor structures (with feature sizes <100 μm) composed of nano-composite selective electrode nanopowders.
- Demonstrate and test microsensor arrays utilizing the nanomaterial selective electrode materials.

In the research project entitled "High-Temperature Nano-Derived Micro-H_2 and -H_2S Sensors", the team worked to develop micro-scale, chemical sensors and sensor arrays composed of nano-derived, metal-oxide composite materials to detect gases like H_2, SO_2, and H_2S within high-temperature environments from 600-1000°C. The initial nanomaterial system investigated was the pyrochlore-structured zirconate family. Doped-$Gd_2Zr_2O_7$ (GZO) nanomaterial compositions were investigated for H_2 resistive-type sensors for applications between 600–1000˚C. The work investigated the mechanism of H_2 sensing for doped-GZO nanomaterials and SnO_2/GZO nano-composites at the elevated temperatures. By integrating 10 vol% nano-SnO_2 into yttrium-doped GZO nanomaterials, a sensitivity of 4.15% was retained for 4000 ppm H_2 levels with a low signal drift of 0.42%/h at 1000°C in a 20% O_2/N_2 gas stream. The signal drift was reduced by over half of that compared to pure nano-SnO_2 at the same conditions. The nano-GZO limited the grain growth of the nano-SnO_2 particles and also prevented the nano-SnO_2 from fully reducing to Sn at high temperatures in a low oxygen atmosphere. It is among the first

resistive-type sensors operating at 1000°C with sensing times of <5 min. This demonstration provided an example of a strategy of combining traditional metal oxide semiconductor and refractory nanomaterial compositions to form sensing nano-composites with new sensing mechanisms, as well as, enhanced chemical and microstructural stability in high temperature environments.

The second nanomaterial system investigated was based on layered-perovskite, sheelite- and wolframite-structured molybdate and tungstate compositions. These materials were studied more for their capability in reversibly reacting with sulfur species. Evaluation of sensing behavior of binary and ternary tungstates and molybdates (WO_3, MoO_3, $SrWO_4$, $SrMoO_4$, $NiWO_4$, $NiMoO_4$, $MgMoO_4$, Sr_2MgWO_6, and Sr_2MgMoO_6) were completed for SO_2, and H_2S. The CO and H_2 cross-sensitivity tests were also completed for abovementioned compounds. The successful compounds ($SrWO_4$, $SrMoO_4$, $NiWO_4$) that demonstrated high sensitivity towards SO_2 were further tested for 4-100 ppm H_2S diluted in both H_2 and syngas composition. After all evaluation considering SO_2 and H_2S sensitivity and cross-sensitivity toward CO and H_2, the $SrMoO_4$ composition emerged as an excellent sensing material for SO_2 and H_2S. The compound was synthesized in four different morphologies; although, all of them showed superior sensing behavior at high temperature, they succumbed to coarsening and lost the high sensitivity. In addition, $SrMoO_4$/MgO solid solution nanomaterials were grown hydrothermally, the these particles unexpectedly showed superior sensing behavior and chemical stability for H_2 up to 150 hours of operation at 1000°C; however, the $SrMoO_4$ nano-flowers showed high sensitivity towards SO_2 and H_2S. Extensive surface, bulk and interface characterization for chemical, electronic, structural and phase analysis of aforementioned materials were completed in order to clarify the sensing behavior difference. And it was concluded that incorporation of Mg into nano-$SrMoO_4$ as an MgO is the reason behind drastic change in sensitivity by stabile compound formation between Mg and S in addition to change in electronic properties.

The work concluded with four nanomaterial compositions, 10 vol% SnO_2/90 vol% $Gd_{1.8}Y_{0.2}Zr_2O_7$, $Gd_{1.6}Sm_{0.4}Zr_{1.9}Sn_{0.1}O_7$, $SrMoO_4$ and $SrMoO_4$/MgO, that were patterned by a microcasting process to a thickness of ~100 μm over DC-sputtered (and patterned) Zr + Pt composite electrodes. The interdigitated electrodes (IDEs) were shown to be stable up to 1200˚C for at least 15 h. The 10% SnO_2/90% $Gd_{1.8}Y_{0.2}Zr_2O_7$ microsensor showed a 9.7% and 4.7% sensitivity at 600 and 1000°C, respectively, to 4000 ppm of H_2 in N_2 (with a 20% O_2). A nano-SnO_2 microsensor had sensitivities of 81.2% and 1.0% at 600 and 1000°C to 4000 ppm H_2 in 20% O_2/N_2. The $SrMoO_4$ nano-flowers showed a very high sensitivity to SO_2; on the millimeter-size platform, the nanomaterial was 10 times more sensitive to SO_2 than H_2. The $SrMoO_4$ nano-flowers showed a very high sensitivity to SO_2 at this temperature. The 500, 1000, and 2000 ppm SO_2 pulses resulted in average sensitivities of ~55%, ~62%, and ~65%, respectively. The opposite case was seen for the $SrMoO_4$/MgO micro-rods with surface nano-features, where the sensors did not sense SO_2, but the 1000, 2000, and 4000 ppm H_2 exposures resulted in sensitivities of ~65%, ~80%, and ~85%, respectively. These responses are ~10-30% increase over the performance of the millimeter-size sensors, with the largest enhancement occurring at the lower exposure concentrations.

I. EXPERIMENTAL METHODS:

The proposed work will be directed at the following areas: ***1)*** Stabilization of nano-composite H_2 and H_2S selective electrodes for high-temperature using refractory, perovskite- and pyrochlore-zirconate electrolyte nanoparticles; ***2)*** Characterization of nano-composite sensor electrode poisoning due to typical impurities in coal syngas; ***3)*** Development of a lost-mold microcasting process to produce micron-scale, three-dimensional sensor structures (with feature sizes <100 μm) composed of nano-composite selective electrode nanopowders; ***4)*** Demonstration of a micro-sensor array composed of stable nano-composite selective electrode materials.

In order to organize the work stated above into logical areas to fluently discuss, the experimental methods will be broken up into two distinct areas (described within two distinct sub-sections): A) Synthesis of the Sensing Nanomaterials and B) Electrochemical Testing of Nanomaterials.

In the case of the nanomaterials sets, two major groups were studied in this work. One set of compositions were based on the pyrochlore structure (with a zirconate composition) for hydrogen sensing. The second set of compositions were based on the wolframite and sheelite structures (with tungstate and molybdate compositions) for sulfur sensing. The experimental methods and discussion sections will be separated into these sub-categories.

A. Synthesis of the Sensing Nanomaterials

1) Synthesis of Zirconate Nanomaterials

Multiple hydrogen sensing material materials were developed: tin dioxide (SnO_2), doped-gadolinium zirconate ($Gd_2Zr_2O_7$), gadolinium stannate ($Gd_2Sn_2O_7$), and gadolinium titanate ($Gd_2Ti_2O_7$). Each system requires its own experimental conditions due to the difference in solubility and hydrolysis of the starting materials. A brief explanation of the procedures will be described and details of the synthesis of each material system will be described further in the results and discussion section.

Tin oxide is well-known for its hydrogen sensing capabilities; therefore, it is serving as the testing baseline for confirmation of processing techniques and comparison studies of the selective nanomaterials. The oxide sensing materials were created using two distinct methods: 1) Metallic oxide powders were formed into inks with macro-scale particles sizes and 2) Compounds of nano-scale particles sizes were formed using the hydrothermal method that will be described.

The first batch of SnO_2 ink was made by mixing 5 g of SnO_2 (stock #11536, VWR) particle sizes less than 10 μm with 3.5 g of binder, J2M, (63/2, Johnson Matthey, UK). Two different microstructures of the nano-scale SnO_2 were produced hydrothermally: nano-spheres and nano-sheets. Each was precipitated by dissolving $SnCl_2 \cdot 2H_2O$ (Alfa Aesar) in either DI H_2O for the nanosheets, or ethanol for the nanospheres, and adding dropwise a base (NaOH or TMAOH) until the pH of the solution reached 13. This solution is then

placed in EZ-Seal autoclave (401A-8336, Autoclave Engineers, PA) for 12 hrs at 180˚C.

The zirconate materials were synthesized using a similar hydrothermal method. As previously described, most studies use solid-state reaction or sol-gel method to create zirconate pyrochlore materials, so appropriate solution conditions and temperatures were investigated to optimize a hydrothermal method for pure gadolinium zirconate and doped zirconates. Gadolinium carbonate (99.99%, VWR) and zirconium dichloride oxide (99.9%, VWR) were co-precipitated with a variety of dopants including yttrium (Y) and samarium (Sm) for the A-site, and Tin (Sn) for the B-site. In some cases, the Zr in the B-site was completely replaced by Sn or Ti to form these respective Gd-pyrochlores. The compositions and precursor solutions are listed in Table 1.

Table 1: Experimental zirconate compositions (all precursors >99%, Alfa Aesar)

Composition	**Dopant Precursor**
$Gd_{1.8}Y_{0.1}Zr_2O_7$	Yttrium (III) nitrate hydrate
$Gd_{1.6}Y_{0.4}Zr_2O_7$	$Y(NO_3)_3 \cdot xH_2O$
$Gd_{1.6}Sm_{0.4}Zr_2O_7$	Samarium(III) Carbonate Hydrate
$Gd_{1.2}Sm_{0.8}Zr_2O_7$	$Sm_2(CO_3)_3 \cdot xH_2O$
$Gd_2Sn_2O_7$	Tin DiChloride
$Gd_{1.6}Sm_{0.4}Zr_1Sn_1O_7$	$SnCl_2 \cdot 2H_2O$

The solutions of these precursors were mixed in the proper ratio with magnetic stirring and were placed drop wise into a basic solution of TMAOH and DI H_2O. The pH of the solution was changed according to the hydrolysis of the precursors and will be detailed in the following section. These solutions were placed in the autoclave at temperatures ranging from 160 - 300˚C for dwell times of 1-10 hours. Once removed from the autoclave vessel, the solution was placed in a centrifuge and the liquid was removed and replaced with ethanol several times. After this washing step, the material was dried at 60˚C overnight and sieved through a 200 mesh screen for characterization.

In order to synthesize the titanate materials, a solution of $TiOCl_2$ was prepared using titanium tetrachloride (99.99% $TiCl_4$, Alfa Aesar) as a starting material. The $TiCl_4$ was chilled and dripped into an ice bath of de-ionized water to form $TiOCl_2$ and HCL via the following reaction [100A].

$$TiCl_4 + H_2O \rightarrow TiOCl_2 + 2HCl \qquad (1)$$

The $TiOCl_2$ solution was mixed stochiometrically with gadolinium carbonate keeping the pH around 6 and reacted in the autoclave.

Crystal structures of the dried powders were characterized by x-ray diffraction (XRD) at room temperature using a Panalyltical X-Pert Pro diffractometer (PW 3040Pro, Westborough MA) with Cu Kα radiation with a scan rate of 4 deg/min in the 2θ range of 10-70˚. Their morphologies were examined using a scanning electron microscope (SEM, JSM-7600F, JEOL, MI) and a transmission electron microscope (TEM, JEM-2100, JEOL, MI) to confirm crystalinity and particle size. The hydrothermal solutions were diluted, sonicated, and dropped onto a for TEM analysis. Both dried and sintered powders were

placed on a carbon film and coated with Au-Pd for SEM micrographs.

2) Synthesis of Tungstate and Molybdate Nanomaterials

Tungstates and molybdates are the choice of sensing materials, due to their well-known properties as reversible adsorbents of sulfur compounds. Multiple hydrogen (H_2) and sulfur (SO_2) sensing materials were developed with different morphologies: those are tungsten trioxide (WO_3), molybdenum trioxide (MoO_3), and molybdates including $SrMoO_4$ and $MgMoO_4$. Double perovskites synthesized by solid state reactions such as strontium magnesium molybdates ($SrMgMoO_6$) and strontium magnesium tungstates ($SrMgWO_6$). The chemistry and structure was found to be very influential on the morphology of these particles; therefore, the processes of forming by hydrothermal methods will be more thoroughly discussed in the results and discussion section.

Crystal structures of the as-synthesized powders were characterized by X-ray diffraction (XRD) at room temperature using a Panalytical X-Pert Pro diffractometer (PW 3040 Pro) with Cu Kα radiation with a scan rate of $2°min^{-1}$. Their morphologies were examined using a scanning electron microscope (JSM-7600F SEM) and a transmission electron microscope (JEM-2100 TEM) to confirm crystallinity and particle size. The EDS spectra were obtained using an Oxford INCA 350 connected to JEOL 7600F SEM. X-ray photoelectron spectroscopy (XPS) was also conducted to have deeper information regarding the weather or not secondary phase formation and/or chemical state analysis. The X-ray source was operated at 15 kV and 25 watts using Al Kα (1486.6 eV) radiation. The films were analyzed by a combination of 117.40 eV survey scan and 23.50 eV detailed scans of relevant peaks. A 0.5 eV step was used for the survey scan and a 0.05 eV step for the detailed scan. Prior to spectral analysis all coatings surfaces were cleaned to remove atmospheric and post-depositional contamination with Ar ion sputter cleaning at 2 kV accelerating voltage for 30 seconds. During measurement, the analysis chamber pressure was maintained at ($\sim 10^{-11}$ Torr). Gold (Au) is used as reference with the binding value 84.5 eV if it is possible; otherwise carbon (C) is used for reference at the value 284.5 eV.

B. Electrochemical Testing of the Nanomaterials

In order to test the effectiveness of each of the pyrochlore nanomaterial compositions and composite systems without needing to develop a micro-patterning process, a macro-scale sensor architecture was used. The electrodes were screenprinted using a platinum ink and fired at 1200˚C for 1 hour to give the electrodes stability during testing. The Pt ink was made from precipitated amorphous Pt powder from Technic Engineered Powders with particle sizes around 1 μm. The electrodes below have a total length of 10 mm with teeth width and teeth spacing of 0.25 mm as seen in Figure2.

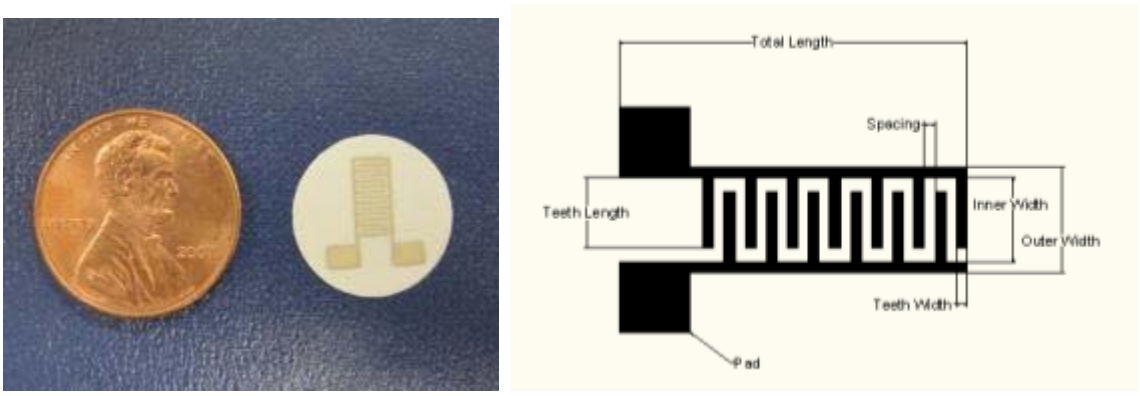

Figure 2: Screenprinted macro sensor design for initial testing with a sensing area 8 mm long and 3 mm wide. Electrode teeth have a total length of 10 mm with width and spacing of 0.25 mm.

Alumina substrates were made with pre-drilled holes located on the electrode pad to allow for the sensor leads to be threaded through for better attachment to the pad. These substrates were fabricated using standard tape-casting methods. The resultant tapes were cut and sintered to 1450˚C for 2 hours. Dried hydrothermal powders of the sensing materials were mixed with a terpineol/ethyl cellulose based ink vehicle, J2M, (63/2, Johnson Matthey, UK) with a solids loading of ~60 vol%. Each of the material systems were painted on the electrodes with a total film thickness of 100 µm. In order to promote adhesion and reduce cracking of the film, the sensors were placed on a hotplate at 65˚C to dry and then fired in the furnace at a heating rate of 1.5˚/min to 600˚C, 5˚/min to 1200˚C and held for 1 hour. Each zirconate sensor was tested at 600˚C, 800˚C, and 1000˚C. Figure 3 represents the total heat cycle the sensor experiences during the test. The sensor was held at each of these temperatures for 6 hours; therefore, by the conclusion of the test, the sensor was held at the elevated temperature for over 20 hours.

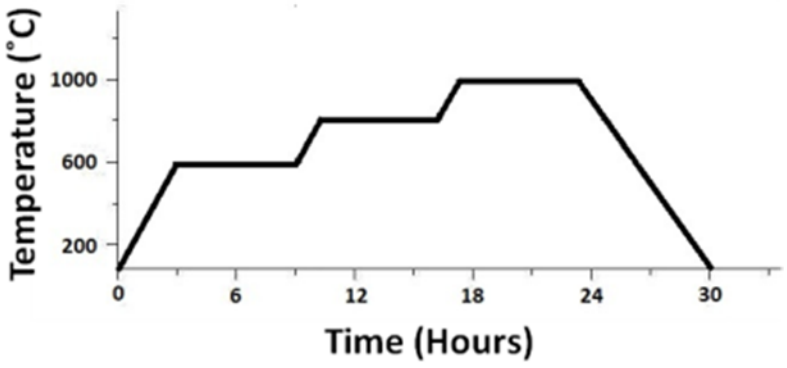

Figure 3: Thermal cycle for sensor testing with dwell times at 600˚C, 800˚C and 1000˚C for over 6 hours.

During each of temperature plateaus, the following flow-rate cycle was used to test for sensitivity, response time, recovery, and repeatability.

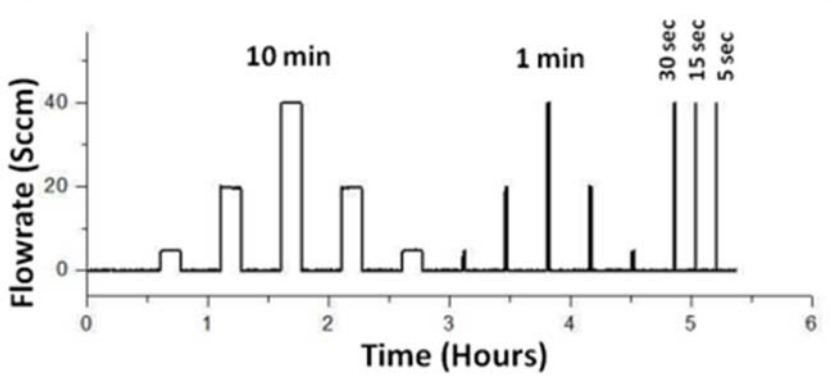

Figure 4: Flowrate of H_2 for macro sensor test consisting of pulses of various ppm level (such as 500, 2000, and 4000 ppm of H_2). The test allows for comparison of sensitivity, repeatability, and response time.

The pyramid in Figure 4 increased the ppm level of H_2 from 500, 2000, to 4000 ppm and decreases back down to 500 ppm. Each of these ppm levels are held for 10 min and then the pyramid is repeated with a hold time of 1 min. A final pulse of 4000 ppm for 30 sec, 15 sec, and 5 seconds was used to test further for response and recovery time. Each gas used was research grade purity from Valley National Gases (Fairmont, WV) and passed through 6 micron filter before being introduced to the mass flow controllers. A 0.5% H_2/N_2 mixture was used as the sensing gas and was balanced with a pure N_2 and O_2 for a given atmosphere and hydrogen content.

Sierra Smart Trak 2 mass flow controllers connected to a National Instrument DAQ board controlled by Labview was used to control the gas flow to the tube furnace. The complete Labview program can be seen in Appendix B. Each mass flow controller was calibrated to the gas mixtures purchased from Valley National Gases with flow rates from 0-50 sccm with an accuracy of ±0.5% of full range. Stainless steel tubing with Swagelock fittings was used to connect the gas tanks to the test stand. A picture of the completed stand can be seen in Figure 5.

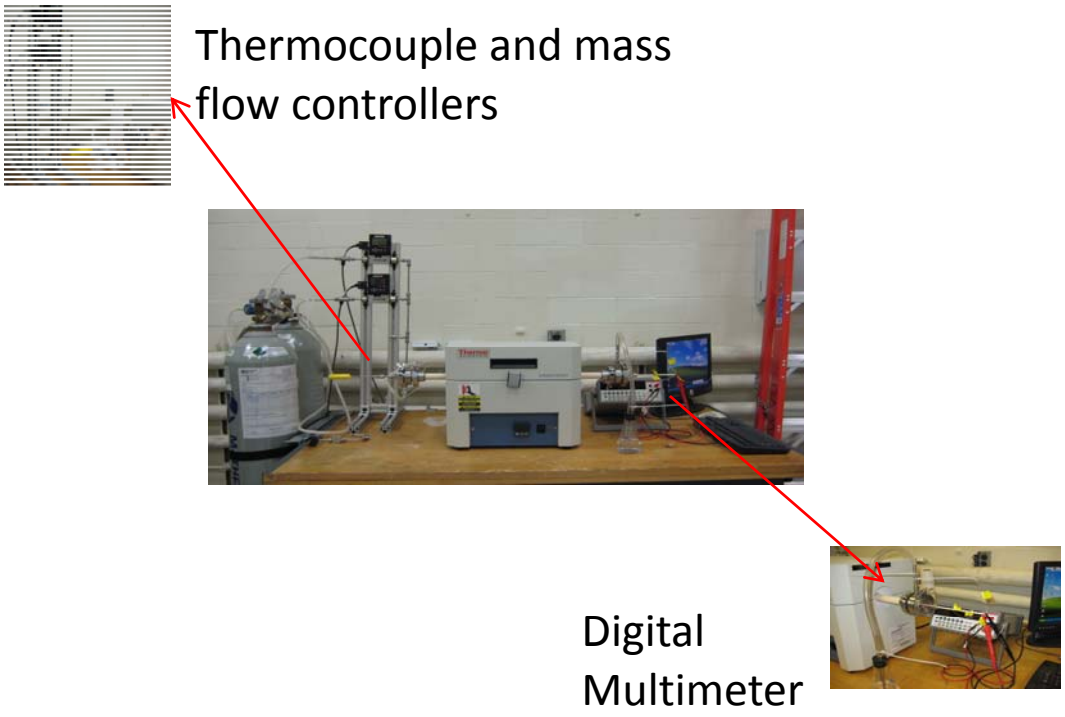

Figure 5: Experimental test setup for hydrogen sensing. Smart track mass flow controllers and the data acquisition were controlled by a LabView program. Sensor was located in middle of the tube furnace attached to Pt wires where the DMM was attached.

A Keithly 2100 DMM was used to measure the resistance of the sensor during the entire test. The material systems were tested for high temperature H_2 sensing, and these results will be discussed below in the results and discussion section.

II. RESULTS AND DISCUSSION:

A. Sensing Nanomaterials

1) Characterization of Zirconate Nanomaterials

Initially, the $Gd_2Zr_2O_7$ was synthesized by dissolving 16.16 g of gadolinium carbonate into 200 g of 1 mol solution of nitric acid, then co-precipitating the gadolinium and zirconium chloride in a basic solution of 100 g TMAOH and 500 ml DI water keeping the pH above 10. This solution was centrifuged and washed several times until the conductivity of the solution was reduced to below 10 mS/cm. 100 g of this solution was placed into the autoclave at temperatures from 180-260˚C for hold times of 1-8 h. Figure 6 shows the XRD results of the powders formed from these initial conditions.

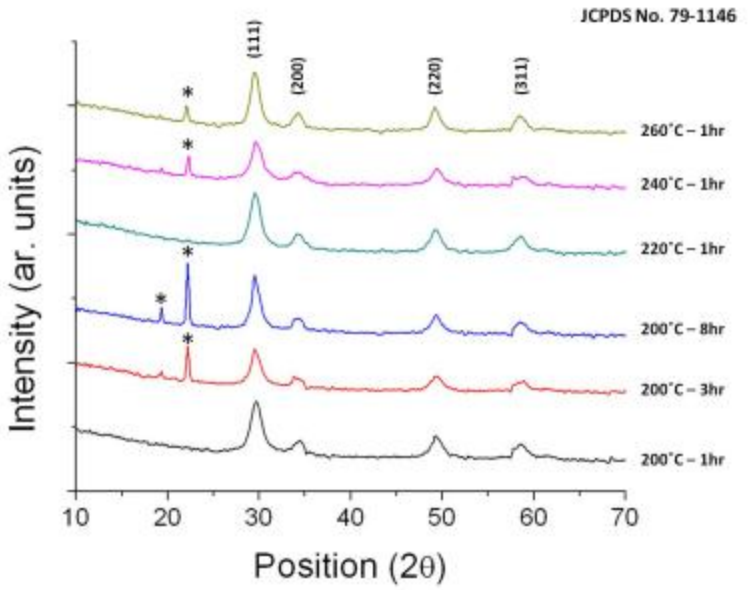

Figure 6: XRD analysis of hydrothermally produced $Gd_2Zr_2O_7$. All patterns are consistent with a defective fluorite crystal structure
***TMAOH**

All the products synthesized by low temperature hydrothermal reactions are identified as the defective fluorite-type crystal structure (JCPDS No. 79-1146). The additional peaks indicated are TMAOH salts (JCPDS No. 38-1727) left over from insufficient washing of the solution after the hydrothermal process. The broadness of the peaks suggests nano-sized nature of the particles. Using equation 14, the particle sizes were calculated to be 5.79 nm, 7.18 nm, and 7.71 nm for 160, 200, and 240˚C for one hour. To confirm these calculations, TEM images were taken of each of the solutions and can be seen below in Figure 7. The sample preparation method was similar to that used for the nano-SnO_2 particles discussed previously, and this same methodology will utilized for other nanomaterials synthesized throughout the rest of this work.

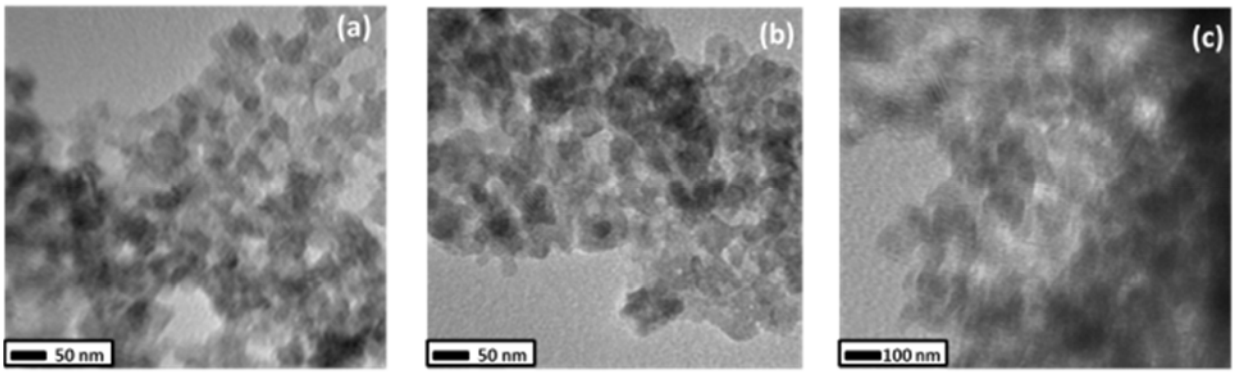

Figure 7: TEM of hydrothermally produced GZO at (a) 160˚C, (b) 200˚C, (c) 240˚C. Particle size is increased from 3 to 6 nm by increasing the hydrothermal temperature from 160 to 240˚C.

Very little difference in particle size was seen between these conditions with average

particles sizes of 3, 4, and 6 nm at 160, 200, and 240˚C respectively. Powder (2 g) from the 240˚C hydrothermal synthesis was taken and 1 g was calcined to 800˚C at a heating rate of 3 deg/min and held with an isothermal hold for 10 h. The other gram of powder was calcined to 1200˚C for 10 hours to monitor coarsening and stability of the grains at high temperature. The XRD of these two powders are presented in Figure 8.

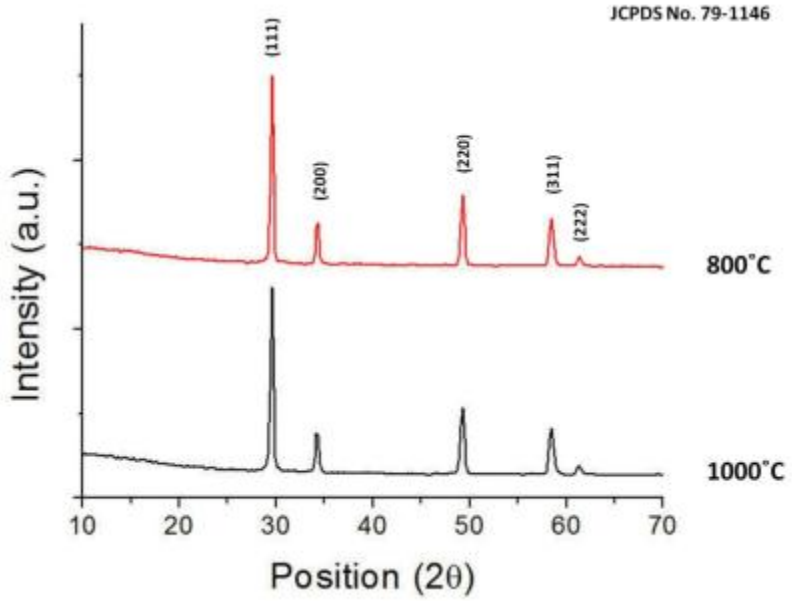

Figure 8: Normalized XRD of calcined zirconate powder. Particle size increases significantly by sintering to 1000˚C compared to as dried hydrothermal powder

By calcining the powder, the main peaks become much sharper, indicating a growth in particle size. The particles sizes for each of the calcination steps were calculated to be 27.26 nm at 800˚C and then 23.3 nm for 1000˚C. To confirm this, SEM images of the powders were taken by pressing sintered powder onto a carbon tab and coated with an Au/Pd coating (Figure 9).

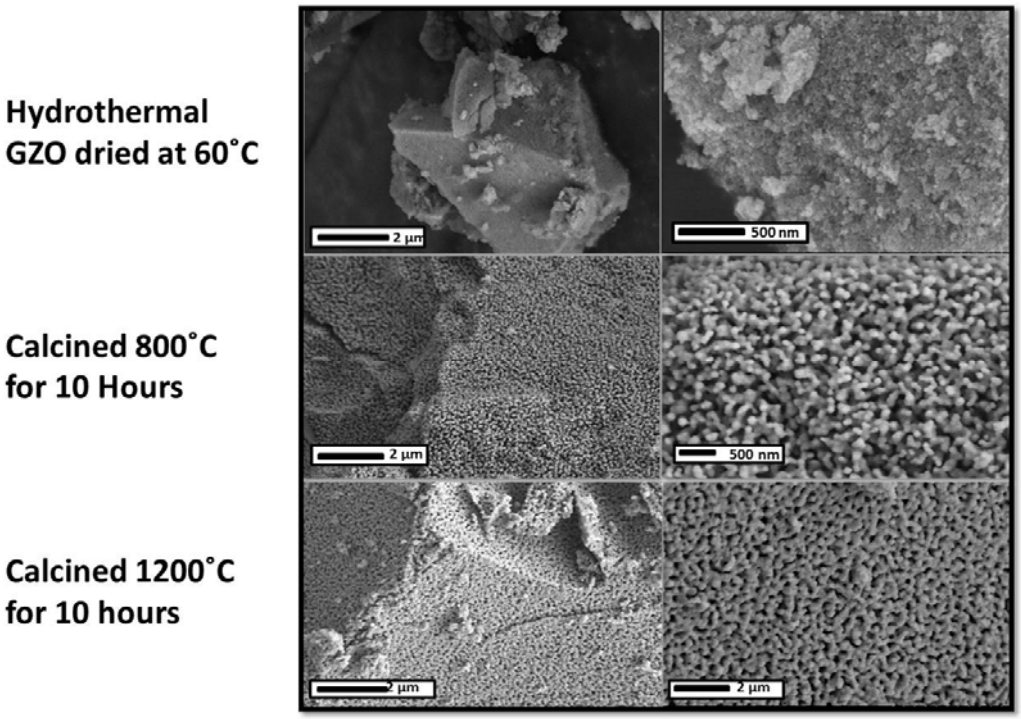

Figure 9: SEM images of sintered Y doped zirconate. Particle size increases from 8 nm (hydrothermal powder) to 80 nm when sintered to 1200˚C for 10 hours

The original GZO particles had an average size of 6-8 nm determined from stereology from TEM micrographs presented in Figure 7. Over the thermal treatment, these particles coarsened to an average particle size of roughly 50 nm at 800˚C (10 hrs) and coarsened to an average particle size of roughly 80 nm at 1200˚C (10 hrs). BET analysis was used to further investigate the change in particle size and porosity of the GZO when thermally processed for 1 to 25 hours at 1200˚C. Table 2 shows that the particles grow from 8nm (hydrothermal powder) to 240nm when sintered. SEM micrographs showed particles around 100 nm when sintered, therefore, it is likely that these particles are agglomerated causing the particle size from BET to be larger. It also indicates that the particle size remains stable when processed up to 24 hours. In addition to the coarsening effects, the density of the loose powder also changed significantly. When processed for 24 hours, the volume of pores decreases from 0.01 to 0.0065 cm^3/g, meaning the material is coarsening and sintering at elevated temperatures which could limit diffusion of the gas through the sensing material during testing and decrease the overall active surface area for gas-solid electrochemical reactions. If the porosity continued to decrease as the sensor is held at high temperatures for an extended time, the sensitivity of the sensor could decrease throughout the life of the sensor.

Table 2: BET analysis of un-sintered and sintered gadolinium zirconate

	Hydrothermal 260˚C 1 hour	Sintered 1 Hour	Sintered 24 Hours
BET Surface Area	114.7 m^2/g (8.27nm)	3.5 m^2/g (244nm)	3.6 m^2/g (234nm)
Adsorption SA of pores	119.5 m^2/g	2.639 m^2/g	2.793 m^2/g
Volume of pores (adsorption)	0.1942 cm^3/g	0.0107 cm^3/g	0.00654 cm^3/g

Substituting on the A- and B- sites of GZO assisted in the stabilization of the material into either a defective fluorite or pyrochlore phase depending on the ratio between the A to B cation radius ratio, which can increase the ionic conductivity of the system. Guillen et al. found that when smaller lanthanides such as yttrium (R_{Gd} =1.053Å > R_Y = 1.019) was substituted on the A-site, an anion deficient fluorite phase was preferred. When larger lanthanides, such as Sm (R_{Gd} =1.053Å < R_Y = 1.079), was used as a dopant, the pyrochlores phase was preferred. In order to investigate the effect of the change in the A- to B-site ratio on the H_2 sensing effects at high temperature, yttrium and samarium were substituted into the A-site to attempt to increase the disorder of the system.

A similar hydrothermal process was used to for doped-gadolinium zirconate as pure gadolinium zirconate. Along with gadolinium carbonate and the zirconium chloride, 2.55 grams of samarium carbonate was dissolved in 10 grams of 1 molar nitric acid and 10 ml of DI water and added to the gadolinium and zirconium mixture before precipitating into a basic solution of TMAOH and DI water keeping the pH above 10. For the yttrium doped zirconate, 1 g of yttrium nitrate hydrate was dissolved in 25 g of DI water an added to the gadolinium/zirconium solution before precipitated. Both $Gd_{1.8}Y_{0.1}Zr_2O_7$ and $Gd_{1.6}Sm_{0.4}Zr_2O_7$ solutions were processed in the autoclave at 240˚C and 260˚C for 1 hour. The autoclave was filled with approximately 100 grams of solution at a solids loading (based on post loading) of 2 wt%. These temperatures were chosen based on the formation of a defective fluorite phase in pure GZO at these hydrothermal conditions as a starting point to see if disordering of the structure pushed the phase to a pyrochlore structure. An XRD analysis was performed on each of the powders and compared to JCPDS No. 79-1146, which represents gadolinium zirconate in pure pyrochlores form, shown in Figure 10.

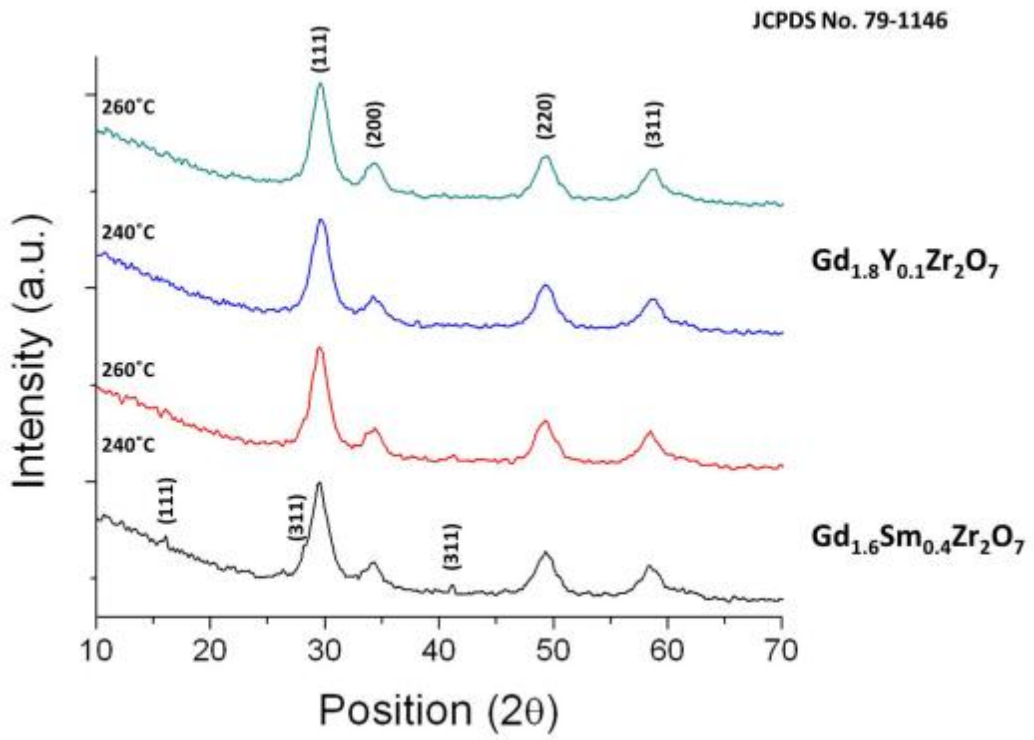

Figure 10: XRD analysis of Sm and Y doped zirconates. Scans are consistent with a single phase defective fluorite phase.

As demonstrated by previous research, replacing gadolinium with a smaller lanthanide forms a defective fluorite phase at 240˚C and 260˚C for one hour dwell times, while larger lanthanide starts to form a pyrochlores phase as indicated by the superstructure reflections at ~15˚ and 42˚. Further examination of the XRD scans indicated a peak shift with the dopant on the a-site structure. A shift toward larger angles is seen with the addition of the smaller lanthanide yttrium with a reduction of the lattice parameters. An opposite result is seen with the replacement of Gd with the larger lanthanide samarium as seen in Table 3.

Table 3: XRD and lattice parameters for pure and doped gadolinium zirconate

	$Gd_2Zr_2O_7$	$Gd_{1.8}Y_{0.1}Zr_2O_7$	$Gd_{1.6}Sm_{0.4}Zr_2O_7$
(111) Peak Position (2θ)	29.4512	29.4910	29.3972
d-spacing (Å)	3.0376	3.0289	3.0384

It is possible that either higher temperatures or longer hold times could be used to stabilize the structure into a pyrochlores phase. Because a pyrochlores phase was seen with the samarium-doped zirconate at the lower 240˚C temperature hydrothermal process, the yttrium-doped solution was processed with hydrothermal temperatures from 260˚C to 300˚C with dwell times of 1, 5, and 10 h to see if the structure changed due to the change in hydrothermal conditions. The XRD results of these hydrothermal reactions are seen for an A-site, Y-doped GZO.

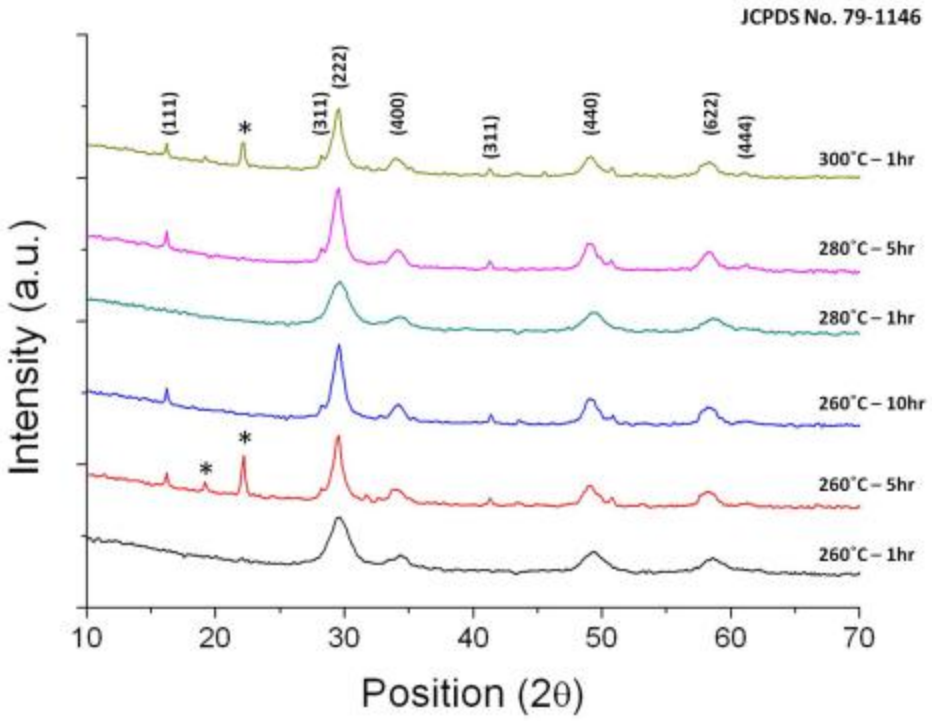

Figure 11: Hydrothermal reaction study on $Gd_{1.8}Y_{0.1}Zr_2O_7$ (*TMAOH residual salts). As the hydrothermal temperature is increased, a pure pyrochlores structure begins to form.

As shown Figure 11, the hydrothermal method can produce GZO in either the fluorite or pyrochlore phase depending on the temperature and hold times. The pyrochlore phase is confirmed by the presence of the superstructure reflections, (111) and (331) at ~15˚ and 38˚ (2θ) respectively. The absence of these superstructure reflections suggests that the lower the reaction temperatures used, then longer reaction times are needed to reach a pure pyrochlore phase. For short reaction times, a temperature of at least 300˚C is needed to form an ordered pyrochlores structure of the GYZ composition.

A similar analysis was performed with the samarium doped gadolinium zirconate ($Gd_{1.2}Sm_{0.8}Zr_2O_7$) were the solution was placed in the autoclave at 260˚C for 1 h, 5 h, and 10 h. XRD and TEM were performed on the washed, with ethanol, and dried (60˚C overnight) solutions from the autoclave. XRD analysis confirms a single phase fluorite phase at 1 and 5 h dwell times and a pyrochlore phase at 10 h which was also seen with the yttrium substituted material.

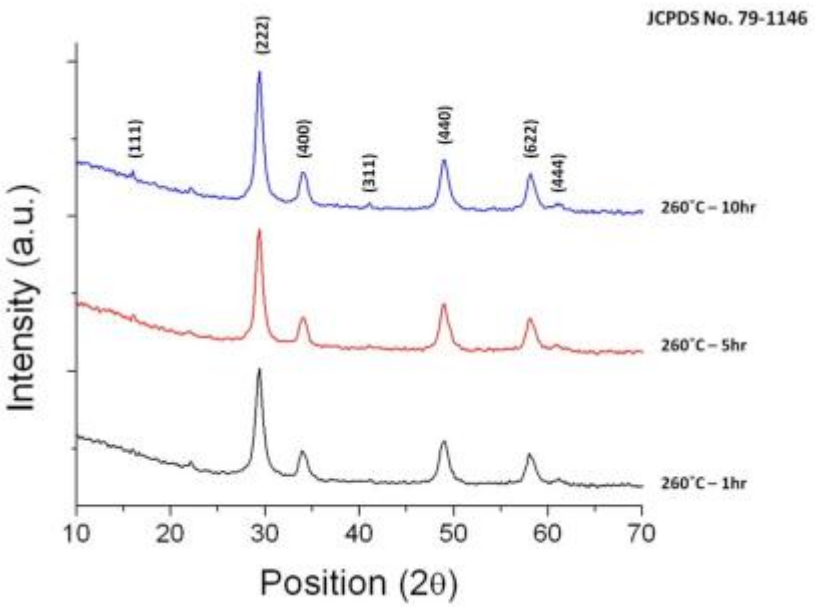

Figure 11: XRD analysis for Sm doped gadolinium zirconate at 260˚C with various dwell times. As the dwell time is increased to 10 hours a pure pyrochlores phase is formed.

Table 4: Particle size calculation from the Scherrer equation and the corresponding TEM images from the powder samples.

	1 Hour	5 Hours	10Hours
Scherrer Calculation	8.64 nm	9.27 nm	10.86 nm
TEM	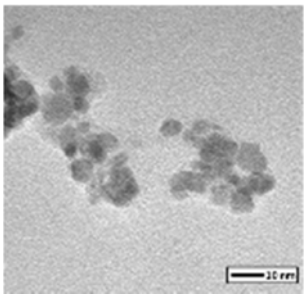	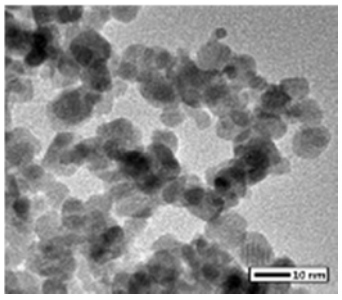	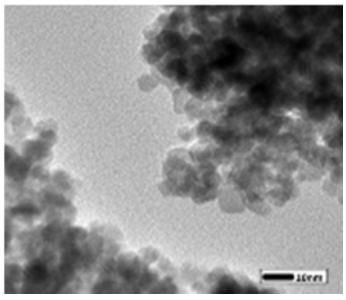

.

The particle size from 1 h to 10 h increased from 8 nm to 10 nm. Longer hold times or higher pressures may be needed to increase the particles size to 20 nm or larger to increase the stability of the nanoparticles at high temperature. Because the Scherrer calculations are consistent with the TEM images, this technique will continually be used to determine the effect of the hydrothermal parameters on the particle size.

Knowing that the A-site substitution has an effect on the conduction of these zirconate materials, a short study was conducted on the amount of dopant that could be successfully

substituted via the hydrothermal route. Solid solutions of $Gd_{2-7}Ln_yZr_2O_7$ with Ln = Sm^{3+} where co-precipitated and processed in the autoclave at 260˚C for one hour. A shift of the (311) peak in Figure 12, the expected enlargement of the lattice parameters when Gd is replaced by a larger cation (103). The d-spacing of the (111) peak increased from 3.03764 Å to 3.03836 Å to 3.0391 Å when the Sm dopant is increased from 0, 0.4, to 0.8, respectively.

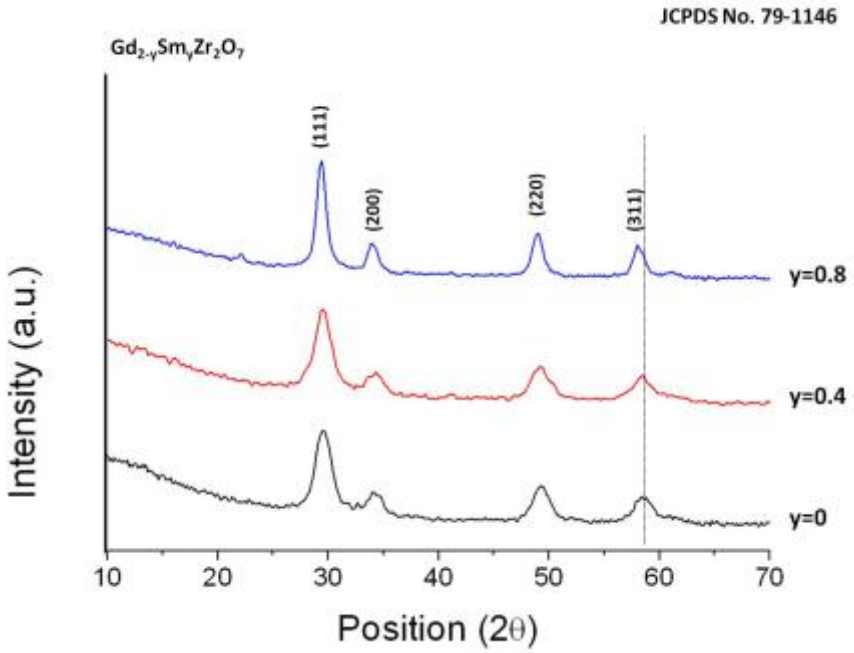

Figure 12: XRD patterns of Sm doped gadolinium zirconate via hydrothermal run at 260˚C held for one hour. Peak shift suggests enlargement of lattice structure indicating the formation of a solids solution between the dopant and zirconate.

The second material system being synthesized is a series of gadolinium tin based pyrochlores. Co-precipitation of the reagents was performed by dissolving 11.15 g of gadolinium carbonate into 85 g of 1 molar nitric and 80 g of DI water. Tin dichloride (3.8 g) was dissolved in 80 g of DI water with 1 gram of 1 molar nitric. These two solutions were mixed under magnetic stirring and the pH was altered using TMAOH. Three separate pH solutions were tested for the optimal conditions for a pure pyrochlores phase. The autoclave was filled with 140 g of solution and processed at 260˚C for one hour to determine the optimal conditions. Figure 13 shows the phase transition for $Gd_2Sn_2O_7$ going from pH=6 to 12.

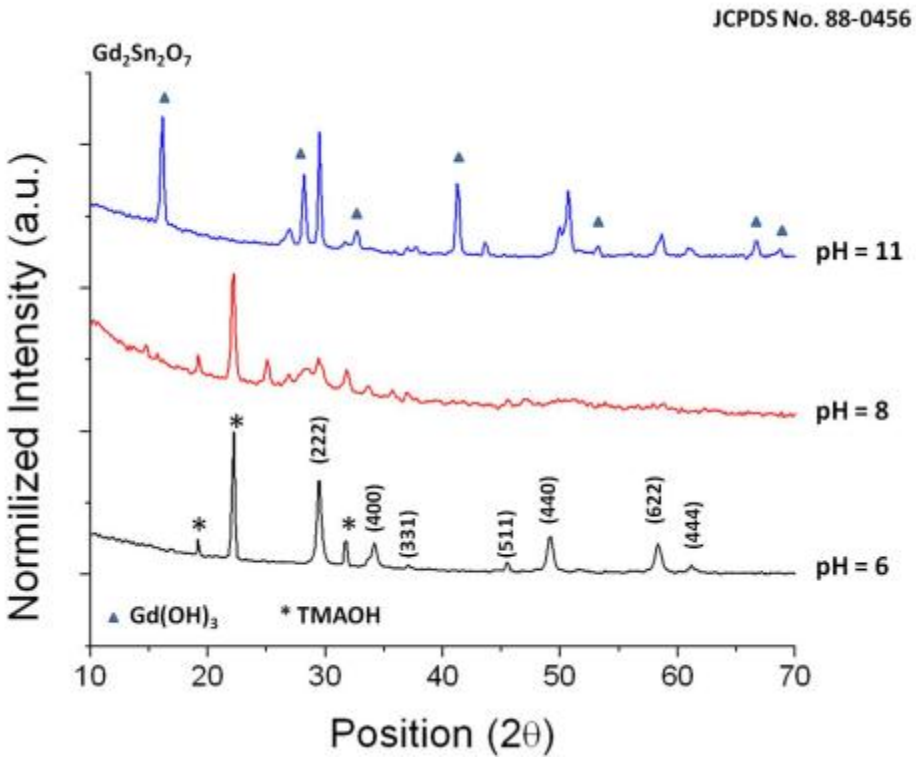

Figure 13: Formation of $Gd_2Sn_2O_7$ via hydrothermal method. Multiple phases are seen at a pH of 11 but as the pH is decreased a single phase pyrochlores structure forms.

The pH of the solution plays a vital role in the formation of a pure pyrochlore phase of these stannate materials as noted by Zhang *et al.*[104A]. Solutions that are more basic (pH>10) form a mixed phase of $Gd_2Sn_2O_7$ and $Gd(OH)_3$. A pH between 6 and 10 gives an amorphous solution with no clear phase, while reducing the pH to around 6 results in a single phase of the pyrochlore structure. Zeng *et al.* related the dependence of phase to the amount of mineralizer via the following reactions for lanthanum stannate.

$$Sn^{4+} + 3H_2O \leftrightarrow H_2SnO_3 + 4H^+ \quad (2)$$

$$H^+ + OH^- \rightarrow H_2O \quad (3)$$

$$H_2SnO_3 \overset{\Delta}{\leftrightarrow} SnO_2 \downarrow + H_2O \quad (4)$$

$$La^{3+} + 3OH^- \rightarrow La(OH)_3 \downarrow \quad (5)$$

$$2La(OH)_3 + 2H_2SnO_3 \rightarrow La_2Sn_2O_7 \downarrow + 5H_2O \quad (6)$$

In the presence of a mineralizer (pH=1), NaOH for the above reaction, the hydrolysis effect of the Sn^{4+} ions is represented by equation 2. When the low pH solution of the lanthanum nitrate and tin chloride is processed in an autoclave, the secondary phases of SnO_2 precipitate out as indicated by equation 4. Small amounts of OH^- left in the solution are counteracted by H^+ ions via equation 3. When the pH of the solution is adjusted above 10 (1 M NaOH) the H^+ ions form from strong hydrolysis effect of Sn^{4+} ions were counteracted

by OH^- which breaks the equilibrium of equation 2 and results in the precipitation of $La(OH)_3$ via equation 5. When the appropriate pH is reached, the single phase $La_2Sn_2O_7$ precipitates, as represented by equation 6. Since the chemical state and solubility of La and Gd are very similar, then it is assumed that the reaction path within the various pH regimes for $Gd_2Sn_2O_7$ was similar. The results from this limited study confirmed this hypothesis.

A solution of gadolinium zirconate with both A- and B-site dopants was prepared with Sm and Sn respectively. 3.04 g of samarium carbonate hydrate and 1.46 g of tin dichloride in an aqueous solution were added to the gadolinium and zirconium solution, as discussed in the previous sections. The pH was again adjusted with TMAOH, similar to that demonstrated for the pure gadolinium stannate, in order to relate the pH, final structure, and amount of tin dopant for a pyrochlore material. The pH of the solution was changed from just below neutral (6) to basic (12) to measure the effects on phase formation. The XRD results of the powder produced for three pH values can be seen in Figure 1.

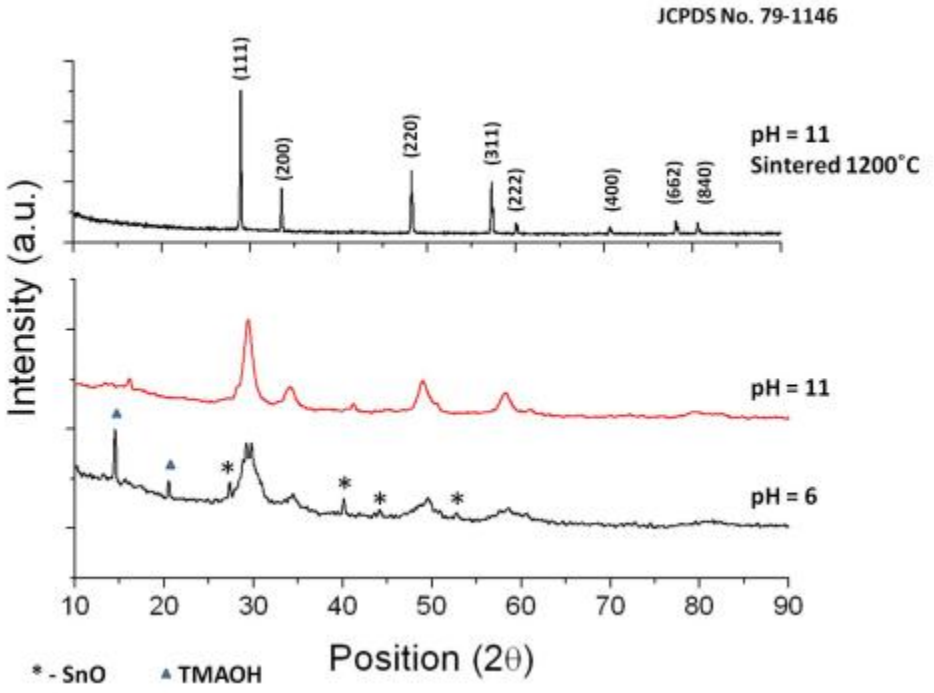

Figure 1: Phase transformation due to change in pH for $Gd_{1.6}Sm_{0.4}Zr_{1.9}Sn_{0.1}O_7$. For a single phase pyrochlores formation a pH of 11 is needed.

The pH of the solution had an opposite effect compared to the $Gd_2Sn_2O_7$ solutions. Lower pHs created a mixed phase of $Gd_{1.6}Sm_{0.4}Zr_{1.9}Sn_{0.1}O_7$ and SnO (JCPDS No. 72-1012), while a very basic pH of 11 created a single fluorite phase of the doped zirconate.

The last material that was synthesized was $Gd_2Ti_2O_7$. A pH of 6 was chosen as a starting point since Sn and Ti have similar solubility. When the solution was held for 5 hours at 260˚C the TiOCl does not fully form a solid solution with the gadolinium. When the dwell time was doubled in the autoclave, the powder is still fairly amorphous until sintered to 1200˚C into $Gd_2Ti_2O_7$ as seen in Figure 2.

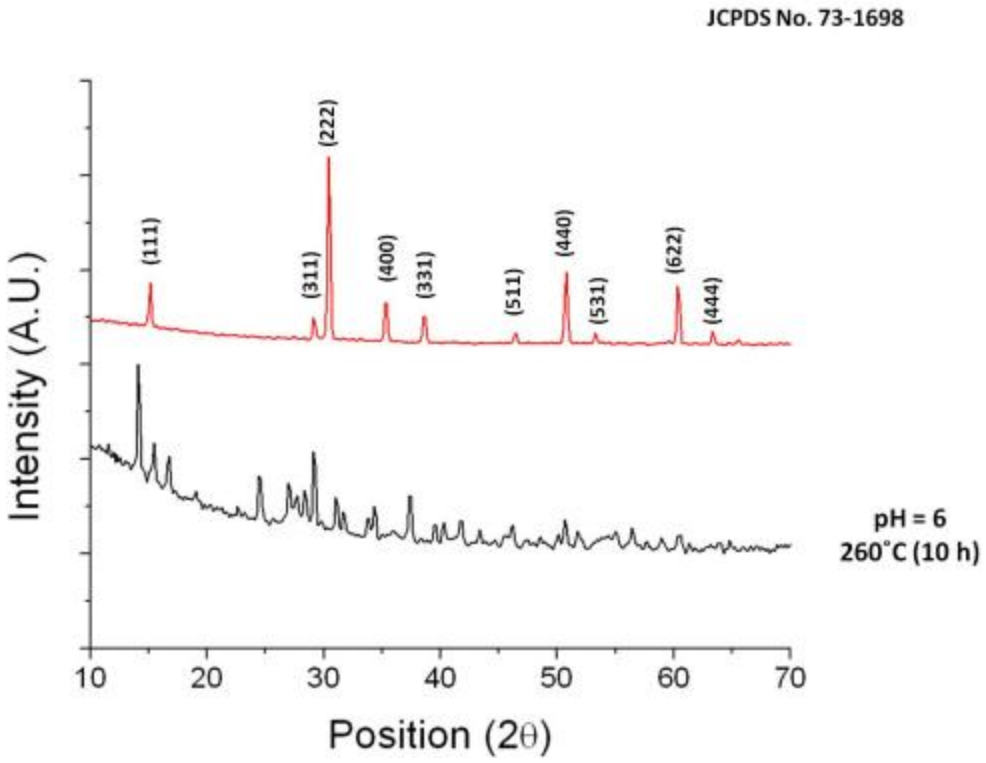

Figure 2: XRD scan of hydrothermally produced $Gd_2Ti_2O_7$, dried and sintered to 1200˚C

2) Characterization of Tungstate and Molybdate Nanomaterials

Magnesium Molybdate ($MgMoO_4$)

$MgMoO_4$ is the first ternary material that was synthesized in this work by the hydrothermal method. The results of the procedures that will be described resulted in various morphologies; the variations were primarily controlled by the slight manipulation of the hydrothermal processing parameters. Due to extremely scarce literature regarding the liquid-based synthesis of molybdate compounds, different dwell time, starting compositions and hydrothermal processing temperatures were included as into experimental parameters investigated. In the only available source in the literature synthesis of the $MgMoO_4 \cdot H_20$ and the $MgWO_4 \cdot H_2O$ was realized by mild hydrothermal conditions by transferring the equal volumes of Na_2MoO_4, and $MgCl_2$ and Na_2WO_4 and $Mg(NO_3)_2$ into Pyrex tubes and keeping at 155°C for three days. Although authors conducted detailed crystal structure analysis there was no morphological data available [182B]. The first experiments included the combination of 1.48 g of magnesium nitrate hexahydrate ($Mg(NO_3)$, ACS, 98.0-102.0%, CAS# 13446-18-9, Alfa Aesar) and 1.23 g of ammonium molybdate tetrahydrate ($(NH_4)_6.Mo_7O_{24}$, ACS, 81-83% as MoO_3, CAS# 12054-85-2, Alfa Aesar) were dissolved in deionized and decarbonized water in separate beakers. After mixing the two solutions, the pH of the final mixture was adjusted to 7 by drop wise addition of ammonium hydroxide. The final mixture was transferred to an autoclave lined with teflon and processed at 80°C for 8 h; however, the final product was mixture of MgO and MoO_3. SEM micrographs presented in Figure 16 show the microstructure and morphology of the as-synthesized powder, as well as, the EDS analysis

of the powder surface. The as-synthesized material showed neither nano-crystalline structure nor stoichiometry of the desired powder.

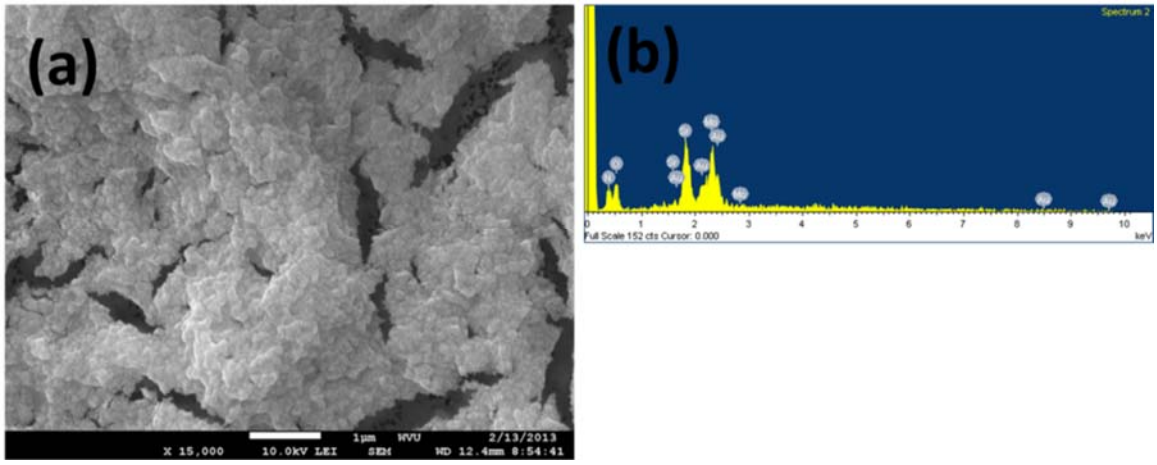

Figure 16: (a) SEM micrograph of $MgMoO_4$ (b) EDS analysis of the as-synthesized powder.

Due to the unsuccessful results obtained in the first experiments, the magnesium nitrate ($(Mg(NO_3)$, magnesium nitrate hexahydrate, ACS, 98.0-102.0%, CAS# 13446-18-9, Alfa Aesar) and ammonium molybdate ($(NH_4)_6.Mo_7O_{24}$) were replaced with magnesium chloride ($MgCl_2$, magnesium chloride hexahydrate, ACS, 99.0-102.0%, CAS# 7791-18-6, Alfa Aesar)) and sodium molybdate (Na_2MoO_4), respectively. In the second set of experiments, 1.02 g of $MgCl_2$ and 1.21 g of Na_2MoO_4 were dissolved in 30 ml of deionized and decarbonized water in separate beakers. After mixing the two solutions, the final pH of the 60 ml solution was adjusted to 11 by drop addition of ammonium hydroxide. The final product was transferred to autoclave with PTFE liner and processed at 160°C for 12 h under auto-generated pressure.

The as-synthesized white powder was washed with de-ionized and de-carbonized water as the pH adjusted to a pH of 10.5 in order to hinder un-wanted agglomeration. The washing procedure repeated until the conductivity (σ) of the solution measured less than 10 $mS.cm^{-1}$. Figure 17a-b shows the microstructure of the as-synthesized powder after drying at 80°C. The SEM micrograph shows that the material is composed of loosely agglomerated particles with a thickness of 20 nm. The material showed very poor crystallinity as can be seen from Figure 17-c that presents the XRD powder diffraction data together with reference JCPDS card numbers of 01-072-2153 for $MgMoO_4$ and 01-047-0457 for hydrogen molybdenum oxide hydrate ($HMoO_3.H_2O$) with for comparison purposes and identification of the obtained powder. As the XRD peak analysis indicates, the material has poor crystallinity and materials contains hydrated molybdenum oxide rather than the desired $MgMoO_4$ phase.

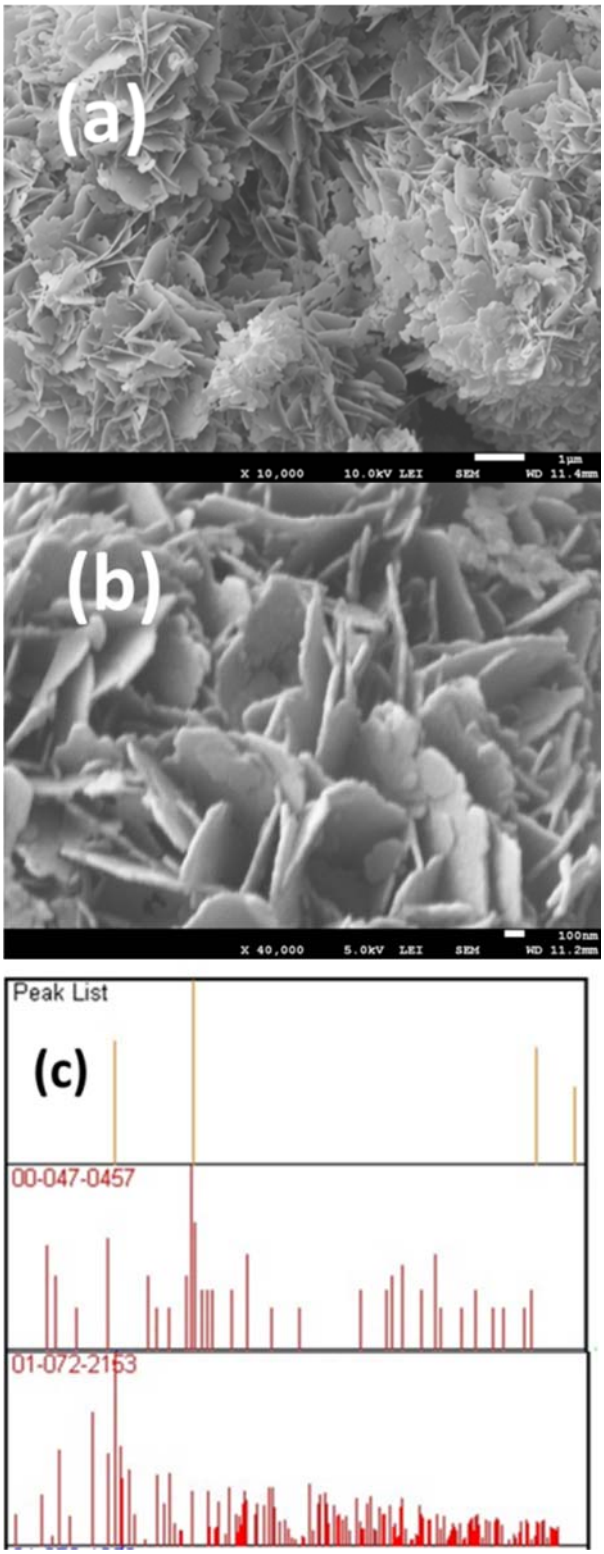

Figure 17: SEM micrographs of the as-synthesized $MgMoO_4$ (a) general view (b) high magnification (c) XRD of the as-synthesized powder.

Another set of experiments was made by increasing the ion concentration to double the previous level. 2.04 g of $MgCl_2$ and 2.420 g of Na_2MoO_4 were dissolved in 30 ml of

deionized and decarbonized water in separate beakers. After mixing the two solutions together, the final pH of the 60 ml solution was adjusted to 11 by drop wise addition of addition of ammonia. The final product was transferred to autoclave with PTFE liner and processed at 160°C for 12 h under auto-generated pressure. Figure 18-a, -b and –c show the micrographs of the as-synthesized powder. As can be seen, the as-synthesized material does not have a homogeneous morphology. Two distinct microstructures were shown in the micrographs. The particles had a flake-like morphology with a wall thickness of ~50 nm. The other morphology was spherical with an average size of 50 to 100 nm. Figure-d shows the XRD powder scan of the as-synthesized material together with reference JCPDS card numbers of MoO_3 and $MgMoO_4$, 01-076-1003 and 01-072-2153, respectively. As the XRD pattern reveals, the material might be interpreted as either MoO_3 or $MgMoO_4$ due to the lack of observed distinguishable $MgMoO_4$ peaks especially located between 2θ values of 10° and 20°. The EDS analysis of the nano-flakes presented in Figure 18-e showed that nano-flakes contain Mg; however, the spherical particles did not. Therefore, it can be concluded that the as-synthesized material consisted of segregated MoO_3 and Mg deficient $MgMoO_4$ compounds.

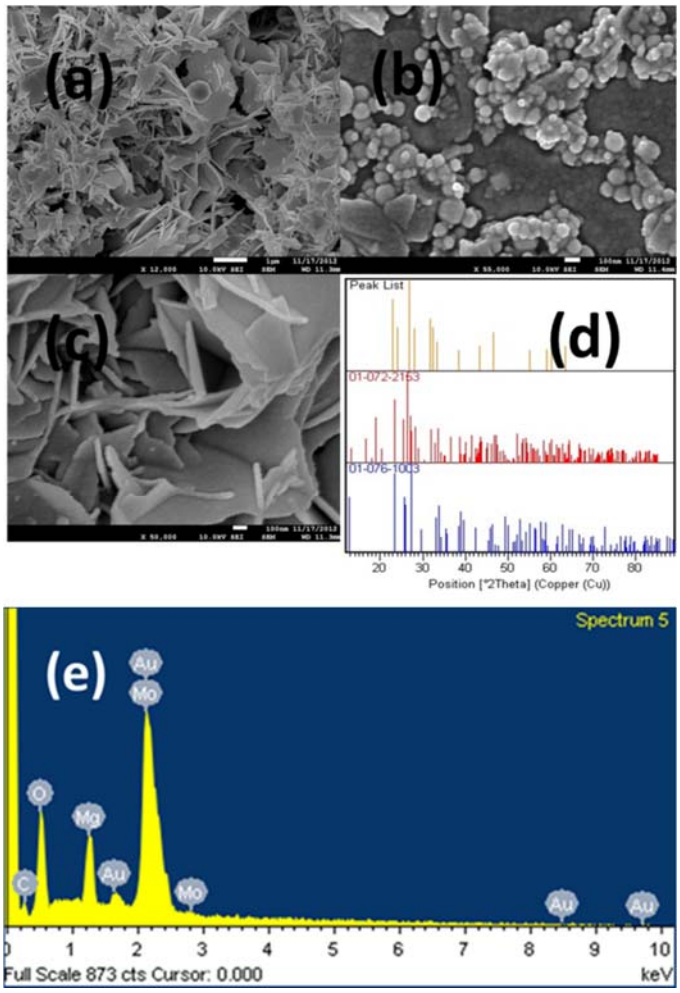

Figure 18: SEM micrographs of the as-synthesized $MgMoO_4$ (a-b) general view (c) high magnification (d) XRD of the as-synthesized powder with reference MoO_3 and $MgMoO_4$ patterns (e) EDS analysis of the as-synthesized nano flakes.

Further experiments were conducted by decreasing the pH concentration of the final solution. Similar solutions were synthesized using 2.04 g of $MgCl_2$ and 2.420 g of Na_2MoO_4 dissolved in 30 ml of deionized and decarbonized water in separate beakers. After mixing the two solutions, the final pH of the 60 ml solution was adjusted to 9 by drop wise addition of ammonia hydroxide. The final product was transferred to the autoclave and processed at 160°C for 12 h under auto-generated pressure. The SEM micrograph of the as-synthesized product presented in Figure 19 reveals that the morphology of the particles were not homogeneous. It can be concluded that lowering the pH increases the material packing, as well as, the amount of the spherical shaped particles. The crystallinity of the nano size flakes must have deteriorated.

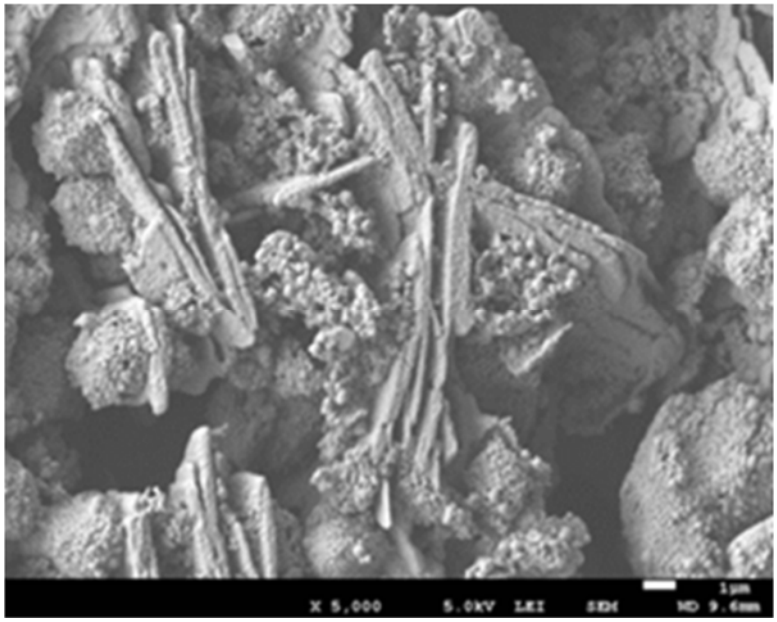

Figure 19: SEM micrographs of the as-synthesized $MgMoO_4$ (4^{th}).

Further experiments investigated the effect of the ion concentration and pH of the solution on the final product. 2.72 g of $MgCl_2$ and 3.22 g of Na_2MoO_4 were dissolved in 30 ml of deionized and decarbonized water in separate beakers. After mixing two solutions in another beaker, the final pH of the 60 ml solution was adjusted to 11.5 with the addition of ammonium hydroxide. The final mixed product was transferred to the autoclave and treated at 160°C for 12 h under auto-generated pressure. Figure 19-a and –b show the microstructure of the as-synthesized material. As the micrographs reveals, the as-synthesized material displays a blade-like morphology with a 10-20 nm thickness and 50-500 nm width and 2000-3000 nm length. XRD scan of the as-synthesized product was compared against the JCPDS 01-084-1686 reference pattern, which is the only reference pattern available in the literature for Magnesium Molybdenum Oxide Hydrate ($MgMoO_4$ (H_2O)). The XRD spectra is shown in Figure 19-c. The data shows that the material has excellent crystallinity without any further heat treatment. Figure 19-d shows the EDS spectrum of the as-synthesized product. As the spectrum reveals, Mg and Mo co-exist and almost have same intensity when the blades are targeted at various locations.

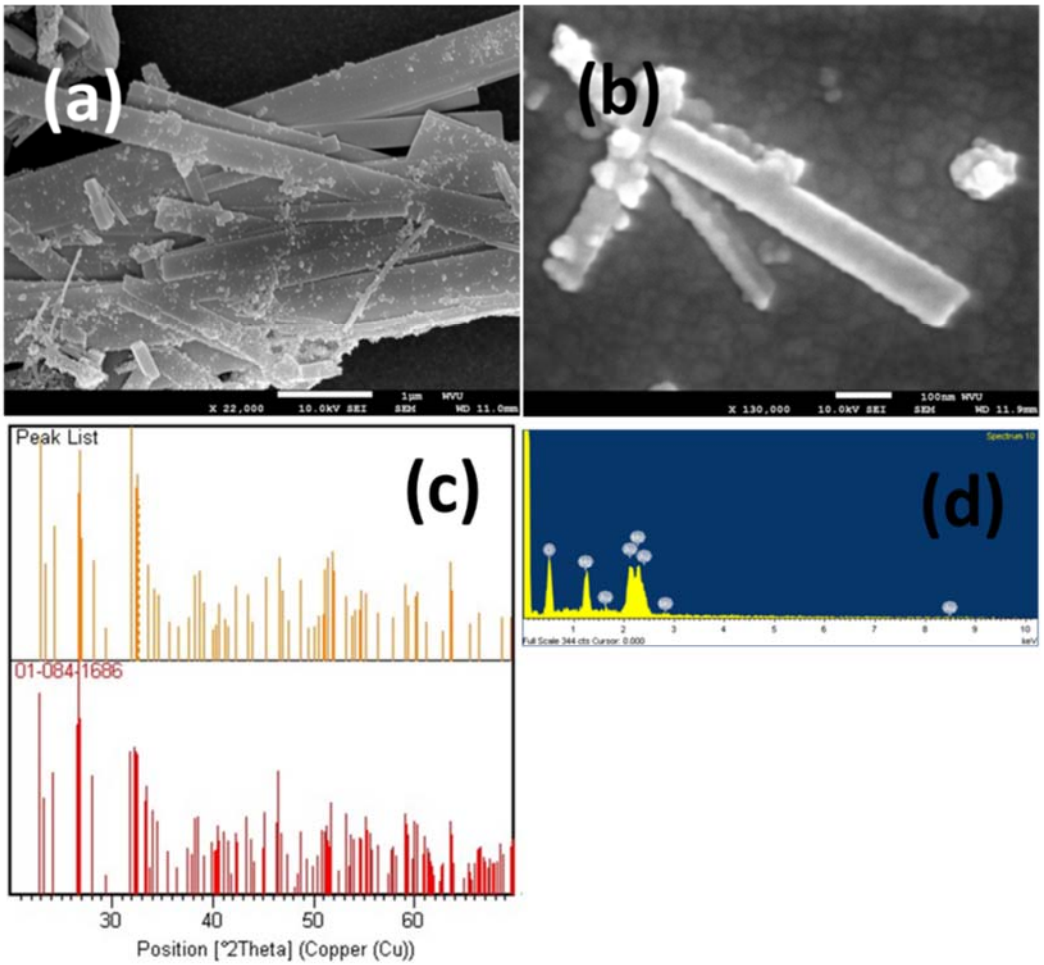

Figure 19: (a-b) SEM micrographs of the as-synthesized $MgMoO_4$ (5^{th}). (c) XRD of the as-synthesized powder with reference $MgMoO_4$ pattern (d) EDS analysis of the as-synthesized nano bundles.

Strontium Molybdate ($SrMoO_4$)

$SrMoO_4$ is a promising material for wide range of applications [177B, 178B]. Figure 20 shows the results of the different hydrothermal routes use to synthesize $SrMoO_4$ nanomaterials. There are two main reasons behind allocation time and effort for different morphological formation of the same compound with the same level of crystallinity and stoichiometry. The first reason was to optimize the surface to volume ratio and reduce the packing density as much as possible by creating anisotropic microstructure, which is desirable for gas sensing applications. The second reason is to define the potential material microstructure possesses low diffusional kinetics in order word high temperature sintering resistive morphology. Liu et *al.* used a simple approach to synthesize $SrMoO_4$ by precipitating it out of ammonium molybdate and strontium nitrate over an aluminum (Al) substrate as a dense thick film over a 24 h reaction time without any surfactants. It was reported that controlling the thickness of the sheets was possible via changing the concentrations of the solutes. Another point should be emphasized in this work is that a very simple deposition/synthesis technique was realized however in all cases the general view of microstructure was densely packed leaves/sheets of material covered over a metal substrate [183B]. A facile, low temperature and novel hydrothermal method was developed

and employed to synthesize the $SrMoO_4$ nanomaterial in this work. In all of the synthesis processes, the same precursor materials were utilized; strontium nitrate ($Sr(NO_3)_2$, (Strontium nitrate, ACS, 99.0% min, CAS# 10042-76-9, Alfa Aeser)) and ammonium molybdate ($((NH_4)_6{\cdot}Mo_7O_{24}){\cdot}4H_2O$, Ammonium molybdate (para) tetrahydrate, 99%, CAS #12054-85-2, Alfa Aesar). In all cases, 1.48 g of strontium nitrate and 1.23 g of $((NH_4)_6{\cdot}Mo_7O_{24}){\cdot}4H_2O$ were dissolved in de-ionized and de-carbonized water in separate beakers. A clear solution was obtained after magnetic stirring the two solutions for 15 min. The pH of the final solution ranged from 4.5 to 5.5. The final product was transferred into a 300 ml PTFE sealed autoclave and kept at 180°C, 120°C and 80°C for 12 and 8 h, respectively with 3°C heating and cooling rate in all cases. After mixing the two solutions, the final pH of the solution was adjusted to the corresponding values indicated in

Table through the addition of ammonia hydroxide. The as-synthesized white powder was washed with de-ionized and de-carbonized water in order to hinder the un-wanted agglomeration. The washing procedure was repeated until the conductivity (σ) of the solution measured less than 10 $mScm^{-1}$.

Table 5 provides the details of the hydrothermal synthesis parameters. Figure 20 shows the micrographs of the as-synthesized $SrMoO_4$ nanomaterials for the nano-teeth, nano-sheet, nano-flowers and nano-rice. Distinctly different morphologies of the same compound were obtained by modifying the hydrothermal reaction temperature, precursor concentration, and pH. The isothermal hold time for the autoclave reaction during the synthesis of the nano-teeth, nano-sheets, nano-flowers and nano-rice were the same (12 h); however, the reaction temperatures were 180°C, 120°C and 80°C, respectively. The decrease in the temperature and increase in the ion concentration affected the growth rate of the co-precipitated $Sr^{2+}$and MO_4^{2-} ions and decrease in feature size and packing density was observed as a general trend. As can be seen from Figure 20-c and –d, at the same pH, higher ion concentration and lower hydrothermal processing and time and temperature resulted in more anisotropic powder morphology in addition to reduction in packing density. This can be attributed to hydrothermal processing time and temperature since it is not likely to see that increase in ion density lead loosely packed microstructure. Liu et *al.* reported that increase in the ion concentration resulted in further increase in the thickness of the sheets and density of the structure as well [183B].

Table 5: Process parameters for hydrothermal synthesis of $SrMoO_4$ with different morphologies.

Morphology	Precursor Materials	Processing Time (h) and Temperature (C°)	Precursor ion concentration (M)		pH
			Anion (MO_4^{2-})	Cation (Sr^{2+})	
Nano-teeth	$Sr(NO_3)_2$ $((NH_4)_6.Mo_7O_{24}){\cdot}4H_2O$	12 & 180	0.0134	0.0934	8
Nano-sheet	$Sr(NO_3)_2$ $((NH_4)_6.Mo_7O_{24}){\cdot}4H_2O$	12 & 120	0.025	0.175	8
Nano-flowers	$Sr(NO_3)_2$ $((NH_4)_6.Mo_7O_{24}){\cdot}4H_2O$	8 & 80	0.05	0.35	8
Nano-rice	$Sr(NO_3)_2$ $((NH_4)_6.Mo_7O_{24}){\cdot}4H_2O$	8 & 80	0.05	0.35	10

Decreasing hydrothermal processing temperature from 180°C to 120°C and doubling the anion and cation concentration from 0.0134 to 0.025 and from 0.094 to 0.175, respectively lead to more isotropic growth as the morphology changed from nano-teeth instead nano-sheet with highly symmetrical spatial growth. It should be noted that the same hydrothermal processing time and temperature, yet different pH level caused drastic change in growth mode and rate. The morphology of the powder has evolved from nano-flower like loosely packed anisotropic structure to densely packed and isotropic rice shaped morphology.

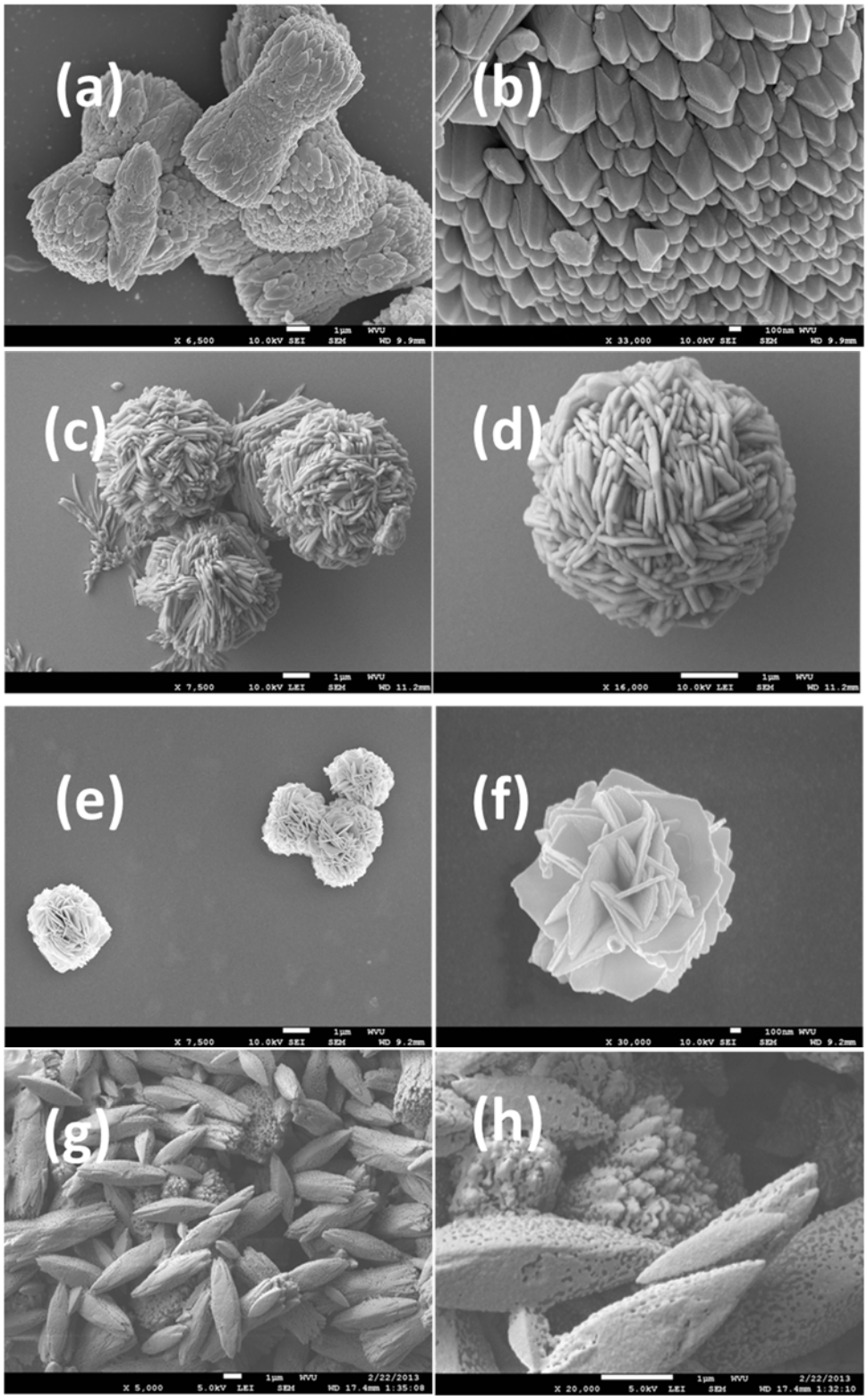

Figure 20: SEM micrographs of (a-b) nano-teeth (c-d) nano-sheet (e-f) nano-flowers and (g-h) nano-rice.

Figure 21 shows the unit cell of the tetragonal scheelite-type structure of the strontium molybdate. The scheelite structure was originally termed after the $CaWO_4$ mineral. For the

structure, the Mo is surrounded by 4 O^{2-} in tetrahedral system; on the other hand, the Sr is surrounded by 8 O^{2-}octahedral symmetry. The scheelite structure is mainly made of MoO_4^{2-} and Sr^{2+} as a charge compensator. It can be concluded that oxygen vacancies have important consequences over the electronic and chemical behavior of the compound. The missing oxygen is most likely coming from the c-directions within the structure, since the Sr-O bonds are weaker than that of Mo-O bonds.

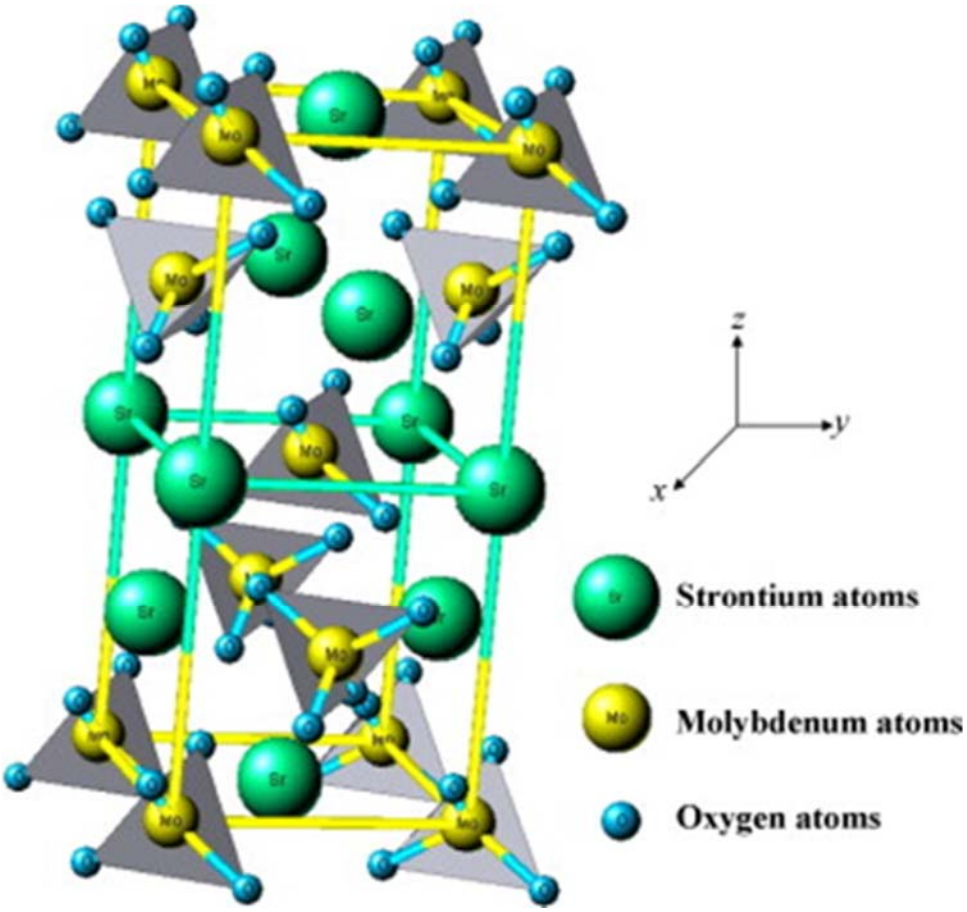

Figure 21: Schematic presentation of Scheelite tetragonal $SrMoO_4$ unit cell [184B].

All of the as-synthesized nano-structures were subjected to XRD analysis to investigate the for crystal structure of each powder. Figure 22 presents the XRD graph of the as-synthesized $SrMoO_4$ nano-flower, and the JCPDS reference pattern (00-008-0482) for the $SrMoO_4$ was also included in the figure. As can be seen in the Figure 22-a, the measured peaks show an excellent match with the reference peaks. All of the diffraction peaks can be indexed with the JCPDS card number 00-008-0482. The sharp and high intensity diffraction peaks of the as-synthesized nano-flower powder showed good crystallinity with no secondary phases present. In all other cases (nano-sheets, nano-teeth and nano-rice), such an excellent match between the measured and reference XRD data were also obtained.

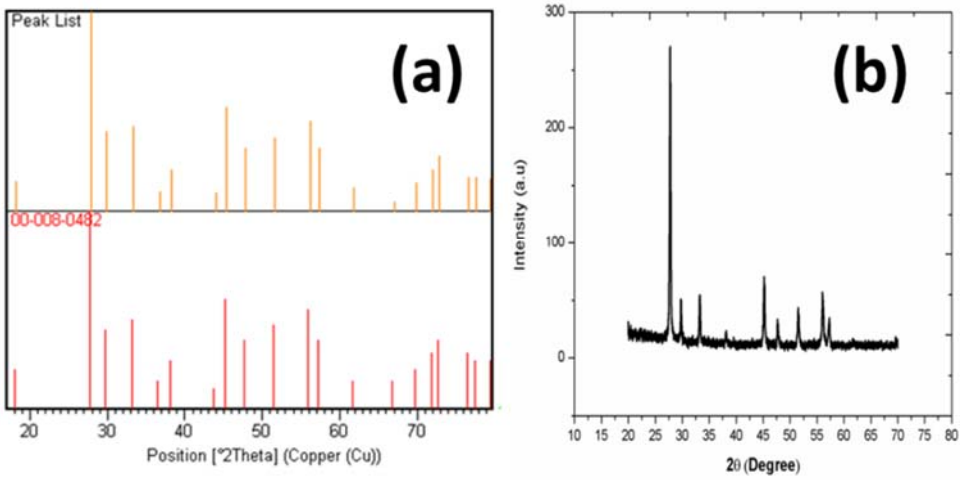

Figure 22: (a) Comparative XRD graph of $SrMoO_4$ nano-flowers with the reference *XRD JCPDS card number 01-085-0586* (b) Measured XRD spectrum of the $SrMoO_4$ nano-flowers.

The XRD pattern was interpreted and specified as the highly anisotropic tetragonal structure of $SrMoO_4$ (JCPDS 00-008-0482). The pattern matches the pattern perfectly with the lattice parameters a=b=5.3944 and c=12.0200. Using the plane spacing and Bragg`s law for diffraction, the lattice parameters were calculated and given in Table 6. As compared to the position given in the JCPDS 00-008-0482, the calculated a- and c-parameters of the as-synthesized nanomaterial show residual stress, which can be attributed to the oxygen vacancies, charge compensation and cation columbic interactions.

Table 6: Comparison of calculated cell parameters and reference data (00-008-0482).

In this study	**In JCPDS no. 00-008-0482**
Crystal system: Tetragonal unit cell, a=b≠c, α=ß=γ=90° (112) plane, peak position; 27.892°, $d_{(112)}$ = 3.1988 Å (204) plane, peak position; 45.302°, $d_{(204)}$ = 2.0008 Å (004) plane, position; 29.907°, $d_{(004)}$ = 2.9989 Å	Space group: I41/a, Space Group number: 88, Scheelite (112) plane, peak position; 27.664°, $d_{(112)}$ = 3.2220 Å (204) plane, peak position; 45.116°, $d_{(204)}$ = 2.0080 Å (004) plane, position; 29.696°, $d_{(004)}$ = 3.0060 Å
a=b=5.3236 Å, c= 12.123 Å, a/c= 0.4391 Å	a=b=5.3944 Å, c= 12.020 Å, a/c= 0.4487 Å
Crystalline Size with Scherrer formula: 35 nm	NA

The quantification of the missing oxygen as well as unlattice/interstitial oxygen are completed by XPS analysis. It was proved that material contains Mo^{5+} up to 5%. It can be concluded that as-synthesized product showed oxygen vacancies and interstitial oxygen to large extent. XPS analysis was conducted in order to quantify the amount of interstitial and/or unlattice oxygen as well as, the amount of Mo in the Mo^{+5} chemical state. The XPS would also assist in determining the level of glassy secondary-phase formation that cannot be detected by XRD. Varhegyi et *al.* stated that the oxygen adsorption to the stoichiometric surface would be very difficult to compare to the non-stoichiometric counterpart [60B]. Another point to be deserved before interpreting the photoelectron spectra of the O, Mo and Sr in $SrMoO_4$ nano-flowers is the stability of adsorbed (chemically or physically) oxygen on the transition metal oxide surface. Not only is the bulk structure important, but also the surface chemistry in the end will be important, especially for gas sensor

applications. The oxygen ion and vacancy content on the surface will dictate much of the functionality of a gas sensor. As stated by Hirschwald, $O^-_{2\,ads}$ to O^-_{ads} transformation occurs at about 200°C and desorption of the latter occurs at 250°C [12B, 185B]. According to this data, the functionality of the semiconducting oxides terminated after 300°C, however although the sensitivity decreases to great extent after 300°C, there many semi conducting metal oxide type sensor in the literature function after 300°C. Therefore, due to functionality of the sensors equipped with the semiconducting sensing material, it might be concluded that the amount of the adsorbed oxygen is less compared to the low temperature regime, and/or involvement of the lattice oxygen and interstitials oxygen. Azad et *al.* [12B] concluded that oxygen cannot be chemisorbed onto an undoped and/or stoichiometric oxide surface since oxygen ions cannot be adsorbed unless their negative charge is compensated by varying density of states on the surface. A similar discussion was stated by Varhegyi et *al.* In addition; Korotcenkov [16B] approved of this conclusion, but also discussed the possibility of a small fraction of monolayer chemisorption for an n-type semiconductor surface. Abraham et *al.* concluded that relatively stable and large amount of interstitial oxygen formation between isolated cation (Mo or W) tetrahedrals in $PbWO_4$ and $CaMoO_4$ tetragonal scheelite structures [155B, 186B]. In addition to that Esaka reported that scheelites containing interstitials oxygen would be more reducing resistant (compositionally stabile) under low oxygen partial pressure environments [187B]. From the point of thermodynamic considerations, a defect structure containing of missing oxygen ions and interstitials oxygen can allow the semiconducting metal oxide to function upon exposure to reducing gas atmospheres at elevated temperatures.

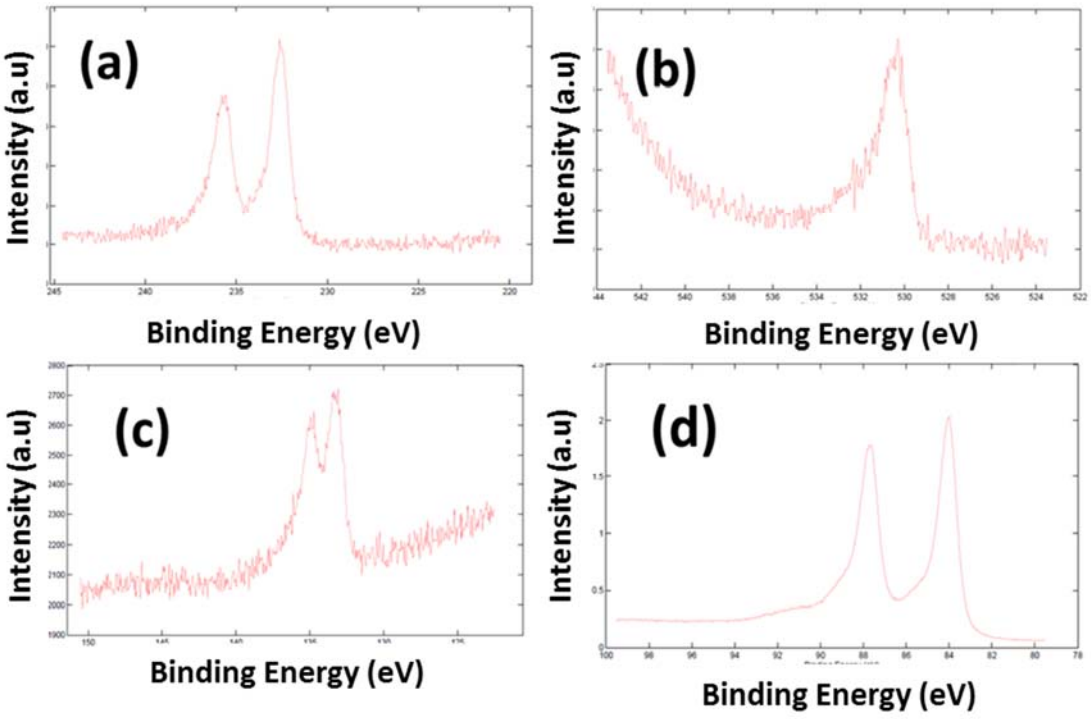

Figure 23: XPS core spectrum of Mo (a) and (b) O^{2-} (c) Sr in as-synthesized $SrMoO_4$ nano-flowers and (d) Au 4f photoelectron line as a reference.

Figure 23 presents the photoelectron spectrum of the Mo, O and Sr in $SrMoO_4$ nano-flowers, as well as, the Au 4f spectrum as a reference. Figure 23-b shows the core photoelectron line of the O^{2-}. After deconvolution of the O 1s spectrum, two main chemical states of the oxygen were determined. Those are located at 529.82 and 531.24 eV. The former is in a good match with the literature for $SrMoO_4$, while the latter for interstitial/adsorbed (un-lattice) oxygen [188B, 189B] Sr $3d_{5/2}$ and $3d_{3/2}$ photoelectron lines are located at 132.60 and 132.40 eV, respectively. Figure 23-a shows the XPS spectrum of Mo 3d doublet. For molybdenum (Mo), the main photoelectron lines were positioned at 232.92 and 236.02 eV. The convolution of the Mo doublets proved that Mo^{5+} chemical state exists in the as-synthesized material and located at 231.9 and 234.96 eV. The deconvolution of the O and Mo main photoelectron lines made it possible to quantify the relative amount of the corresponding chemical states. Approximately 20% of the O^{2-} was located on un-lattice (adsorbed/interstitial) locations. Un-lattice oxygen can be thought of as adsorbed O^{2-} down to 10 nm from surface, which is a characteristic sampling depth of the XPS.

Core Structure Approach

Constructing porous networks of 1-D materials such as, nanowires and nanorods have attracted much attention recently due to their intriguing electronic, optical and mechanical properties. The construction of porous network made of nanomaterials is of great importance to sensor designers due to its theoretical extraordinary gas permeability capability and high surface area. A limited number of reports appeared on synthesize of transition metal oxide structures such as ZrO_2 in 1-D structures. Wang et *al.* synthesized ZrO_2 nanorods by using $ZrNO_3$ and NH_4F, but the material synthesized was 25 in length and 5-10 nm in width, looks more like beans not nanorods. Another attempt made by Pei *et al.* The ZrO_2 was hydrothermally synthesized by zirconium hydroxide, however material showed non-homogeneous morphology changing form nanorods to spherical particles, however Xia et al made successful attempt and synthesized ZrO_2 nanowires by using electrospinning [190B, 153B, 191B, 192B, 193B]. Ogihara et *al.* tried to use carbon nanofibers as template for synthesizing Al_2O_3, SiO_2 and ZrO_2 nanotubes, wall thicknesses of them were 30, and 10-20 nm [194B]. Unfortunately nano scales materials succumb to coarsening and sintering effects at high temperature, therefore it is the challenge to keep the nanomaterials nano at elevated temperatures (>800°C). There are two possible solutions to hinder/stop coarsening, those are Zener pinning by benefiting from the influence of fine-refractory-stabile particles on the movement of low and high angle grain boundaries by exerting a pinning pressure. The second technique is growth/deposite of the nanoscale material over a a core refractory-oxide structure preferentially with epitaxial match. İn current study both both technques were used in order to stop/hinder the coarsening of the nanomaterial for sensor applications.

MgO nanorods

MgO nano-rods were synthesized via a hydrothermal method by repeating the procedure described by Ghamdi et *al.* [195B]. The hydrothermal process begins with the synthesis of a gel which was initiated synthesized by dissolving 6.44 g of magnesium acetate (Magnesium acetate tetrahydrate, ACS, 98.0-102.0%, CAS 16674-78-5, Alfa Aesar) into 75 deionized and decarbonized water and magnetically stirred 30 min. 1.2 gram urea (ACS,

99.0-100.5%, CAS 57-13-6, Alfa Aesar) first dissolved in again deionized and decarbonized water**.** The urea was added drop-wised added to the previously prepared magnesium acetate solution, and after stirring the total 100 ml solution for 10 min, the solution was added into autoclave sealed with teflon for 2 h at 180°C. The measured pH before the autoclave hydrothermal process was 7.5; after the hydrothermal run the pH was 9. The washing procedure repeated until the conductivity (σ) of the solution measured less than 10 $mScm^{-1}$. Figure 24-a, -b and -c show the SEM micrograph of the as-synthesized MgO nanorods with different magnifications. In order to evaluate the high temperature sintering/coarsening resistance of the compound, the powder was held for 5 h at 1000°C. The final microstructure is shown in the Figure 24-d. As can be seen from the SEM micrograph, the MgO nano-rods did not coarsen and retained their needle-like morphology at the temperature regime of interest.

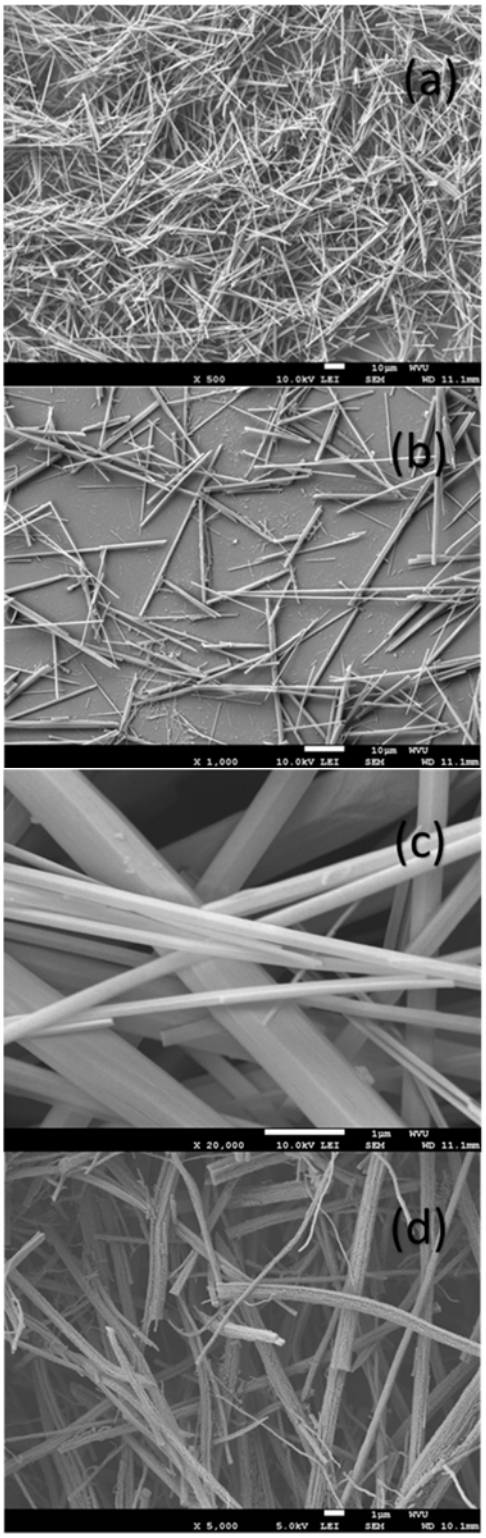

Figure 24: MgO nanorods as-synthesized (a-c) and (b) heat treatment after 5 h at 1000°C.

Figure 25 shows the EDS spectrum of the as-synthesize powder. The detected Au in the spectrum originated from the sputtered coating needed to eliminate charging effects during

the SEM investigation of the surface. The EDS data shows nearly a 1 to 1 ratio, which is what would be expected for the stoichiometry of the MgO. The XRD data showed the material has very good crystallinity (not included).

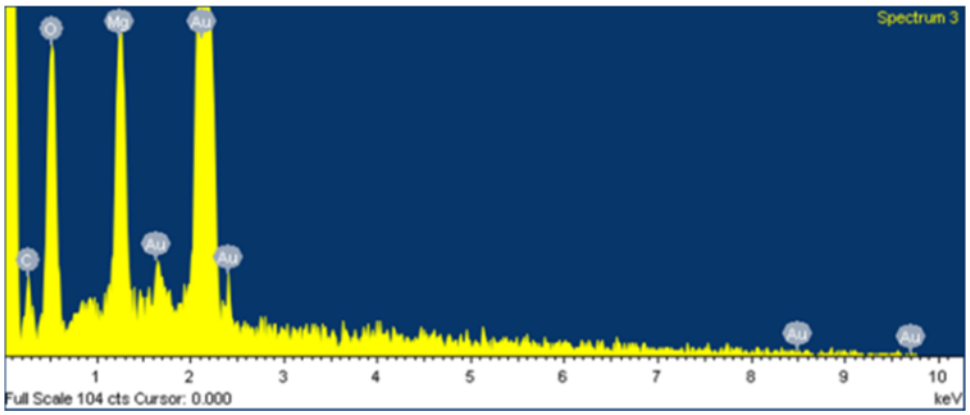

Figure 25: EDS spectrum of as-synthesized MgO nanorods.

B. Sensor Testing of the Sensing Nanomaterials

1) Sensor Testing of Zirconate Nanomaterials

Initial hydrogen testing was performed on the common sensing material SnO_2. SnO_2 ink was painted on Pt electrodes and heated at 3˚/min to 1000˚C and held for one hour to stabilize the microstructure of the sensor. In this test, the sensors were heated and held at 400˚C, 600˚C, and 800˚C for 5 hours at each temperature in an oxygen free atmosphere. When the temperature was stabilized, 0.5% H_2/99.5% N_2 (5000 ppm H_2) was pulsed through the test chamber for 15, 5, and 1 min twice at each time interval with 40 min of pure nitrogen in between each pulse to test for response time and repeatability. Test results for an undoped macro SnO_2 (Alfa Aesar) hydrogen sensor can be seen in Figure 26 for the three temperatures.

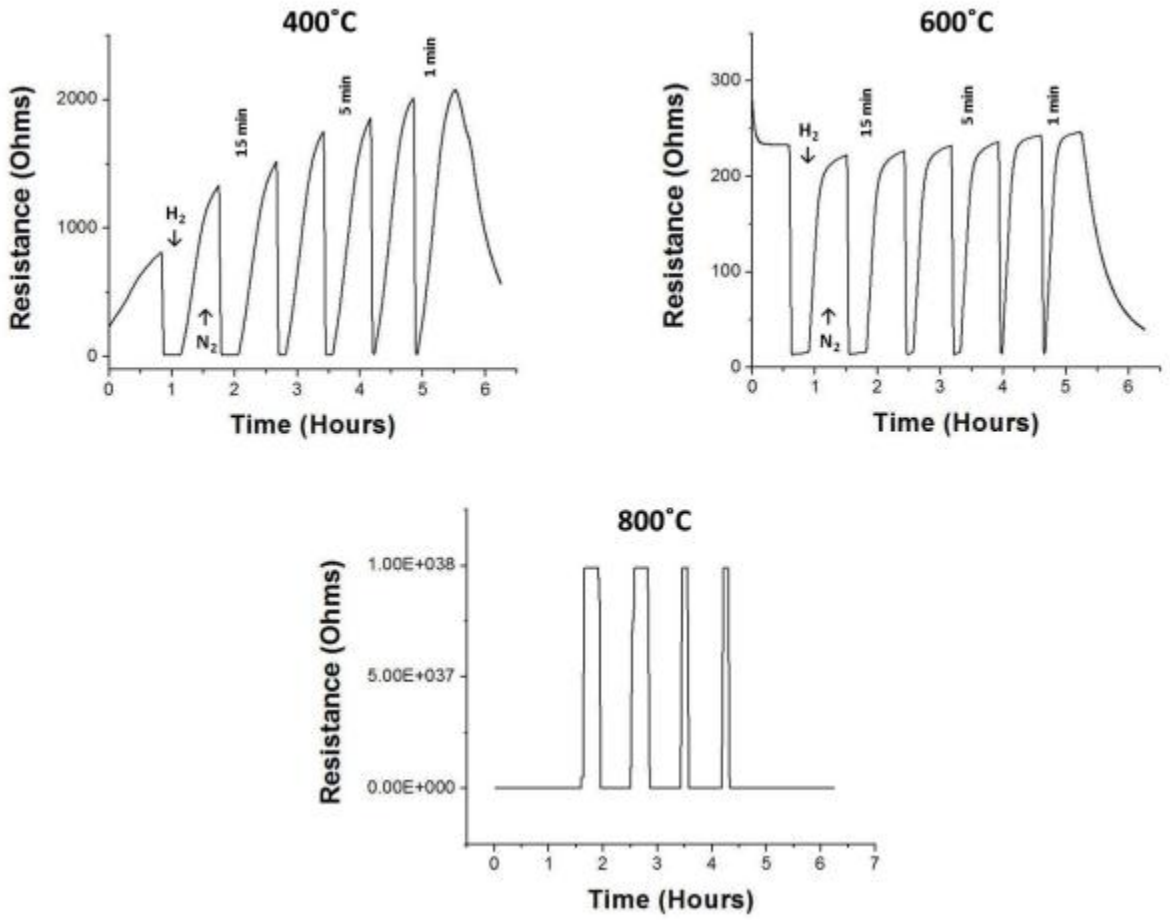

Figure 26: SnO_2 undoped hydrogen sensor at 400˚C, 600˚C, and 800˚C (0.5% H_2) in an inert atmosphere. Sensor was highly sensitive up to 800˚C where the sensor signal began to deteriorate due to microstructural changes.

At 400˚C, when the hydrogen is introduced in the chamber the sensor reaches the same resistance even with a 1 min pulse. However, the sensor is not able to fully recover once the hydrogen is shut off. This same response was seen by Hubner at 350˚C where a quick response to hydrogen is seen but the sensor was not able to fully recover even with a 3 hour exposure to pure nitrogen [106A]. At 600˚C the sensor is much more stable and responds to the same resistance with each pulse, as well as, the sensor recovers to the same resistance within the 40 min of pure nitrogen. When the sensor reaches 800˚C the sensor begins to lose it functionality most likely due to the reduction of SnO_2 to Sn on the surface. At this point, the sensor has been at elevated temperatures for over 15 hours. Once the hydrogen is introduced, the sensor resistance spikes and then returns within range of the DMM once it is turned off. It is well known that Sn begins to reduce around 800˚C in inert atmospheres which is the likely cause for the breakdown of the sensor [105A]. In oxygen atmospheres, SnO_2 conducts through adsorbed oxygen on the surface of the sensor, but in the absence of oxygen the conduction mechanism changes. The conduction of the material is controlled by surface donors and can be represented by the following equations,

$$\frac{1}{2}H_2^{Gas} + O_o \leftrightarrow OH_o^+ + e^- \quad (7)$$

which can be broken down into two separate reactions, the formation of the donor,

$$\frac{1}{2}H_2^{Gas} + O_o \leftrightarrow (OH)_o \quad (8)$$

and the ionization of the donor level by capture of an electron for the conduction band [106A],

$$(OH)_o \leftrightarrow (OH)_o^+ + e^- \quad (9)$$

According to Equation (7), as the concentration of electrons in the conduction band increases, the sensor decreases in resistance which is consistent with the experimental results. Experimental results for SnO_2 for gas sensing is not available for temperatures above 600˚C.

SEM images of the sensors were taken after testing to investigate any microstructural changes such as coarsening or cracking that may disrupt the sensor response (Figure 27).

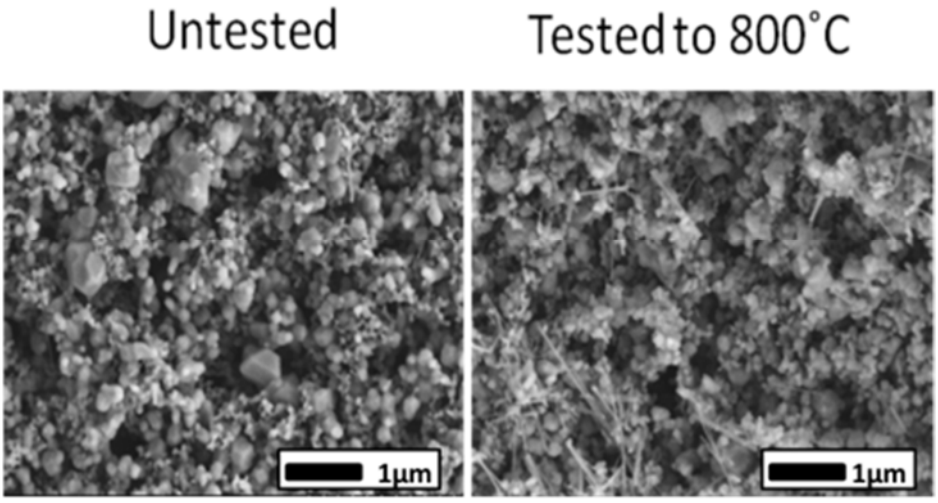

Figure 27: SEM images of SnO_2 sensor before and after testing. After testing in inert atmosphere at temperatures above 700˚C, Sn whiskers can be seen from the SnO_2 reducing fully to its base metal.

The complete reduction of the tin oxide to the metallic form of tin is seen in the figure above. Tin nanowires are forming in reducing atmosphere at elevated temperatures which would quickly degrade the sensor's ability to function. When the Sn reduces, electrons are released into the conduction band dropping the resistance of the whole system, essentially, shorting the system creating these spikes or overloaded signals in Figure 26.

Promoting the sensing material with precious metals such as Pt or Pd is known to enhance a sensor's response and recovery to hydrogen [105A]. These metals both act as a catalyst and aid in the dissociation of the H_2 molecules, and provide an additional path for the H_2 between the surface and the interface. A Pt solution was made by dissolving platinum

pentanedionate (Pt 49.430%, Alfa Aesar) with xylene and dropped onto the surface of the SnO_2 hydrogen sensor and heated to 600˚C to remove any organics in the solution. The sensor was promoted until it reached 2 wt% Pt. The same pulsing test was repeated for the enhanced sensor and can be seen below in Figure 28.

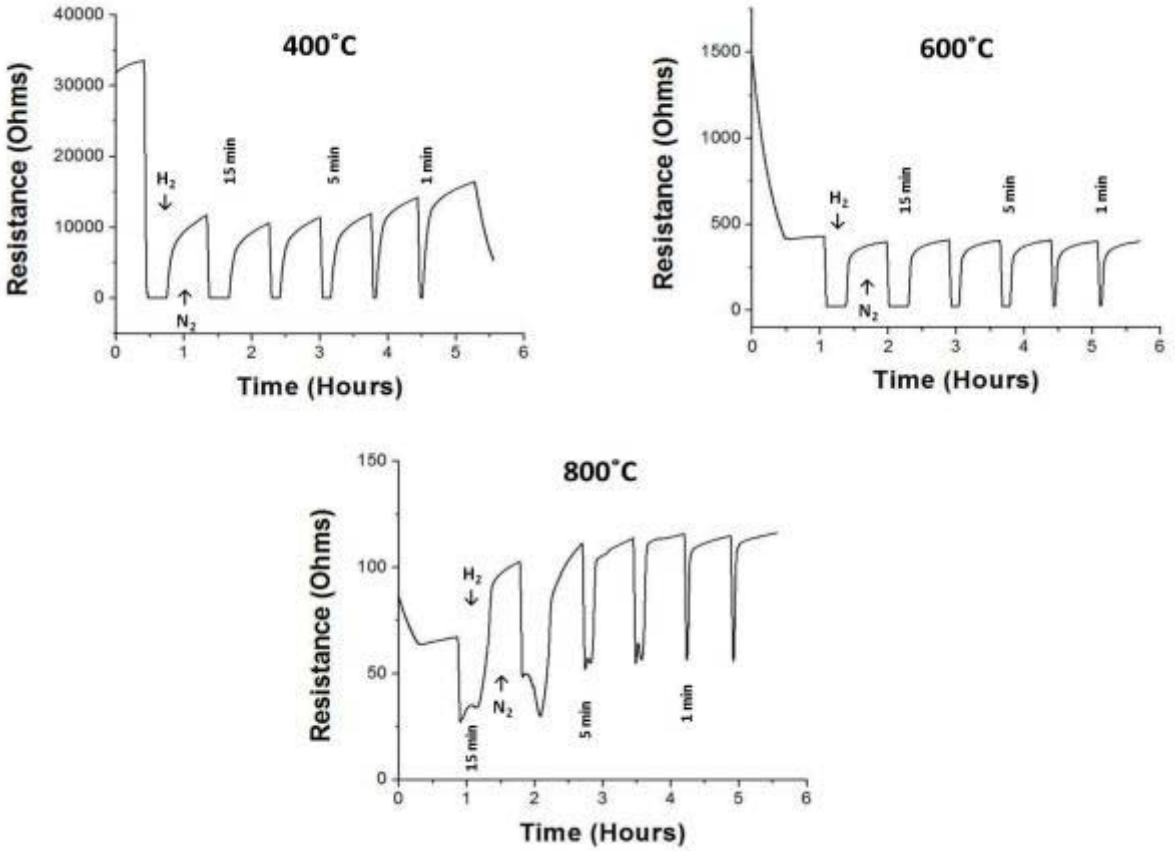

Figure 28: Pt enhanced SnO_2 sensor at 400˚C, 600˚C, and 800˚C (0.5% hydrogen) in an inert atmosphere. Pt allowed for quicker response times and stabilized the sensors signal at 800˚C.

By enhancing the sensor with Pt, the sensor exhibits a much more stable response at the two lowest temperature steps and retains its functionality at 800˚C. It is most likely the platinum that is sustaining the conduction at 800˚C. The material is porous which allows for the Pt solution to disperse throughout the sensor instead of only remaining on the surface allowing the Pt to carry the reaction via spillover effect. Another point of interest for semiconducting metal oxide sensors is the diffusion mechanism seen during recovery of the sensor once the reducing gas is turned off. The main bulk point defect, oxygen vacancies, can increase or decrease the bulk conduction depending on the oxygen partial pressure. They can also diffuse from the interior of the grains to the surface or vice versa in order to equilibrate the oxygen in the atmosphere with the oxygen composition in the oxide [109A]. This diffusion through the bulk is indicated by the curvature of the sensor response as seen in Figure 28 when the H_2 is turned off.

The macro powder from Alfa Aesar was tested again using the testing parameters discussed

in the experimental section of this section. Figure 29 is the response of the macro SnO_2 powder in a 20% oxygen atmosphere at 800˚C and 1000˚C.

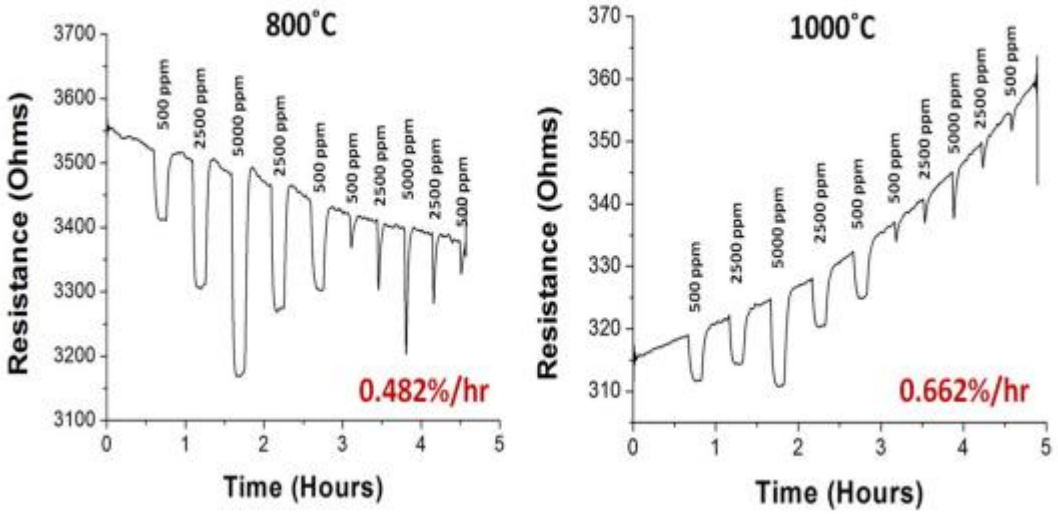

Figure 29: Macro SnO_2 powder from Alfa Aesar in 20% oxygen atmosphere. Sensor had good sensitivity towards each concentration of H_2 but signal drifted indicating microstructural changes during the test.

The macro powder exhibits good sensitivity, response, and recovery. Another interesting observation is the lack of diffusion seen upon the sensor's recovery when the hydrogen is turned off. At these elevated temperatures (>800˚C), the kinetics are fast enough that equilibrium between the oxygen in the atmosphere and the oxygen in the bulk material is rapidly established (110). As discussed earlier in this section, the sensing mechanisms for hydrogen sensing in an inert atmosphere is different than for an oxygen atmosphere. When oxygen is present in the atmosphere, the bonding of hydrogen to adsorbed oxygen on the sensors surface drives the response kinetics which is represented by the following equation.

$$H_2^{Gas} + O_s^- \leftrightarrow H_2O + e^- \qquad (10)$$

An electron is donated to the conduction band reducing the resistance of the sensor when a reducing gas bonds to surface oxygen ions. When comparing the sensitivity of the macro SnO_2 sensor in an inert and 20% oxygen atmosphere, it is clear that the sensor has a greater response (10x) to hydrogen in an inert atmosphere as seen in Figure 30.

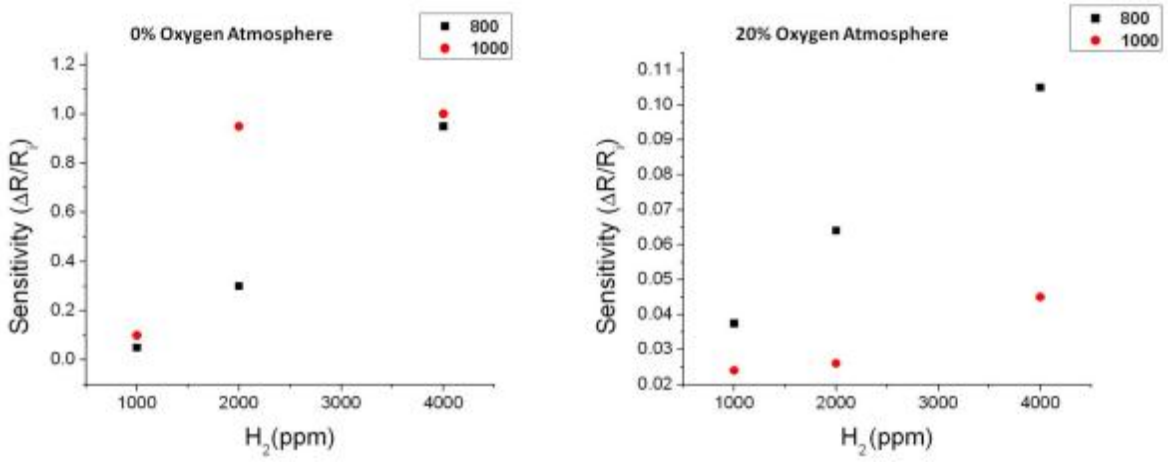

Figure 30: Effect of sensitivity of SnO_2 to hydrogen due to oxygen content in the atmosphere. Sensor has greater sensitivity (up to 10x) to hydrogen in an inert atmosphere.

The higher sensitivity in inert atmosphere can be explained through the reaction mechanisms of the SnO_2. Hubner discovered that when oxygen is present, the reactions represented by Eq. 7 and Eq. 10 are both contributing to the sensor response. However, the ionization of donors in Eq. 8 does not increase the concentration of free charge carriers. The ionization of donors is completely compensated by the ionization of acceptors, and does not contribute to the sensitivity of the SnO_2 making the signal response weaker than if oxygen was absent from the atmosphere.

The main drawback to this composition is its instability at elevated temperatures. This is clearly seen in the two graphs. At 800˚C the baseline resistance decreases steadily throughout the test possibly indicating the particles are necking. At 1000˚C, the baseline resistance increases, possibly indicating further coarsening/sintering of the particles. The drift could also be attributed to a further reduction mechanism of the Sn or an instability of the electrodes. This change in resistance is being defined as the percent "drift" in the data as indicated in red in Figure 29. The drift was calculated by the following equation,

$$\left[\frac{(R_i - R_f)}{R_i}\right] \Big/ t \times 100\% \qquad (11)$$

Where R_i is the initial baseline resistance (atmospheric conditions), R_f is the final baseline resistance, and t is the duration of the test in hours. At 1000˚C the sensor is seeing a 0.662% drift per hour. At this elevated temperature, the drift may be attributed to coarsening and or a destruction of the SnO_2 to its base metal.

In order to further determine the cause of the drift, the resistance of the bare electrodes was measured by connecting the IDEs with a Pt line printed down the center of the electrode teeth. The results of the tests for the screenprinted electrodes can be seen in Figure 31. The electrodes remained stable with less than 0.05%/hr performance change at 1000˚C, and contribute little resistance to the sensor (50 ohms at 1000˚C). Typical sensors resistances seen at 600, 800, and 1000˚C for this research are around $3x10^6$, $2x10^5$, and

$2x10^4$ ohms. The electrodes contribute less than 0.2% at 600˚C, 0.02% at 800˚C, and 0.002% at 1000˚C. The electrodes would be the most likely cause of the drift at 600˚C, since it is unlikely that the morphology of the particles are changing at low temperatures after being sintered to 1200˚C; however, at 1000˚C the electrodes contribute very little to the drift making coarsening or reduction of the material the most likely candidate for the drift.

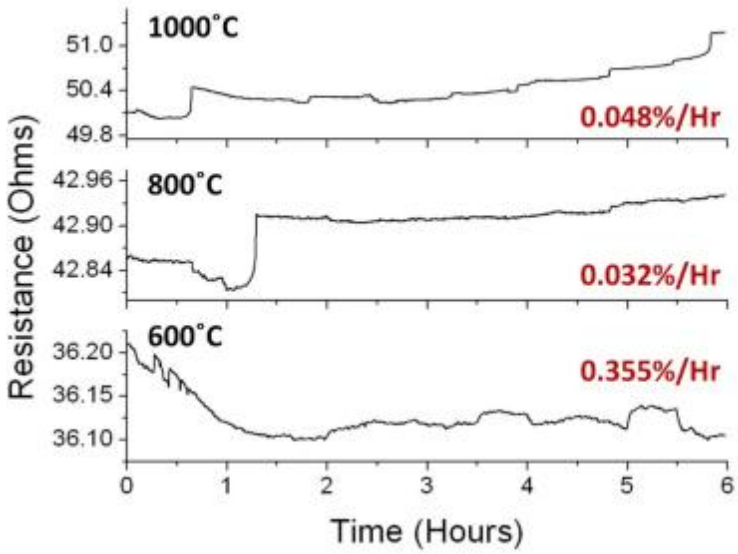

Figure 31: Resistance of screenprinted Pt IDE at 600, 800, and 1000˚C in 20% oxygen. The Pt sensitivity to H_2 can be seen at 600˚C. However, the electrodes contribute less than 0.2% to the total resistance at that temperature.

Surface enhancement is not the only method for increasing sensitivity and response/recovery time in gas sensors. By decreasing the particle size, we can also increase the sensitivity and response time due to in the increase in reactive surface area; therefore, a series of nano SnO_2 was also tested. Results of the response of the WVU agglomerated SnO_2 in a 20% oxygen atmosphere can be seen in Figure 32. Although the sensor has a strong response to the hydrogen, the sensitivity is less than the macro SnO_2 at 800˚C and equivalent to the macro powder at 1000˚C.

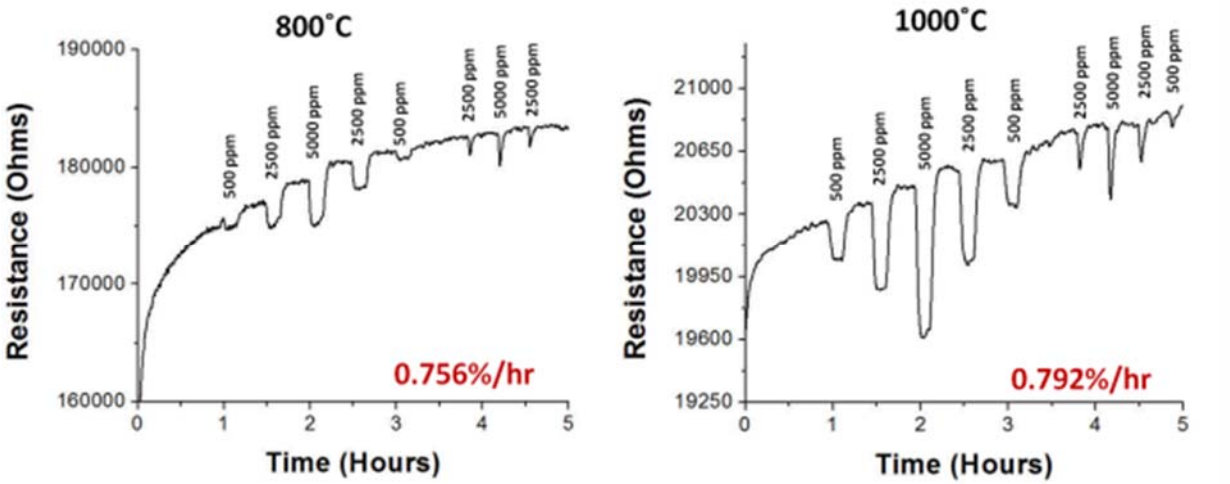

Figure 32: WVU nano ordered agglomerates in 20% oxygen atmosphere. The sensor shows a strong response to the various concentrations of H_2 but see greater drift than the larger Alpha Aesar particles due to microstructural changes during testing.

When comparing the sintered particle sizes of the two powders, the macro powder (Alfa Aesar) had grown to an average of 60 nm while the WVU agglomerated SnO_2 had grown to particles up to 90 nm as seen in Figure 33 which would account for the slightly smaller sensitivity.

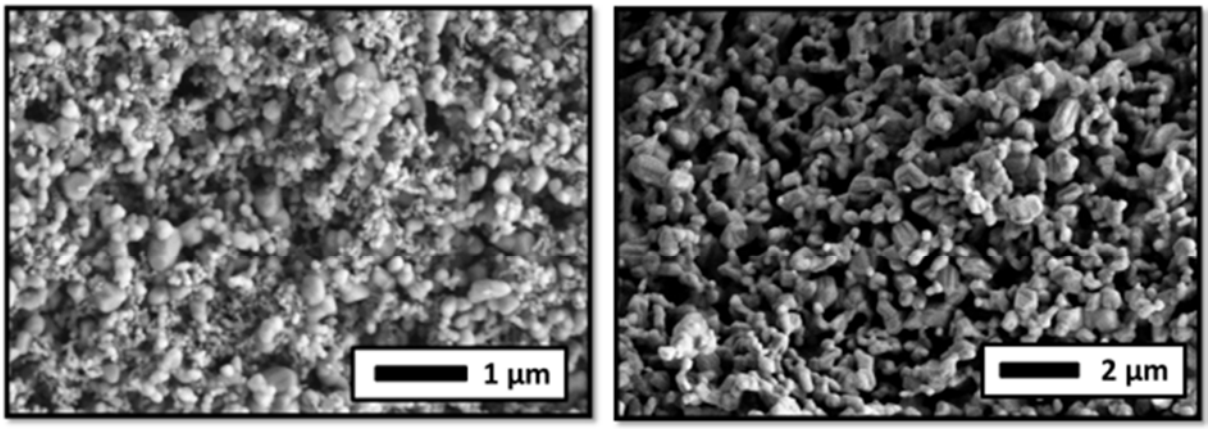

Figure 33: SEM micrographs displaying the microstructure of the (a) Alfa Aesar SnO_2 and (b) nano-SnO_2 agglomerates on the sensor after sintered to 1200˚C for one hour. Both powders sintered to particles sizes over 50 nm.

As with the macro powder, the sensitivity of the nano-SnO_2 agglomerates were much higher in an inert atmosphere. At each temperature, the sensitivity increase from 1000, 2000, to 4000 ppm H_2 were almost identical creating a trend in the sensor's response as seen in Figure 34.

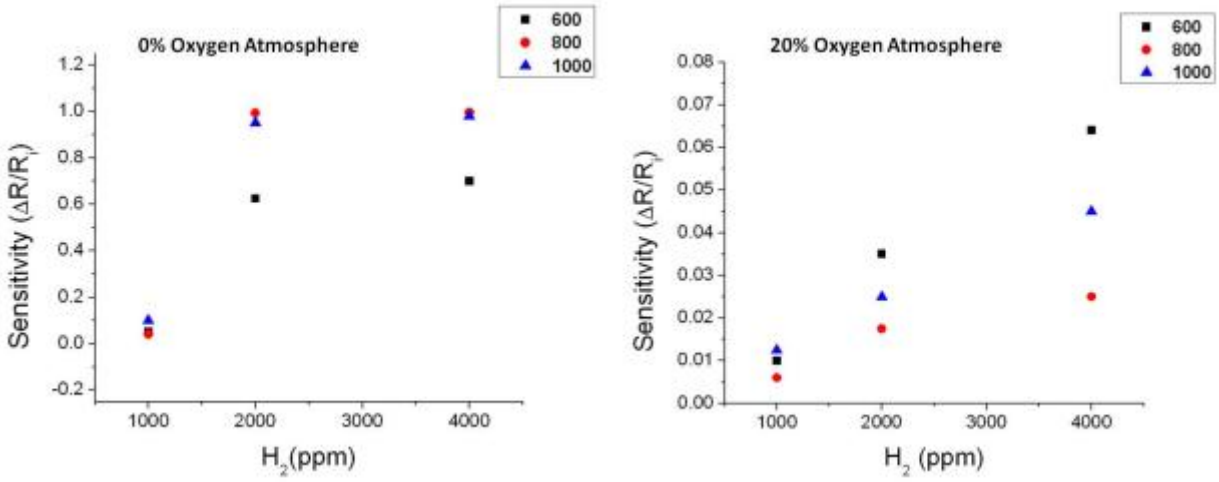

Figure 34: Sensitivity of nano-agglomerated SnO_2 to various hydrogen contents in inert and 20% oxygen atmospheres. A trend in sensitivity can be seen as the temperature is increased.

The previous section described the sensing properties of SnO_2 at elevated temperatures in various oxygen atmospheres. Although TPR data has been shown for SnO_2, there have not been any papers on the actual sensing capabilities of the highly reduced sensor. These experiments show that there are two main issues that limit the application of this material to high temperatures and low pO_2. The first issue is aligned with, coarsening/sintering of this material which destroys the potential high surface area of the nanomaterial. The second issue is the reduction of this material to SnO_x and eventually to Sn metal at these high temperatures. Therefore, the alternative Gd zirconate material was evaluated with similar conditions to demonstrate its intrinsic response at the same conditions before incorporating it into the SnO_2 composite systems. As described in the previous section, the zirconates were doped with both yttrium (Y=0.1) and samarium (Sm=0.4) on the A-site of the pyrochlore. During these tests, the sensors were heated to 600˚C, 800˚C, and 1000˚C and 0.5% hydrogen (5000 ppm) was pulsed for 15, 5, and 1 min with a 40 min interval of pure nitrogen in between each pulse to allow the sensor to stabilize. Results for the yttrium doped, un-promoted sensor are shown in Figure 35.

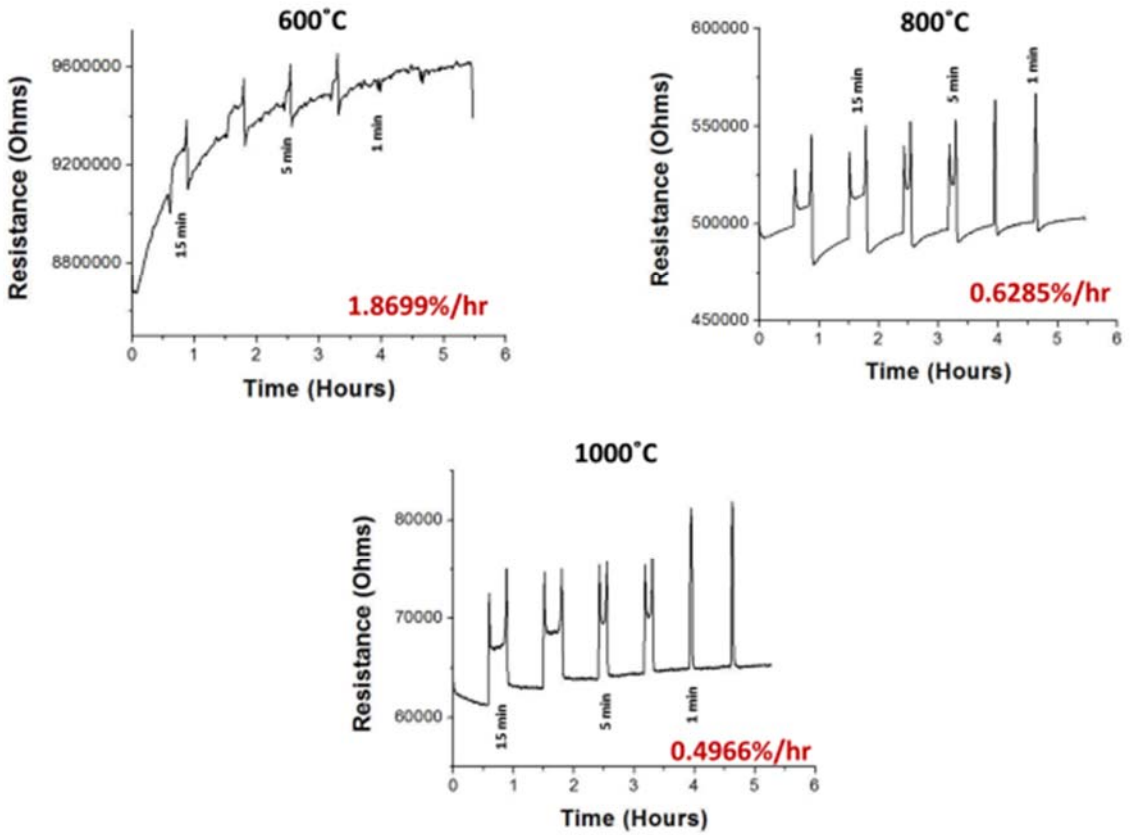

Figure 35: Un-promoted Y-doped zirconate testing of 0.5% hydrogen at 600˚C, 800˚C, and 1000˚C in inert atmosphere. The zirconate material show high sensitivity to H_2 and is fairly stable at 1000˚C.

As previously mentioned, gadolinium zirconate is a purely ionic conductor; therefore, the donation of electrons has no effect on the response of the sensor to a reducing gas. The increase in stability and sensitivity of the sensors as the temperature increases seem to indicate that these zirconates have a high working temperature. Unlike the SnO_2 hydrogen sensors which never fully recover at these temperatures due to slow diffusion, the zirconates recover almost as quickly as they respond to the introduction of hydrogen. Not only does this material have a strong p-type-like response to the hydrogen, sharp peaks at the onset and shutoff of hydrogen can be seen at each pulse. This is most likely caused by the stripping of the oxygen off the surface/grain boundaries from the hydrogen bonds. Once the surface is completely stripped of oxygen the material loses its ability to conduct due to an overwhelming number of oxygen vacancies and a sharp increase in resistance is seen. Ionic conductivity can be represented by,

$$\sigma_i = c_i(z_i q)\mu_i \qquad (12)$$

where σ_i is equal to the defect carrier density, c_i, multiplied by its charge, $z_i q$, and the ion mobility, μ_i (Takamura et al. 2000). Although ionic conduction is usually increased with the increase of oxygen vacancy concentration (as seen in Equation 12), there is a point where too many oxygen vacancies reduces the conduction due to a possible disordering of

the lattice structure which obstructs oxygen mobility.

Since there is no oxygen in the atmosphere, in order to regain equilibrium between the atmosphere and the material, oxygen migrates from the bulk to the surface and the resistance decreases and stabilizes. An opposite reaction occurs once the hydrogen is removed from the atmosphere and the oxygen migrates back to the bulk. Ionic conduction if based on Frenkel defects or oxygen vacancies within the system, Equation 13, but the equilibrium with the gas phase through reduction and/or intrinsic electron-hole generation must be taken into account, Equations 14 and 15.

$$O_o^x \leftrightarrow V_o^{\cdot\cdot} + O_i'' \quad (13)$$

$$O_o^x \leftrightarrow \frac{1}{2}O_2 + V_o^{\cdot\cdot} + 2e' \quad (14)$$

$$nil \leftrightarrow e' + h^{\cdot} \quad (15)$$

In order to better understand the zirconate's reaction to hydrogen, TPR analysis was used to determine the adsorption characteristics of the material. During the test at each heating rate, no significant H_2 adsorption was detected even though a very broad peak seems to be present from 300˚C-700˚C, as seen in Figure 36.

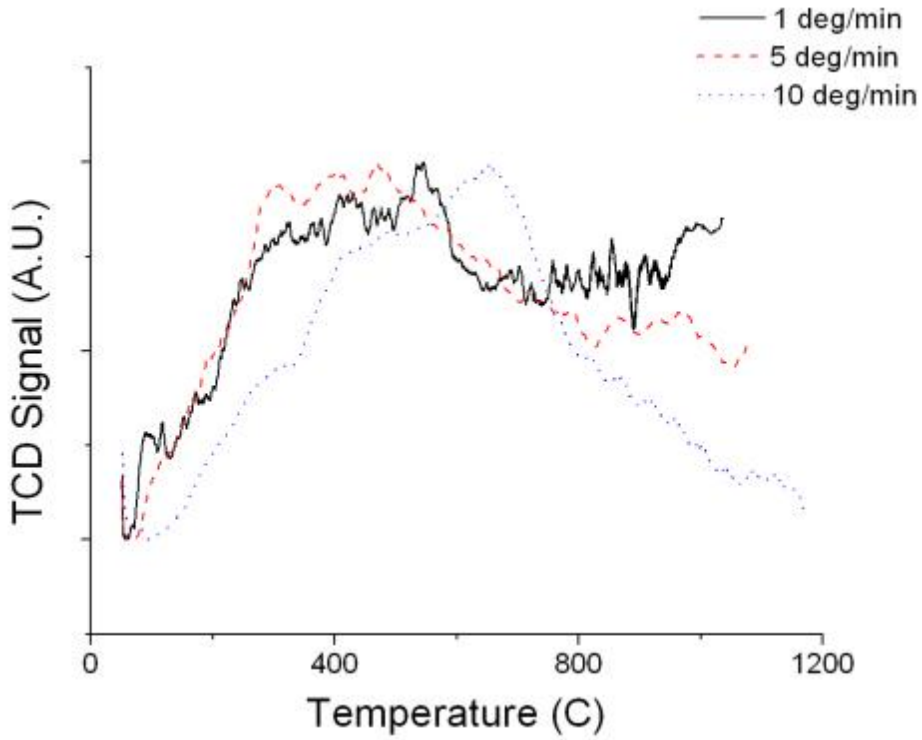

Figure 36: TPR analysis of pure GZO with heating rates of 1, 5, and 10 deg/min in a 10% H_2/Ar flow of 50 ml/min. The zirconate shows little to no hydrogen adsorption at these temperatures.

The Sm doped zirconate also performed better at higher temperatures, becoming the most sensitive and stable at 1000˚C. The un-promoted test results can be seen in Figure 37.

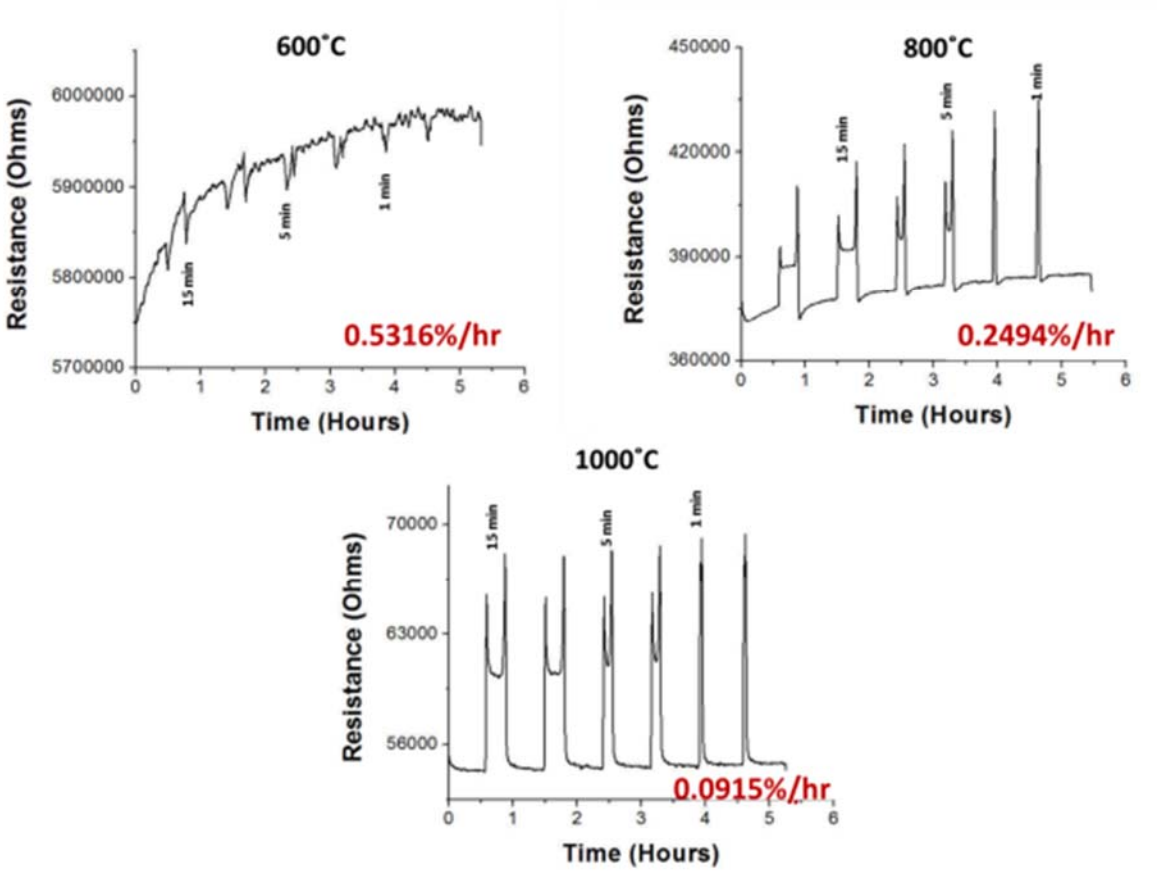

Figure 37: Un-promoted Sm-doped zirconate testing of 0.5% hydrogen at 600˚C, 800˚C, and 1000˚C in inert atmosphere. Much like the y-doped zirconate, the Sm-doped sensor exhibits strong sensitivity to H_2 and gets increasingly more stable as the temperature increases.

When comparing the two dopants, little difference is seen in the sensitivities of the two materials. Figure 38 shows that the Y-doped system has slightly higher sensitivity than the Sm doped system until a temperature of 1000˚C is reached. Because of the similarities between the systems and lesser cost of the yttrium precursor, the Y-doped zirconate was used throughout the rest of the study for composite system testing.

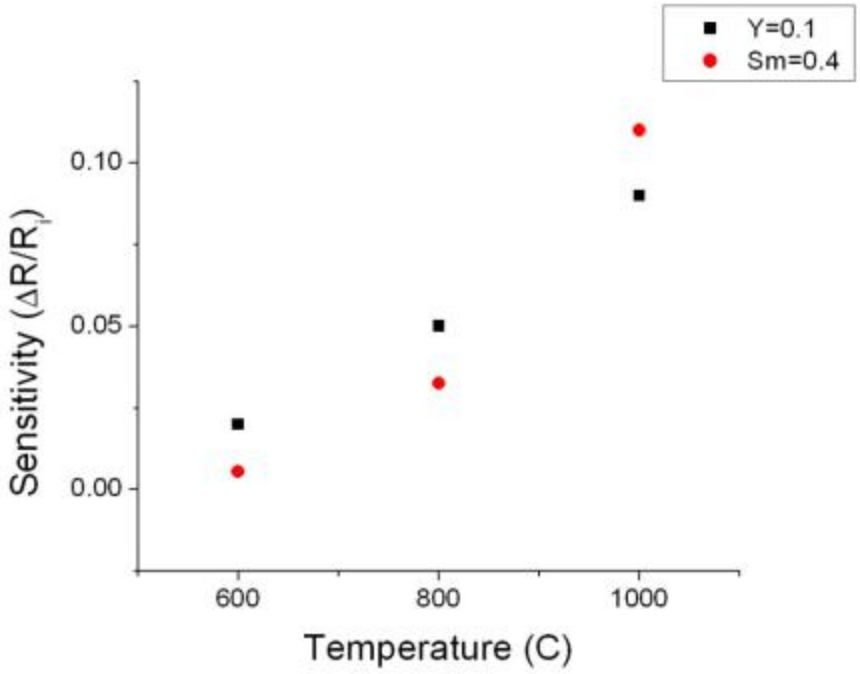

Figure 38: Sensitivity of two A-site doped gadolinium zirconate systems, yttrium and samarium at 600, 800, and 1000˚C in an inert atmosphere. Both material systems have increased sensitivity as temperature increases.

As noted by Tuller, gadolinium zirconate is a pure ionic conductor and meaning the conduction does not change with oxygen partial pressure. However, when oxygen is introduced into the atmosphere, the sensor's behavior changes to from a p-type like response to an n-type-like sensor as seen in Figure 39.

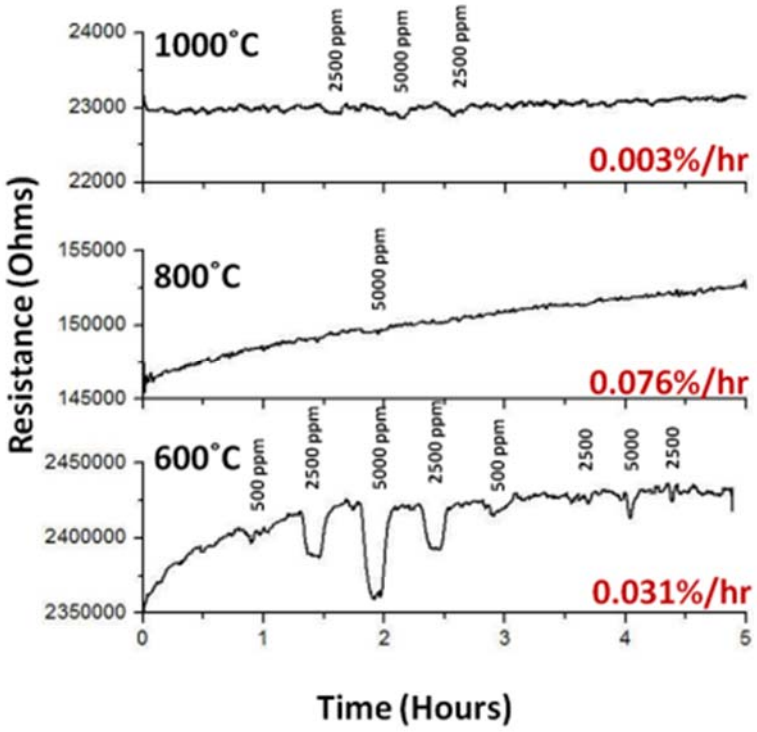

Figure 39: Y-doped zirconate in 20% oxygen atmosphere. Sensor shows some sensitivity towards H_2 at 600˚C but has no response at 800˚C and very little response at 1000˚C most likely due to the lack of hydrogen adsorption seen in the TPR results.

At 600˚C the sensor has relatively good sensitivity and response time, but as the temperature increases the sensitivity of the sensor decreases. As shown in Figure 36, a broad reduction peak centered about 500˚C, but no TCD signal is seen at elevated temperatures in the TPR plot which might be the cause for the decreased sensitivity to H_2 at these higher temperatures. At lower temperatures (600˚C), hydrogen bonds with the oxygen within the surface and the bulk of the zirconate forming H_2O and forming an oxygen vacancy which increases the conductivity of the material. Unlike the inert atmosphere, these surface vacancies can be re-filled with oxygen from the atmosphere making diffusion from the bulk less likely. These two reactions can be seen with the following equations,

$$H_{2,gas} + O_{o,Zr}^{x} \leftrightarrow H_2O + V_{o,Zr}^{\cdot\cdot} + 2e^{-} \qquad (16)$$

$$O^{2-} + V_{o,Zr}^{\cdot\cdot} \rightarrow O_{o}^{x} \qquad (17)$$

As the temperature increases, the hydrogen no longer interacts with the surface resulting in no sensor response at intermediate temperatures (800˚C). When the temperature reaches 1000˚C, there is enough mobility in the system to allow for hydrogen bonding with oxygen in the bulk of the material recovering a small portion of the sensor's sensitivity due to bulk reduction processes that increase the lattice conductivity. The big advantage to this material system is the stability at high temperatures. The percent drift decreases from 0.031%/hour to 0.003%/hour at 1000˚C. Figure 40 shows that the particle size remains unchanged even after being at elevated temperatures (> 600˚C) for over 24 hours. Particle size remains on

average at 130 nm with necking of the particles and large pores throughout the structure.

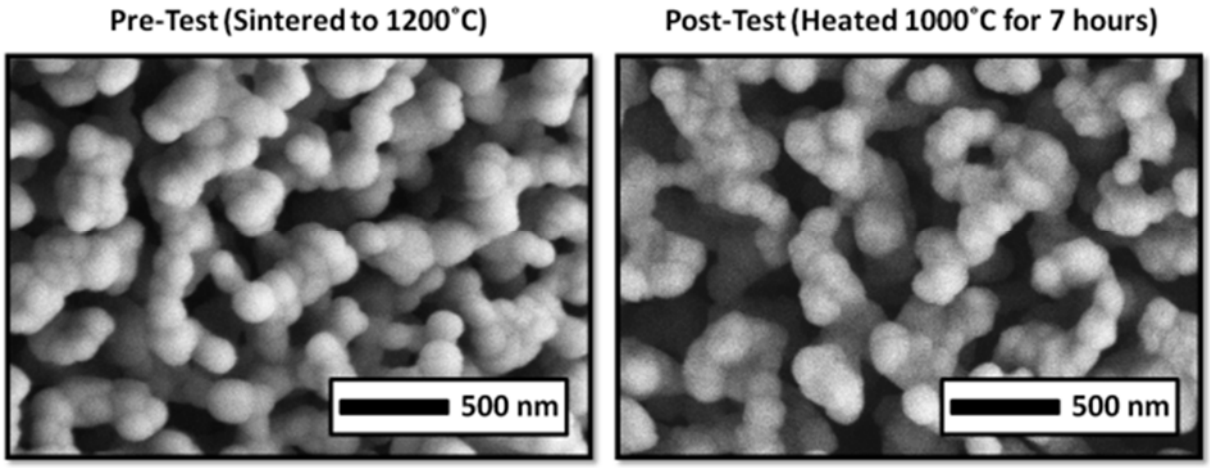

Figure 40: SEM micrographs of sintered and post-tested GZO sensor. Particle size remains unchanged when tested at 1000˚C for 7 hours.

Testing so far has shown two major problems for high temperature sensing with gadolinium zirconate, 1) there is low hydrogen adsorption at high temperatures, and 2) the nanomaterials particle junctions are instantly being disordered with a high volume of defects regardless of the H_2 content in inert or low oxygen atmospheres. Therefore, other absorption species such as SnO_2 sensor and Pt enhancement of the GZO was investigated. First, the Pt enhancement showed higher absorption especially at 600˚C, but a saturation of the sensor signal appeared at a much faster rate due to the increased formation of oxygen vacancies from the catalytic activity of the Pt.

In this section, SnO_2, will be used in two distinct ways to promote the sensitivity of the sensor at high temperatures. The first method is to use the SnO_2 as a traditional MOS chemiresistive sensor, but support it with a small percent of GZO to pin the grain growth of the SnO_2 and to provide an oxygen source when the SnO_2 reduces in low oxygen atmospheres. Yang *et al*. formed composite sensors consisting of SnO_2 and mesoporous silica (SBA-15) and found that the addition of the SBA-15 greatly increased the sensitivity of the sensor at 250˚C. They found that an interaction between the SBA-15 and the SnO_2 allowed for more oxygen to be adsorbed onto the surface which increased the sensing properties of the sensor (111). As long as the SnO_2 is percolated throughout the sensing material, its electronic conduction is believed to be higher than that of the doped-GZO and should carry the sensing mechanism. The following reactions will be under consideration during the testing of these composites, the reaction between adsorbed oxygen and the reducing gas,

$$H_{2,gas} + O_{ad}^{-} \leftrightarrow H_2O + e^{-} \qquad (18)$$

$$\frac{1}{2}H_{2,gas} + OH_{ad}^{-} \leftrightarrow H_2O + e^{-} \qquad (33\ 19)$$

ionic conduction of the zirconate,

$$H_{2,gas} + O_{o,Zr}^{x} \leftrightarrow H_2O + V_{o,Zr}^{\cdot\cdot} + 2e^{-} \quad (20)$$

$$O^{2-} + V_{o,Zr}^{\cdot\cdot} \rightarrow O_o^x \quad (21)$$

And the interaction between the zirconate and the SnO_2,

$$4e^{-} + O_{2,surface} \rightarrow 2O_x^{2-} \quad (22)$$

$$O^{2-} + V_{o,Zr}^{\cdot\cdot} \rightarrow O_o^x \quad (23)$$

A composite materials of the nano-SnO_2 and the doped zirconate was made by mixing a 10, 50, 90 vol% of SnO_2 hydrothermal solution with the zirconate material solution and ball milled overnight to ensure an even mixture. A complete comparison of these systems can be seen in Figure 41 at 1000˚C in a 20% oxygen atmosphere. N-type or n-type "like" response is seen in each of the material systems.

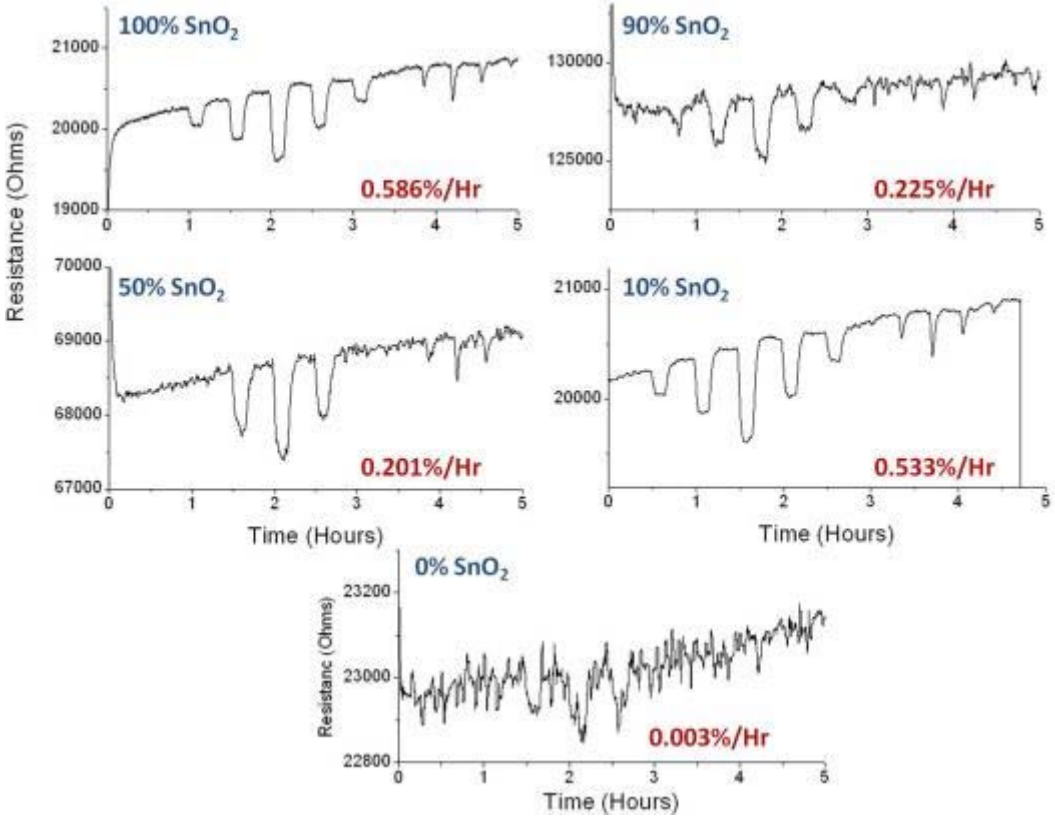

Figure 41: Comparison of composite sensor systems at 1000˚C in 20% oxygen atmosphere. Addition of SnO_2 greatly increases the sensitivity compared to pure GZO with 10% SnO_2/90% GZO composite system having the strongest sensitivity at 1000˚C.

In comparison to the pure zirconate sensor, the composite systems show an increased sensitivity. Each of the systems also has an increased stability from the pure-nano SnO_2. Figure 42 shows the analysis of each of these systems at 600˚C, 800˚C, and 1000˚C. The systems with the highest sensitivity are both 100% SnO_2 and the 10% SnO_2/90% zirconate composite. However when you look at the stability of the 100% SnO_2 sensors, it drifts

over 0.6% per hour of testing while the composite systems containing GZO decreases the drift to 0.2% per hour or lower.

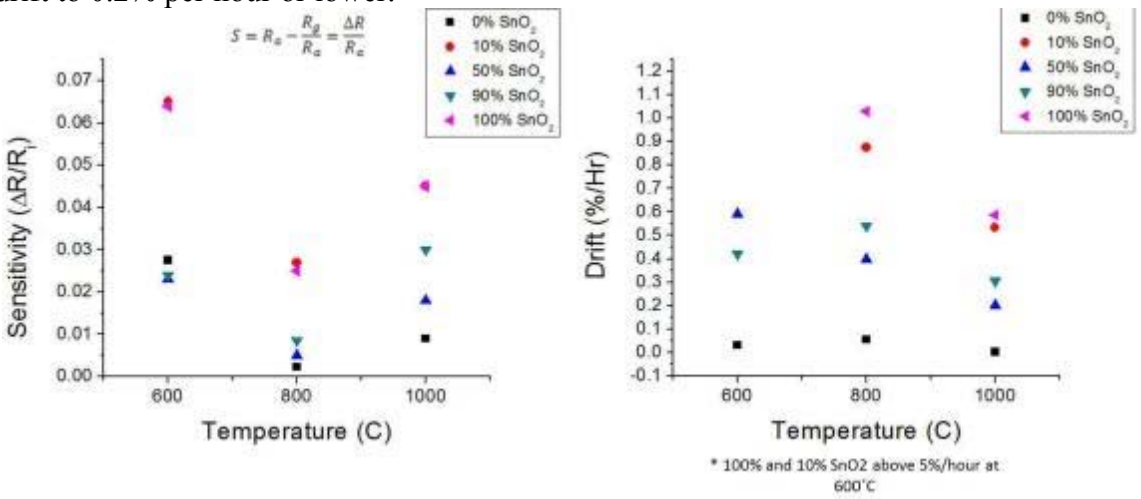

Figure 42: Sensitivity and stability of SnO_2 composite systems in 20% oxygen atmosphere. Addition of SnO_2 increases the sensitivity of each material system but also increases the drift at each temperature.

It is believed that in composite systems containing at least 50% SnO_2, the SnO_2 is carrying the sensing mechanism, since there is enough material percolated through the sensor to create SnO_2 pathways and the zirconate is mainly stabilizing the grain growth in high oxygen atmospheres. To confirm this theory, SEM micrographs were taken of each sintered composite system to compare grain size and porosity (Figure 43).

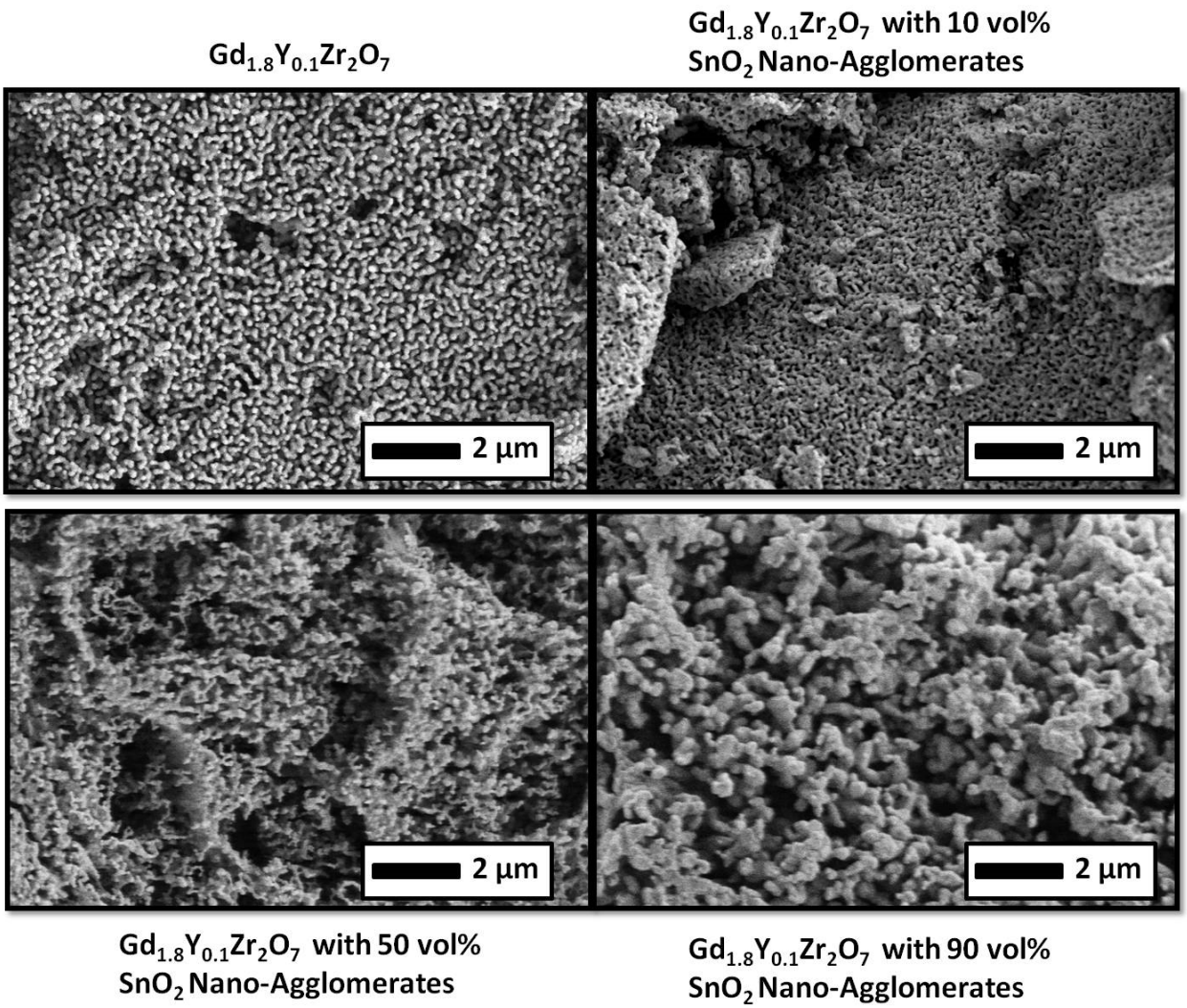

Figure 43: SEM micrographs of SnO_2/GZO composite sensors sintered to 1200˚C. As vol% of SnO_2 increases the porosity of the material increases. The grain size of the composites also increases from 80 nm to 300 nm as the vol% increases from 0 to 90%.

In a pure zirconate system, the particles sizes are more uniform at around 80 nm when sintered to 1200˚C (as seen in Figure 43). When SnO_2 is incorporated into the GZO, the particle size and porosity changes. At 10% SnO_2, the particle sizes are about 60 nm and sinter similarly to GZO with necking and evenly distributed pores. As the SnO_2 is increased to 50%, the particles are reduced to 50 nm or less and have increased porosity; however, when increased to 90% the particles sizes are less uniform and range from 100 – 300 nm with small GZO particles distributed throughout at around 80 nm. Even though the particles in the 90% SnO_2 are the largest of each of the systems, the particle size is greatly reduced from pure SnO_2 sensor which sintered up to 1 µm.

Temperature programmed reduction (TPR) was used to investigate the 10% SnO_2 composite powder further (Figure 44). When compared with its constituents, the composite reduction peak is over 100˚C higher than pure SnO_2 and follows the pure

zirconate profile closely at lower temperatures. The hydrogen adsorption 10% of the hydrogen adsorption of the pure SnO_2 meaning that the gadolinium zirconate is not contributing to the sensitivity of the sensing material, but is increasing the stability of the tin allowing for hydrogen sensing at temperatures above 600˚C without the material breaking down.

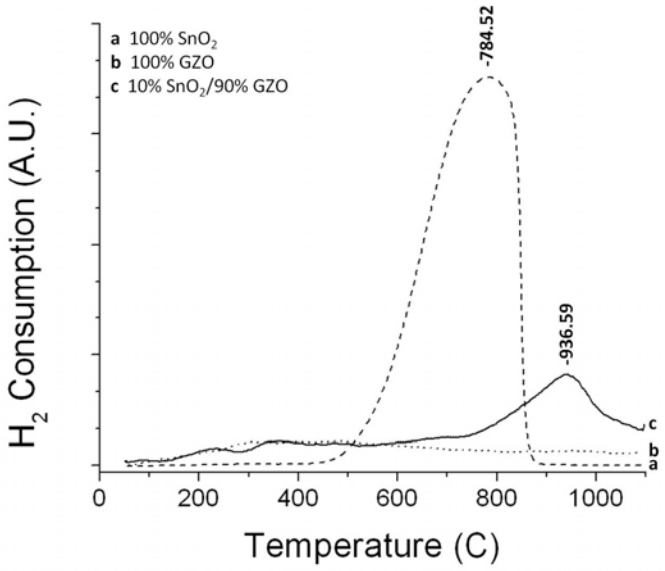

Figure 44: TPR profiles of GZO, SnO_2, and 10% SnO_2/90% GZO at 5 deg/min. Pure GZO shows no H_2 adsorption, but by incorporating 10 vol% SnO_2, H_2 adsorption is seen along with an increased reduction temperature (937˚C) of the system when compared to pure SnO_2 (785˚C).

It is possible that the GZO is donating oxygen to the SnO_2, stabilizing it at temperatures where it would normally reduce to SnO and eventually to Sn metal.

The composite system containing 10% SnO_2 was tested at 1000˚C at various oxygen concentrations in order to try to understand the improved sensitivity and mechanisms behind its response. It is believed that 10 vol% of SnO_2 is not enough to form percolation paths of the semiconducting material, so the conduction is being controlled by the interaction/interface between the SnO_2 and the zirconate and is most likely purely ionic. Figure 45 reveals that by changing the oxygen partial pressure, the mechanisms for sensing also changes.

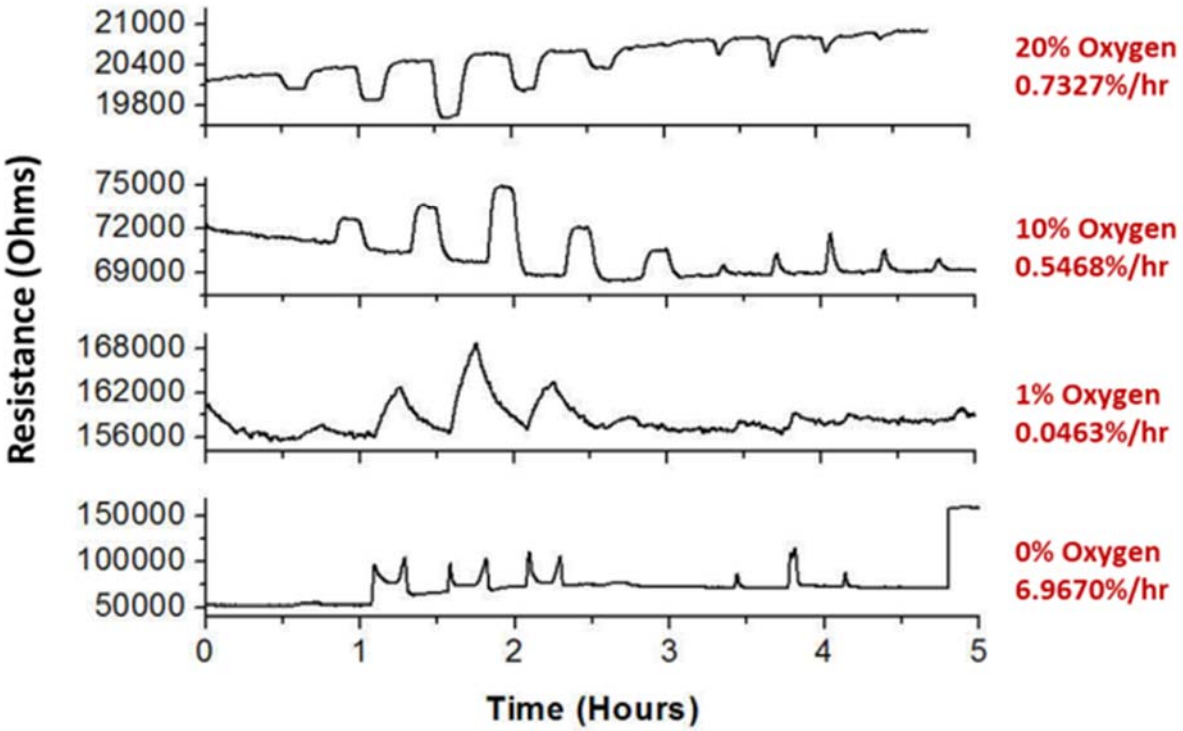

Figure 45: 10% WVU nano agglomerates and 90% y-doped zirconate at 1000˚C in different oxygen atmospheres. Material exhibits n and p-type like responses depending on the oxygen partial pressure.

Remembering that GZO is a purely ionic conductor at all oxygen partial pressures, it is most likely that each of these responses is ionic in nature even though the response resembles an n-type or p-type semiconductor response. It is clear that the addition of SnO_2 increases H_2 adsorption, as seen in the TPR results, onto the surface increasing the sensors sensitivity compared to the pure zirconate material. In a 20% oxygen atmosphere the reaction occurs at the grain boundary junction for an ionic conductor. As the hydrogen bonds with the oxygen along that junction, the conduction increases creating an n-type-like response. As the oxygen partial pressure decreases, the number of oxygen vacancies increases. As the oxygen vacancies increase to a certain point, the addition of hydrogen in the atmosphere decreases the ionic conduction across the contact junctions decreasing conductivity and increasing the resistance. There is a saturation point with oxygen vacancies where conduction is actually hindered instead of increasing the oxygen conduction possibly, because of a skewing or distorting of the lattice structure due to too many vacant sites. At lower levels of oxygen partial pressure, the diffusion of oxygen from the bulk can be seen. Once the oxygen at the surface is cleared from the initial onset of hydrogen, there is an oxygen gradient throughout the bulk and the oxygen diffuses to the top to maintain equilibrium. At 10% oxygen atmosphere, the diffusion is not seen which is most likely due to there being enough oxygen in the atmosphere to maintain the equilibrium of the system without the assistance from the bulk. This test also infers that at higher oxygen concentrations the mechanism for sensing is controlled by the grain boundaries whereas at lower oxygen concentrations the bulk is driving the reaction.

There are a number of reactions that can occur at the junction between the atmosphere, the SnO_2, and the zirconate, much like a triple phase boundary in a solid oxide fuel cell. Three different mechanism will be discussed to describe the in conduction, 1) Adsorption on the surface of the Sn (Equations 24 & 25), 2)charge transfer on the surface (Equations 26 & 27), and or charge transfer through the bulk (Equation 28), 3) reaction with zirconate surface (Equation 29-31), 4) conduction through the bulk (Equation 32) [112A].

$$H_2O_{gas} + \blacksquare_{Sn} \leftrightarrow H_2O_{Sn} \quad (24)$$

$$H_{2,gas} + 2\blacksquare_{Sn} \leftrightarrow 2H_{Sn} \quad (25)$$

$$H_{Sn} + OH^-_{GZO} \leftrightarrow H_2O + e^-_{Sn} + \blacksquare_{Sn} \quad (26)$$

$$H_{Sn} + O^{2-}_{GZO} \leftrightarrow OH^-_{GZO} + e^-_{Sn} + \blacksquare_{Sn} \quad (27)$$

$$H_{Sn} + O^x_{o,GZO} \leftrightarrow H_2O + V^{\cdot\cdot}_{o,GZO} + 2e^-_{Sn} \quad (28)$$

$$H_2O_{gas} + \blacksquare_{GZO} \leftrightarrow H_2O \quad (29)$$

$$H_2O_{gas} + O^{2-}_{GZO} \leftrightarrow 2OH^-_{GZO} \quad (30)$$

$$O^{2-}_{GZO} + V^{\cdot\cdot}_{O,GZO} \leftrightarrow O^x_{O,GZO} + \blacksquare_{GZO} \quad (31)$$

$$2e^- + O^X_{O,GZO} \leftrightarrow O^{2-}_{GZO} \quad (32)$$

During the adsorption process, either hydrogen or water is adsorbed onto a free surface site of the Sn making it available to bond with oxygen or hydroxides on the surface of the zirconate and forming a hydroxide or releasing water into the atmosphere, respectively. Another reaction that can be occurring is the reaction of the hydrogen in the atmosphere with bulk oxygen in the zirconate, forming a vacancy in the bulk. This vacancy is filled by charged oxygen ions along the surface of the zirconate (equation 32), creating a cycle which drives the conduction of the material. When the oxygen partial pressure is reduced, it has been reported that hydrogen covalently bonds with two oxygen atoms on the lattice surface to form two hydroxyl protons and two electrons. Knowing that when oxygen is reduced in the atmosphere, equations 27 and 30 a more likely reaction in these conditions. When the oxygen is reduced to the point that SnO_2 is no longer stable, and oxygen transfer from the GZO, keeps the SnO_2 from reducing to its base metal and forms an oxygen vacancy in the GZO. This transient response can be seen in the composite material when the oxygen is 1% in the atmosphere. Each of these reactions can be seen in Figure 46.

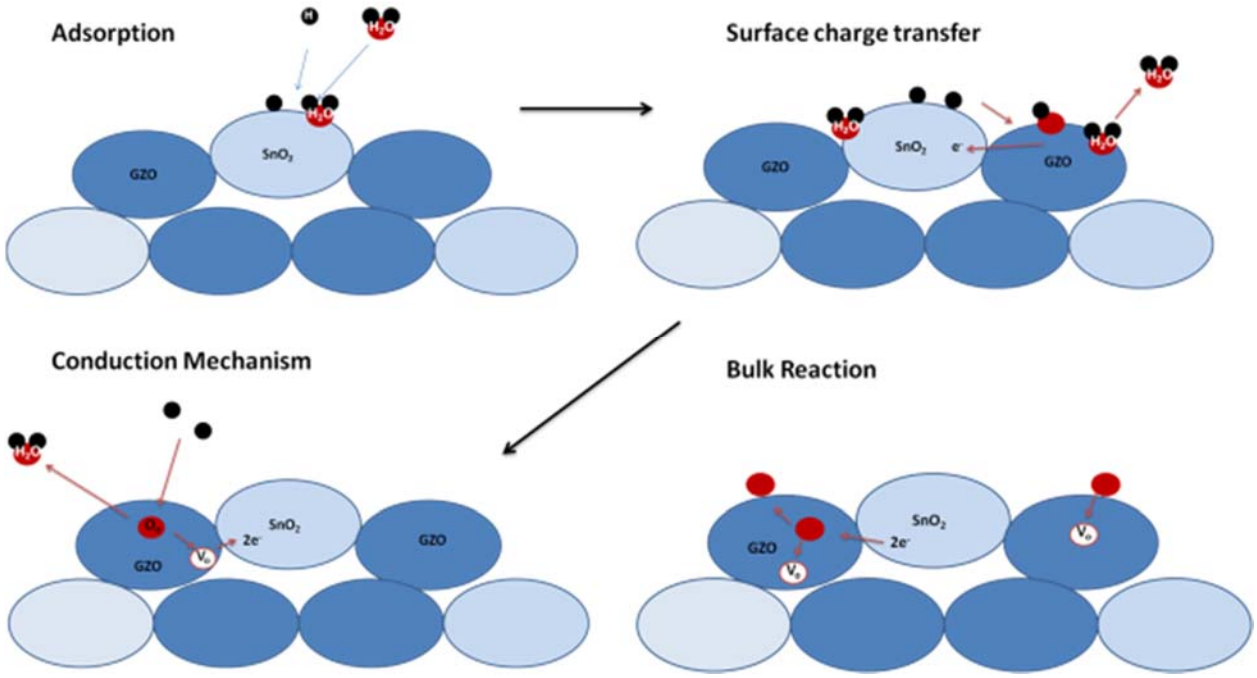

Figure 46: Conduction mechanisms of composite sensors described in equations 24-32. Hydrogen is adsorbed on the surface of the SnO_2 where it reacts with surface oxygen or lattice oxygen of the zirconate. Conduction occurs through the formation and filling of oxygen vacancies in the zirconate.

Knowing that ionic conduction is dominant in 10% SnO_2 at each oxygen partial pressure, both the 50% and 90% SnO_2 was tested for its conduction mechanisms in different oxygen atmospheres. Figure 47 shows the response of these sensors in inert and 20% oxygen atmospheres at 600, 800, and 1000˚C. In theory, the 90% SnO_2 composite sensor should behave as a semiconducting material, but have increased stability which was seen in Figure 45. However, a 50% composite could exhibit behavior from either or both systems.

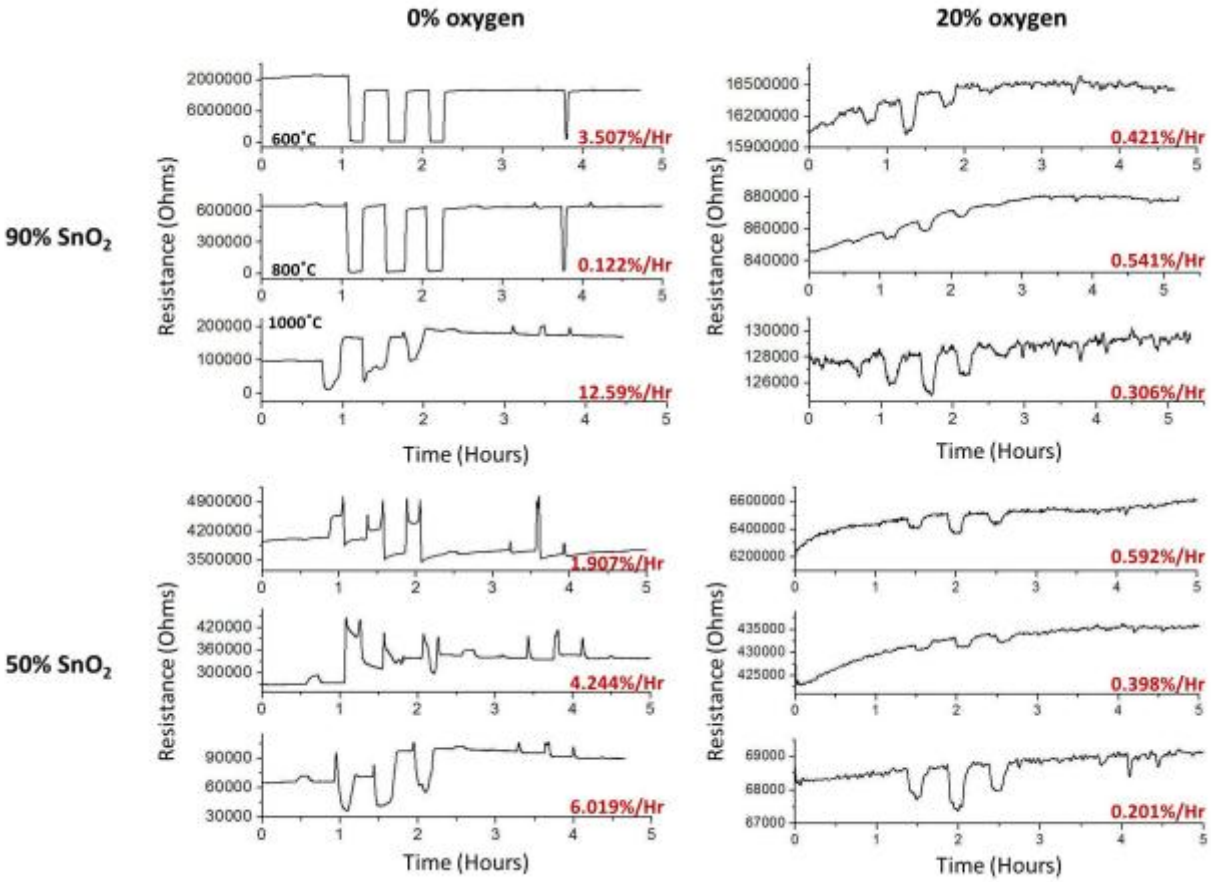

Figure 47: Response of 50 and 90% SnO_2 composite sensors in inert and 20% oxygen atmospheres at 600, 800, and 1000˚C. The 90% SnO_2 composite sensor behaves similarly to a pure SnO_2 sensor but has increased stability at elevated temperatures. The 50% composite sensor behaves similarly to that of the 10% composite sensor at low temperatures but has a mixed conduction behavior at 1000˚C.

As predicted, the 90% composite sensor behaves similarly to a SnO_2 sensor but maintains its stability at elevated temperatures in an inert atmosphere due to the oxygen transfer from the GZO. The 50% SnO_2 sensor at lower temperatures in an inert atmosphere exhibits the same characterizes of the ionic 10% SnO_2 sensor which leads to the belief that the ionic conduction via hydrogen spillover, or reactive electrolyte mechanism are stronger than the adsorption/desorption kinetics of the SnO_2. At 1000˚C, a mixed conduction behavior is seen, where at lower hydrogen contents, ionic conduction is seen but when 2000 ppm of hydrogen is introduced for an extended period of time, the reduction of the SnO_2 cannot be compensated by the bulk oxygen transfer from the GZO and a n-type semiconductor response is seen.

Various $Gd_2B_2O_7$, where the B-site is various ratios of Zr an Sn, have been investigated by Tuller *et al.* for their disordered structures and mixed conductivity (Takamura et al. 2000)[113A]. He found that a complete substitution of Sn on the B-site produced a purely ionic material, but as Zr was increased on the B-site a mixed conductor was formed. Two different pyrochlore materials were synthesized and tested in a 20% oxygen atmosphere.

First, the B site of GZO was completely replaced by Sn, then 10% of the B site was doped by Sn as a comparison to the SnO_2/GZO composite systems. Comparisons of these two systems along with GZO, SnO_2, and the 10% SnO_2 composite systems are shown in Figure 48.

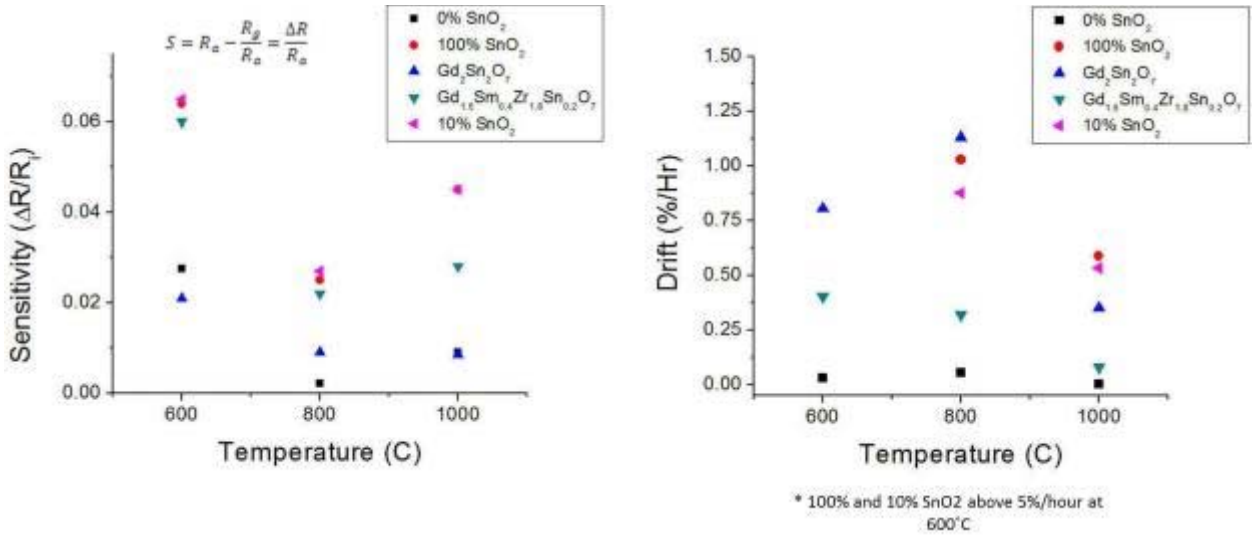

Figure 48: Comparison of GZO and stannate pyrochlores for sensitivity to 4000 ppm of H_2 and their drift in 20% oxygen atmosphere. Stability and sensitivity of the zirconate sensor is enhanced by incorporating Sn into the lattice structure.

When the B-site of the zirconate is doped by 10% with Sn, the sensitivity of the sensor is almost equivalent to the 10% SnO_2 at 600 and 800˚C. When comparing the stability of the slightly doped GZO system, the material is more stable than the composite materials having less than 0.08% drift per hour at 1000˚C whereas all other compositions excluding pure GZO all had drifts over 0.4% per hour. By completely replacing the B-site with Sn, the sensitivity has a 50% decrease compared to the 10% SnO_2 composite system and has greater drift than most other sensing materials. Tuller reported that substitution of Sn on the B-site for Zr in the $Gd_2Zr_2O_7$ composition resulted in a decrease in the ionic conductivity of the pyrochlores solid-solution [Yu and Tuller et al. 1996]. Figure 49 shows the ionic conductivity of $Gd_2(Zr_{1-x}Sn_x)_2O_7$ solid-solutions measured by Tuller *et al.* The graph shows that the ionic conductivity is highest for pure $Gd_2Zr_2O_7$ with a value of $10^{-1.75}$ S/cm [Yu and Tuller et al. 1996]. Their data shows a minimum conductivity at x=0.8 (x=Sn), and then a slight increase in conductivity to $10^{-4.25}$ S/cm for the pure $Gd_2Sn_2O_7$ composition. Tuller *et al.* stated that the strong covalent Sn-O bond is believed to be the source of the reduced oxygen ion mobility, and thus, the lower ionic conductivity with the increase of Sn.

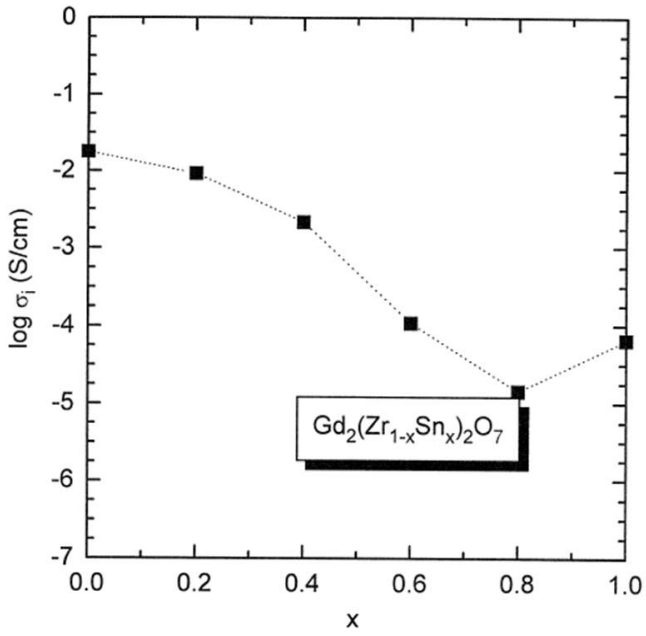

Figure 49: Ionic conductivity versus Sn dopant on the B site of GZO at 1000˚C. Ionic conductivity decreases with the increase of Sn on the b-site of the pyrochlores (81).

Much like the Sn/GZO composites sensors, it is important to understand the effect of the sensor's response in different oxygen environments. When looking at the response of the $Gd_{1.6}Sm_{0.4}Zr_{1.8}Sn_{0.2}O_7$ pyrochlore under varying oxygen environments, diffusion from the bulk can be seen at 20%, 10%, and 1% oxygen levels (Figure 50).

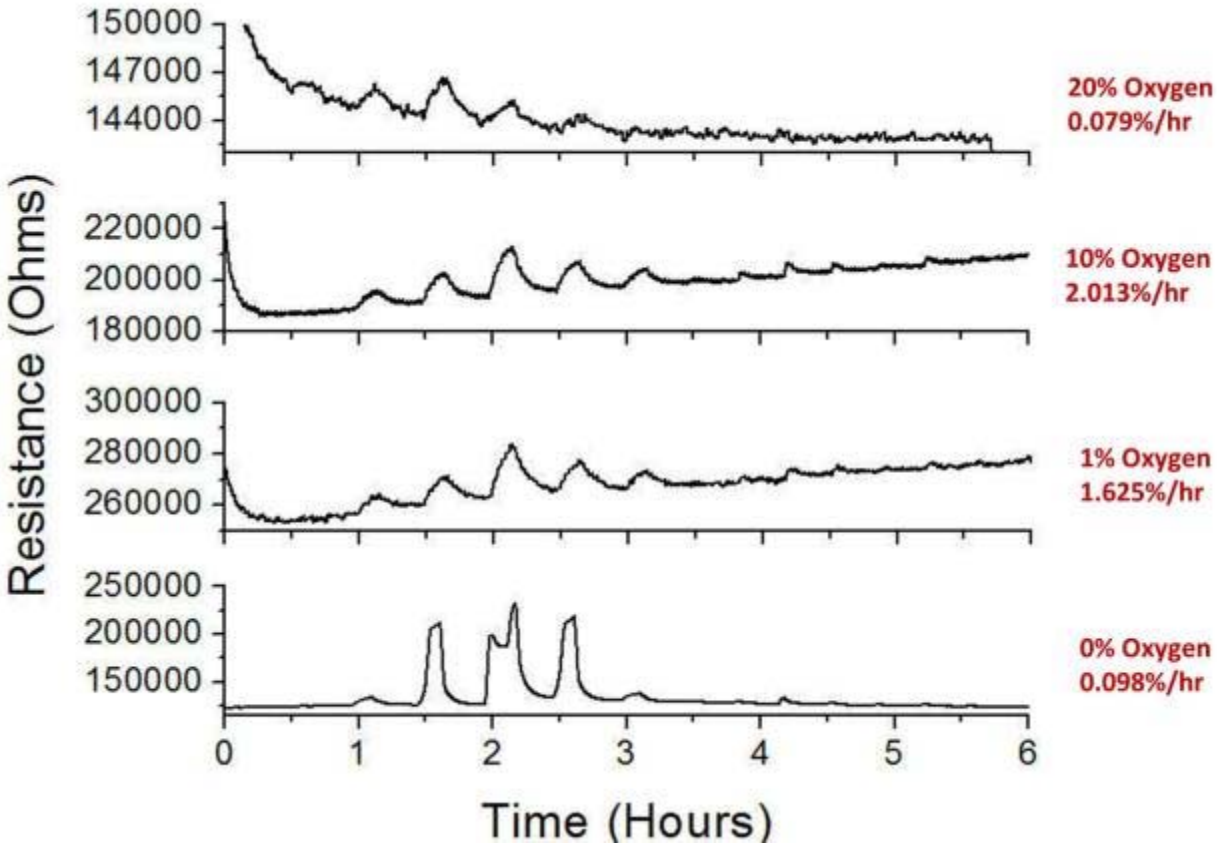

Figure 50: Ionic response of $Gd_{1.6}Sm_{0.4}Zr_{1.8}Sn_{0.2}O_7$ at 1000˚C at 0, 1, 10, and 20% oxygen atmospheres. Material exhibits similar mechanisms at each oxygen atmosphere with oxygen diffusion curves seen at the response and recovery of H_2.

The conduction mechanism is consistent with each oxygen environment. A p-type like response is seen at each oxygen partial pressure. Since this composition is still a complete ionic conductor, the same mechanisms drive the reaction as the pure gadolinium zirconate material (GZO). Frenkel defects are the pathways for oxygen conduction, equation 33, and the bulk oxygen tries to reach equilibrium with the oxygen in the atmosphere through equation 34.

$$O_o^x \leftrightarrow V_o^{\cdot\cdot} + O_i'' \quad (33)$$

$$O_o^x \leftrightarrow \frac{1}{2}O_2 + V_o^{\cdot\cdot} + 2e' \quad (34)$$

The main difference between the two materials is that the Sn-doped systems have hydrogen adsorption at high temperatures, where very little to no adsorption was seen in the pure GZO sensors. By incorporating the Sn into the pyrochlore structure, the completely ionic material maintains its p-type like response, unlike the SnO_2/GZO composite systems where the conduction mechanisms was dependent on temperature and oxygen partial pressure.

Diffusion curves on the introduction and exiting of hydrogen gas can be seen similar to response curves seen in CuO gas sensors. The curvature is consistent with each reaction and follows an exponential curve in the various partial pressures indicating that the

diffusion coefficient is consistent in this range of oxygen partial pressures. Yu and Tuller investigated the conduction of tin doped gadolinium zirconate at temperatures ranging from 750-1050˚C and a range of oxygen partial pressures. As the percentage of tin is increased, the ionic conduction decreases. At a certain point, p-type and n-type conduction at high and low Po_2 respectively begin to appear as seen in Figure 51[114A].

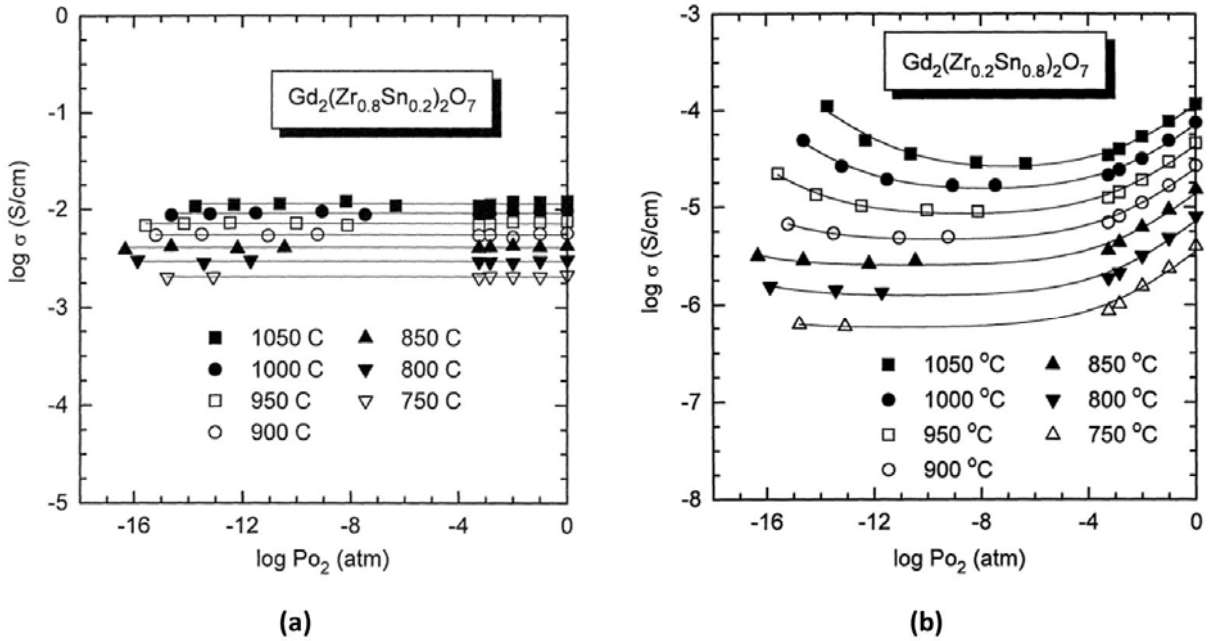

Figure 51: The log conductivity as a function of log oxygen partial pressure for $Gd_2(Zr_{1-x}Sn_x)_2O_7$ with (a) x=2, and (b) x=0.8. Pure ionic conduction is seen for a zirconate only slightly doped with Sn but as Sn is increased mixed conduction is present [Yu and Tuller et al. 1996].

When comparing the sensor tests from $Gd_2Sn_2O_7$ with the conduction measurements from Tuller's work, the lower temperatures are consistent with the ionic conductivity results seen in Figure 51 and the $Gd_{1.6}Sm_{0.4}Zr_{1.8}Sn_{0.2}O_7$ is also consistent with the ionic region found by Tuller. In inert atmospheres the sensor's response becomes unstable, as seen in Figure 52. Tuller noted that the n-type region usually seen with mixed ionic conductors at low oxygen partial pressures was not seen with GSO [Yu and Tuller et al. 1996]. He contributed this to a decomposition of the phase which was also seen with the pure GZO sensors. The decreased sensitivity, 40% decrease for 4000 ppm H_2 at 1000˚C, is due to both the reduction of ionic conductivity and the increase in activation energy when

compared to $Gd_{1.6}Sm_{0.4}Zr_{1.8}Sn_{0.2}O_7$.

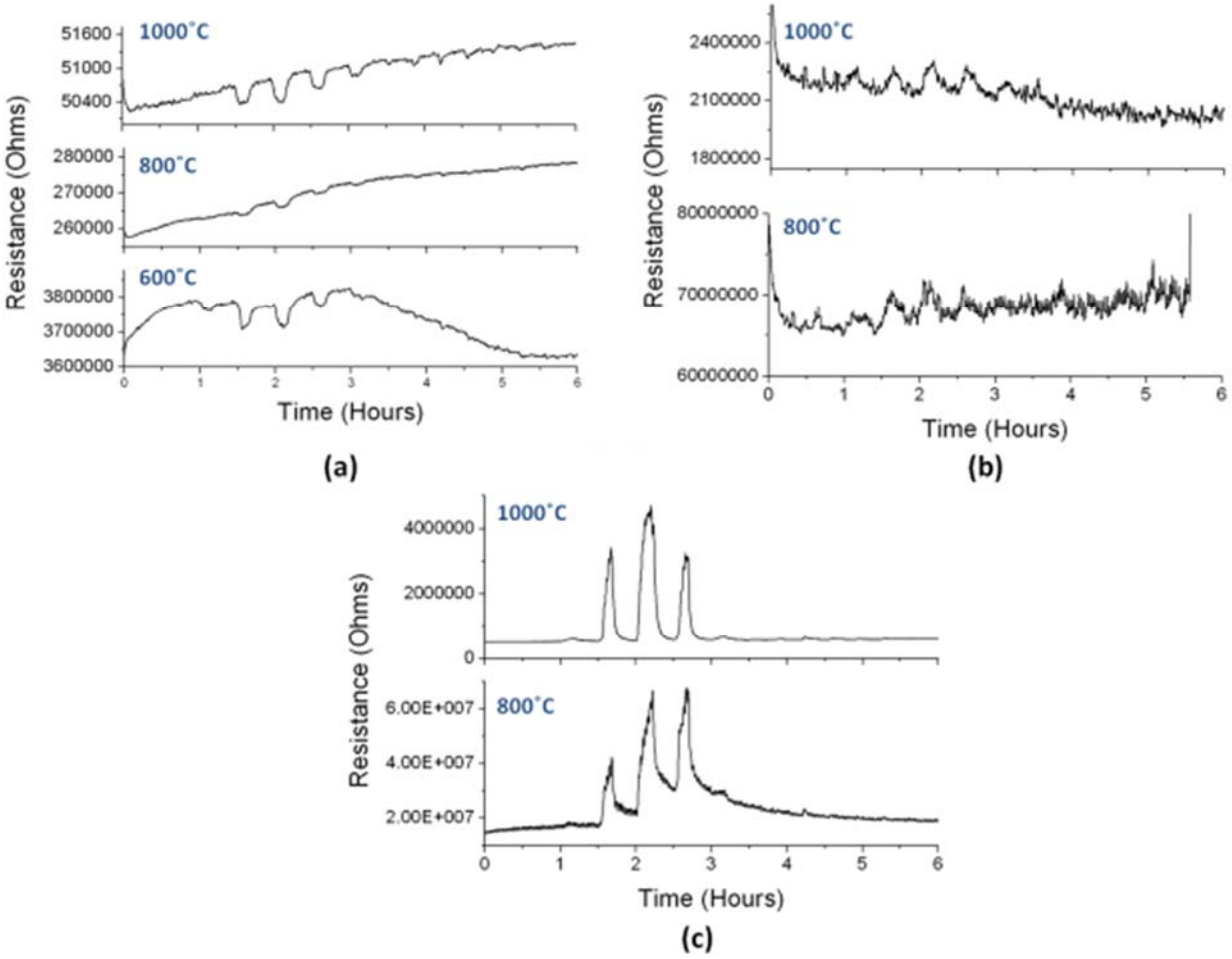

Figure 52: Complete $Gd_2Sn_2O_7$ tests in (a) 20% oxygen, (b) 10% oxygen, (c) 0% oxygen. Material showed increase in drift and decrease in sensitivity as compared to a zirconate doped by 2% Sn on the b-site.

2) Sensor Testing of Tungstate and Molybdate Nanomaterials

Parameters such as selectivity, sensitivity, cross-sensitivity, response and recovery time were characterized. In the literature, sensitivity of a sensor is usually represented by equation given in Eq. 35, where R_a is the resistance in dry air and R_g is the resistance in the target gas. The response time is defined by the sensor to reach 90% of the total resistance variation due to the change in concentration of the target gas.

$$\boldsymbol{S = R_a - \frac{R_g}{R_a} = \frac{\Delta R}{R_a}} \qquad \text{(Eq. 35)}$$

The sensing material was printed to a thickness of ~300 µm onto platinum (Pt) electrodes and sintered at 1200˚C. In order to promote the adhesion between the substrate and printed sensing material (and to reduce cracking in the sensing material), the sensors were placed on a hotplate at 90˚C for half an hour to dry and then heat treated in a box-furnace with a heating rate of 2˚min^{-1} to 600˚C and then 4˚/min to 1200˚C, and held for 1 hour at that temperature.

Figure 53 shows the total heat cycle that each sensor was exposed to during the test. During these tests, the sensors were heated and held at 600˚C, 800˚C, and 1000˚C for 8.5 hours, and then the sensors were cooled down to room temperature under atmospheric conditions unless otherwise indicated. In a few situations, the sensor was cooled down under N_2 flow in order to conduct chemical analysis of the final sensing material.

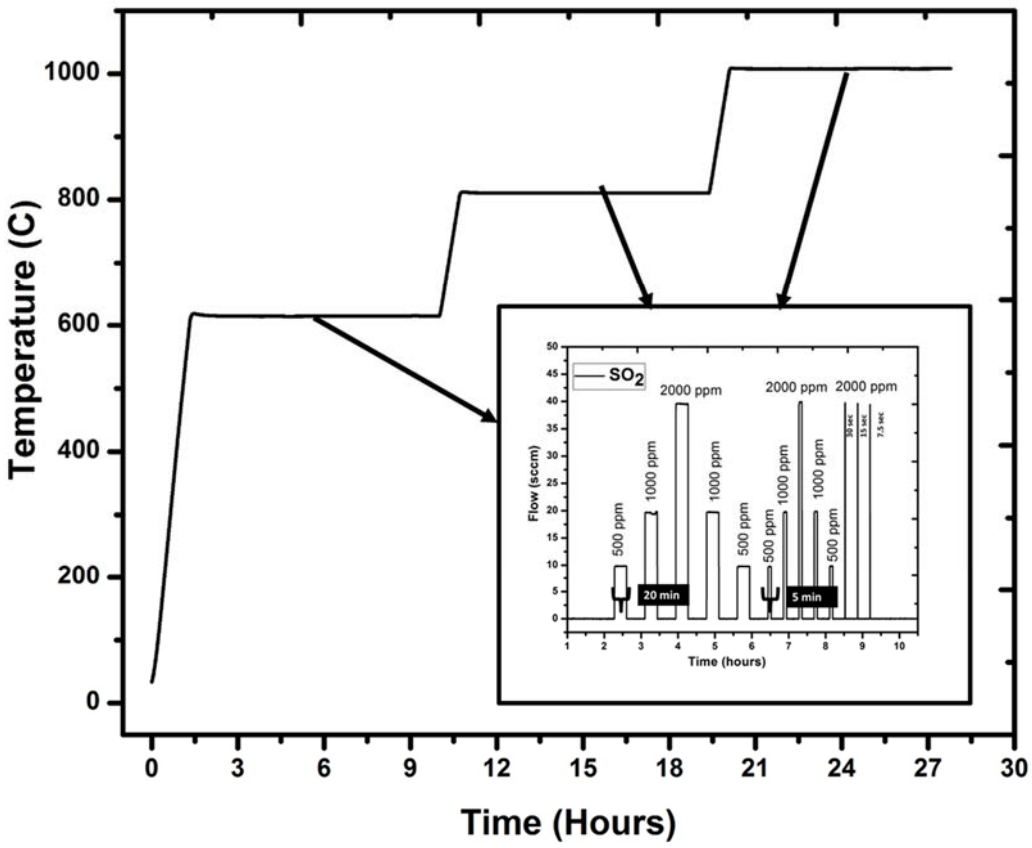

Figure 53: Thermal cycle for sensor testing.

Figure 54 shows the concentration of the target gas and time of exposure during holds at the designated temperatures. In every case, the total flow was adjusted to 50 sccm by adjusting the flow of hydrogen (H_2), nitrogen (N_2) and oxygen (O_2) via the digital mass flow controllers (MFCs). Three different concentration levels of target gas balanced with a pure nitrogen (N_2, 99.99%, Matheson Ultra High Purity grade) were tested at three different exposure times (at three different temperature regimes, 600, 800, 1000°C). Three different ultra-high purity O_2 (Matheson research Grade 99.998%) partial pressures (1, 5 and 20 %) were further tested for the selected compounds in order to understand the contribution of ionic conduction to the total electrical conduction. The exposure cycle presented in Figure 54 increased the ppm level of SO_2 from 500 to 1000, and then to 2000 ppm, and then decreased back down to 500 ppm. Each of these gas concentrations were held for 20 min and then the pyramid was repeated with a hold time of 5 min. A final pulse of the maximum concentration was placed on the sensors for 30 sec, 15 sec, and 7.5 seconds in order to test the response and recovery time. Each of these pulses balanced with pure N_2 and 1% O_2 (05 sccm) was kept present during the entire hold at designated temperature. A 30 min holding

time in pure N_2 was placed on the sensors between each pulse in order to allow the sensors to recover before further exposure testing.

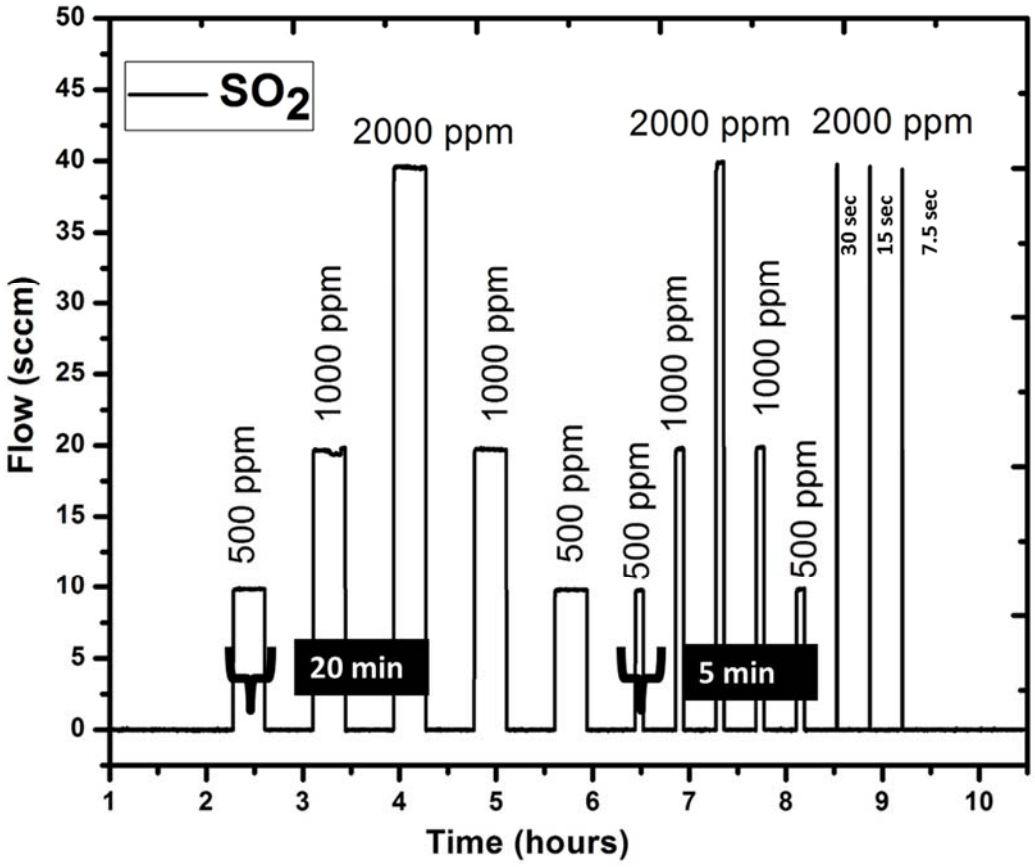

Figure 54: Flow rate of target gases for sensor tests.

The select sensing materials were also tested in the presence of 1000, 2000 and 4000 ppm for H_2 and CO. The successful compounds that showed high sensitivity toward SO_2 were further tested for 50-100 ppm H_2S as well as syngas composition. The syngas is consist of 32% H_2, 40% CO, 20% CO_2, 1% O_2, 1% Steam (H_2O), 1 % H_2S, 5% N_2. Table 7 presents the material systems tested.

Table 7: Material systems tested for H_2S, SO_2 and H_2 sensing.

Target Gas	Molybdates				Tungstates			
	MoO_3	$SrMoO_4$	$SrMgMoO_6$	$NiMoO_4$	WO_3	$SrWO_4$	$SrMgWO_6$	$NiWO_4$
SO_2	X	X	X	X	X	X	X	X
H_2		X	X	X		X	X	X
H_2S		X						X
CO		X	X	X		X	X	X
Syngas		X						

Evaluation of sensing behavior of binary and ternary tungstates and molybdates (WO_3, MoO_3, $SrWO_4$, $SrMoO_4$, $NiWO_4$, $NiMoO_4$, $MgMoO_4$, Sr_2MgWO_6, and Sr_2MgMoO_6) were completed for SO_2, and H_2S. The CO and H_2 cross-sensitivity tests were also completed for abovementioned compounds. The tests were conducted at three different temperatures (600, 800 and 1000°C) in the presence of 500, 1000 and 2000 ppm of the testing gas (SO_2 primarily). The successful compounds ($SrWO_4$ and $SrMoO_4$) that demonstrated high sensitivity towards SO_2 were further tested for 4-100 ppm H_2S diluted in both H_2 and syngas composition.

$SrMoO_4$ Nano-flowers and Commercial Grade Powder

$SrMoO_4$ adopts tetragonal scheelite crystal structure and reported to be stabile up 1000°C under 15% H_2/Ar [198B]. Figure 55 shows the testing results of the commercial grade micron size $SrMoO_4$ (Alfa Easer, Strontium molybdenum oxide, 99.9%, CAS 13470-04-7). The material showed very good sensitivity and accurate output, and excellent repeatability at especially 1000°C. It was not observed that sensor signal output switch from n-type to p-type or opposite as it was observed for WO_3, MoO_3 and $NiMoO_4$. The sensitivity at 1000°C was 20% decreased in resistance, which has not been observed so far any of the materials tested for 2000 ppm of SO_2. For these reasons, the material was subjected to further investigation by synthesizing various nanomaterial morphologies of this composition.

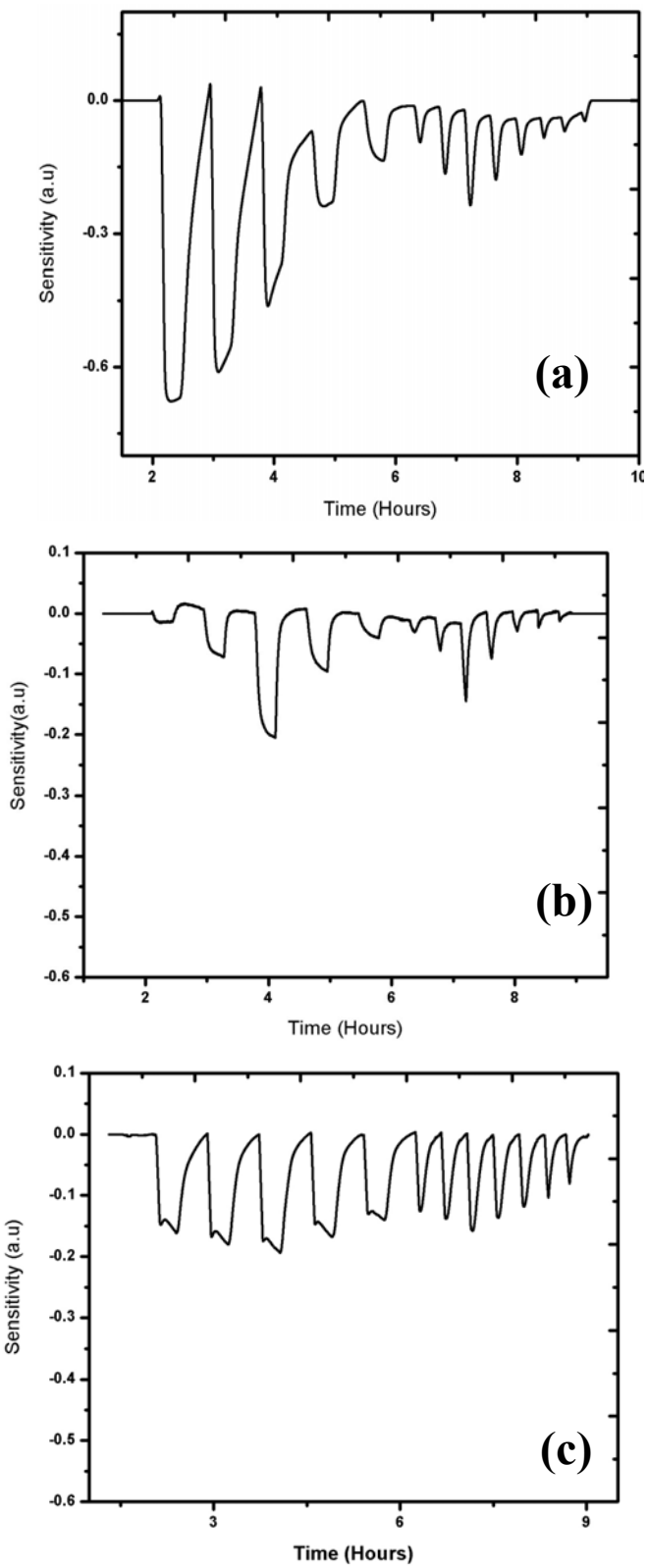

Figure 55: $SrMoO_4$ micron response to SO_2 under 1% O_2 partial pressure (a) 600°C and (b) 800°C and (c) 1000°C.

Different $SrMoO_4$ nanomaterials were tested at the same conditions with the previous compounds. In comparison to other morphologies of $SrMoO_4$, the nanoflowers showed the highest sensitivity at all three temperatures. Therefore; only testing results of $SrMoO_4$ nanoflowers were shown in Figure 56. The results revealed that the sensitivity at 600°C for the $SrMoO_4$ was 90%, with the resistivity decreasing upon exposure to SO_2 at the first exposure. The following exposures in the testing procedure showed that sensitivity was up to 40%. At the 800°C and 1000°C testing temperatures, the sensitivities of $SrMoO_4$ nanoflowers was almost 50% higher compared to the $SrMoO_4$ commercial powder. The change in resistance is defined as the percent drift in the data. The sensor signal also was smooth and drift was not observed. In other words material recovered to its initial resistance once the target gas removed from testing chamber. Another significant point is that nano strontium molybdate was more accurate to distinguish different concentrations of the target gas. It is noteworthy to indicate that the $SrMoO_4$ was tested for the first time for SO_2 in the literature. Figure 56-c shows sensitivity versus time graph at 1000°C. As can be seen from the graph, the material not only demonstrates reasonable repeatability, but also the sensing material permits the ability to distinguish between different concentration levels of the target gas.

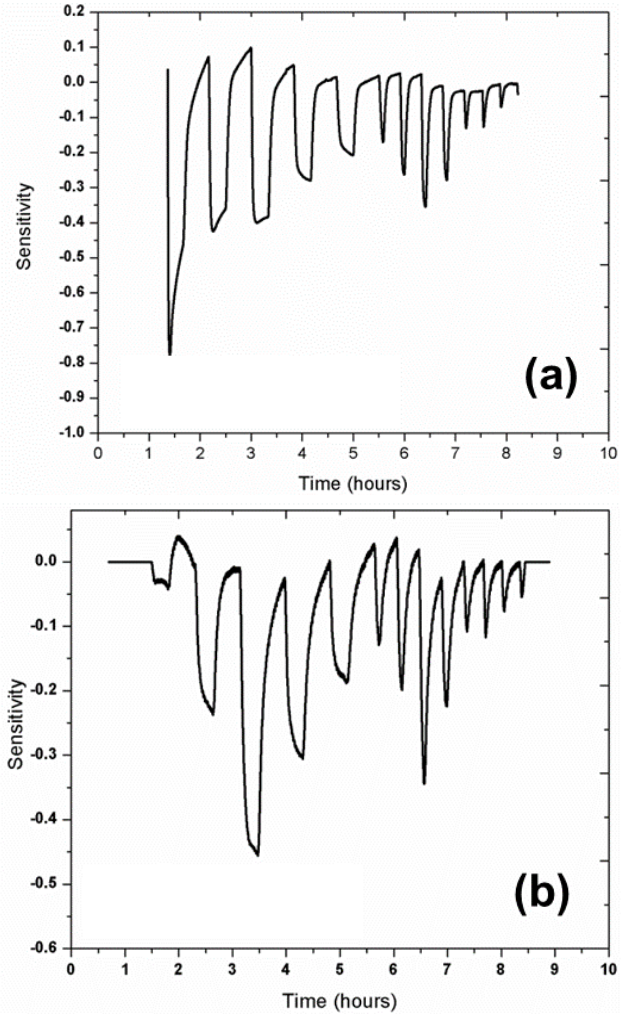

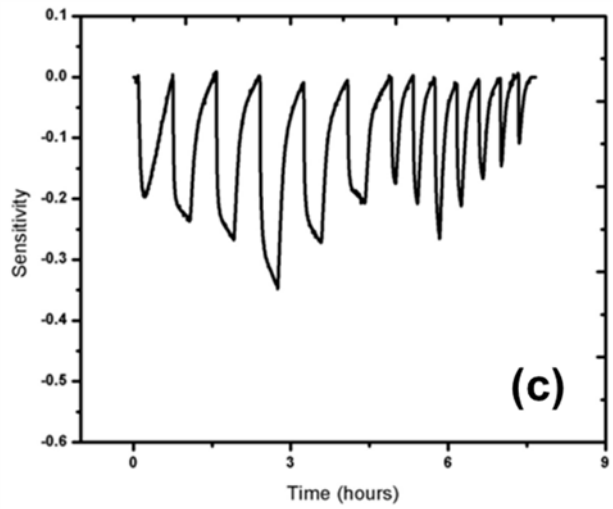

Figure 56: $SrMoO_4$ nanoflowers sensor response to SO_2 under 1% O_2 partial pressure (a) 600°C (b) 800°C and (c) 1000°C.

The $SrMoO_4$ nanoflowers were also tested for H_2 cross-sensitivity under 1% O_2 partial pressure and the results were very promising. The concentration of H_2 (4000 ppm at maximum) was twice as much as SO_2 (2000 ppm at maximum). The sensitivity was much smaller for the H_2 sensing compared to SO_2, and there was even no sensitivity at 600°C against H_2, at this temperature the sensing material was not even electrically conductive. It can be summarized from Figure 57 that at 1000°C, the sensitivity towards SO_2 was 10 times that of H_2.

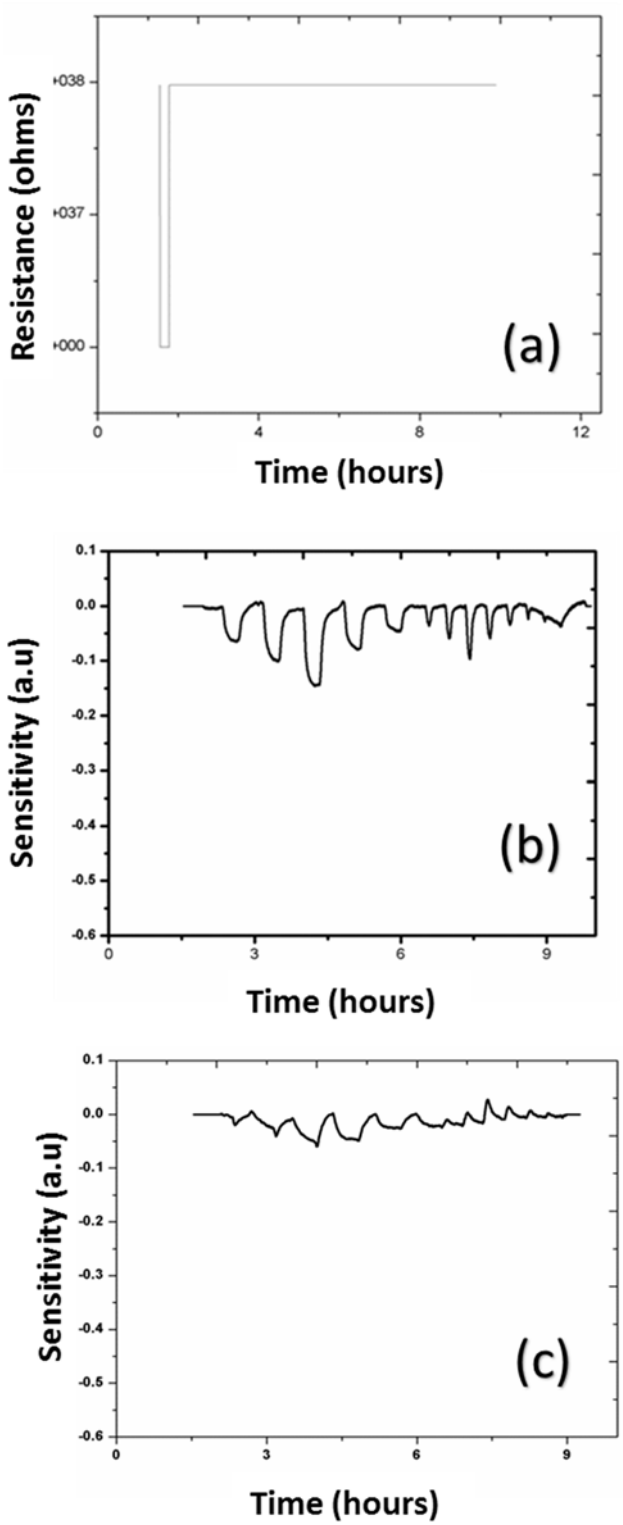

Figure 57: $SrMoO_4$ nanoflowers sensor response to H_2 under 1% O_2 partial pressure (a) 600°C (b) 800°C and (c) 1000°C.

As a brief summary, it can be concluded that micro-WO_3, WO_3 nanorods, micro-MoO_3, and micro-$SrMoO_4$ were evaluated for SO_2 sensing at three different high temperatures (600, 800 and 1000°C). XPS analysis was completed for WO_3 nanorods to better understand the sensing mechanism. Even though MoO_3 itself did not show reasonable sensitivity towards SO_2, the $SrMoO_4$ composition showed highly reliable sensitivity and repeatability without drift at 1000°C. The reason behind the failure of the WO_3 nano-rods at high temperature was investigated, and it can be concluded that both coarsening and reduction of the sensing semiconducting oxides were the prime causes of the sensing failure. Nano-$SrMoO_4$ was synthesized with different microstructures and the SO_2 testing results for best material was presented. $SrMoO_4$ nano-flowers showed the highest SO_2 sensitivity and lowest H_2 cross sensitivity at 1000°C.

$SrWO_4$

The $SrWO_4$ composition was also tested using the same sensor platform. Figure 58 shows the $SrWO_4$ sensor response to SO_2 under 1% O_2 partial pressure. As known from initial experiments and literature, WO_3 showed reasonable sensitivity towards SO_2. At 600°C under 1% O_2 (mix N_2), the sensor response was accompanied by a resistivity increase upon exposure to SO_2 for $SrWO_4$ in contrast to what observed in WO_3. The $SrWO_4$ sensitivity toward SO_2 was higher than that of the nano-WO_3 at 600°C by showing 90% chance in the resistance, which was 20% change in WO_3 case. At 800°C, the sensing behavior of $SrWO_4$ (see Figure 58-b) was not reliable and large drift was also observed. In addition, the sensor did not recover totally and could not sense 70% of the gas pulses. Figure 58-c shows the sensor response at 1000°C. The $SrWO_4$ showed good and smooth response to SO_2 characterized by a resistance decrease up to 20% decrease in resistance upon exposure to 2000 ppm of SO_2 balanced with N_2 and 1% O_2. $SrWO_4$ was tested for the first time as a gas sensing material; therefore the switch from p-type to n-type behavior cannot be compared with the literature. However, the sensing response change upon an alteration in the testing environment oxygen content and/or temperature (p-type to n-type or opposite) is typical characteristic of WO_3.

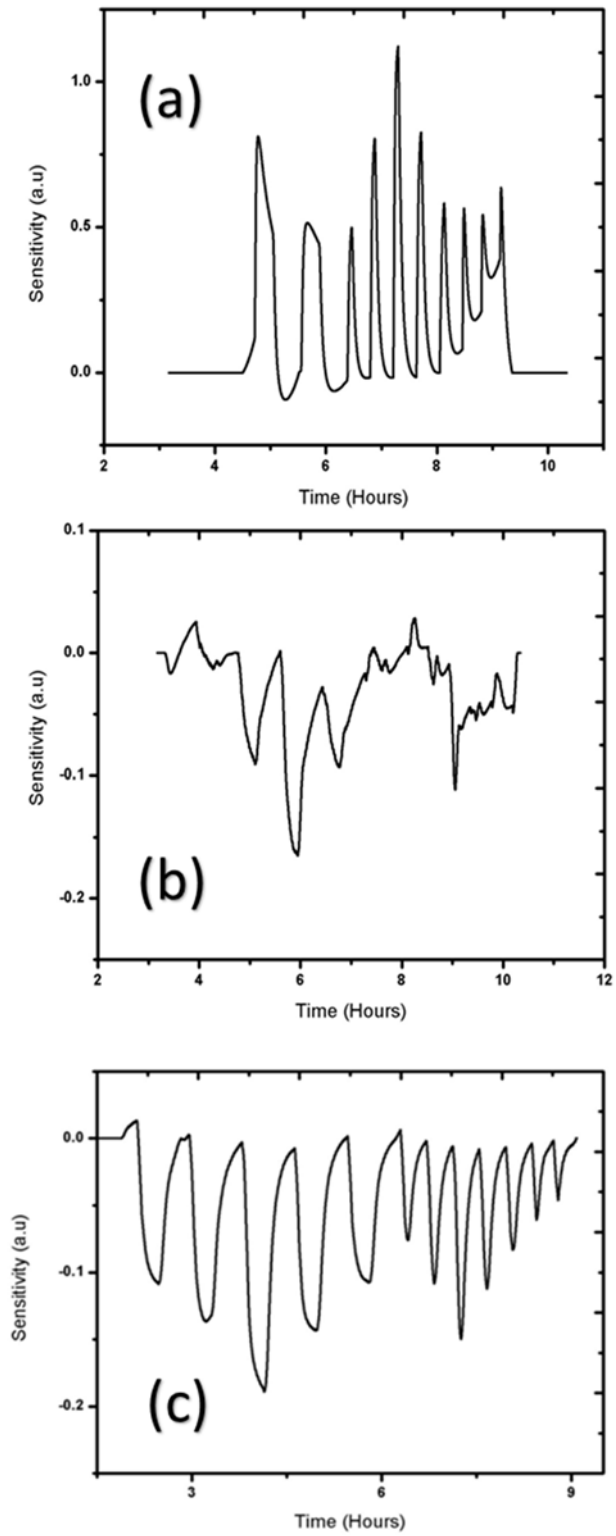

Figure 58: Micron size $SrWO_4$ sensor response to SO_2 under 1% O_2 partial pressure (a) 600°C (b) 800°C and (c) 1000°C.

Hydrogen sulfide (H_2S) testing of selected compounds

The materials showed high sensitivity toward SO_2 and low cross sensitivity to H_2 tested against hydrogen sulfide (H_2S). Two different approaches were employed to have better understanding over sensing mechanism and evaluate the successful implementation of potential sensor material under real service environment. The H_2S tests were completed at the commercial partners testing facilities and following testing procedure was developed and carried out for all H_2S testing. The sensors for H_2S were heated to 800°C at 5°C/min in N_2 and then held near 800°C overnight with data collection the entire time. The total flow of all gases into the oven was set at 100 sccm. In first type of test, the H_2S was derived from a gas blend with 200 ppm of H_2S and a balance with H_2 and select of sensing material was tested for 5, 50 and 100 ppm of H_2S. In the second type of test, the sensing material was exposed to 4, 34 and 64 ppm of H_2S balanced in syngas is consist of 32% H_2, 40% CO, 20% CO_2, 1% O_2, 1% steam (H_2O), and 5% N_2. Once the magnitudes of the flows were established, the balance of the total 100 sccm flow was made up of N_2 from a tank.

As expected, the $SrWO_4$ sensing material showed better high temperature behavior and showed better sensing and sensitivity behavior. The results are shown in Figure 59-a and –b. The compound showed a p-type response to 5 ppm H_2S at 800°C; however, the rest of the responses were n-type in behavior. The material showed high sensitivity toward the H_2S which can be attributed to highly stable 2+ state of the Sr in the $SrWO_4$ lattice Even though $SrWO_4$ showed reasonable sensitivity, the compound was not able to distinguish between different levels of H_2S. As seen in the Figure 58-c and-d, there is no distinguishable difference between 50 ppm and 100 ppm of H_2S exposure.

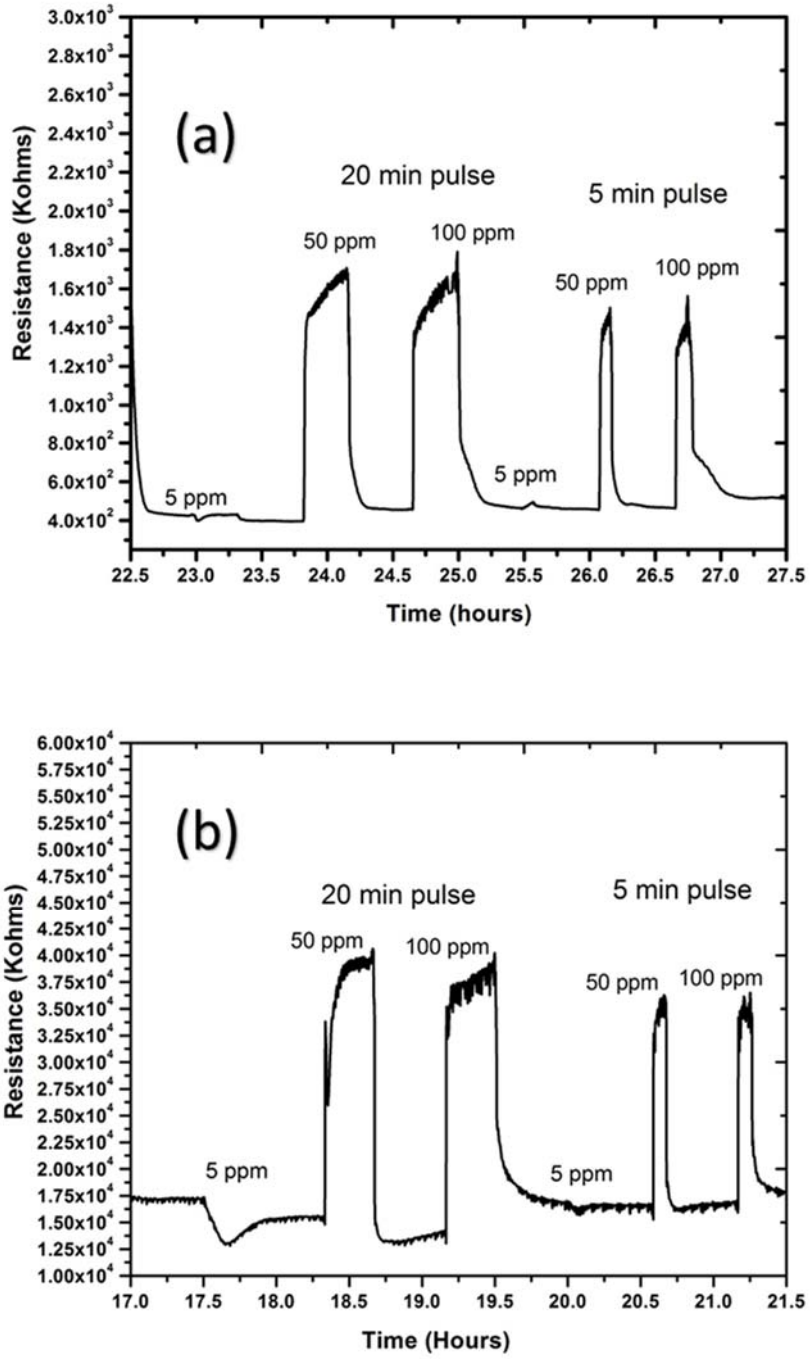

Figure 59: H_2S testing of $SrWO_4$ (a) 800 and (b) 1000°C.

The $SrMoO_4$ nanoflowers were tested for H_2S and the results are shown in Figure 60-a and –b shows the results of the compound against H_2S. The compound showed n-type sensing response to the target gas at all concentration levels and testing temperatures. The responses at 800°C showed a difference between the exposure to 50 and 100 ppm

concentration levels of the target gas. Moreover, the difference in the gain of the sensor response increased at 1000°C. The compound showed stable electrical conductivity at high temperature like $SrWO_4$ that can be seen on the graphs presented in the Figure 59-c and –e. $SrMoO_4$ adopts tetragonal scheelite crystal structure which has low symmetry, inversion center in the middle of the unit cell and relatively open crystal structure. The early study by Hayashi et *al.* stated that $SrMoO_4$ transfers from scheelite to perovskite after 1200°C under very low oxygen partial pressure (log P (O_2)=-12.45). Another study reported that $SrMoO_4$ can be reduced under 15%H_2/Ar conditions at temperatures higher than 1000°C. Another point is to be deserved is that ABO_3 ($SrMoO_3$) is not stabile phase, even under room conditions with the help of humidity it's tend to oxidize to scheelite structure [202B]. It was also shown that ABO_3 (A=Sr, Ba B=Mo) oxidation starts at 250°C [198B].

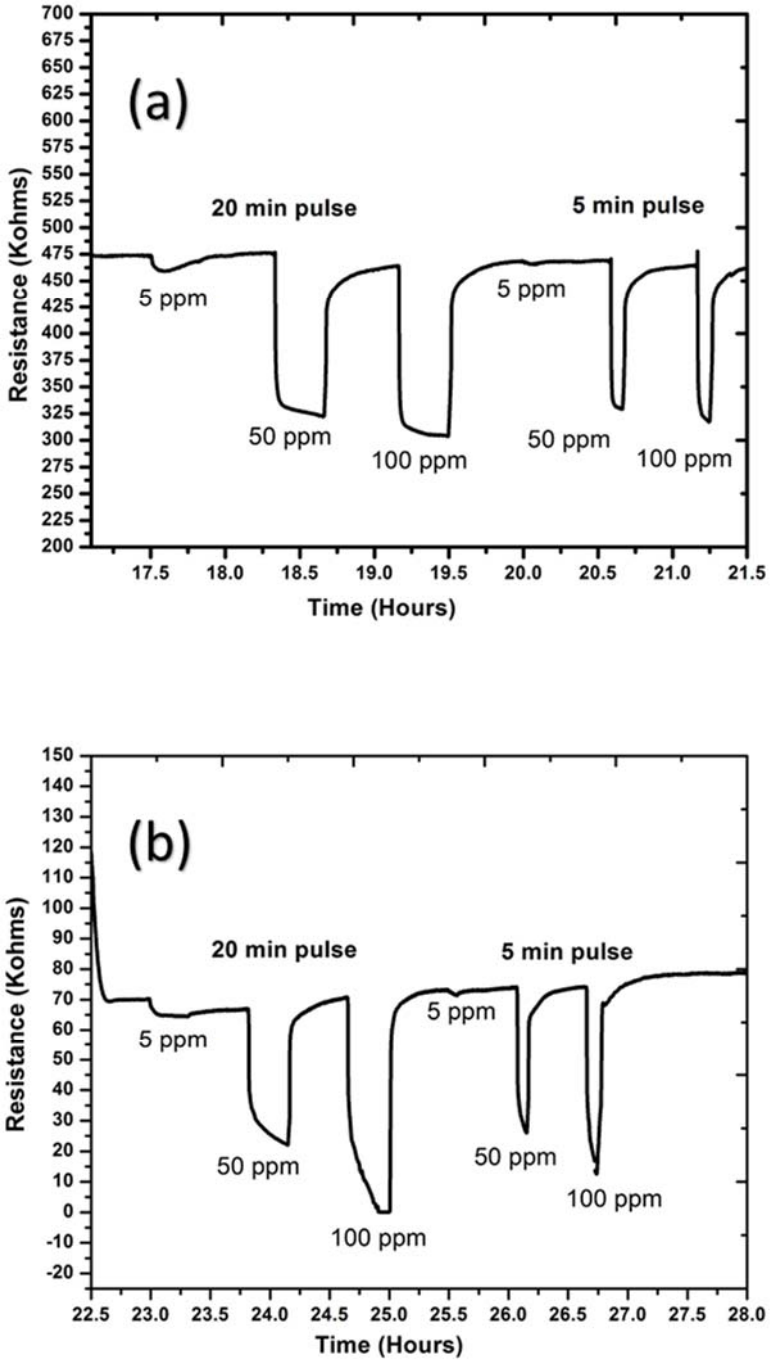

Figure 60: H_2S testing of $SrMoO_4$ (a) 800 and (b) 1000°C.

The testing results for syngas composition is given in the Figure 61-a and –b. Syngas is consist of 32% H_2, 40% CO, 20% CO_2, 1% O_2, 1% Steam (H_2O) and 5% N_2 and sensor exposed the different levels of H_2S at 800 and 1000°C for 5 and 20 minutes. During steady

stead conditions 4, 34 and 68 ppm of H_2S introduced the testing chamber and the $SrMoO_4$ nano showed p-type sensing behavior. The missing signal at the 1000°C is 68 ppm exposure. It is not sensing material malfunction, most likely at that point the contact/connection between sensor pad and DMM was disturbed. Sensor unexpectedly showed p-type sensing behavior. This is the first time $SrMoO_4$-nano showed n/p type switch in terms of sensing behavior. Apart from this sensor showed up to 60% resistance change upon exposure to different levels of H_2S.

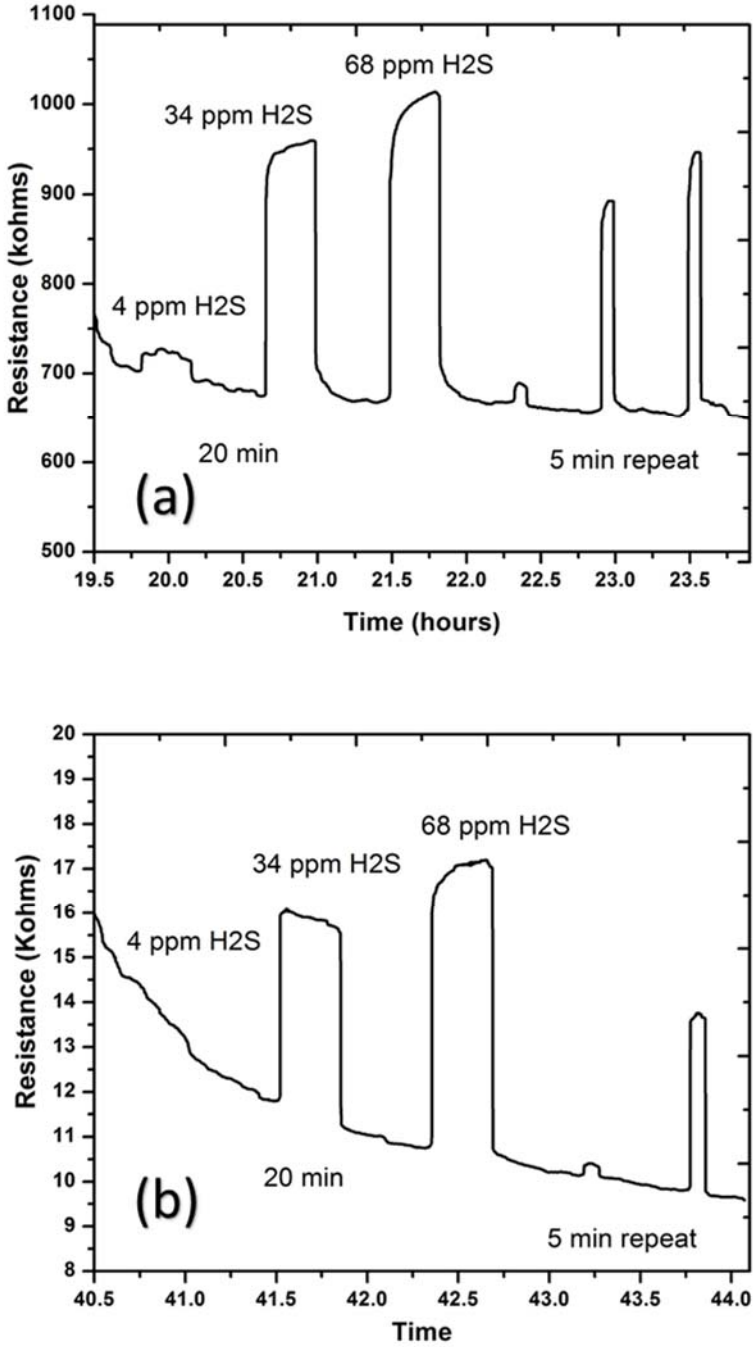

Figure 61: Syngas testing results of $SrMoO_4$-nano at 800°C (a) and 1000°C (b) upon exposure to 4, 34 and 68 ppm levels of H_2S.

Summary and nanomaterial stabilization efforts

Figure 62 shows the comparison of the sensitivities of the different sensing materials at 1000°C against SO_2 under 1% O_2 partial pressure condition. $SrMoO_4$ nano-flowers showed the highest sensitivity toward SO_2 at 800°C and 1000°C among all other compounds tested.

However, at an elevated temperature of 1000°C, the sensitivity of the compound decreased compared to the low testing temperatures. In addition, the $SrMoO_4$ nano-flowers possessed the highest sensitivity against H_2S exposure among the other materials tested (see Figure 58). Moreover, the material showed very stability and sensitivity toward H_2S in syngas stream as well.

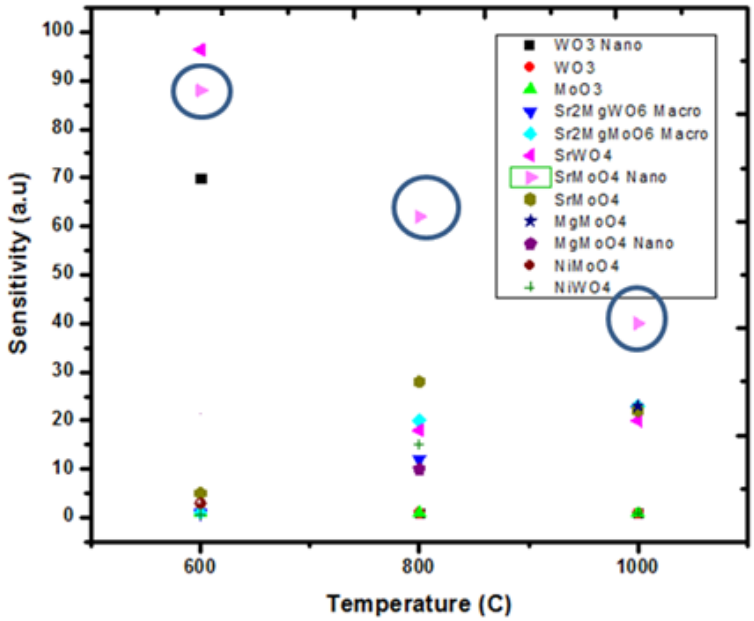

Figure 62: Testing results of different oxides in nano and macro scale at 1000°C for 2000 ppm SO_2 balanced in N_2 at 1% O_2.

After evaluation all of the material systems (considering SO_2 and H_2S sensitivity and cross-sensitivity toward CO and H_2), the $SrMoO_4$ emerged as a choice sensing material for SO_2 and H_2S. The compound was synthesized in four different morphologies; although all of them showed sensing behavior towards the sulfur compounds at high temperature, they succumbed to coarsening and lost the high sensitivity. The coarsening issue can be seen clearly in the SEM micrographs presented in Figure 63-a and –b. The $SrMoO_4$ nanostructures turned into 5-10 micron particles that were densely packed regardless of the initial morphology.

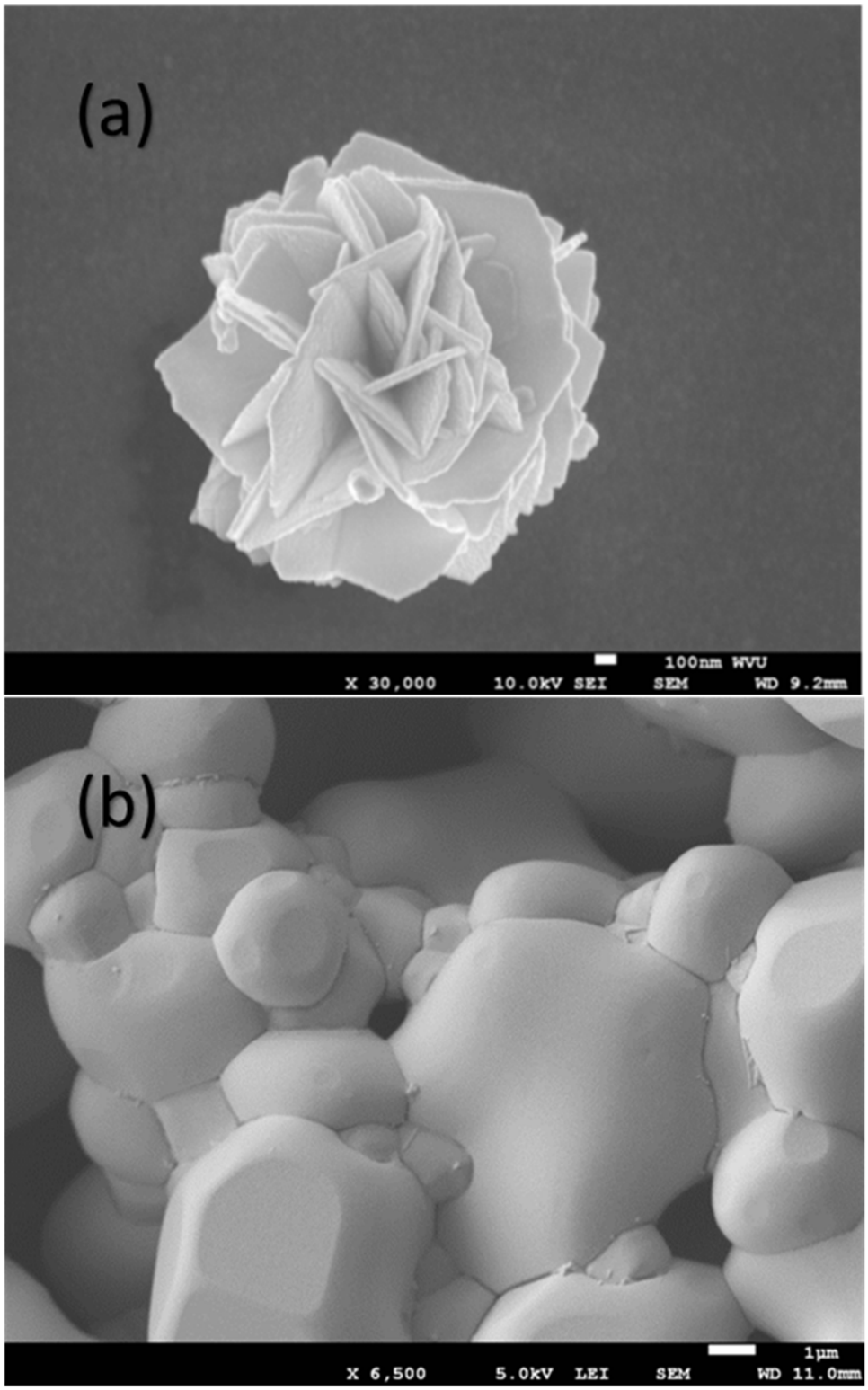

Figure 63: SEM micrographs of the $SrMoO_4$ nano-flowers (a) as-synthesized and after full scale testing (b).

Nanomaterials are known to be unstable at elevated temperatures due to sintering and coarsening mechanisms, and these issues drawback their prospective utilization within advanced sensors at high temperature. In order to retain the high surface area of the synthesized $SrMoO_4$ nanomaterials, strategies were required to limit the sintering and grain growth processes of this material. In order to retain the high surface area of the synthesized nanomaterials, this work focused on strategies to limit the sintering and grain growth processes. Two different strategies with different stabilizing mechanisms were proposed in order to hinder/stop the coarsening/sintering process. The strategies chosen were grain and substrate pinning of the chosen nanomaterial through the distribution of coarsening resistant secondary phase among nanomaterial grains and the bonding of nano-granular microstructure over a stable refractory substrate where thin film grains are usually pinned to their 2 D substrates at low thicknesses, and the grains cannot grow. Also, if the substrate is refractory then the substrate will be stable to high temperatures. If it is in fiber form, then the refractory fiber will only have a few connections to permit transport that would significantly hinder the coarsening and sintering related diffusion.

Grain pinning strategy was realized by dispersing 10% wt. in-house made CeO_2 nano-particles by solvent exchange method to $SrMoO_4$. In order to evaluate the temperature resistivity of the mixture, 5 h heat treatment at 1000°C was conducted. Figure 64shows the SEM micrograph of the $SrMoO_4$ with the secondary phase CeO_2 after heat treatment. As seen in the SEM micrograph, partial success was obtained through this method, where the grain growth was hindered to some extent. However, the densely packed grain morphology would not result in an increase in the sensitivity. Because of that this composition was not used as a sensing material and this strategy abandoned.

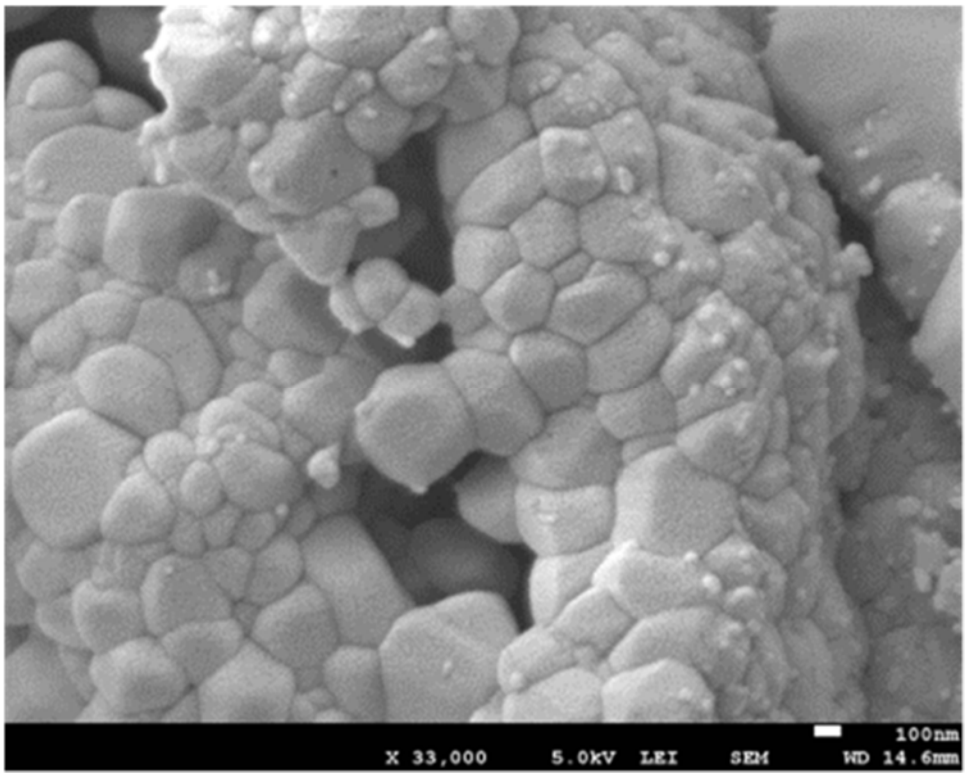

Figure 64: SEM micrograph of 10% wt. CeO_2 mixed with $SrMoO_4$ by solvent exchange after annealing at 1000°C for 5 h.

In order to realize second strategy, MgO nano-rods were synthesized via hydrothermal route. Figure 65-a shows the SEM micrograph of the as-synthesized MgO nanorods. In order to evaluate the high temperature coarsening resistance of the compound, the fibers were heat treated to 1000°C for 5 h. The final microstructure of the MgO fibers are shown in the 65-b. As can be seen from the SEM micrograph, the MgO nano-rods did not coarsen and retained their microstructural formation at the temperature of interest.

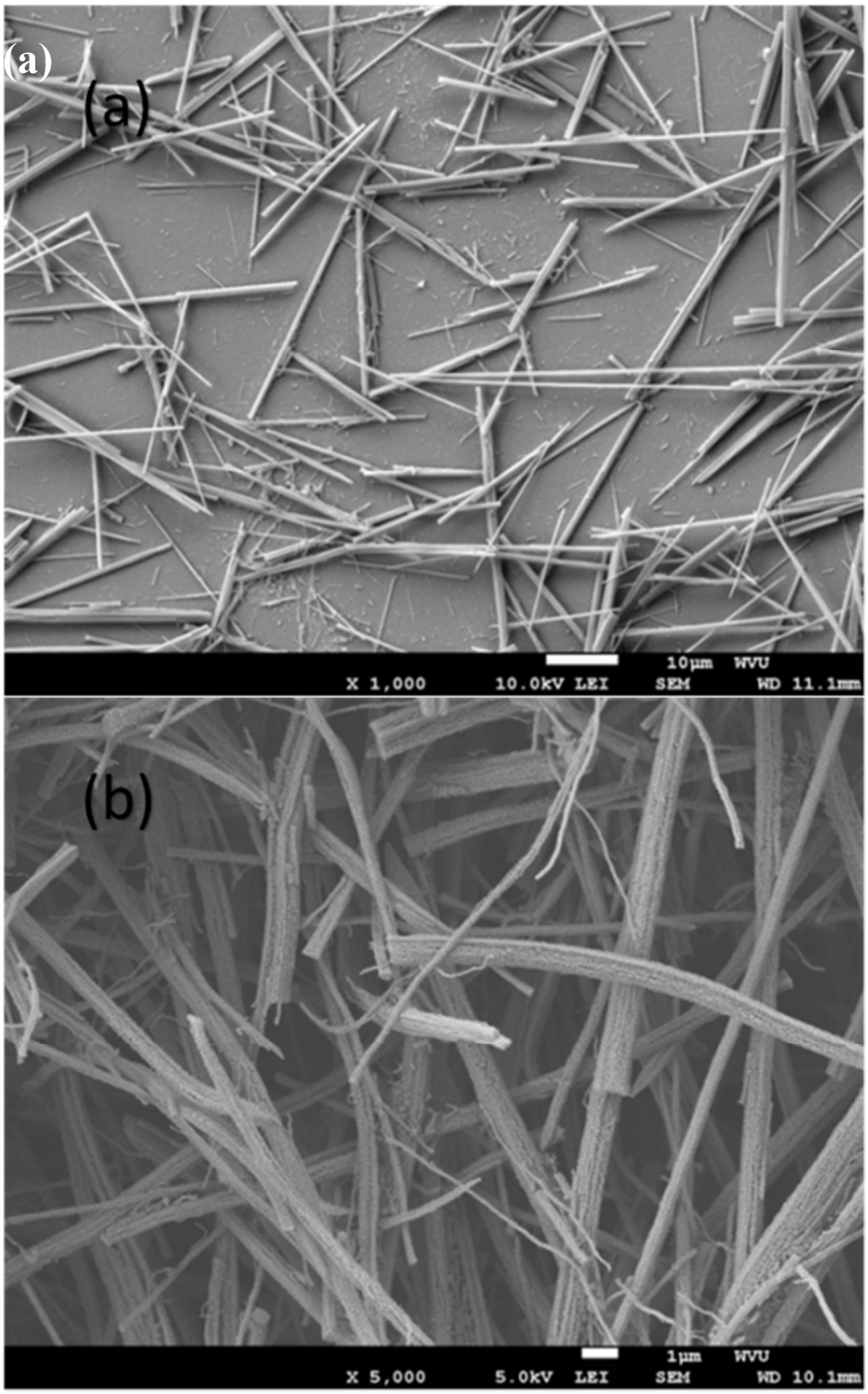

Figure 65: SEM micrograph of the MgO nanorods (a) as-synthesized and (b) heat treatment after 5 h at 1000°C.

$SrMoO_4$ nanoflowers showed superior sensing behavior against SO_2 compare to other compounds and low cross-sensitivity toward H_2 and CO. Figure 66-a and -b shows the

sensitivity results of the tested compounds against SO_2. Figure 66-c shows testing result of the $SrMoO_4$ nano structures against H_2. As seen in the sensitivity graph, the material showed very low cross-sensitivity toward H_2. The sensitivity was ~0.5% reduction in resistance upon exposure to 4000 ppm of H_2. That low level of cross-sensitivity further increases the usability of the material as a SO_2 sensor. The $SrMoO_4$ showed n-type sensing response to target gas at all concentration levels and testing temperatures. Post-exposure characterizations were completed on this compound which included XPS and SEM-EDS, in order to better establish an understanding of the sensing mechanism and the final chemical state of the compound after exposure to a reducing atmosphere. Figure 66-a shows comparison of the sensitivities against SO_2 at 1000°C under 1%O_2 partial pressure. High sensitivity of the $SrMoO_4$ nano-flowers diminishes as the temperature increases. Therefore, the $SrMoO_4$ nano-flowers were grown over MgO core structure via hydrothermal route.

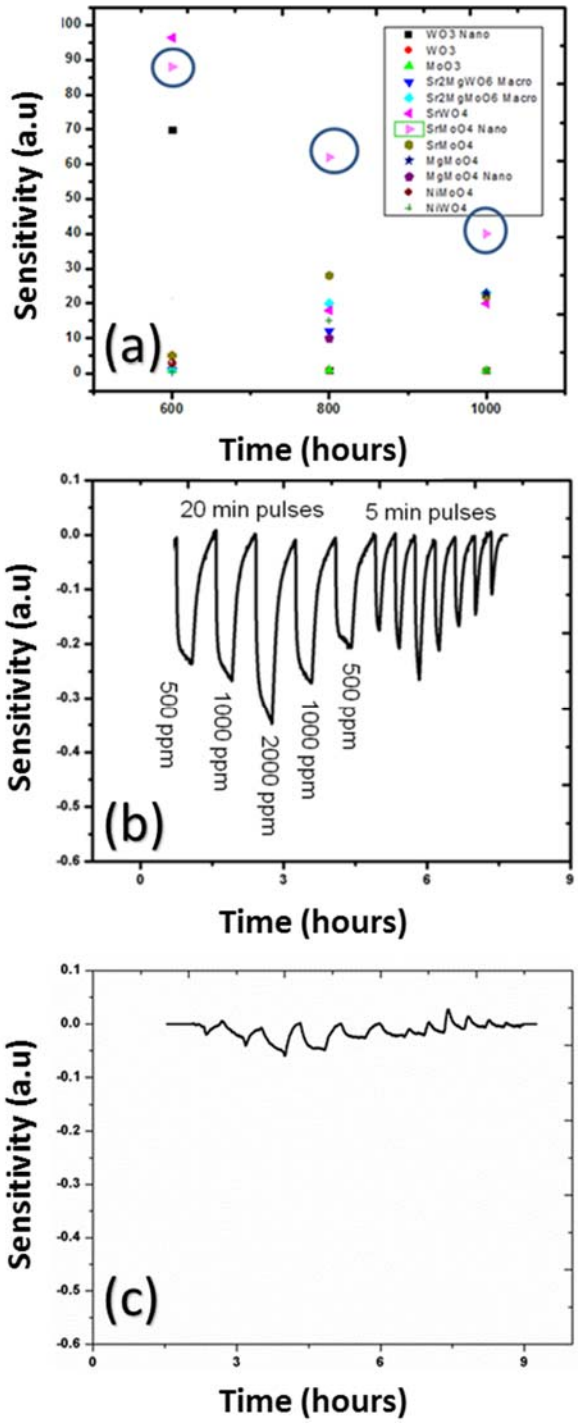

Figure 66: (a) Testing results of different oxides in nano and macro scale at 1000°C for 2000 ppm SO_2 balanced in N_2 with 1% O_2 Sensor signal of $SrMoO_4$ nano-flowers in response to (b) SO_2 (c) H_2.

There was no modification to the hydrothermal processing route parameters that were presented previously for the synthesis of $SrMoO_4$ nanoflowers. Figure 67-a and -b presents the SEM micrograph of the $SrMoO_4$ decorated over MgO core structure at low and high magnifications, respectively. In order to evaluate high temperature resistance of the

templated growth material, the materials were heated to 1000°C and held for 5 h. The resulting microstructure is presented in the SEM micrograph shown in the Figure 67-c. The microstructure of the nano-$SrMoO_4$ decorated over the MgO fiber was highly resistant to effects of the high temperature conditions. The highly porous microstructure was preserved after preliminary annealing practice at 1000°C for 5 h. The nano-$SrMoO_4$ decorated over MgO will be termed as $SrMoO_4$/MgO in the rest of the work.

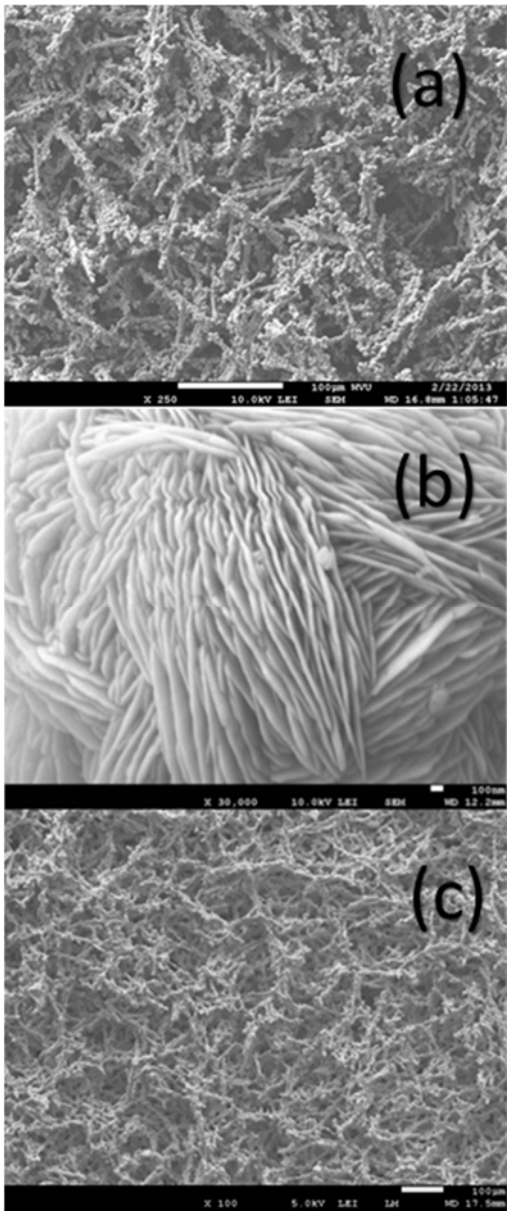

Figure 67: (a-b) As-synthesized $SrMoO_4$ nanoflowers growth over MgO nanorods ($SrMoO_4$/MgO) low and high magnification (c) after 5 h at 1000°C heat treatment.

$SrMoO_4$/MgO was tested against exposure of H_2S, SO_2, H_2 and CO on the previously described sensing platform. The H_2S testing was completed at the facilities of the commercial partner (NexTech Materials, Ltd., Lewis Center, OH, USA) with the same testing parameters previously described. Figure 68 shows the testing results of

$SrMoO_4$/MgO for SO_2 at 600, 800 and 1000°C. $SrMoO_4$/MgO engineered material unexpectedly showed very low sensitivity toward SO_2 at all of the testing temperatures. Further tests were conducted over different sensors of same material and similar results were obtained. The reasons behind the $SrMoO_4$/MgO`s different selectivity against SO_2 was the subject of intensive investigation by utilizing various advanced characterization methods, which included TEM, Raman, XPS-UPS, TPR and mass spectroscopy. This work was completed in order to better understand whether or not Mg incorporation into the parent compound lattice and caused changes in the electronic properties of the $SrMoO_4$. These changes would include the band-gap/work function (Φ), density of states in the band-gap and/or MgO target surface/gas interactions that also may change the characteristics of the sensor output.

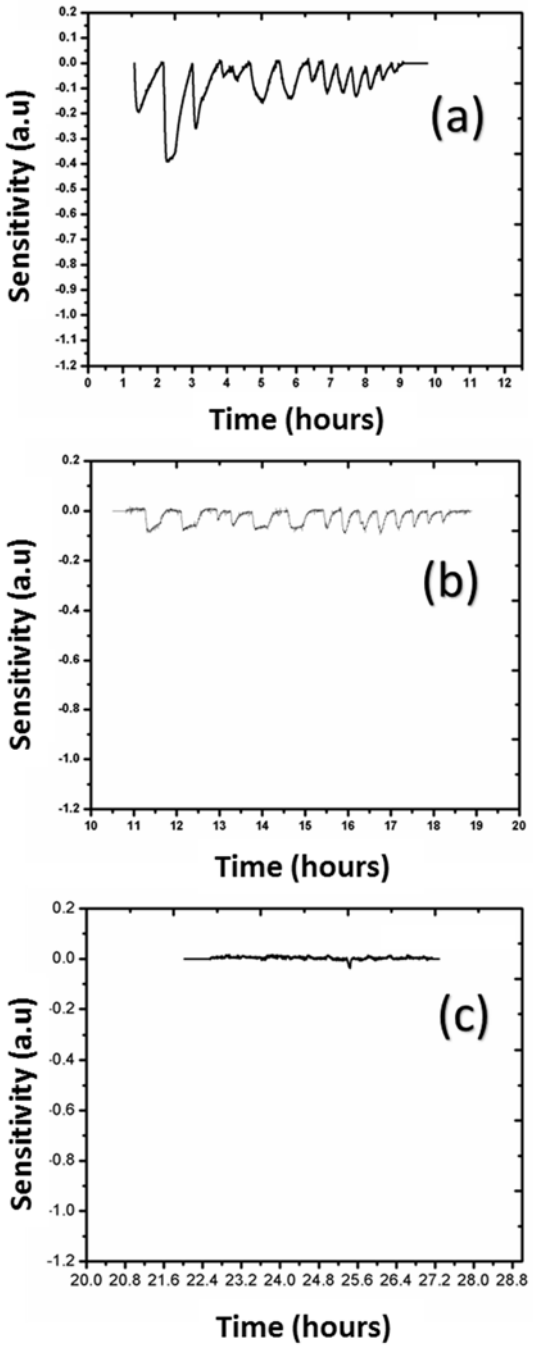

Figure 68: Sensor signal of $SrMoO_4$/MgO core structure in response to different levels of SO_2 with different time of exposure (a) 600°C (b) 800°C (c) 1000°C.

Figure 69 shows the CO cross-sensitivity tests of the $SrMoO_4$/MgO at three different temperature regimes (600, 800 and 1000°C). In this case, the results are not drawn in sensitivity scale since the material did not show any reasonable sensor response to target gas (CO). Therefore, the y-axes in those graphs are drawn in resistance values (Ohms). This behavior of material was already estimated due to $SrMoO_4$`s preliminary tests. As can clearly be seen from the graphs, the compound did not sense the CO at all temperatures.

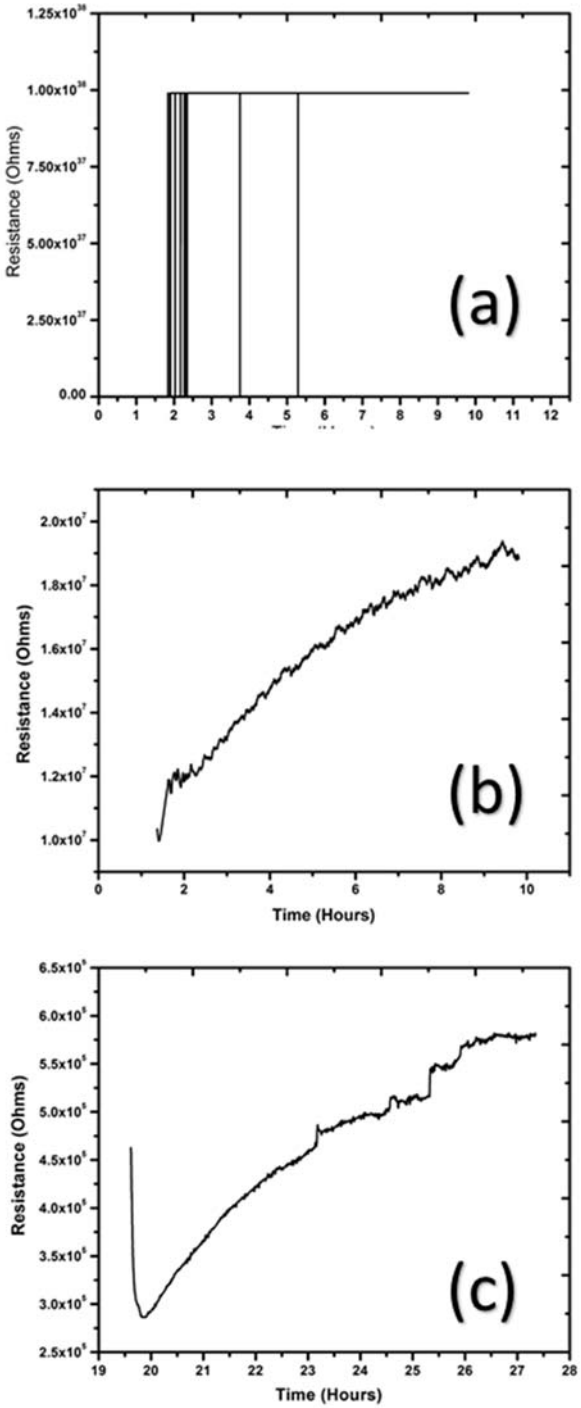

Figure 69: Sensor signal of $SrMoO_4$ /MgO core structure in response to different levels of CO at (a) 800°C and (b) 1000°C.

Figure 70 shows the H_2 cross-sensitivity tests of the $SrMoO_4$/MgO at three different temperature regimes 600, 800 and 1000°C in accordance to testing procedure previously described. The $SrMoO_4$/MgO sensor did not give any output signal and electrically not conductive at 600°C. The material unexpectedly showed a very good sensing behavior

against H_2 at 800 and 1000°C. The opposite occurred for the $SrMoO_4$ nano-flowers structure. At especially 1000°C, almost 85% change in resistance was observed and the sensor showed similar behavior even after 5 successive tests that covered almost 150 hours of operation at 1000°C. Again, the different sensors were tested and similar sensing capabilities observed for this material and target gas composition.

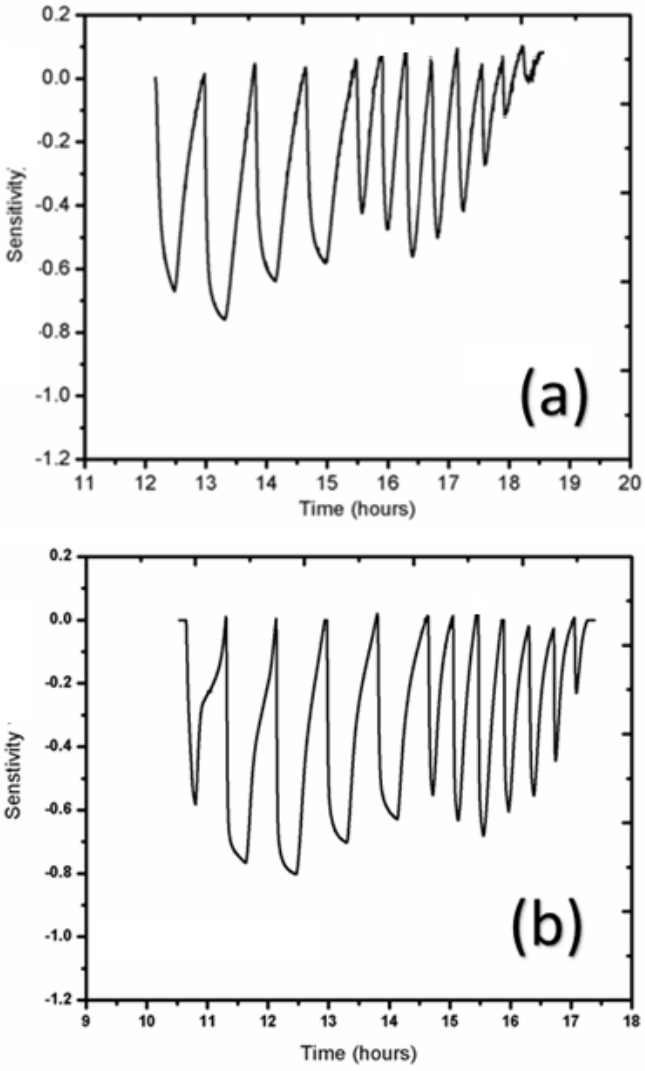

Figure 70: Sensor signal of $SrMoO_4$/MgO core structure in response to different levels of H_2 with different time of exposure (a) 800°C (b) 1000°C at 1% O_2 partial pressure.

As a first step in order to explain the difference in sensing behavior of the materials ($SrMoO_4$ nano and $SrMoO_4$/MgO), the MgO core structure itself was extensively characterized by Raman, XRD, XPS, TPR and SEM-EDS. It is known that MgO nanorods are stable at the temperature regime of interest; however, they are not stable during wet chemical processing. In order to synthesize the $SrMoO_4$ nano-flowers via hydrothermal method, the pH must be adjusted to ~7-8 and at that pH surface of the MgO core structure fist starts to amorphousization and dissolve to the solution at the same time leaving behind a precipitation area for MoO_4^{2-} and Sr^{2+} ions.

Figure 71-a and-b shows the as-deposited state of the nano/micro rods. The as-deposited state of the powders showed very good level of crystallinity (XRD spectrum not included showed single phased highly crystallized material). Figure 71-c shows the Raman spectrum of the MgO after treating at the desired level of pH ~8. The Raman spectrum of the crystallized MgO should have a peak around 3600 cm^{1-}. However, the treated sample did not possess that vibrational mode, or indeed, any vibrational modes. This clearly shows that material lost the crystallinity not from surface, but also at least 1 µm depth, which is typical penetration depth of the utilized laser during measurement. Figure 71-d and –e show the morphological evolution of the powders during the pH treatment that mimics the synthesis conditions. After observing this morphological alteration during deposition, it was decided to conduct further analysis over this core structure and $SrMoO_4$/MgO particles alone in order to help clarify the material composition, electronic and chemical structure. These areas are thought to all contribute to the changed sensing behavior of the compounds against H_2 and SO_2 exposure. Most of the attention was focused on the difference between the $SrMoO_4$ nano-flowers and $SrMoO_4$/MgO structure through extensive characterization for chemical, electronic, structural and phase analysis of aforementioned materials by means of X-ray photoelectron spectroscopy (XPS), Raman, ultraviolet photoelectron spectroscopy (UPS) and ultraviolet-visible light absorption spectrum (Uv-Vis), temperature programmed reduction (TPR) and atomic absorption spectrum (AAS).

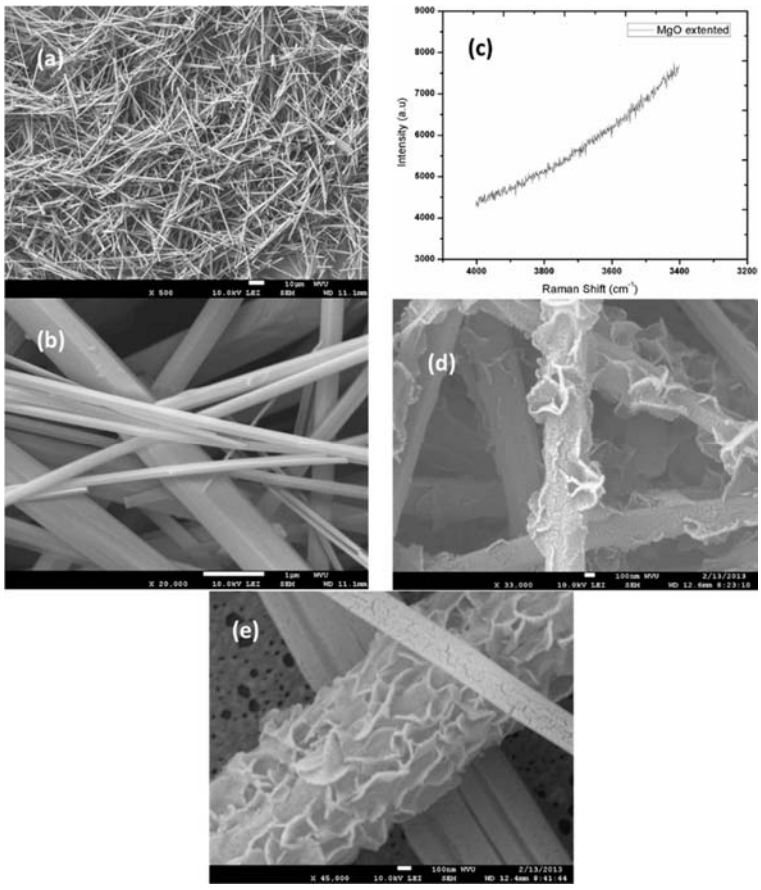

Figure 71: (a-b) As-synthesized MgO core structure (c) Raman spectrum of pH 8 treated MgO (d) SEM image of pH 8 treated MgO (e) higher magnification of pH 8 treated MgO.

The TPR technique is used to characterize the reduction behavior of the oxides as well as catalytic activity of the surfaces toward H_2. Kubo et *al.* conducted TPR analysis for scheelite $SrMoO_4$ and perovskite $SrMoO_3$ in the 25-800°C temperature window with 10% H_2/Ar gas mixture. Authors concluded that reduction of SrMoO4 to $SrMoO_3$ starts at 650°C under hydrogen flow without any oxygen background. In the same study it was also reported $BaMoO_4$ and $SrMoO_4$ have two H_2 consumption peaks located around 600 and 725°C, however $SrMoO_4$`s $H_2$ consumption was almost twice as much as $BaMoO_4$`s H_2 consumption. Authors also concluded over the stability of the $SrMoO_4$ and $SrMoO_3$ by taking TG profiles of them. $SrMoO_3$ weight gain started around 300C until 725°C, after this point there was no further weight gain. And it was confirmed with calculations that $SrMoO_3$ transformed in to $SrMoO_4$ [198B, 205B]. In this work, the technique was utilized in order to shed light over different H_2 adsorption/consumption behavior of the $SrMoO_4$-nano and $SrMoO_4$/MgO. Figure 72 shows the measurements results of the $SrMoO_4$-nano and $SrMoO_4$/MgO. The temperature increased from room temperature to 900°C with the 5°C/min heating rate. As can be seen from the Figure 72-a $SrMoO_4$-nano showed two consumption peaks. They were located at 580 and 825°C. Those values were close to reported in the Kubo et *al.*`s work, however it should be noted that firs adsorption occurs at around 25°C lower than that of the reported value in Kubo et *al.*`s work [198B], however the second absorption peak located around 125°C higher compare to their work. Figure 72-b provide the result of the TPR measurement of $SrMoO_4$/MgO. As seen in the figure it showed totally different absorption/consumption behavior in terms of peak position, number and intensity. First of all $SrMoO_4$/MgO showed a sole maxima around 540°C and the signal output which is proportional to the consumption of H_2 was almost 10 times of $SrMoO_4$-nano. This difference in H_2 consumption could axiomatically attributed to incorporation of MgO into the $SrMoO_4$-nano lattice as well as surface and modify the electronic and catalytic behavior of the compound.

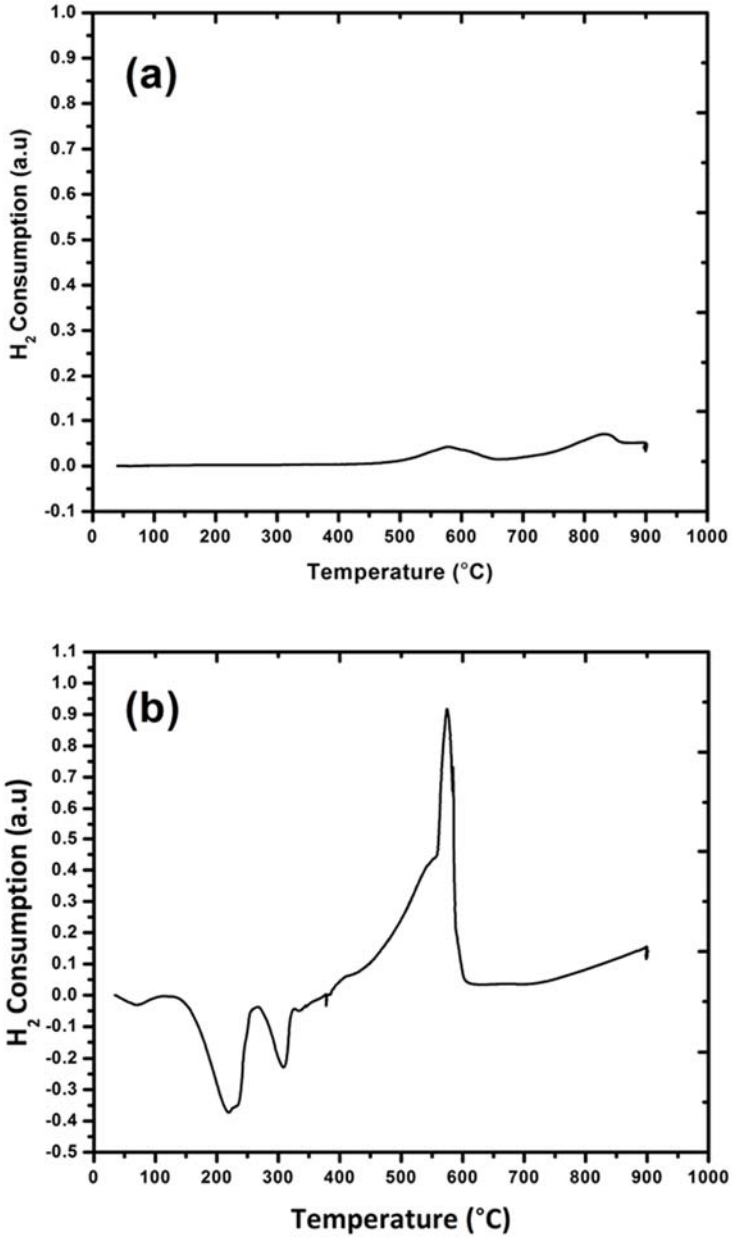

Figure 72: TPR measurements of $SrMoO_4$-nano (a) and $SrMoO_4$/MgO (b) heating rate 5C°/min.

In order to shed light over the difference in sensing behavior of the aforementioned compounds, the first step was to quantify the mount of Mg that was incorporated into the $SrMoO_4$ nanoflowers ($SrMoO_4$/MgO) by atomic absorption spectrum (AAS). Before AAS examination of the $SrMoO_4$/MgO material, XRD analysis was conducted, however it was not possible to determine the MgO. The AAS technique is known for its high certainty for the quantitative determination of chemical elements by employing the absorption and subsequent emission of visible light despite lacking of providing information regarding to chemical, structural and electronic structure of the material of interest. According to AAS analysis of the $SrMoO_4$/MgO, the material contained 3.1% (atomic unit) Mg. After

calculation of the atomic concentration of the Mg incorporation into $SrMoO_4$ matrix, it was focused on the chemical and electronic aspect of the integration**.** For this purpose, as well as determination of the chemical state condition of supposedly remaining core structure, the compositional depth profiling maps of the synthesized material were obtained via XPS and are presented in Figure 73. The thickness of the depletion layer was calculated to be approximately 10 nm, which makes photoelectron spectroscopy (XPS) very useful technique.

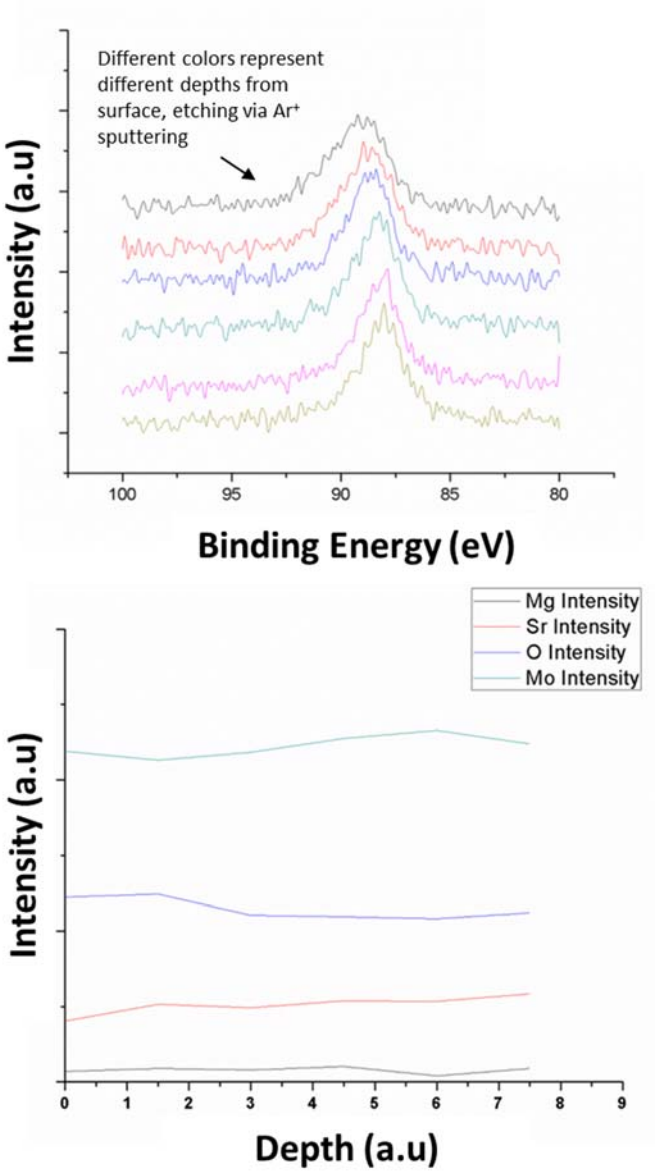

Figure 73: (a) Mg 2p photo-electron line at different depths (b) concentration of the Mo, O, Mg and Sr thorough the $SrMoO_4$/MgO template growth structure.

Figure 73-a represents the chemical state of the Mg throughout the different depths of the as-synthesized $SrMoO_4$/MgO structure. As can be observed form the graph, Mg changes its chemical state through the depth profile. At the surface of the as-synthesized powder,

the material contained Mg in two different compounds (MgO and $Mg(OH)_2$). As the analysis depth increased, a shift in the main photoelectron line occurred towards lower binding energy. This shift can be attributed to the decrease in the amount of $Mg(OH)_2$ and the increase in MgO phases. Another point to mention is that despite the fact that the $Mg(OH)_2$ phase diminished, a shoulder on the high energy binding site still existed. The deconvolution of the peak fits very well to the reported binding values of the Mg in the SMM ($SrMgMoO_{6-\delta}$). It could be argued that the binding energy of the Mg in $SrMoO_4$ and SMM would be different; however, it should be noted that Mo has the decisive effect on the chemical environment of the compound. The most important result of the XPS analysis is shown in Figure 73-b. The figure provides atomic concentrations of the Sr, Mg, O and Mo in different colors through the depth of the as-synthesized material. A significant change in the concentration of the aforementioned elements was not observed. In other words, (as expected) the core structure of the MgO was totally lost, with it forming a secondary phase (MgO and/or $Mg(OH)_2$ or it going into the $SrMoO_4$ lattice as a substitutional solid solution formation discussed above. While the latter was the focus of the Raman investigation, in order to further confirm and determine the amount of the phase precisely. Yet, it should be noted that substitution of Mg with Sr is not likely due to different size of these cations and $MgMoO_4$ as discussed previously has different crystal structure than that of $SrMoO_4$. Figure 74 shows the Raman spectra of the micron, nano, templated and SMM powders, respectively. The Raman technique is sensitive to vibrational modes [206B, 207B]which can be altered by changes in bond lengths and coordination geometries in the crystal structure, allowing it to characterize any substitutional solid solution formation, such as $SrMg_xMo_{1-x}O_4$ and/or Mg incorporation into the $SrMoO_4$ lattice. This substation would cause the peak to broaden, as observed in the Raman data of the SMM ($SrMgMoO_{6-\delta}$) powder. Raman is capable of detecting down to 0.5% substitution in $SrMoO_4$ lattice as main peaks get broad; however, this was not observed in the case of $SrMoO_4$/MgO powder. It should be considered that Raman is not a surface sensitive technique, therefore presented results represent the bulk of the material. In the case of substitutional solution formation, the corresponding amount of it would be less than 0.5%.

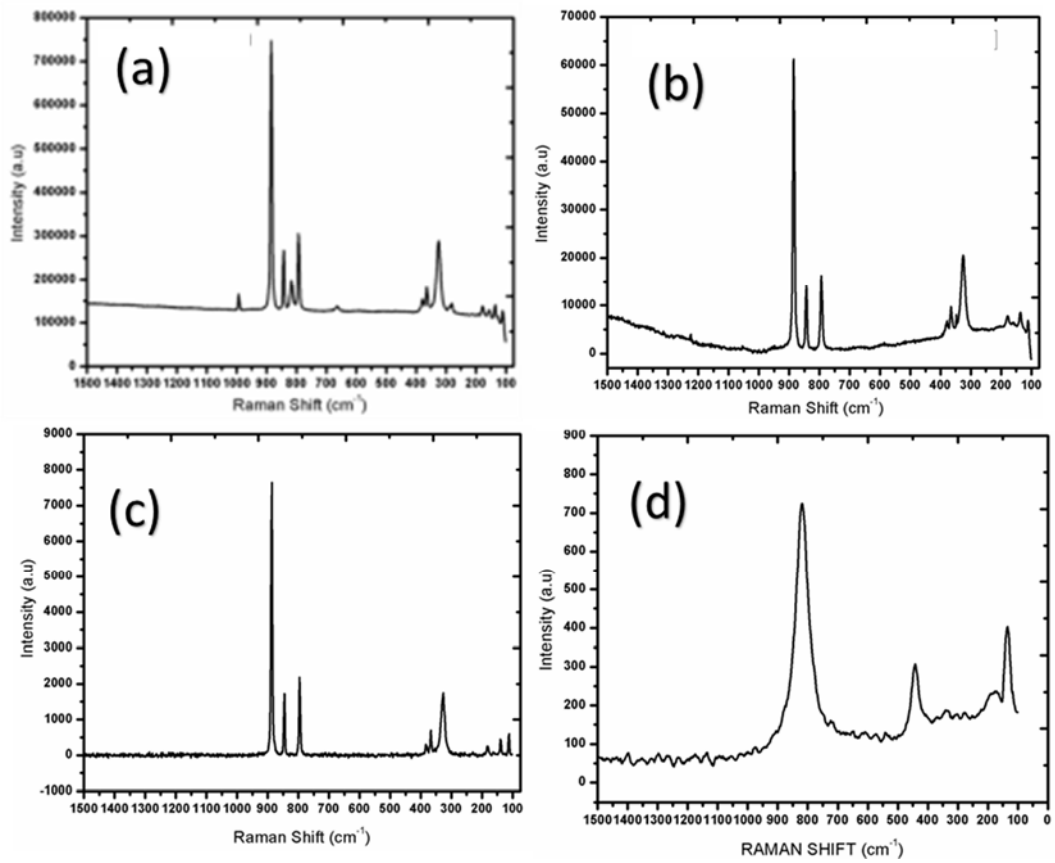

Figure 74: Raman spectrum of the as-synthesized (a) $SrMoO_4$-micron (b) $SrMoO_4$-nano (c) $SrMoO_4$/MgO (d) SMM powders.

Other important consequences of Mg incorporation can be observed in electronic aspects; therefore, the work function and band-gap measurements were conducted via ultraviolet photoelectron spectroscopy (UPS) and ultraviolet-visible light absorption spectrum (Uv-Vis), respectively.

The surface of the sensing material ($SrMoO_4$-nano and $SrMoO_4$/MgO) engages in charge exchange (e^-) with the absorbed and/or approaching gaseous material. Charge exchange between the solid surface and absorbed species depends on the solid surfaces`s work function, which further depends on chemical environment, defect structure, vacancy concentration and cation oxidation state. In order to explain observed reduction in the band gap in $SrMoO_4$ nano compare to $SrMoO_4$+MgO work functions were determined. Average cation oxidation state proportional to work function (φ_m). In other words, oxygen deficiency is disproportional to work function (φ_m). Work-function measurements showed that the measured values for the nano-$SrMoO_4$, $SrMoO_4$-micron and $SrMoO_4$/MgO are 9.3, 8.2 and 7.7 eV, respectively. Regarding the band gap, possible Mg will change the band gap and will create defects related to the bands in the main gap. Figure 75 shows the band-gap measurements of the micron-$SrMoO_4$, nano-$SrMoO_4$ and $SrMoO_4$/MgO. Oxygen deficiency (δ) in $SrMoO_4$/MgO is higher in comparison $SrMoO_4$ nano [8B]. XPS analysis was conducted on the as-synthesized on the surface of $SrMoO_4$/MgO powder. It was concluded that 17% of the O^{2-} was located on unlattice (interstitial) locations. This is also

further supports the lower working value measured in the case of $SrMoO_4$/MgO.

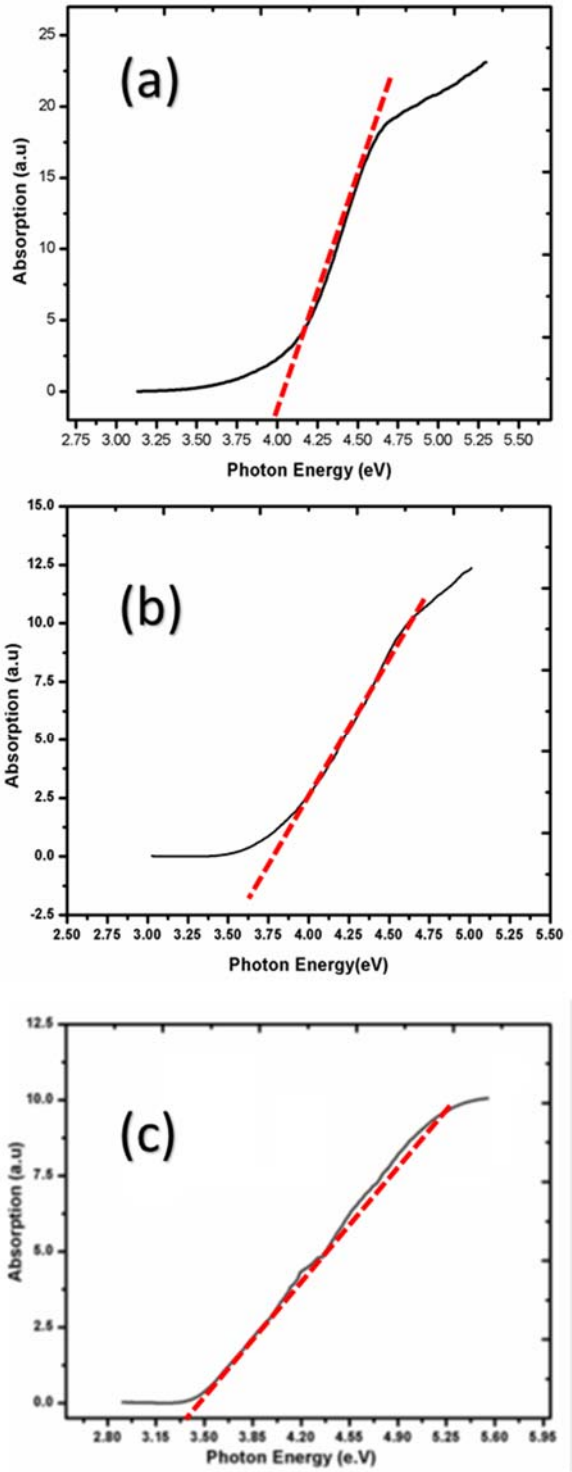

Figure 75: Band-gap measurements of (a) $SrMoO_4$-micron (b) $SrMoO_4$-nano (c) $SrMoO_4$/MgO.

The measured values for the band-gaps are 3.9, 3.6 and 3.2 eV for abovementioned compounds, respectively. The band-gap values for the micron- and nano-sized powder are in a good match with literature [176B, 184B]. Vidya et *al.* synthesized nano $SrMoO_4$ with

the average crystalline size 20 nm by modified combustion process and reported 3.7 eV for optical band-gap of the compound [208B]. The reason for the reduction in band-gap value of $SrMoO_4$/MgO compared to that of nano-$SrMoO_4$ can be axiomatically attributed to two reasons. One reason is that Mo atoms may be missing from the $SrMoO_4$ during the deposition process and/or reduction in the un-lattice (interstitial) oxygen sites. The substitution of Mg into Mo would result in opposite effect regarding to the band-gap height. It is known that quantum confinement and structural disorder and stress results in a decrease in the band gap, which may explain the decrease in the band gap $SrMoO_4$-nano compare to $SrMoO_4$-micron [180B]. However it should be noted that the band gap value (3.9 eV) determined for micron size $SrMoO_4$ powder may not reflect the real optical band gap of the compound due to secondary SrO phase formation which was determined by XRD and further confirmed by Raman spectrum.

Beside the chemical and electronic effect of the Mg incorporation into $SrMoO_4$, the structural formation of the secondary phase on the surface has an important consequences regarding to the catalytic action of the MgO against H_2. Incorporation of Mg into the $SrMoO_4$ is shown and quantified by AAS and further proved by XPS. The unexpected sensing behavior of the $SrMoO_4$/MgO can be attributed to modification of the electronic/chemical structure and catalytic effect of the Mg, as was detected by XPS on the surface of $SrMoO_4$/MgO. The difference in the electronic structure of the nano-$SrMoO_4$ and $SrMoO_4$/MgO was observed both in band-gap and work function values. Incorporation of MgO into $SrMoO_4$, as well as a secondary phase and/or surface layer, are both possible as describe by the above characterization. As small as <0.5% substituted into the structure may have occurred, as is the detection limitation o Raman technique. In order to have better understanding over sensing mechanism, the exactly same amount of MgO that was determined by AAS and XPS was incorporated into $SrMoO_4$ nanoflowers by mechanically mixing and stirring. The first and second tests of the mechanical mix are presented in Figure 76-an and-b, respectively. As seen from the graphs, mechanical mixing does not permit the sensing of SO_2 at 1000°C as its templated counterpart ($SrMoO_4$/MgO) does not either at 1% O_2.

In summary, there are two Schottky barriers in sensor, first between the grains and the second one is located between sensing material and Pt (platinum) electrode due to work function difference of Pt and sensing material. Pt is known to behave like Schottky contacts rather than Ohmic at high temperature [209B]. Work function of Pt is 5.7 eV [201B], basically it becomes decisive at high temperature due to its barrier effect for flowing electrons. Less the difference more the electron flow. In other words the high sensor signal output. Lower work function the SrMoO4/MgO (7.6 eV) in comparison to the $SrMoO_4$ Nano (9.3 eV) increases its sensitivity, apart from its catalytic action against H_2 and lower band gap, porous micro-structure as well.

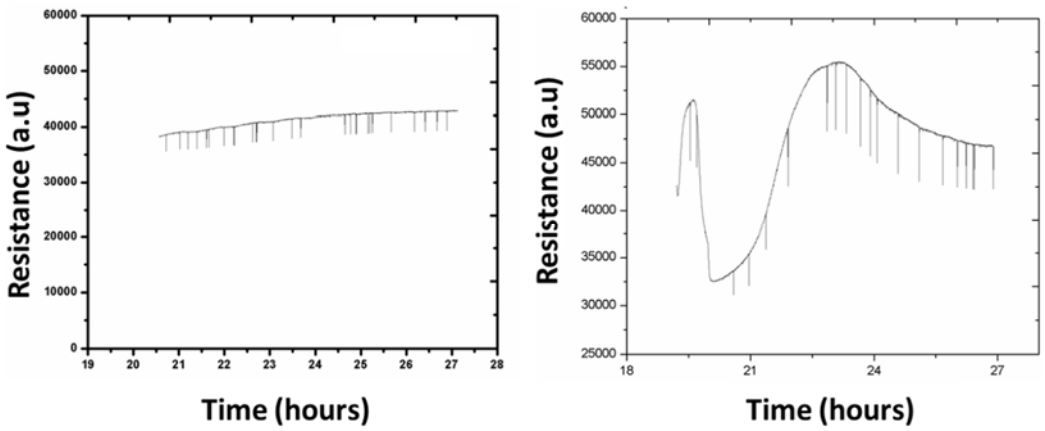

Figure 76: $SrMoO_4$ and MgO mechanically mixed and tested for SO_2 at 1000°C under 1%O_2 partial pressure (a) first (b) second repeat.

$SrMoO_4$/MgO growth introduced O^{2-} intersitials all the way through the material so this also has positive effect over H_2 sensing together with its porous structure and the MgO catalysis effect. As the $SrMoO_4$ crystallized during autoclave procedure and MgO dissolves and forms $Mg(OH)_2$ during this oxygen can be trapped in the relatively large scheelite structure. Despite the ccp cation packing in the tetragonal scheelite due to corner sharing and isolation of the B site cation tetrahedra, the tetragonal structure has relatively lower packing density and further compressible to orthorhombic and monoclinic phases [211B, 158B, 155B]. In addition to this, octahedral interstitials are not occupied in the tetragonal scheelite [155B]. At this point it should be noted that scheelite structure has more prone to formation of interstitial oxygen as well as transportation of oxygen vacancy while the former is not likely in perovskite structure (ABO_3) [212B]. This discussion supports the XPS data showed that up to 17% of the O^{2-} was located on unlattice (interstitial) locations. However it is not clear the reason behind formation of high amount of interstitial oxygen in $SrMoO_4$-nano in comparison to $SrMoO_4$/MgO. Both the work function and band gap measurements showed that MgO incorporation into $SrMoO_4$-nanolattice affected the both amount of interstitials oxygen as well as cation oxidation state.

The reason behind this insensitivity toward SO_2 is that the stable compound formation between Mg and S. After the formation of metastable MgS phase fomation on the surface; it reacts with oxygen to form the corresponding sulfate ($MgSO_4$), and/or $MgSO_4$ can form from, MgO, SO_2 and O_2. $MgSO_4$ is impermeable to further SO_2 diffusion and that is the reason behind insentisivty of the $SrMoO_4$/MgO toward SO_2 [213B]. Compound formation between Mg and S are well reported in literature for MgO with the increasing temperature beyond the 500°C. Above this temperature, the surface sulfur starts to accumulate in the form of $MgSO_4$ and /or MgS. It was also reported by Lee *et al.* that the exposure of MgO to SO_2, in order to promote SO_2 transformation to SO_3, the formation of a very stable compound of Mg and S was formed ($MgSO_4$) and even could not even removed from surface during regenerative cracking conditions [214B]. The same authors also reported that SO_2 exposed MgO could not recover after 500°C [63B].

The XPS spectrum $SrMoO_4$/MgO sensor material after testing to SO_2 and cooled down to room temperature (under constant N_2 flow) is presented in Figure 77. As seen in the graph

presented, the sulfur (S) was detected on the surface in the form of $MgSO_4$ and to small extent MgS (Figure 77-a). The binding energies of sulfur in $MgSO_4$ and MgS are 168.9 and 165.0 eV, respectively. The values are in an excellent match with the literature [215B]. The further examination conducted over the O peak position in order to confirm the sulfate and/or sulfide formations. The Figure 77-b shows that the oxygen XPS spectrum taken from the SO_2 tested sample surface. Sugiyama et *al.* also reported the O^{2-} peak position in magnesium sulfate ($MgSO_4$) and reported that the value is 532.3 eV, which is higher than ordinary peak position of the O found in oxides.

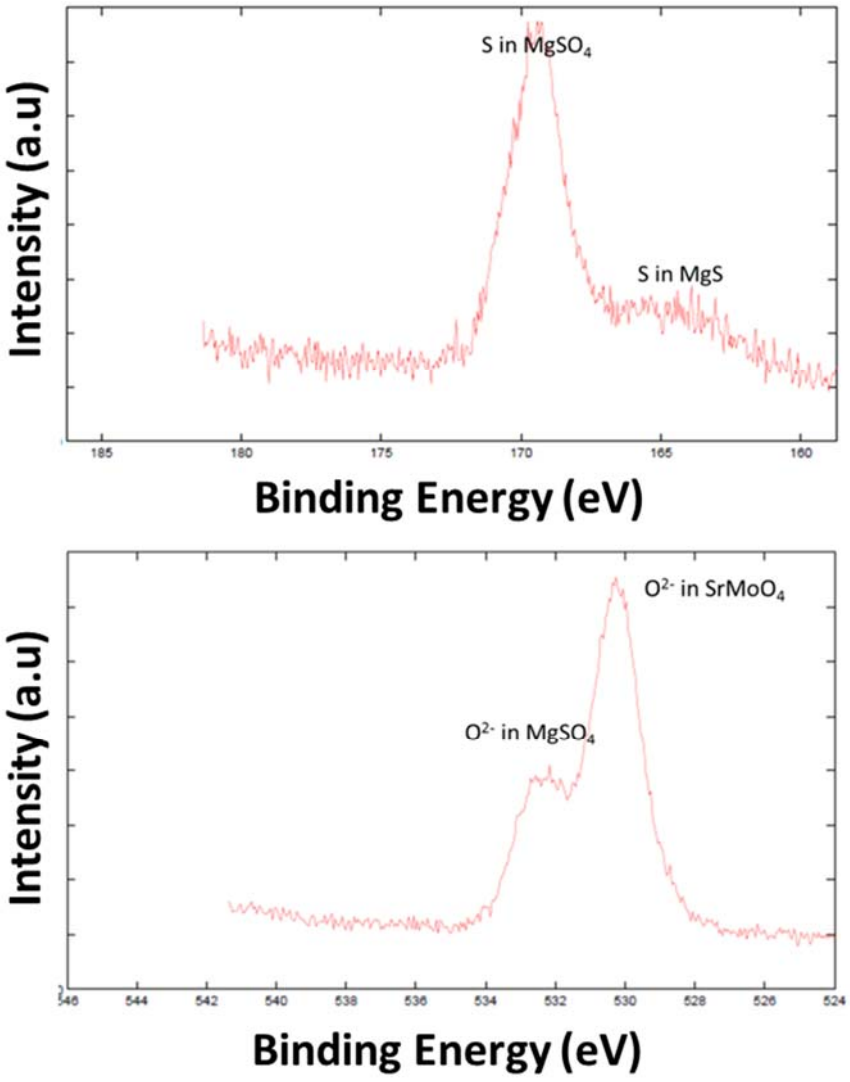

Figure 77: XPS analysis of S (a) and O 2p (b) positions from full scale SO_2 tested $SrMoO_4$/MgO sensor.

The (111) surface of MgO is particularly reactive to H_2. The unique catalytic properties of the defective MgO surfaces also depend on steps, kinks, and point defects (ion vacancies and substitutions). On the (100) MgO surface, H_2 has a small adsorption energy and does not dissociate [216B, 217B]. In order to explain the excellent sensing properties of $SrMoO_4$/MgO against H_2, the mechanical mixture of $SrMoO_4$ and MgO was further tested

for H_2, and the resulting sensitivity graph is given in Figure 78. The figure shows better response than SMM, but worse than $SrMoO_4$/MgO. So, the catalytic activity of the Mg is important but also electronic modification of the Mg created on the surface of the nano-$SrMoO_4$ is also important. The differences can be observed by the work function and band gap, as well as, the highly porous structure of $SrMoO_4$/MgO makes the difference compared to nano-$SrMoO_4$ and MgO mechanical mixture.

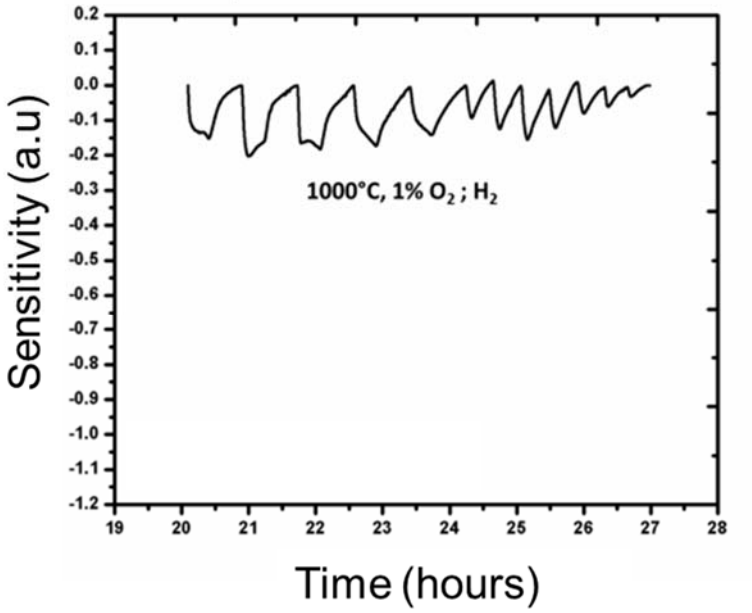

Figure 78: $SrMoO_4$ and MgO mechanically mixed and tested for H_2.

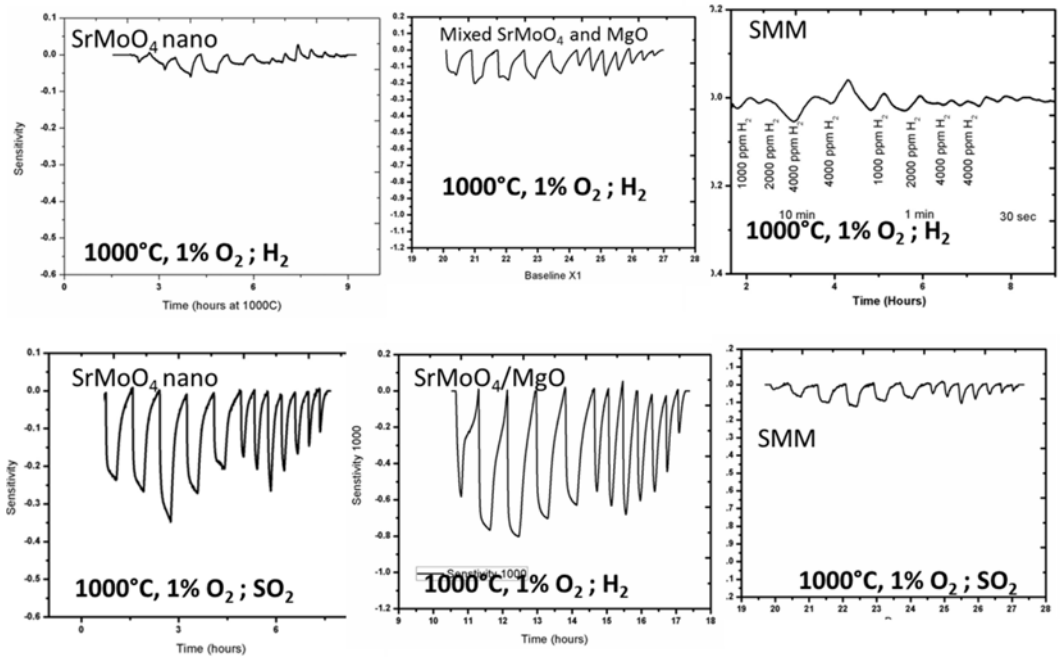

Figure 79: Summary of the sensing capabilities of different compounds towards SO_2 and H_2 at 1000°C under 1%O_2.

C. High-temperature Microsensor Development and Testing

1) Micro-electrode Development

The thermal stability limitations of Pt films with various adhesion layers (Ti, Ta, Zr, and Hf) were characterized at 800 and 1200°C for various annealing times. The microstructural stability of the Pt thin films with the incorporation of Zr within the bulk was characterized by SEM, EDS and XPS, electrical resistivity measurements and stability tests after high temperature annealing procedures. The different migration behaviors of the refractory metals within Pt were shown to be the main variable that controlled wetting, sintering, and coarsening of the Pt films on alumina surfaces. The movement or chemical reaction of these adhesion layers, or lack thereof, dictated the formation of hillock formations and breaking of the percolated Pt conductive network. The deposition of the Hf adhesion layer showed a high level of microstructural stability (compared to the Ti, Ta, and Zr) to the highest operating temperature (1200°C). The Hf was also incorporated within the bulk Pt conductive layer by depositing an alternating layer structure of Hf and Pt metal. This conductive film was utilized in order to apply a Zener-pinning strategy to limit Pt grain boundary mobility. The incorporation of the Hf within the bulk Pt layer was found to be less successful in controlling the microstructural degradation at the highest annealing temperatures compared to that found with the use of Zr within the bulk Pt film. The combination of utilizing the Hf adhesion layer, as well as, the incorporation of Zr within the bulk Pt conductive layer resulted in a film with the greatest microstructural stability over a wide temperature range. This combination significantly hindered de-wetting and grain growth processes. The electrical resistivity measurements confirmed the retention of the percolated conductive network. In the end, a Pt composite multilayer film was developed that could withstand high-temperature exposure up to 1200°C for 48 h, which is beyond most reasonable, high-temperature chemical sensor applications or MEMS processing (and/or operation) conditions. Moreover, the stable films demonstrated in this work were sputtered at ≤200°C, which provided the opportunity to utilize a simple lift-off patterning process during device fabrication with a select photoresist composition. This is important since wet-etching processes of the bilayer/multilayer films may prove to be difficult due to the different chemical solubility of these metals in aqueous solutions. The final manufactured IDEs verified the compatibility of these complex electrode structures/compositions with basic lift-off patterning techniques.

The use of only an adhesion layer of Ti or Zr below the sputtered Pt film resulted in the unwanted dewetting and coarsening/sintering of the film after high-temperature exposure. A strategy is required to control the migration of the adhesion layer away from the substrate interface and to limit the migration of the Pt grain boundaries, which results in unwanted grain growth. One method recently [138B, 140B, 129B] demonstrated for controlling the later mechanism is through the introduction of Zr metal into the Pt layer through a co-sputtering of Zr and Pt, or through sequential depositions of each of these constituents. The dispersion of refractory particles (such as nano- or micro-ZrO_2 or Zr/Pt intermetallics) drastically reduces the low- and high- angle grain boundary mobility within the polycrystalline film. This mechanism is usually termed as Zener pinning in the literature. However, these previously demonstrated strategies are energy consuming, and/or require

specialized deposition control (for co-deposition and processing control) to balance varying deposition rates of the two species. In order to access a similar grain-pinning strategy, this work proposes a two-layer adhesion film which consists of an initial Zr adhesion layer in contact with the oxide substrate and a secondary defective layer of Zr film deposited over the initial adhesion layer. After the deposition of the second defective Zr film, the Pt film is deposited over the Zr film, where it both infiltrates and coats over the secondary Zr layer. This deposition procedure results in the formation of a functionally gradient film from the original Zr adhesion layer to the outer Pt top layer, as shown in the cross-sectional illustration in Figure 80-a. Figure 80-b shows the typical cross-sectional illustration of simple bilayer coating for visualization purposes.

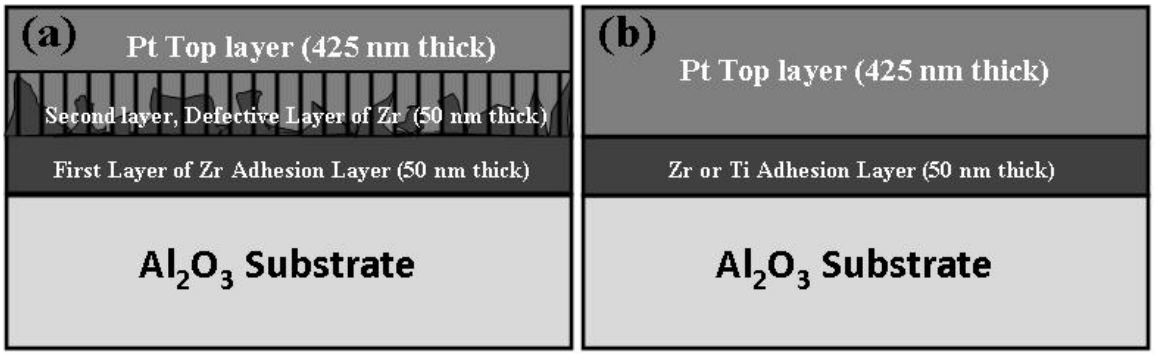

Figure 80: Cross-sectional schematic illustrations of (a) functionally gradient composite Zr and Pt films (Zr/Zr+Pt/Pt), during Pt film deposition, in-situ formation of co-continuous composite of Zr and Pt, called Zr+Pt shown in shaded region. (b) Bilayer coatings of Zr/Pt or Ti/Pt (Illustrations are not scaled to real dimensions of the abovementioned layers.

Figure 81 shows the high magnification SEM images of the above-mentioned two Zr layers. Figure 81 shows as-deposited state of the first adhesion Zr thin film deposited with the same processing parameters and thickness (50 nm) used in the deposition of the adhesion layer for the Zr/Pt bilayer coating. This layer shows significantly high surface coverage compared to the second defective layer, which is shown in Figure 81-b. The second Zr layer is also deposited to 50 nm thickness, but a 25 W power input and a primary gas pressure of 150 mTorr was utilized instead 100 W and 50 mTorr, respectively. The defective layer was generated by modification of the deposition parameters, where the parameter change resulted in a decrease in the incident energy of the deposited Zr. This effect of primary gas pressure and power on the microstructure formation is well documented in literature for sputtered thin films [141B,142B]. The initial layer provided a durable adhesion layer, while the latter layer provided a porous Zr framework, which would be later infiltrated with the deposition of 425 nm thick Pt top layer to form a co-continuous composite microstructure. This in-situ formed co-continuous network of Zr and Pt layer will be termed Zr+Pt throughout the paper (see Figure 81-a). The Zr granular network between the Pt grains would further assist in pinning of the Pt grain boundaries by upward diffusion beyond the Zr+Pt co-continuous layer. The total thin film coating, with the first layer being the Zr adhesion layer, second layer being the Zr+Pt co-continuous layer and top layer being pure Pt, will be termed as Zr/Zr+Pt/Pt thorough the current work.

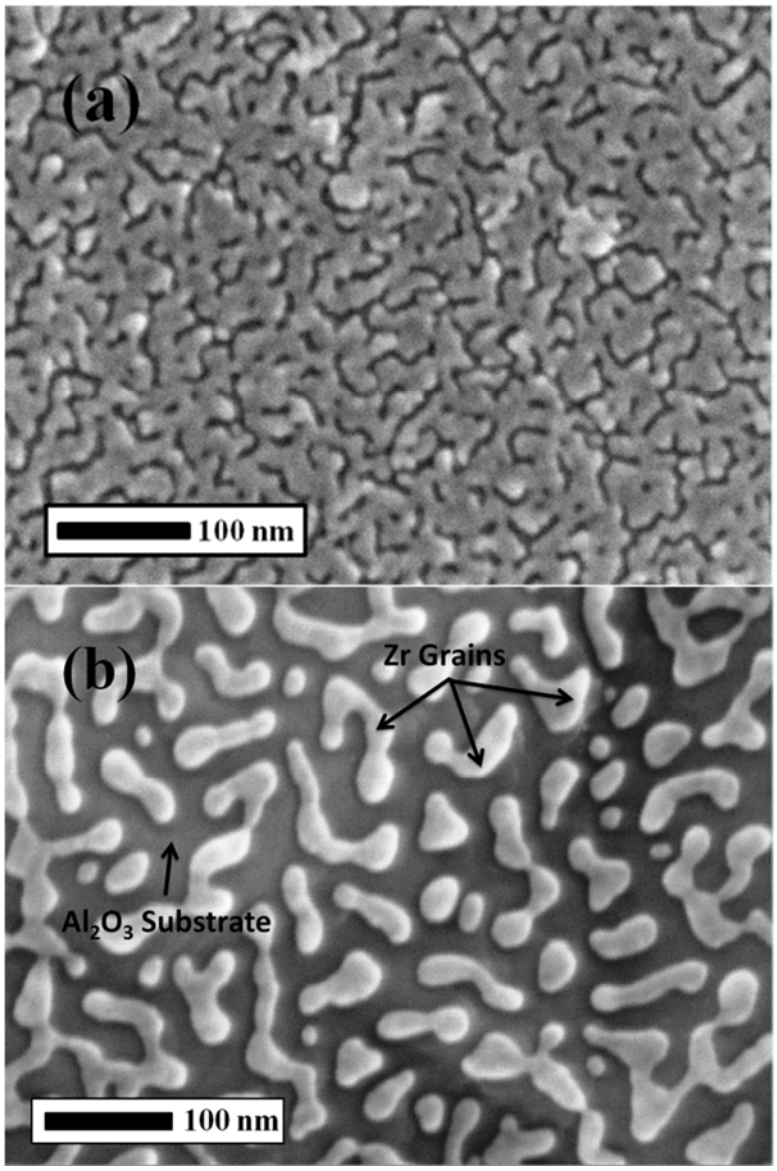

Figure 81: SEM micrographs of as-deposited state of (a) First layer of Zr adhesion layer common in Zr/Pt and Zr/Zr+Pt/Pt (b) Defective layer of Zr utilized in Zr/Zr+Pt/Pt coating as a second layer of double adhesion layer.

Figure 82-a through -f displays SEM micrographs of the Zr/Zr+Pt/Pt coating after annealing at 1200°C for 0-24 h. The as-deposited state of Pt is shown in Figure 82-a, and this SEM micrograph displays an average grain size of ~15 nm. The other micrographs show the successive destruction of the thin film microstructure as the isothermal hold is increased. The microstructure remained continuous during the annealing process, but larger, isolated pores with a size of 3-5 μm began to emerge throughout the microstructure after 1 h at 1200°C (as shown in Figure 82-b). After annealing for 5 h at 1200°C, the coarsening of these isolated pores began to accelerate and merge with other larger isolated pores. Figure 82-c displays the SEM micrograph of the Zr/Zr+Pt/Pt coating after an annealing time of 5 h. Although the Zr/Zr+Pt/Pt microstructure appeared to begin to evolve, the percolation was not compromised and was far superior over that displayed by the Pt

film with only the Zr adhesion layer (Zr/Pt). The rate of coarsening and coalescence of the exaggerated pores began to subside after the 5 h annealing, where the microstructure did not alter between the 5 h and 8 h isothermal annealing. Figure 82-d shows the SEM micrograph of the 8 h annealing at 1200°C. Figure 82-e displays the microstructure after 15 h annealing. After the 15 h annealing, the larger pores grew extensively and the coalescence of these pores began to compromise the percolation of the Pt phase. The percolated granular network of Zr/Zr+Pt/Pt thin film was finally destroyed after 24 h annealing, as shown in the SEM micrograph presented in Figure 82-f.

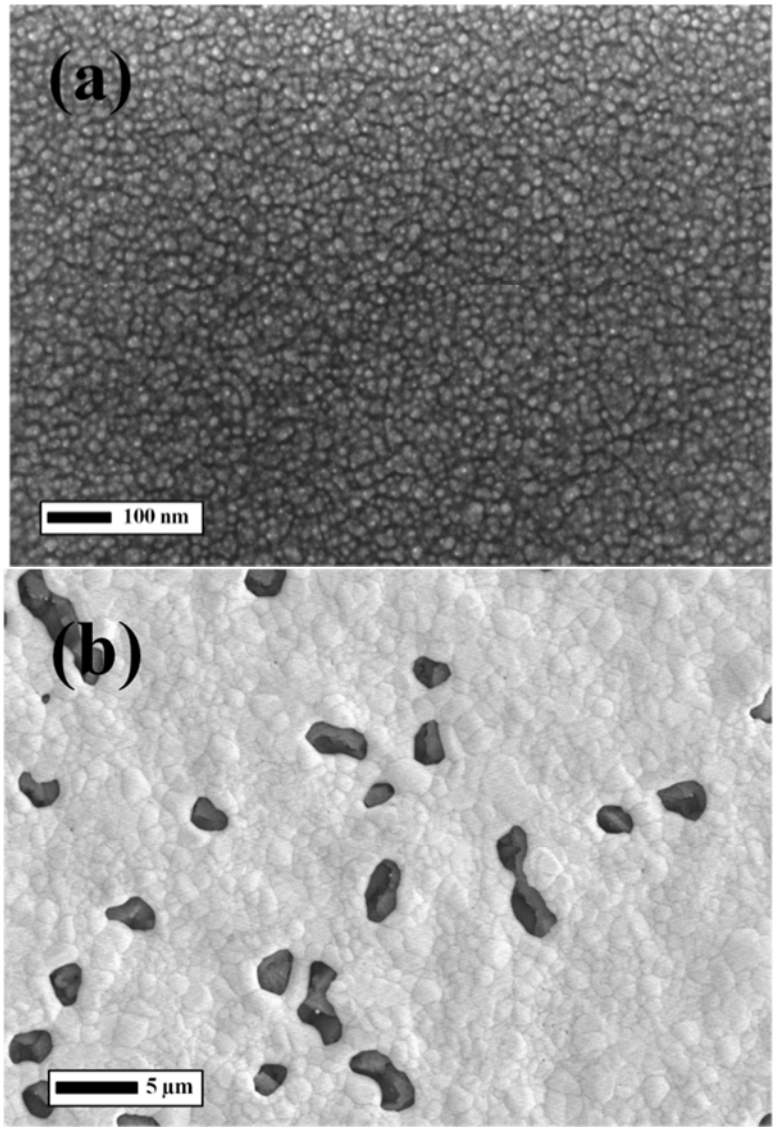

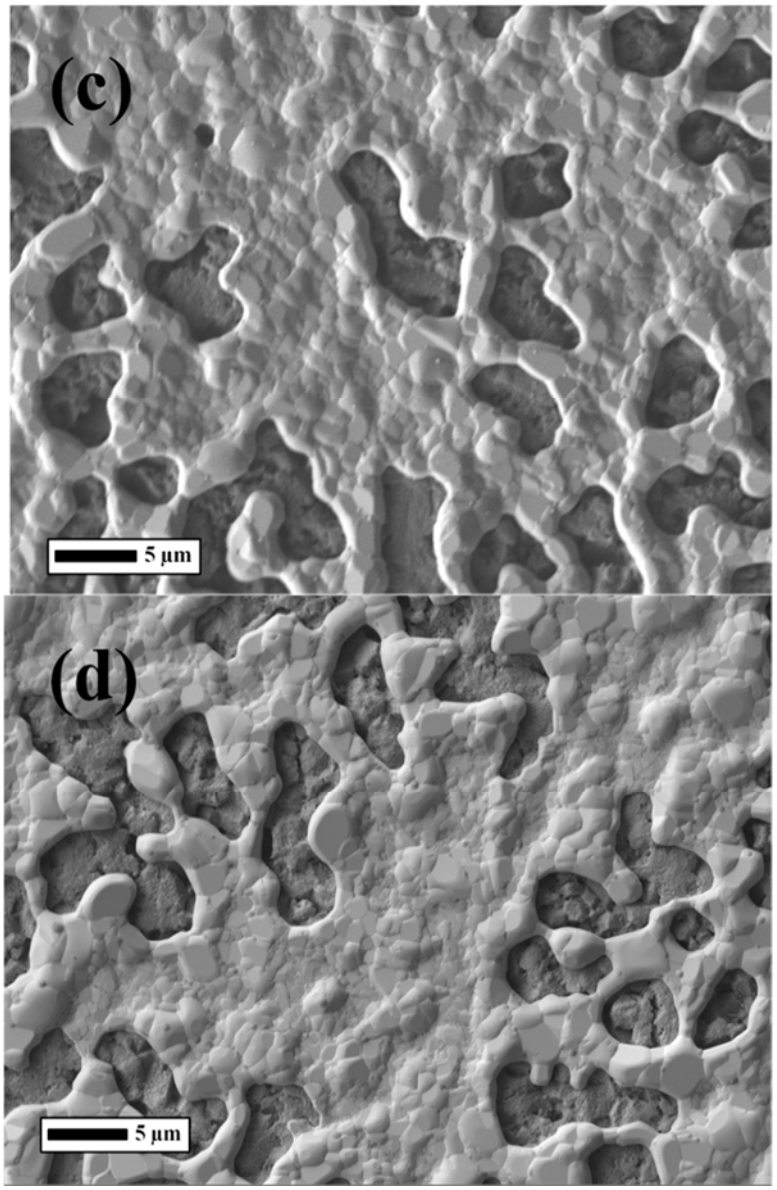
(c)
5 µm
(d)
5 µm

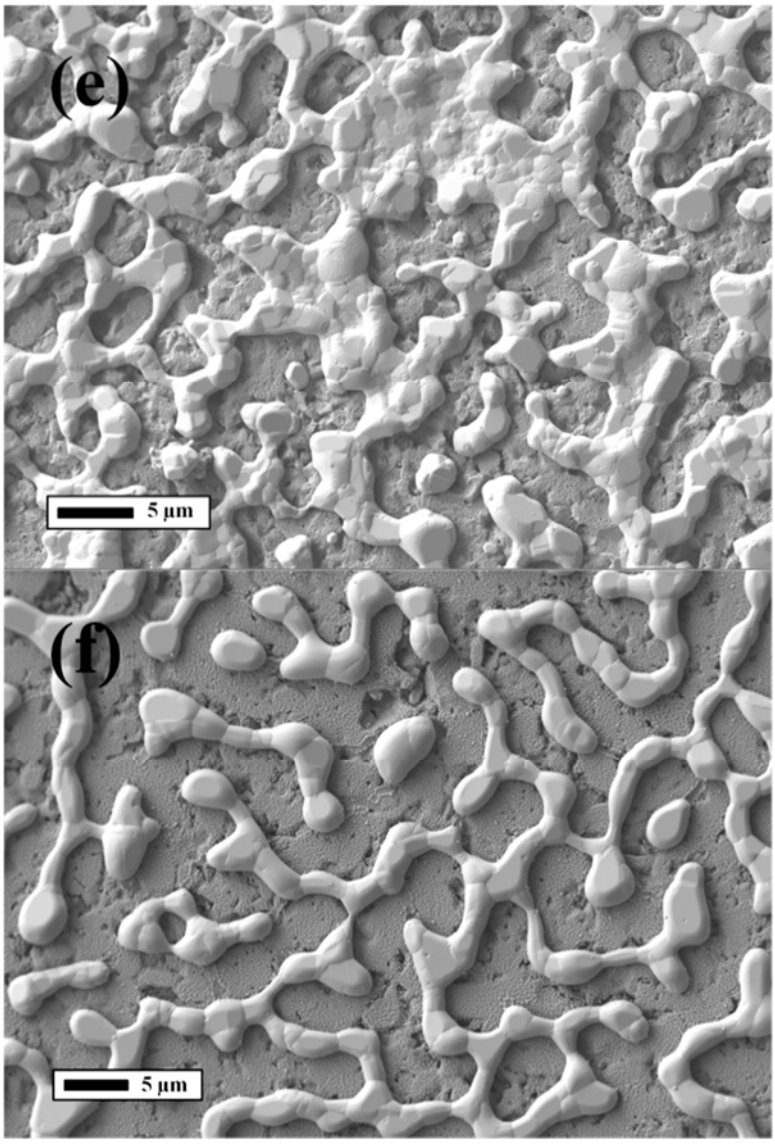

Figure 82: Zr/Zr+Pt/Pt thin film (a) as-deposited state, after annealing at 1200°C for (b) 1 h (c) 5 h (d) 8 h (e) 15 h (f) 24 h.

In contrast to the Pt coatings utilizing just the Ti and Zr adhesion layers (Figure 83), the Pt coating consisting of the double Zr adhesion layer demonstrated superior stability over the extended high-temperature annealing. Higher magnification SEM micrographs of the Zr adhesion layer (which may be observed through pores in the Pt thin film) are shown in Figure 83-a and -b after 5 and 15 h annealing practices, respectively. It is worthy to note that the grain growth also occurred in the Zr adhesion layer, where the grains were growing at an average rate of ~5 nm/h. The pores grew at a similar rate, but the kinetics was considerably slower than that of shown for the Pt films. Figure 83-c shows an SEM micrograph of the Zr adhesion layer after the 24 h annealing. This annealing practice highly disturbed the Zr adhesion layer as well as the Pt top layer (see Figure 83-f). The image shows that the Zr adhesion layer was thoroughly disturbed beneath the Pt top layer. At some locations, the alumina substrate became visible due to the coarsening of the adhesion layer.

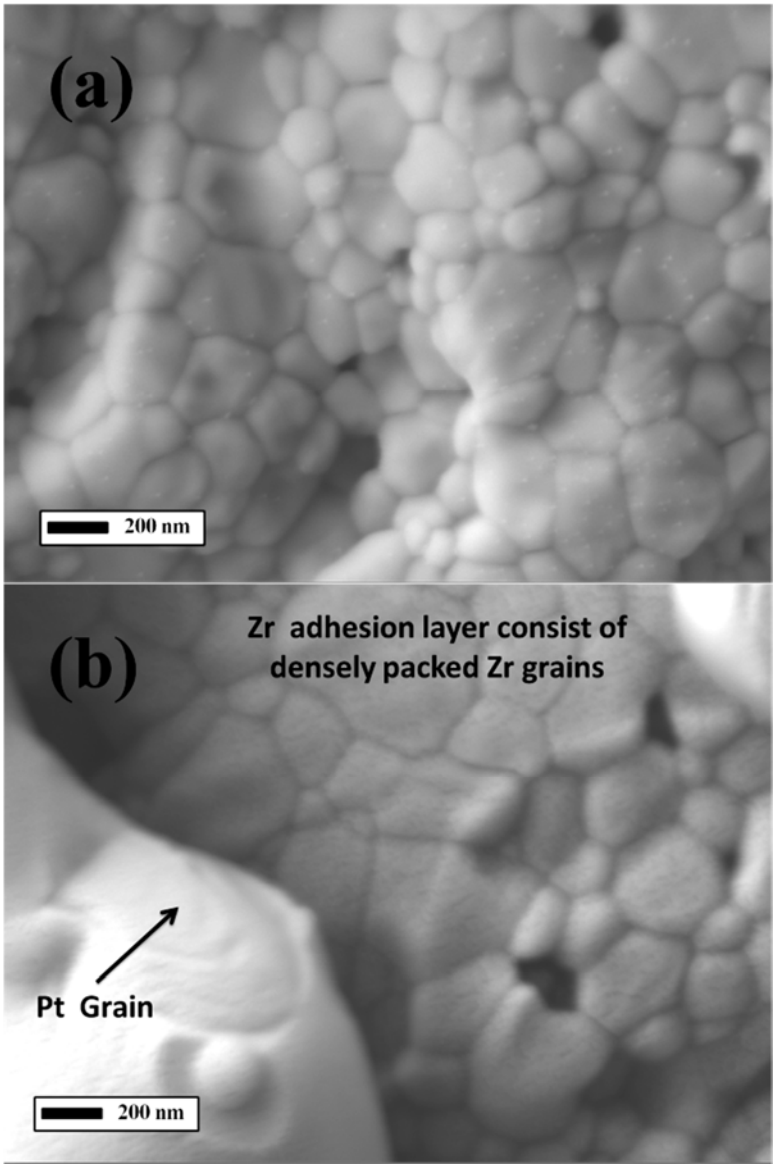
(a)
200 nm
(b)
Zr adhesion layer consist of densely packed Zr grains
Pt Grain
200 nm

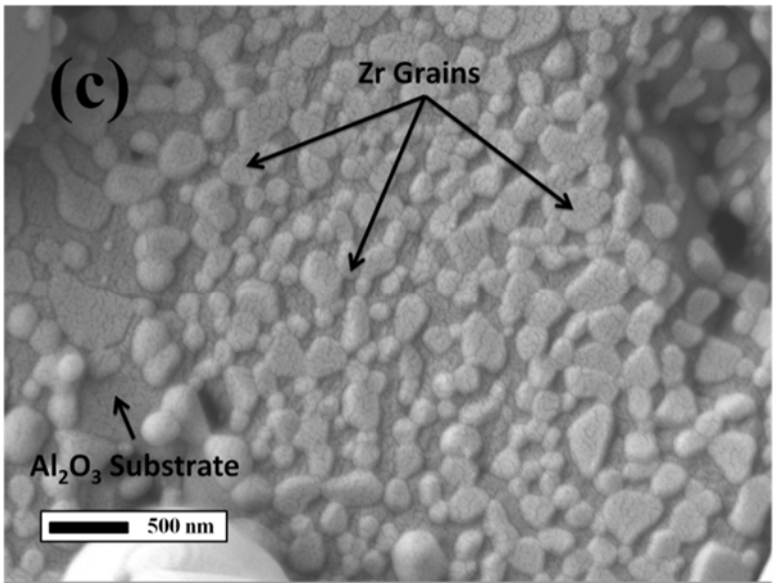

Figure 83: High magnification SEM micrographs of adhesion layer in Zr/Zr+Pt/Pt after annealing at 1200°C for (a) 5 h (b) 15 h (c) 24 h.

XPS depth profiling of Zr/Pt and Zr/Zr+Pt/Pt

The superior high-temperature stability of the Zr/Zr+Pt/Pt thin film compared to the Zr/Pt thin film demonstrates the applicability of the Zener pinning effect on the control of the Pt grain growth and dewetting characteristics. By introducing Zr into the Pt bulk composition from the start, the driving force for the diffusion of Zr from the adhesion layer into the bulk was decreased. This diffusion is driven by the chemical gradient across the thickness of the film. Therefore, the incorporation of the Zr into the Pt film limited migration of Zr from the adhesion layer, as is typically the case for various adhesion metals such as Ti, Ta, and Zr [138B]. Therefore, the preservation of the adhesion layer between the oxide and Pt film resulted in the desired effect where the hillock and dewetting degradation mechanisms were minimized. Also, the coarsening/sintering of the Pt grains was controlled by the presence of the Zr, which limited the microstructural evolution of the bulk electrode thin film. In order to shed light over the distribution of the Zr in Pt, XPS depth profiles of the Zr/Pt and the Zr/Zr+Pt/Pt thin films were completed by Ar ion etching through the Pt metallization towards the alumina substrate (as described in detail within the experimental section). XPS depth profile spectra were taken in the vicinity of the Zr, Pt and O main photoelectron lines.

The XPS depth profiles of the thin films are shown in Figure 84, where the 0 nm marker represents the outside surface of the Pt metallization, and the entire thin film thicknesses were roughly 450 and 475 nm for Zr/Pt and the Zr/Zr+Pt/Pt, respectively (thus, the alumina substrate interfaces is located accordingly). The figures show that the Pt concentration throughout the thin films does not change considerably; however, the Zr concentration increases rapidly toward the interface at different depths from surface for the above-mentioned thin films, as expected. As seen from the graphs in Figure 84, detection of Zr started at the 375 nm and 275 nm depths from the surface for Zr/Pt and Zr/Zr+Pt/Pt thin films, respectively. The early detection of the Zr in Zr/Zr+Pt/Pt is in direct consequence of the Pt deposition over the defective Zr layer, where the Pt infiltrated the Zr architecture

during deposition. In the Zr/Pt layer, the Zr content gradually rose from the 375 nm until a depth of ~412.5 nm. In the case of double-layered thin film, the Zr was first detected at the 275 nm depth and gradually rose to 375 nm, and this concentration was finally limited to a constant value between ~375-425 nm. In the Zr/Pt case, the adhesion layer identified in Figure-a could not provide the same diffusional source of Zr. The stable phases such as $ZrPt_3/ZrO_2$ are formed within the Pt grain boundaries during the high-temperature annealing process, which has an important effect on the high temperature behavior of the Pt thin film due to the pinning of the Pt bulk grains.

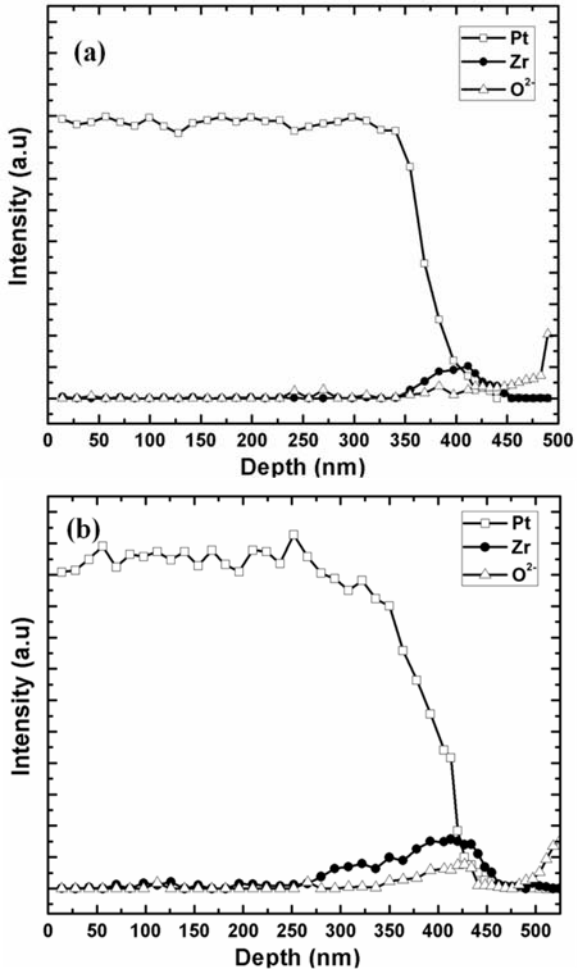

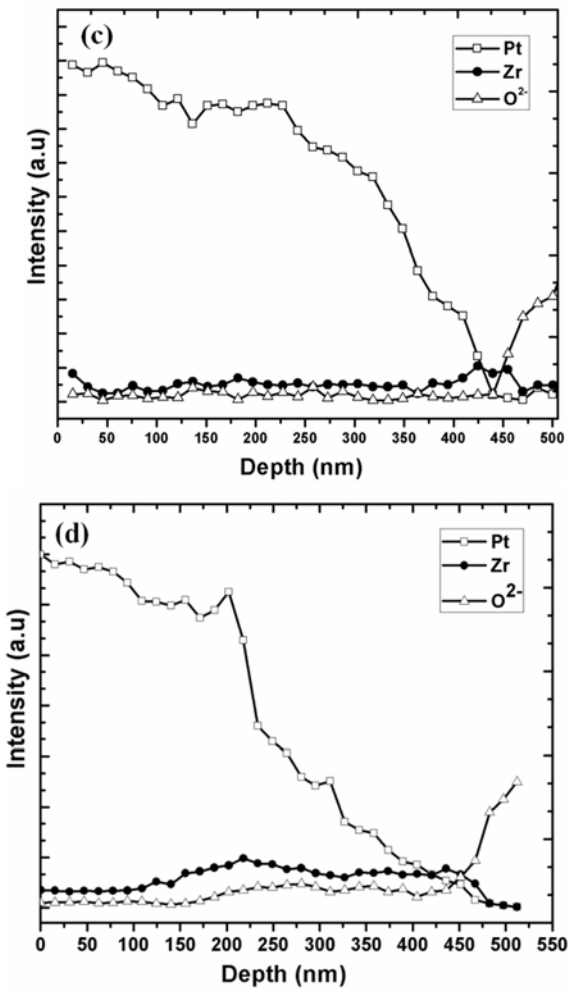

Figure 84: XPS depth profiling of as-deposited (a) Zr/Pt (b) Zr/Zr+Pt/Pt and annealed for 1h at 1200°C for the (c) Zr/Pt (d) Zr/Zr+Pt/Pt thin films.

The higher stability at the elevated temperature for the Zr/Zr+Pt/Pt thin film was previously attributed to the distribution and amount of the second phase precipitants among the Pt grain boundaries in the form of ZrO_2 and $ZrPt_3$. Further XPS depth profiling analysis was conducted in order to examine the concentration/distribution of the Zr through the thin films of Zr/Pt and Zr/Zr+Pt/Pt after 1 h annealing at 1200°C. The indicated time and temperature used for annealing the samples was chosen, since samples annealed for further time lost the surface percolation, especially in the case of the Zr/Pt and Zr/Zr+Pt/Pt films, but more profoundly in the former (see Figure 79-b and Figure 82-b). This annealing temperature was also aligned with the operational temperature for the perspective application (where the sensor operation is perceived to be <1200°C). The thin films must be further annealed above this temperature in order to stabilize the microstructure of the electrode and sensing material. In addition, the refractory sensing material (oxide in many cases) must be bonded to the substrate at temperatures >1000°C, and thus the electrodes must be stable to this additional processing step. Therefore, the 1 h at 1200°C annealing practice could be thought of as the final step before operational usage. Figure 84-c and –d show the aforementioned XPS depth profiling of the thin films of Zr/Pt and Zr/Zr+Pt/Pt,

respectively. XPS spectra of the 28 different locations through the coating thicknesses from the surface to the substrate interface were taken in order to better understand the overall distribution and concentration of Zr across this depth. Three significant locations (near surface, middle zone and substrate interface) were analyzed in detail for the chemical state and identification of the Pt and Zr in both Zr/Pt and Zr/Zr+Pt/Pt thin films. The ZrO_2 phase was analyzed by using the Zr 3d core photoelectron line, which includes the doublet, positioned at the 185.5 eV and 183.1 eV for the $3d_{3/2}$ and $3d_{5/2}$. The intermetallic $ZrPt_3$ phase, which is significant in this work due to its low electrical resistivity [137B], was analyzed by inspecting detailed scans of Pt 4f and Zr 3d photoelectron lines. The formation of $ZrPt_3$ shows its presence at the Pt 4f and Zr 3d spectra as shoulders on the high and low binding energy sites, respectively. The Pt main photoelectron lines are located at 72.5 eV ($4f_{7/2}$) and 75.8 eV ($4f_{5/2}$) for the intermetallic phases in both Zr/Pt and Zr/Zr+Pt/Pt thin film. These values for Zr and Pt are a good match with the reported literature values [138B, 143B, 144B] .

As seen in the graph shown in Figure 84-c, the Zr distribution through the Zr/Pt thin film was restricted to the adhesion layer substrate interface. The 50-400 nm zones contain 5 % Zr in the form of ZrO_2 and $ZrPt_3$, while the latter is a minor contributor since it constitutes 15% of the total Zr phase. On the other hand, as seen in the Figure-d, the Zr/Zr+Pt/Pt thin film (which contains the defective adhesion layer) showed a well distributed and high amount of Zr phase in the form of ZrO_2 and $ZrPt_3$ starting from surface to the adhesion layer substrate interface. The $ZrPt_3$ consisted of nearly 30 % of the total Zr phase within this film. The high amount and overall distribution of the Zr through the Pt electrode is important to the microstructural stability identified for this film. The chemical state and concentrations analysis were conducted at three different depths; the depths were 0 nm (after surface cleaning with Ar^+, 2 minutes at 4 kV accelerating voltage), 225 nm (considered mid-depth) and 450 nm (considered the substrate-thin film interface). It was possible to conduct elemental concentration analysis, since the detailed spectra of the Zr 3d, Pt 4f and O 1s photoelectron lines were obtained at the same time. The surface of the Zr/Pt thin film contained 8% ZrO_2, whereas the Zr/Zr+Pt/Pt surface included 4.5% ZrO_2. In both of these thin films, the amount of $ZrPt_3$ intermetallic phase counted for less than 5% of the total Zr content at the surface. At the mid-depth (225 nm), the Zr/Zr+Pt/Pt thin film showed significant increase of Zr content (25% in total). This increase includes the increase in the total intermetallic phase percentage to 30 % of total, while the ZrO_2 phase was 70% of the total. At the same depth, the total amount of Zr in the Zr/Pt film was only 5%. At the substrate-thin film interface, the Zr content was about 10% of the total composition in the Zr/Pt thin film, while it showed 15% for the Zr/Zr+Pt/Pt.

Micro-electrode fabrication was completed by optical lithography over highly-polished Al_2O_3 polycrystalline substrates with optimized coating architectures including Hf/L-Zr+Pt and Zr/Zr+Pt/Pt . The choice of photoresist was dictated by the deposition temperature. The positive resist AZ 3330-F, which is generally used for reactive-ion etching (RIE) procedures, was spin-coated over the alumina substrates to a thickness of 3.5 μm in order to have reasonable surface adhesion during the film deposition procedure at the elevated temperature (200°C). A conventional photolithography process was carried out to define the electrode pattern within the photo-resist. After the pattern was transferred, the wafers

were given a post-bake at 120°C for 5 minutes to strengthen the photoresist. Different types of electrodes were deposited successfully by the previously described deposition processes at 200°C. Figure 85-a, -c and -d shows the micro-electrodes with a 1.5×5 mm and 50 μm finger spacing. As the micrographs reveal, the pattern quality was satisfactory with the desirable sharp image transfer.

To this point, the discussion on the stability of the Pt electrodes has been reserved for continuous thin films deposited over a ~5 cm^2 sample (without patterning). The continuous planar films represented the ideal case for the thermal stability of a patterned IDEs for micro-devices. However, the nature of the lift-process, which includes other processing variables, may inject processing factors that could affect the microstructure or architecture of the film (and thus limit the high temperature life-expectancy). These variables would be primarily aligned with the influence of the photoresist during deposition and the potential development stage, which may produce surface/edge defects or film under-cutting.

IDEs with the Hf/L-Zr+Pt multilayer and Zr+Pt bilayer coatings were annealed at 1200°C for 15 h. Figure 85-a and -b present the Zr+Pt bilayer electrode after annealing at 1200°C for 15 h. As seen from the micrographs, the micro-electrode microstructure was altered into isolated Pt grains and/or clusters of Pt grains. Figure 85-c shows the SEM micrograph of the as-deposited Hf/L-Zr+Pt microelectrode. Figure 85-d shows that the Hf/L-Zr+Pt micro-electrode after annealing at 1200°C for 15 h. As the micrograph reveals, the pattern quality was highly preserved, with even the corners and edges remaining distinct in shape; however, the percolation of the film deteriorated as expected from the previous thin film experiments, but the quality remained superior to the Zr+Pt bilayer micro-electrode. As seen from Figure 85-e, the edge of the Hf/L-Zr+Pt micro-electrode coarsened to a greater extent compared to the middle zone. The electrical resistivities of the IDEs were measured and the results were similar to that measured for the un-patterned electrodes which indicate no significant pattern or continuity loss.

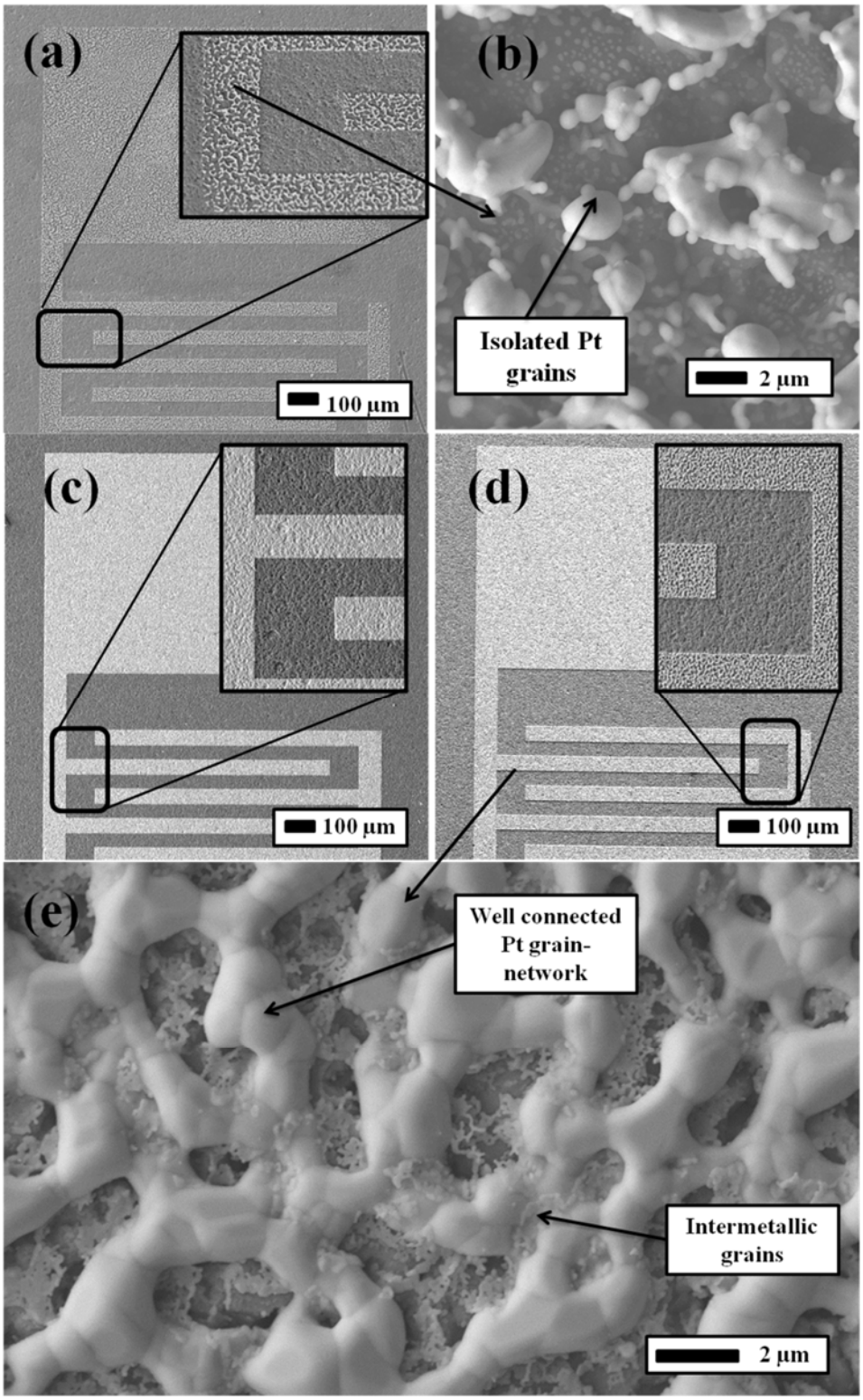

Figure 85: (a) Zr+Pt bilayer electrode after annealing at 1200°C for 15 h, inset shows the edges closely (b) High magnification SEM image shows the edge of Zr+Pt electrode after annealing at 1200°C for 15 h. (c) As-deposited Hf/L-Zr+Pt multilayer electrode, inset shows the edges closely (d) High magnification SEM image shows the

edge of 15 h 1200°C annealed electrode. (e) High magnification SEM image shows the edge of Hf/L-Zr+Pt electrode after annealing at 1200°C for 15 h.

Figure 86 shows SEM micrographs of the as-deposited micro-electrodes with Zr/Zr+Pt/Pt coating architecture. The general view of the Zr/Zr+Pt/Pt micro-electrode with 600 × 1350 µm and 20 µm finger spacing can be seen in Figure 86-a. Figure 86-b shows the higher magnification of the as-deposited microelectrode. As the SEM images reveal, the pattern quality was quite satisfactory where the pattern edges are sharply defined.

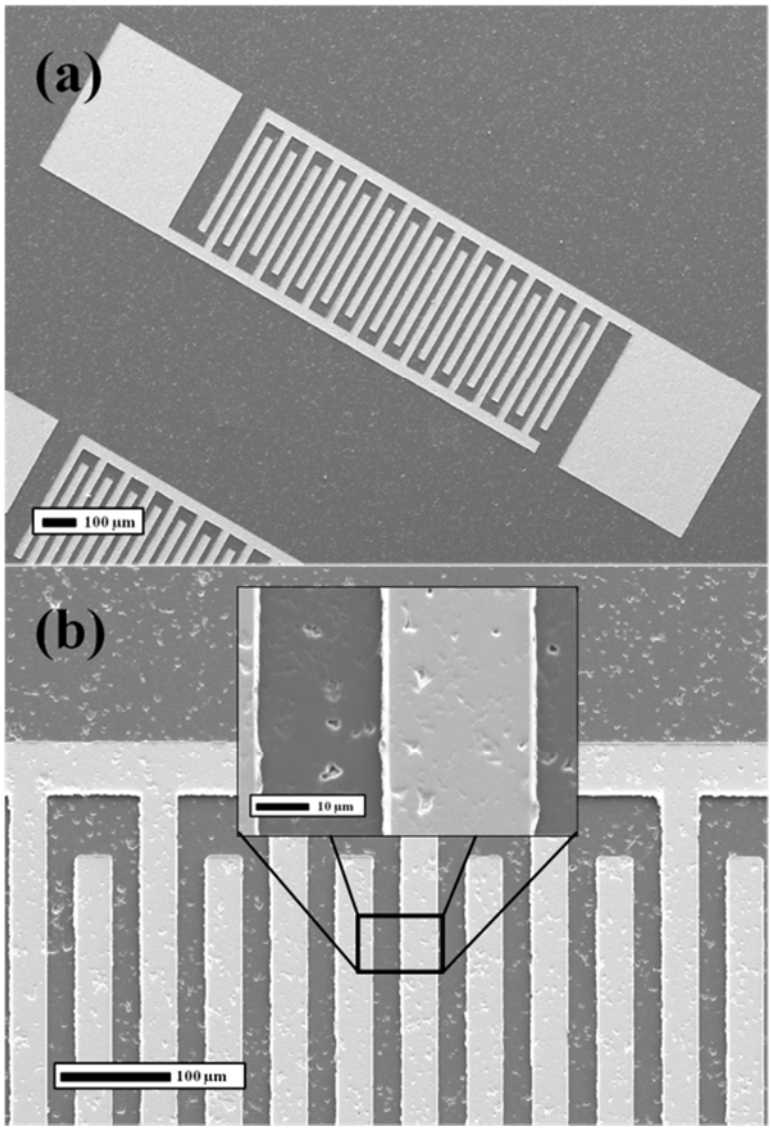

Figure 86: SEM micrographs of as-deposited Zr/Zr+Pt/Pt microelectrodes, showing (a) general view and (b) high-magnification images (inset shows edges clearly defined).

Figure 87 shows SEM micrographs of the Zr/Zr+Pt/Pt microelectrodes after annealing 15 h at 1200°C. As seen in the Figure 87-a and -b, the IDE pattern, including adhesion layer, was preserved with even the most vulnerable part of the pattern (corners and edges)

showing high definition. As seen from Figure 87-c, Pt microstructure coarsened to a greater extent at the edge of the electrode compared to the middle zone. In these regions, some disturbances of the Pt over Zr were observed. Although limited coarsening was seen for the Pt top layer (see Figure-b inset), the patterned Zr/Zr+Pt/Pt thin film retained a high level of percolation without isolation into discrete islands (see Figure 87-c), which is not valid for Ti/Pt and Zr/Pt. The conductive and continuous Pt top layer was not lost after the high temperature annealing, and the electrode pattern retained the high level of percolation leading to excellent electrical performance in Zr/Zr+Pt/Pt microelectrodes.

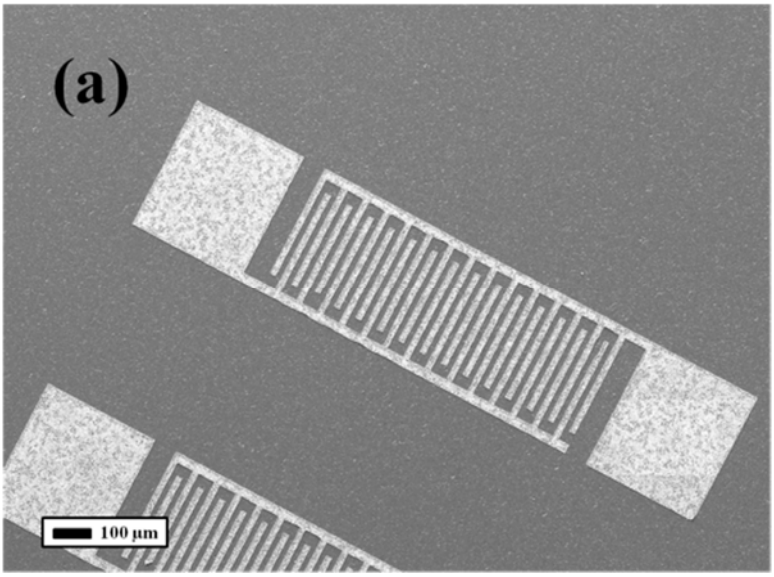

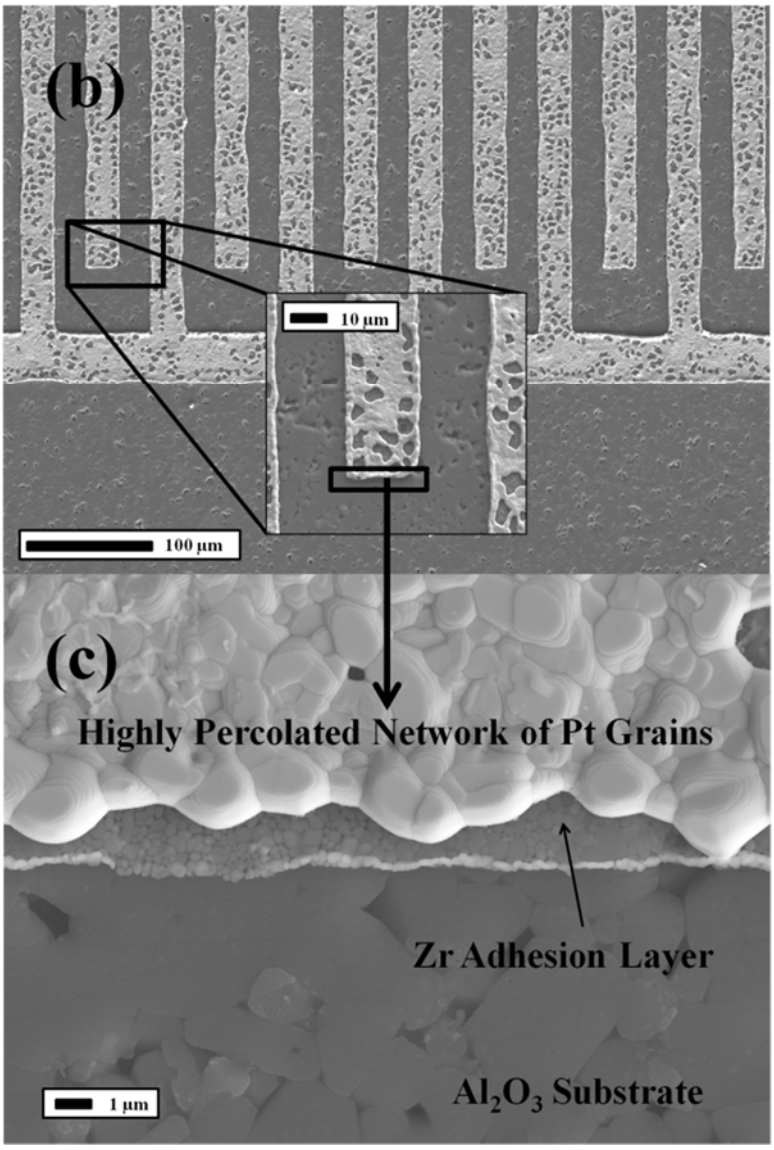

Figure 87: SEM micrographs of the Zr/Zr+Pt/Pt microelectrodes after annealing at 1200°C for 15 h (a) general view (b) high-magnification close-ups for showing edges clearly (c) high-magnification taken form imminent edge of the microelectrode shows Pt top layer and adhesion layer over substrate.

For comparison purposes, the Zr/Pt thin film micro-electrode was manufactured and annealed at 1200°C for 15 h. SEM micrograph of the Zr/Pt micro-electrode after annealing is presented in Figure 88-a. As seen in the image, the microstructure of the Zr/Pt micro-electrode presents non-conductive islands of Pt. The microstructure of the Zr/Pt microelectrode reveals a difference compared to Zr/Zr+Pt/Pt microelectrode which is annealed with same conditions (see Figure 87-c). For further comparison, screen-printed IDEs that are typically used for miniature sensor manufacturing in the mm- to cm-size range were prepared. The Pt ink used for screen-printing was made from Pt powder purchased from Technic Engineered Powders with particle sizes around 1 µm. The screen-printed electrodes had a total length of 10 mm with finger width and finger spacing of 400 µm and 10 µm in film thickness. The thick film (screen-printed) electrode with the large

grain size Pt should resist the effect of coarsening/sintering at these high temperatures compared to thin film micro-electrodes. Figure 88-b shows the SEM micrograph of the screen-printed electrodes after annealing at 1200°C for 15 h. After annealing, the IDEs formed with the screen-printed Pt powder showed a highly disrupted microstructure. The microstructure displayed separate Pt islands in the size range of 5 µm with various size pores separating these islands. The microstructure is in far contrast to that shown for the Zr/Zr+Pt/Pt thin film micro-electrode structure processed at the same conditions (see Figure 87-b).

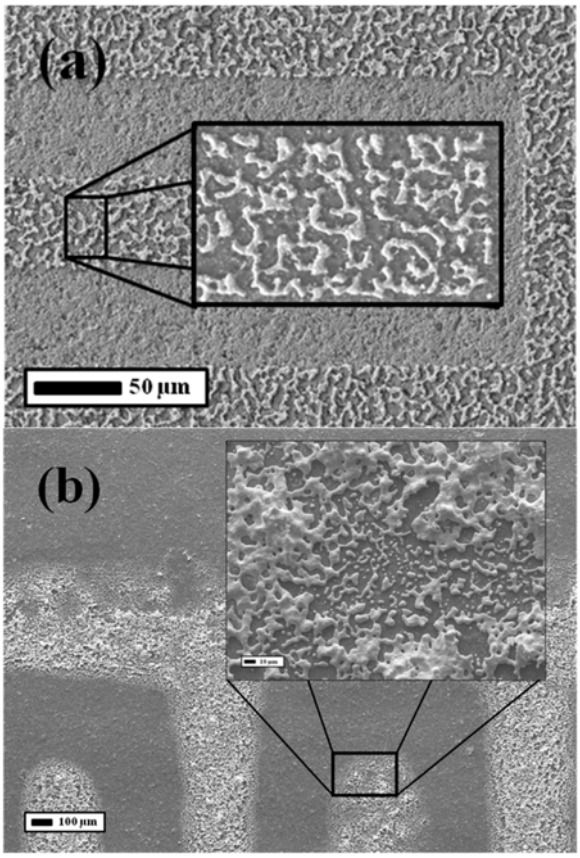

Figure 88: SEM micrographs of (a) the partial view of Zr/Pt microelectrode and (b) the partial view of screen-printed Pt macroelectrode after annealing at 1200°C for 15 h.

2) Microsensor Fabrication

Microelectrodes for sensor fabrication were completed by optical lithography over highly-polished Al_2O_3 polycrystalline substrates with the optimized coating architectures for Zr/Zr+Pt/Pt. This architecture was used due to its highly reliable microstructure and cost (which includes the amount labor needed for patterning and deposition). A conventional photolithography process was carried out to define the microelectrode pattern within the photo-resist. AZ 3300-F (AZ Electronic Materials) photoresist was deposited on a polished alumina substrate in a spin-coater (Laurell Technologies, 400 spinner) to a thickness of 3.5

μm and was baked at 110°C for 5 min before exposure. The substrates were placed in a mask aligner (Suss Microtech, MA6), exposed, and baked at 120°C for 5 min. The substrate was then developed in an ultrasonic bath of AZ 917 developer until the pattern was fully etched away. After the pattern was transferred, the wafers were given a post-bake at 120°C for 5 min to strengthen the photoresist. The patterned substrate was located in a sputtering station (Magnetron Sputtering, CVC 610 DC) and the deposition of two layers of zirconium (Zr) as an adhesion promoter and grain pinning phase was followed by a 425 nm thick layer of platinum. The details of microelectrode fabrication are provided in section 3.5. The electrodes were annealed at 1200°C for 1 h to stabilize the microstructure for high temperature testing. Figure 89 shows the microelectrodes with a 1.5 ×5 mm and 50 μm finger spacing. As the micrographs reveal, the pattern quality was very good with the desirable sharp image transfer. The microelectrode was further heat treated at 1000°C for 10 h in 1% O_2 balanced with N_2 atmosphere in order to quantify the drift in the resistance. It was seen that the resistance of the as-deposited microelectrode was 1.5 ohms and after heat treatment it increased to 2.1 ohms. It can be concluded that microelectrode architecture is drift-free once considering the typical resistance value of optimized sensing material is in the range of mega ohms.

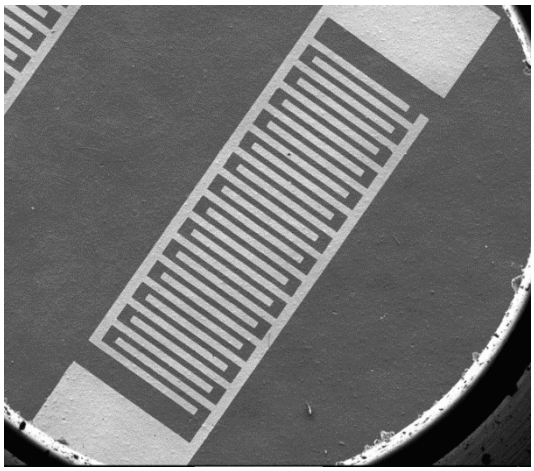

Figure 89: SEM micrograph of the Zr/Zr+Pt/Pt type microelectrode seen in as-deposited state.

Microsensor Fabrication via Lost Molding Technique

In order to deposit the sensing material over electrode, a lost-mold microcasting process was used which was optimized by Wildfire et *al.* [17B]. Figure 90 shows a schematic cross-section of the microsensor through the manufacturing steps. The process starts with the deposition of the high temperature compatible electrode pattern onto highly polished Al_2O_3 substrate. STEP 1 through STEP 5 show electrode deposition schematically. STEP 6 through 11 summarize the application of SU-8 25 (MicroChem Corp. MA) negative photoresist over patterned electrodes as well as casting of sensing material into the molds[17B].

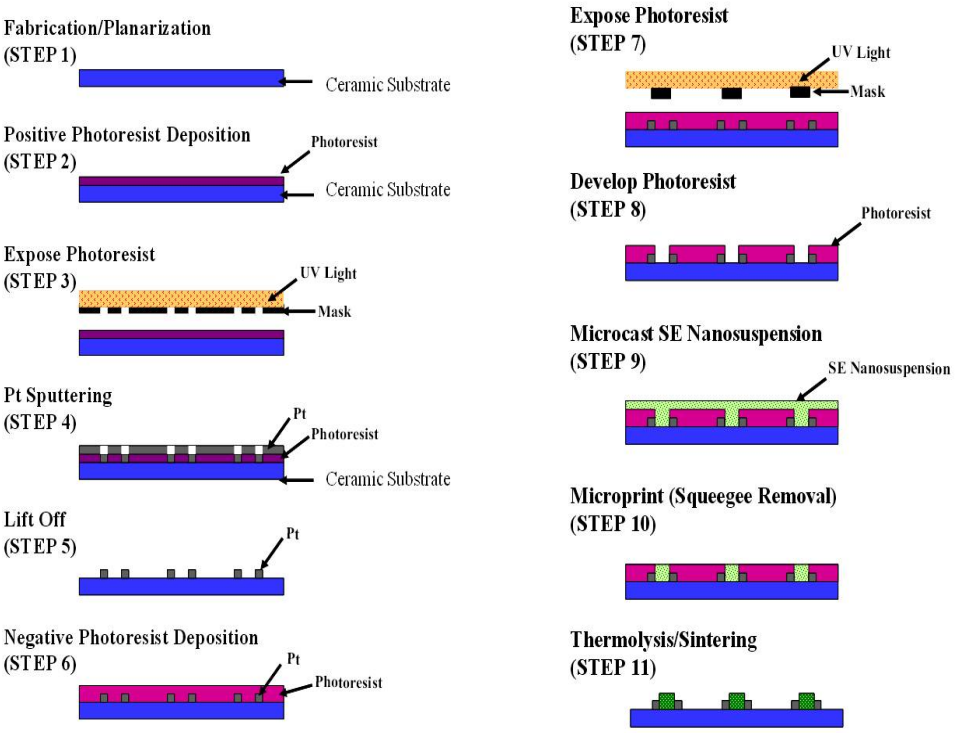

Figure 90: Schematic of the microcasting process microsensor [17B].

Once the micromold fabrication was completed, the depth of the channels were measured by profilometer precisely. The thickness profile of the molds is given in the Figure 91. An optimized microcasting system developed by Wildfire et *al.* used and a thick film photolithography method that was able to produced molds up to 50 and 100 µm depth with good lateral resolution [17B].

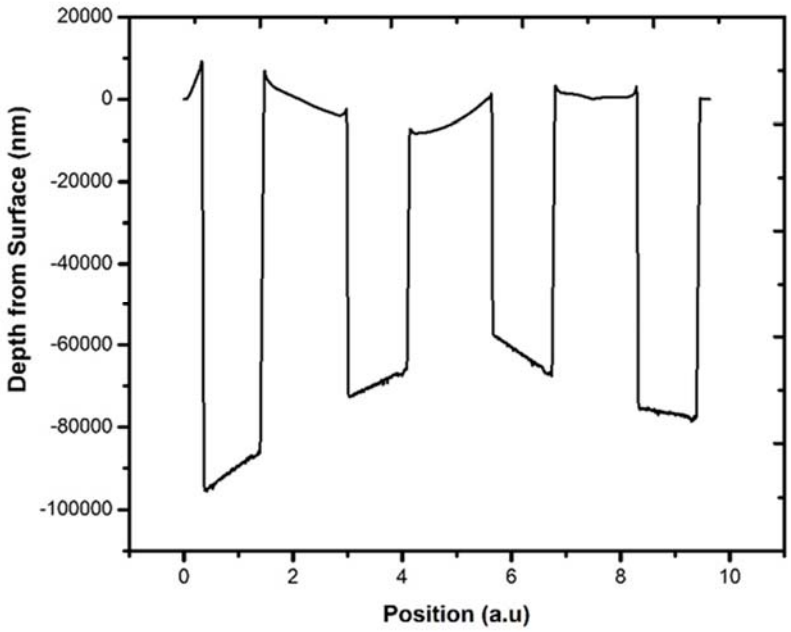

Figure 91: The thickness profiles of the molds made of SU-8.

Microcasting was completed with non-aqueous inks of previously optimized and determined choices of sensing materials; $SrMoO_4$ nanoflowers and $SrMoO_4$/MgO for H_2S/SO_2 and H_2, respectively. Each of the material systems was casted on the IDEs with an approximate film thickness of 50 μm by using two channels located in the middle of the pattern. The two other channels also could be used, but were not the chosen due to their large depth. The inks consisted of 70 wt% of nano but agglomerated hydrothermally produced ceramic powder and a terpineol/ethyl cellulose ink vehicle, J2M, (Johnson Matthey, UK) that was sonicated in order to break agglomerates and increase the dispersion. The microcasting process was accomplished via a stenciling process using a screenprinter (DEK, Weymouth, UK) in order to have repeatable deposition thicknesses. Upon compilation of casting the substrate was placed in a high-temperature box-furnace and burned out, sintered and stabilized in a two-step process with heating rates of 1˚/min to 600˚C and form that temperature to 1200˚C with 5˚/min with a one hour dwell time at 1200˚C. Figure 92 shows the SEM micrograph of the microsensor after sintering and the stabilization heat treatment.

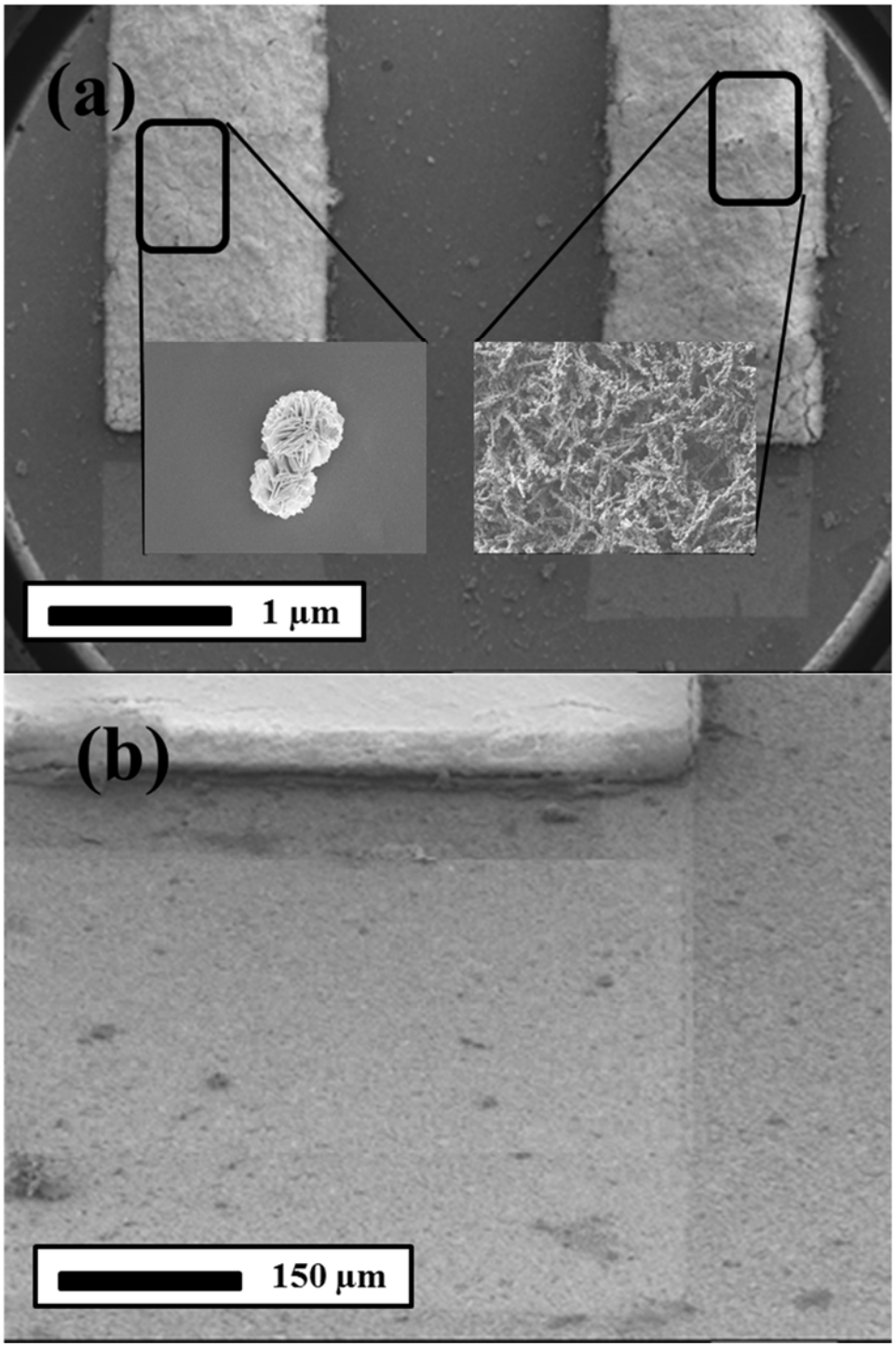

Figure 92: SEM micrographs of (a) $SrMoO_4$/MgO and $SrMoO_4$ nanoflowers sensing material deposited over Zr/Zr+Pt/Pt type microelectrode (b) close-up of edge.

3) Microsensor Electrochemical Testing

Microsensors Containing Zirconate Nanomaterials

Before comparing test results it is important to know the difference in the interdigitated electrodes (IDE) parameters for each sensor platform. The previously discussed macro sensors were based on a screen printed IDEs containing 11 teeth spaced at 250 µm. The micro-IDEs are sputtered and have 29 teeth spaced 50 µm apart. Both the number of teeth and spacing will have a great effect on the performance of the sensor. The complete set of IDE parameters can be seen in Table 8.

Table 8: Macro and micro IDE parameters for high temperature testing.

	Teeth/Gap Spacing	Number of Teeth	Width of Sensing Area	Length of Sensing Area
Macro IDE	250 µm	11	3 mm	8 mm
Micro IDE	50 µm	29	1.2 mm	3 mm

Not only will the geometry of the electrode play a part in the sensors' performance but also the deposition technique used. Figure 93 compares the micro-views of each electrode system. Figure 93(a) shows the uneven electrode and spacing thicknesses that result from the screenprinting technique. The ink system used in screenprinting also forms islands of Pt along the printed lines especially when annealed as seen in the SEM image of the screenprinted electrode. This isolation of Pt might be the main contributor to the signal static seen in the macro-sensor testing.

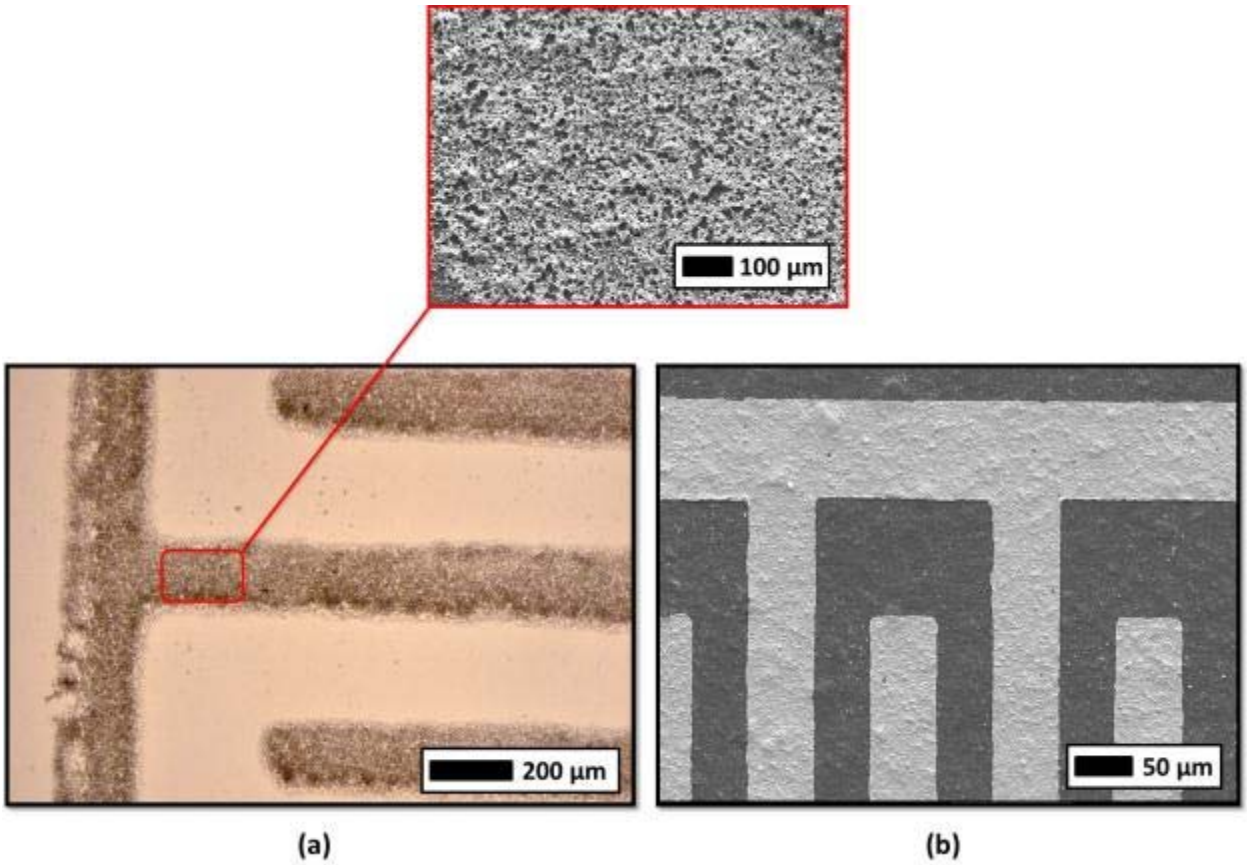

Figure 93: Comparison of IDE microstructure and geometry (a) micrograph and SEM picture of screenprinted Pt macro IDE, (b) SEM picture of sputtered Pt micro IDE

Control of the geometry and stabilization of the Pt grains can be achieved by using a photoresist patterning and sputtering technique as seen in Figure 93(b). To see how the microstructure and geometry affect the performance of the high temperature sensors, a few materials were selected for comparison. The first system tested was the 10% SnO_2/90% GZO composite sensor in a 10% oxygen atmosphere. As seen in Figure 94, the signal noise of the sensor is greatly reduced at 1000˚C. The micro-sensor also exhibits better sensitivity and response time as compared to the macro sensor platform. At 600˚C, the macro-sensor needs 9.6 min to reach 90% of the maximum sensor response to 4000 ppm of H_2 while the micro sensor only needs 3.6 min, which is a 63% reduction in response time. The sensitivity to 4000 ppm of H_2 also increased from 0.029 to 0.048 from a macro sensor platform to a micro sensor platform at 600˚C. However, at 1000˚C an increase in sensitivity is not seen for the micro-sensor.

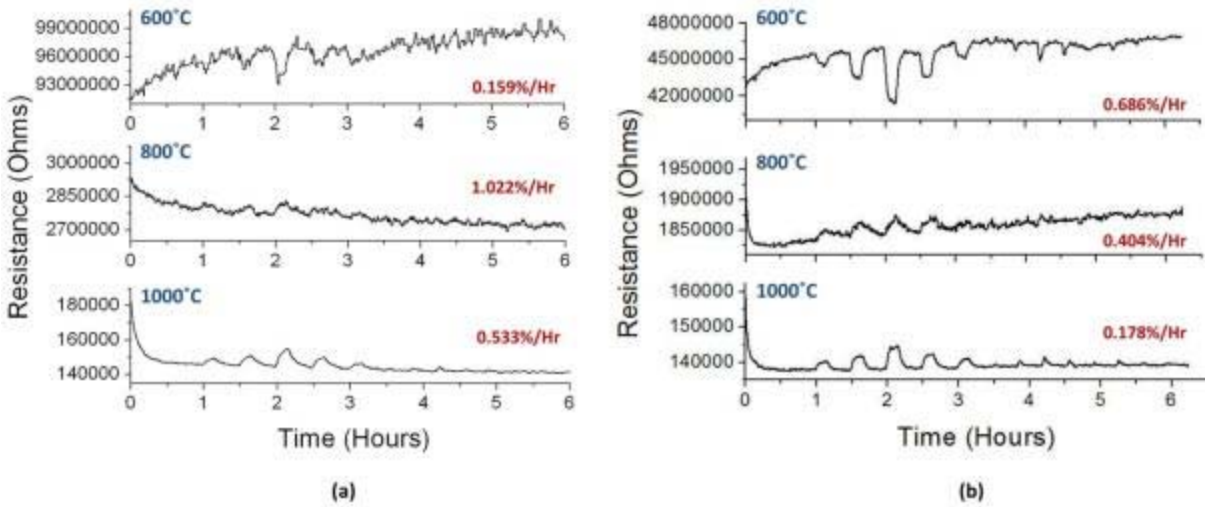

Figure 94: Comparison of 10% SnO_2/90% GZO in 10% oxygen atmosphere (a) macro-sensor platform, (b) micro-sensor platform

It has been shown in several studies that by decreasing the spacing of the electrodes, both the response time and sensitivity could be improved [S. Capone et al. 2001] [138A][141A]. When looking at the IDEs used in this study, the conductive pathway for the sensing material was decreased by using a micro-sensor platform, resulting in an improvement of the response time of the sensor. However, by switching to a micro-sensor IDE, the sensing area (surface area) is also decreased which might explain the mixed results in sensitivity for the micro sensor. When considering high temperature sensors, the grain size must be taken into account. The same ink systems were used for each sensor platform. For a 10% SnO_2/90% GZO composite sensor, the particles size is on average 60 nm. Since the grain boundaries are controlling the conduction as previously discussed, reducing the number of grains between electrodes (smaller electrode spacing) decreases the response time but does not improve sensitivity. Because the total sensing area has been reduced and the grain size remains constant, it is best to compare the sensitivity of these sensors per surface area. Figure 95 demonstrates the difference in sensitivity comparison when looking at sensitivity in respect to sensing surface area. At 600˚C the micro sensor has a 200% increase in sensitivity per mm^2. If the grain sizes could be reduced, a larger percent increase in sensitivity would be expected.

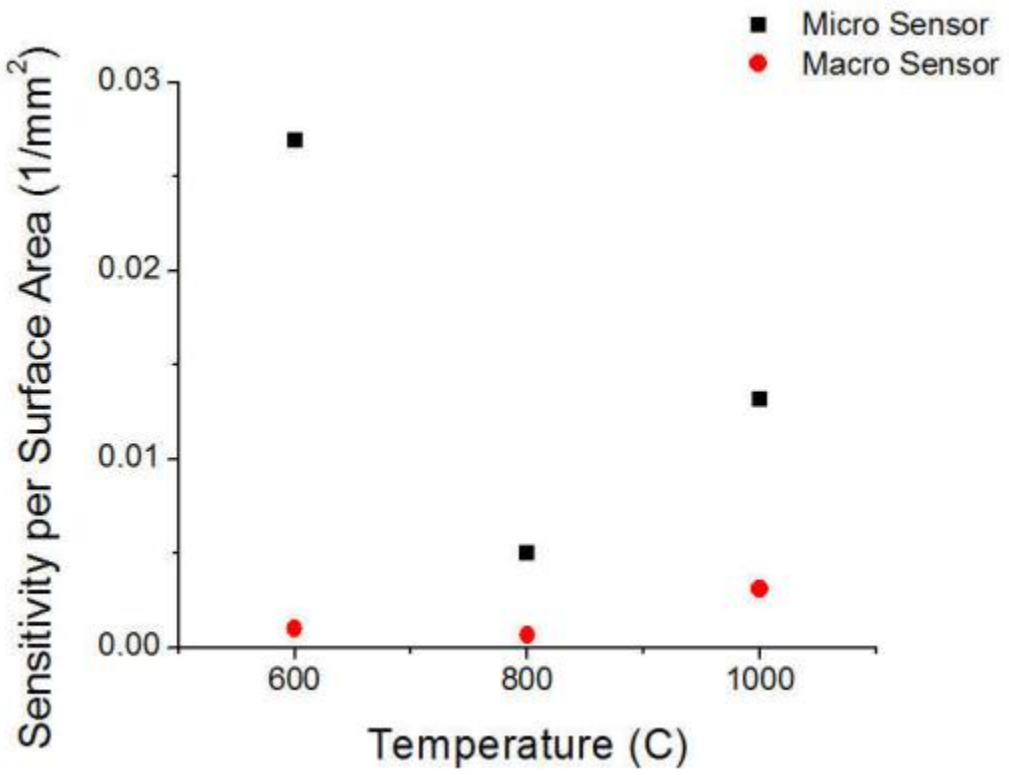

Figure 95: Comparison of sensitivity per surface area of 10% SnO_2/90% GZO composite macro and micro sensor platforms.

Similar results were seen for both the $Gd_{1.6}Sm_{0.4}Zr_{1.8}Sn_{0.2}O_7$ and SnO_2 sensors, as seen in Figure 96 and Figure 97. For the $Gd_{1.6}Sm_{0.4}Zr_{1.8}Sn_{0.2}O_7$ material system, diffusion curves were seen for the response and recovery of the sensor at 1000˚C. The slow diffusion of oxygen from the bulk to the surface of the macro-sensor prevented it from reaching the maximum sensor response for the hydrogen; nor did it reach the plateau that was seen in other sensors. With the micro-sensor platform, the diffusion of the oxygen through the bulk of the sensing material does not hinder the sensing performance. The micro-IDEs allow for a quick response and produce a stable output at 1000˚C. The response time was reduced from 8.4 min to 1.8 min at 1000˚C for 4000 ppm of H_2.

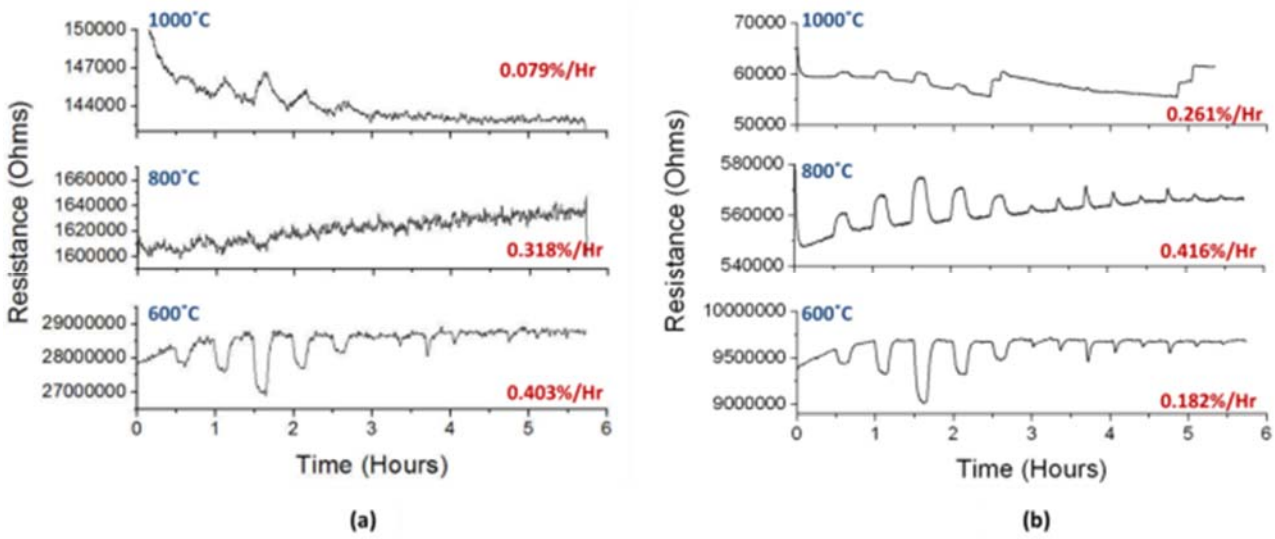

Figure 96: Comparison of $Gd_{1.6}Sm_{0.4}Zr_{1.8}Sn_{0.2}O_7$ sensor in 20% Oxygen atmosphere (a) macro-sensor platform, (b) micro-sensor platform.

For the pure SnO_2, the greatest improvement in response time and sensitivity can be seen at 600˚C in Figure 97. The quick pulses of 4000 ppm of H_2 at the end of the sensing test can clearly be seen with responses almost equivalent to the full 15 min pulses of H_2 at the beginning of the test. The response time was reduced to less than a minute for the micro-sensor platform for a pure semiconducting material. The stability of the sensor was increased by 93% at 600˚C

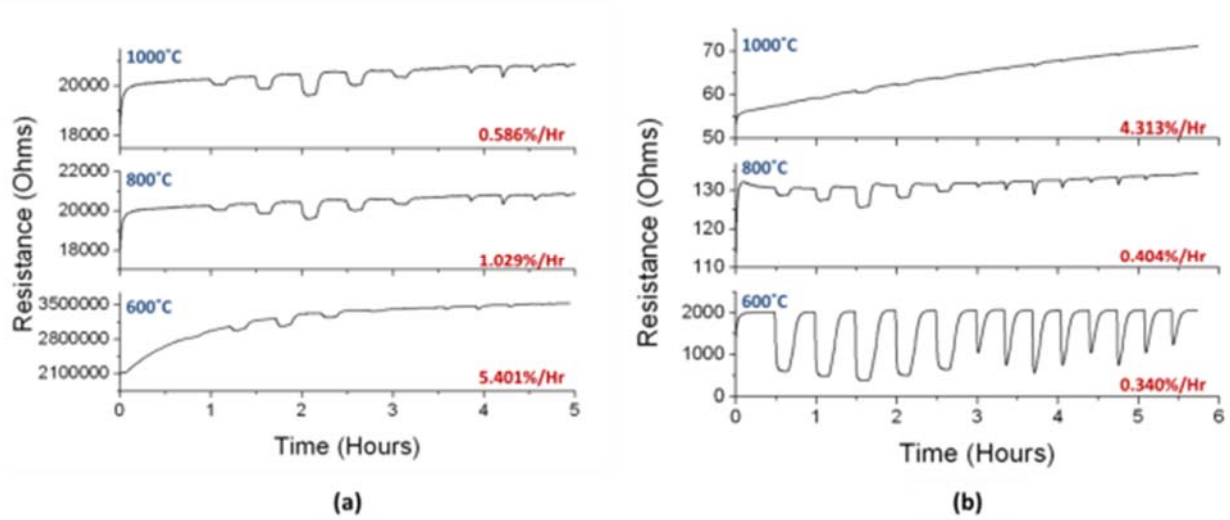

Figure 97: Comparison of pure SnO_2 sensors (a) macro-sensor platform (b) micro-sensor platform.

Again, comparing the sensitivity per surface area of these two materials systems, the micro sensor IDE shows greatly improved sensitivity at each testing temperature as seen in Figure 98. In most cases, the sensitivity per surface area is increased by over 100%.

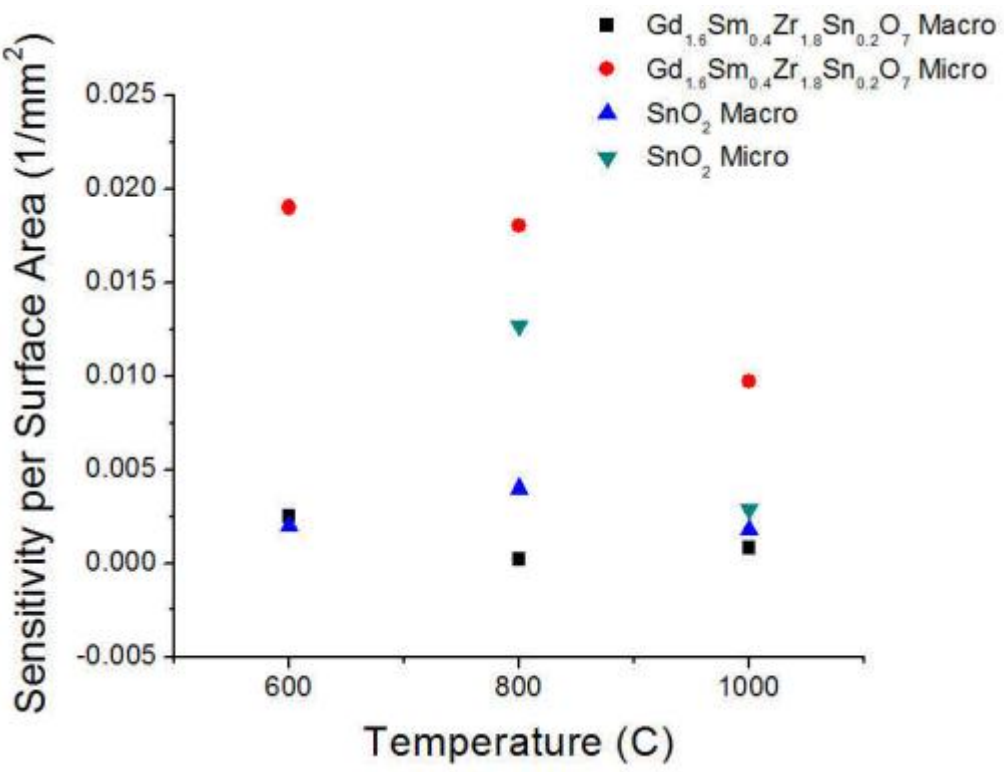

Figure 98: Comparison of sensitivity per surface area of SnO_2 and $Gd_{1.6}Sm_{0.4}Zr_{1.8}Sn_{0.2}O_7$ macro and micro sensors in 20% Oxygen atmosphere. The sensitivity for each material system improved by 100% by incorporating into a mico sensor platform.

As with the macro-sensor IDEs, the micro-sensor IDEs were tested for their contribution to the overall resistance and drift of the sensor system. The test result for the sputtered micro-sensor can be seen in Figure 99. The electrodes remained stable with less than 0.05%/hr change at 800˚C and 1000˚C. At 600˚C, the drift was 0.355%/hr, and it can clearly be seen that the electrode is adding to the sensitivity of the sensor system. Typical sensors resistances seen at 600, 800, and 1000˚C for this research are around $3x10^6$, $2x10^5$, and $2x10^4$ ohms, respectively. The electrodes contribute less than 0.2% at 600˚C, 0.02% at 800˚C, and 0.002% at 1000˚C. The electrodes would be the most likely cause of the drift at 600˚C, since it is unlikely that the morphology of the particles are changing at low temperatures after being sintered to 1200˚C; however, at 1000˚C the electrodes contribute very little to the drift making coarsening or reduction of the material the most likely candidate for the drift.

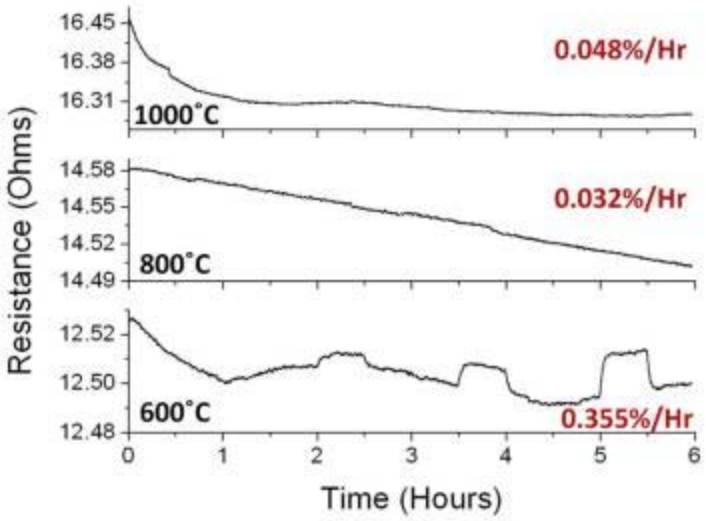

Figure 99: Micro Electrode test in 1% oxygen at 600˚C, 800˚C, and 1000˚C. The Pt sensitivity to H_2 can be seen at 600˚C. However, the electrodes contribute less than 0.2% to the total resistance at that temperature.

The film thickness also greatly impacts the performance of the gas sensor. Zhang performed a study on the interaction between the electrodes and the film thickness of the sensor [P. Zhang 2008]. He found that for a film thickness of 100 µm, 84.8% of the total electronic current flows within the first 30 µm of the sensing film thickness from the substrate. Within the first 50 µm nearly all the current flows (96.9%) within this distance from the substrate as shown in Figure 100. This is however also dependent on the porosity level and total resistance of the sensing material.

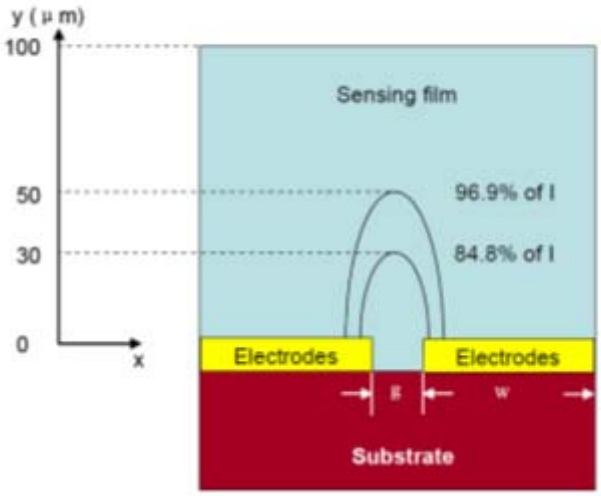

Figure 100: Schematic view of the current distribution in the sensing film [P. Zhang 2008]

From this analysis, it can be seen that on the top surface the current change is small, meaning the resistance change is small for a given applied voltage and a thin sensing film

would be preferred for a quickly responding sensor. Korotcenkov *et al*. reported that thick film SnO_2 sensors are more responsive to H_2 as the thickness of the film decreases from 300 nm to 100 nm [G. Korotcenkov 2008]. In this study when incorporating the sensing materials into a micro sensor platform the sensing film thickness is decreased considerably from 100 µm to 50-60 µm. For mesoporous materials, diffusion is governed by Knudsen diffusion,

$$D_k = \left(\frac{4r}{3}\right)\sqrt{\frac{2RT}{\pi M}} \qquad (36)$$

Where r is the pore radius, M is the molecular mass of the diffused gas, T is the temperature, and R is the universal gas constant [142A]. The time it takes for a molecule of gas through a certain thickness can be calculated using Einstein's relation for transport,

$$\langle x^2 \rangle = 2D_k t \qquad (37)$$

Where x is the thickness of the film, D is the diffusion coefficient, and t is time. Assuming the microstructures for each sensor platform is the same, these two equations can be used to compare the times it would take for hydrogen to diffuse through the two thicknesses. This will give a better understanding of substantial time difference between the two platforms. For the $Gd_{1.6}Sm_{0.4}Zr_{1.8}Sn_{0.2}O_7$ sensor at 1000˚C for a 100 µm thick film with pore sizes of 80 nm the diffusion time is $4.78E^{-5}$ seconds to reach the electrode. For a 50 µm thick film, the diffusion time reduces to $1.19E^{-5}$ seconds. Although the response time for the thinner film is a quarter of the time for the thick film, the diffusion time is still fractions of a second. The diffusion only accounts for a small percentage of the total response time and therefore is not the main cause of the difference in response time between the two sensor platforms. However, more testing is needed to determine the true effect of the film thickness reduction. AC impedance testing of the micro sensors would also determine the role between the sensing material and electrode interaction for this film thickness.

Microsensors Containing $SrMoO_4$ Nanomaterials

The spacing between the fingers is what significantly affected the response rate of the sensor. Figure 101-a and -c presents the testing results of the $SrMoO_4$ nano-flowers for SO_2 in the micro- and macro-scale chemi-resistive sensor architecture. Figure 101-b and -d shows the testing results of the $SrMoO_4$/MgO for H_2 in micro- and macro-scale chemi-resistive sensor architecture at 1000°C under 1%O_2 partial pressure against different levels of SO_2 and H_2. It is known that the sensitivity and response time can be increased and decreased for designated target gas, respectively by including nanomaterials on a macrosensor platform or by reducing the size of the electrode system for the sensors [17B, 54B]. As seen in the Figure 101-b, the 1000, 2000, and 4000 ppm H_2 exposures resulted in sensitivities of ~67%, ~81%, and ~87% in the $SrMoO_4$/MgO microsensor, respectively. These responses are up to 30% increase in comparison to performance of the macrosensor (see Figure 101-d). As seen in the Figure 101-a and –c, the sensitivity data for different concentration levels of SO_2 for the $SrMoO_4$ nanoflowers tested on the micro and macrosensor platforms at 1000°C are remarkably different as also observed in the

$SrMoO_4$/MgO case. The average measured sensitivities were ~24%, ~29%, and ~37% for the 500, 1000, and 2000 ppm of SO_2, respectively for macro sensor platform, however for microsensor platform these values almost doubled and were ~55%, ~63%, and ~67% for the 500, 1000, and 2000 ppm of SO_2, respectively. As seen from the results, the microsensors not just only increased the sensitivity, but also decreased the response and recovery times. The difference in performance for the $SrMoO_4$ nanoflowers and $SrMoO_4$/MgO in the micro platform can be attributed to nature of the materials. The highly porous network of the later, in which H_2 molecules can easily diffuse through and reach more surface are of the sensing material.

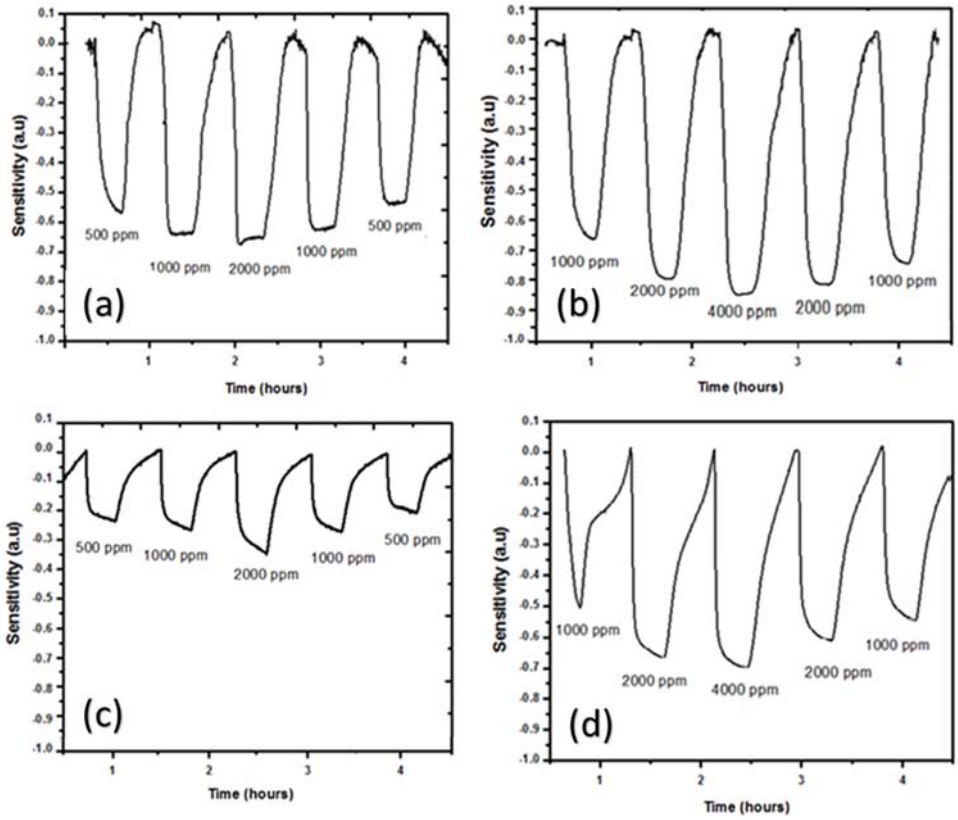

Figure 101: Response of microsensor equipped with (a) $SrMoO_4$ nano-flowers tested for SO_2 (b) $SrMoO_4$/MgO tested for H_2. Response of macrosensor (c) $SrMoO_4$ nano-flowers tested for SO_2 (d) $SrMoO_4$/MgO tested for H_2.

D. CONCLUSIONS:

So far in literature, a stable high temperature chemiresistive sensor has not been found. Typically, chemiresistive sensors have issues with stability and sensitivity due to the traditional metal oxide semiconducting materials used for this sensor platform. This research has provided several material systems that not only sense hydrogen at temperatures up to 1000˚C, but that are stable and have improved cross-sensitivity resistance to CO. Reaction mechanism for each material system ranging from traditional metal oxide semiconductors, to composite systems were demonstrated for a variety of environments. With each of these materials, optimal operating conditions were found for each material system allowing for sensors or sensor arrays to be tailored for the application. Another key aspect of this work was to incorporate the new material system to a micro-sensor platform. Typically, micro-sensors are composed of thin films deposed by CVD processes which greatly limit the composition of the sensing material and usually fail under high temperatures due to microstructural growth and delamination. A novel process was developed to form micro-porous 3-D features of sensing material onto a micro-sensor IDE. This micro-casting process allows for a wide array of materials to be deposited with precision onto an IDE or multiple materials for a sensor array. Finally, the micro-sensors tested with exhibited improved response time and stability compared to the macro-sensor platform. Specific conclusions for each of the major nanomaterial systems (pyrochlore zirconate and sheelite molybdates/tungstates) are presented below.

Zirconate Nanomaterials

The initial main goal was to control the size and shape of $Gd_2B_2O_7$, which is related to growth mechanism, controlling the phase of the nanomaterials, and exploring the material system's capacity for dopants. Previous research has shown that the pH of the solution effects the phase and solubility of the materials. An optimum pH, usually between 6-8, produces a single phase pyrochlore, while going above or below this range produces secondary phases. Most studies use low temperature and extended hold times for hydrothermal synthesis. This research focused on the use of high temperatures (> 240˚C) and shorter dwell times (1-10h) to form a pure pyrochlore or defective fluorite phase. Each material system was successfully formed with a high temperature hydrothermal route. For a pure $Gd_2Zr_2O_7$ material, it was found that for temperatures near 240˚C, dwell times of 5hrs or more were needed to for a pure pyrochlore phase. If the temperature was increased to 300˚C only a dwell time of 1h was needed for the pure pyrochlore phase and resulted in particles sizes around 7 nm. Similar results were found with doping the A-site of GZO with yttrium and samarium. XRD confirmed decrease or increase in the lattice structure with yttrium and samarium up to 20 and 40% substitutions respectively. Hydrothermal synthesis conditions of $Gd_2Ti_2O_7$ and $Gd_2Sn_2O_7$ for a single phase structure was found to be optimal when the pH=6 due to the solubility of the starting materials.

Another key parameter for highly sensitive gas sensors is limiting grain growth and increasing porosity for thick films. By incorporating traditional MOS materials with highly refractory zirconate materials decreased particle size when sintered at 1200˚C from 1 μm for pure SnO_2 to 50 nm for a 10% SnO_2/90% GZO composite material. Porosity was also increased as the vol% of the SnO_2 was increased but as the vol% increases the particle size

also increases.

The goal for testing the zirconates on the macro-sensor platform was to find a system that is stable at 1000˚C for hours of operation and has low to no sensitivity to CO and remains stable with these contaminates in the environment. Two methods were used to develop a high temperature sensor, 1) incorporate traditional MOS materials into a composite system with zirconates to pin grain growth of the MOS materials and to provide an oxygen source for the MOS materials at high temperatures, 2) utilizing various doped Gd-based pyrochlores as the MOS or metal-oxide mixed ionic-electronic conductor (MIEC) as the active material with the chemi-resistive sensor architecture. The composite sensors (SnO_2/GZO) showed high sensitivity to H_2 and improved stability over pure SnO_2 sensors at temperatures >600˚C. Not only did the GZO limit the grain growth of the SnO_2 particles, but prevented the SnO_2 from fully reducing to Sn at high temperatures in a low oxygen atmosphere in the 10% SnO2/90% GZO sensor. In the sensor with a larger percentage of SnO_2 (50%-100% SnO_2) the MOS carries the conduction and sensing mechanism of the sensor. At lower percentages of SnO_2 the MOS acts as a promoter to the GZO ionic conductor. AC Impedance testing supports the theory that the conduction mechanism for the composite sensor is based on reactions at the grain boundary between the SnO_2 and the zirconate. The most promising results came from incorporating Sn into a solid-solution with GZO. By incorporating the Sn into the pyrochlore structure, the sensitivity of the GZO was drastically increased and maintained its stability up to 1000˚C. It was also highly resistant to CO cross-sensitivity making it the best candidate for a high temperature chemiresistive sensing material. Research could be continued in many different ways. The effect of particle size on the sensors performance needs further investigation. Comparison of the conduction mechanism n-type and doped n-type MIEC materials to see if surface reactions are controlling the conduction. Also, long-term stability testing is needed to see if the drift of the sensors tapers off or if there is a burn-in period for stabilization.

Finally, the zirconate materials were incorporated into micro sensor arrays for gas sensing at high temperature. The focus has been on the fabrication techniques that can be used to create porous 3-D networks of metal-oxide semiconducting materials. A microcasting system was developed using ceramic substrates and a thick film photolithography technique that produced molds up to 90 μm thick with good resolution and high aspect ratios with various geometries. Several ink binder systems were tested to determine which system would produce a stable 3-D structure that remained porous after sintering to temperatures around 1200˚C. A 20 vol% solids loading was required to create a stable structure with each evaluated binder system. It was also determined that the aqueous based slip casting system produced the most stable structure with little deformation after sintering. By using a layered Zr/Pt IDE, the sensor's response, and stability was greatly improved. For a 10% SnO_2/90% GZO composite sensor in a 10% oxygen atmosphere the sensitivity was increased by 200% at 600˚C. For a $Gd_{1.4}Sm_{0.6}Zr_{1.8}Sn_{0.2}O_7$ sensor in 20% oxygen atmosphere, the sensitivity was increased by 100% at each temperature and stability was increased by 93% at 600˚C. Response time is also decreased by incorporating the materials into a micro sensor design. At 600˚C the response time was reduced to less than a min while at 1000˚C the response time was decreased from 8.4 to 1.8 min. The effect of film thickness on the response rate, sensitivity, and recovery rate could be further

investigated to optimize the micro sensor platform. Variation of the IDE dimensions could also improve the sensor's performance. Lastly, AC impedance testing could be used to further investigate the IDE's role in the micro sensor's conduction.

Molybdate/Tungstate Nanomaterials

Baseline testing of current SO_2 and H_2S sensing materials were completed. Nanomaterials as an active sensing layer that are stable at high temperatures are completed by templated growth of $SrMoO_4$ over MgO ($SrMoO_4$/MgO). This material showed high resistance to sintering and high accuracy, stability, and sensitivity toward H_2 due to MgO incorporation into $SrMoO_4$ matrix. Although the sintering of the $SrMoO_4$ nanoflowers could not hinder, the material performed very good sensitivity, stability, accuracy and long term stability against SO_2. The chosen material system ($SrMoO_4$ nanoflowers) was further tested for up to 100 pmm of H_2S diluted in H_2 as well as syngas composition and showed very promising sensing capabilities as well as accuracy in order to determine the different level of the target gas under extremely reducing atmosphere. The reasons behind sensitivity of the chosen two material systems for H_2 and SO_2 were characterized by Raman, XPS-UPS, XRD, EDS-SEM, AAS, TPR and TEM. The compound formation between Mg and S is the reason behind insensitivity of the $SrMoO_4$/MgO against SO_2, while its high sensitivity toward H_2 can be attributed to its highly porous microstructure and catalytic action of the surface. ECR was utilized for exploring the surface kinetics of the SO_2 over $SrMoO_4$ nanoflowers and it was concluded that interacting can be distinguished to discrete sections, etching like surface interacting and subsequent diffusive part.

As discussed above, new IDEs were required to produce and test the microsensors at the temperatures of interest. In conjunction with the work on the various nanomaterial systems, new Pt-based electrodes were required to be developed. The reason for this work is aligned with the thermal stability limitations of Pt films with various adhesion layers (Ti, Ta, Zr, and Hf) were characterized at 800 and 1200°C for various annealing times. The deposition of the Hf adhesion layer showed a high level of microstructural stability (compared to the Ti, Ta, and Zr) to the highest operating temperature (1200°C). The Hf was also incorporated within the bulk Pt conductive layer by depositing an alternating layer structure of Hf and Pt metal. The electrical resistivity measurements confirmed the retention of the percolated conductive network. In the end, a Pt composite multilayer film was developed that could withstand high-temperature exposure up to 1200°C for 48 h, which is beyond most reasonable, high-temperature chemical sensor applications or MEMS processing (and/or operation) conditions. It was further investigated that alternative a DC sputtering process for fabricating a functionally-gradient Pt and Zr composite microstructure with three deposition steps. The resultant microstructure of the composite electrode thin film was shown to be stable up to 1200°C. The microstructural stability of the Zr/Zr+Pt/Pt film architecture was attributed to the distribution of Zr throughout the bulk of the film during the three-step deposition process. Co-deposition of Hf and Pt would result high microstructural stability due to high stability of Hf compare to Zr.

The microsensors utilized with the nano compositions of the optimized sensing material systems not just only increased the sensitivity, but also decreased the response and recovery

times. In the case of microsensor platform, the $SrMoO_4$/MgO reported a sensitivity increase of 40% compared to the macro platform. However, in the case of usage of micro platform of $SrMoO_4$ nanoflowers, compared to the macro platform of $SrMoO_4$ nanoflowers, the increase in sensitivity was up to 65%. The process regarding the synthesis of MgO nanorods can be optimized toward reducing the diameter of the as-synthesized products. This would result in more surface area after templated growth of sensing material.

E. GRAPHICAL MATERIALS LIST(S)

None

F. REFERENCES:

[100A] S.J. Kim, S.D Park, Y.J. Jeong, Homogeneous precipitation of TiO2 ultrafine powders from aqueous TiOCl2 solution. 4, 1999, Journal of American Ceramic Society, Vol. 82, pp. 927-932.

[101A] L. Gao, H. Zhu, L. Wang, G. Ou, Hydrothermal synthesis and photoluminescence properties of Gd2Zr2O7:Tb3+ phosphors. 2011, Materials Letters, Vol. 65, pp. 1360-1362.

[102A] Hammond, C. The Basics of Crystallography and Diffraction. 3rd. Oxford : Oxford Science Publication, 2009.

[103A] J.A. Diaz-Guillen, A.F. Fuentes, M.R. Diaz-Guillen, J.M. Almanza, J.Santamaria, C. Leon. The effect of homovalent A-site substitutions on the ionic conductivity of pyrochlore-type GdZrO. 2009, Journal of Power Sources, Vol. 186, pp. 349-352.

[104A] T. Zhang, K. Wei Li, J. Zeng, Y. Wang, X. Song, H. Wang, Sythensis and structural characterizatoin of a series of lanthanide stannate pyrochlores. 2008, Journal of Physics and Chemistry of Solids, Vol. 69, pp. 2845-2851.

[105A] Eranna, G. Metal Oxide Nanostructures as Gas Sensing Devices. Boca Raton, Fl : Taylor and Francis Books, 2012.

[106A] M. Jubner, R.G. Pavelko, N. Barsan, U. Weimar.Influence of oxygen backgrounds on hydrogen sensing with SnO2 nanomaterials. 2011, Sensors and Actuators B: Chemical, Vol. 154, pp. 264-269.

[107A] P. Tobias, A. Baranzahi, A.L. Spetz, O. Kordina, E. Janzen, I. Lundstrom. Fast chemical sensing with metal-insulator-silicon carbide structures. 1997, IEEE Electronic Device Letters, Vol. 18, pp. 287-289.

[108A] M. Batzill, U. Diebold, The surface and materials science of tin oxide. 2005, Progress in Surface Science, Vol. 79, pp. 47-154.

[109A] Korotcenkov, G., [ed.]. Chemical Sensors Volume 1: General Approaches. s.l. : Momentum Press, 2010.

[110A] M. Fleischer, H. Meixner, Fast gas sensors based on metal oxides which are stable at high temperatures.. 1997, Sensors and Actuators B, Vol. 43, pp. 1-10.

[111A] J. Yang, K. Hidajat, S. Kawi, Synthesis, characterization and sensing properties of nano-SnO2 supported on SBA-15 as highly sensitive cemiconductor gas sensors.. 2008, Journal of Materials Chemistry, Vol. 19, pp. 292-298.

[112A] M. Vogler, a. Hutter, L. Gauckler, J. Warnatz, W. Bessler, Modelling study of surface reactions, diffusion, and spillover at a Ni/Ysz patterned anode. 5, 2009, Journal of the Electorchemical Society, Vol. 156, pp. B663-B672.
[113A] Tuller, H., Semiconduction and mixed ionic-electronic conduction of nonstoichiometric oxides: impact and control. : Solid State Ionics, 1997, Vol. 94, pp. 63-74.
[114A] Yu, Tae-Hwan. Electrical Properties and Structural Disorder in Stannate Pyrochlores. Materials Science and Engineering. s.l. : Massachusetts Institute of Technology, 1991.
[115A] U. Weimar, W. Gopel, AC measurements on tin oxide sensors to improve selectivities and sensitivities. 13, s.l. : Sensors and Actuators, 1995, Vol. 26.
[116A] S. Birlasekaran, Y. Jianhong. s.l., Frequency response characteristics of gas sensors. Measurement, 1999, Vol. 26, pp. 229-247.
[117A] N. Barsan, U. Weimar. s.l, Understanding the fundamental principles of metal oxide based gas sensors; the example of CO sensing with SnO2 sensors in the presence of humidity.: Journal of Physics: Condens. Matter, 2003, Vol. 15, pp. R813-R839.
[118A] M.A. Ponce, R. Parra, R. Savu, E. Joanni, P.R. Bueno, M. cilense, J.A. Varela, M.S. Castro. s.l., Impedance spectroscopy analysis of TiO2 thin film gas sensors obtained from water-based anatase colloids.: Sensors and Actuators B: Chemical, 2009, Vol. 139, pp. 447-452.
[119A] M.A. Ponce, P.R. Bueno, J. Varela, M.S. Castro, C.M. Aldao. s.l., Impedance spectroscopy analysis of SnO2 thick-films gas sensors.: Journal of Material Science: Material Electronics, 2007, Vol. 19, pp. 1169-1175.
[120A] V.S. Srinivasan, M.K. Patra, V.S. Choudhary, M. Mathew, A. Pandya. 7, s.l., Phase change annealing effects on electrical and optical properties of tin oxide thin films.: Journal of optoelectronics and advanced materials, 2010, Vol. 12, pp. 1485-1489.
[121A] S.H. Hahn, N. Barsan, U. Weimar, S.G. Ejakov, J.H. Visser, R.E. Soltis, CO sensing with SnO2 thick film sensors: role of oxygen and water vapour.. 2003, Thin Solid Films, Vol. 436, pp. 17-24.
[122A] G. Jime'nez-Cadena, J. Riu, F.X. Rius., Gas Sensors Based on Nanostructured Materials. 2007, Analyst, Vol. 132, pp. 1083-1099.
[123A] Ayyub, P.Aligned Nanorod Arrays: Additive and Emergent Properties (Review). 2009, Journal of Cluster Science, Vol. 20, pp. 429-451.
[124A] M. Graf, A. Gurlo, N. Barsan, U. Weimar, A. Hierlemann, Microfabricated gas sensor systems with nanocrystalline metal-oxide sensitive films. 2006, Journal of Nanoparticle Research, Vol. 8, pp. 823-839.
[125A] L. Francioso, M. Russo, A.M. Taurino, P. Siciliano, Micrometric patterning process of sol–gel SnO2, In2O3 and WO3 thin film for gas sensing applications: Towards silicon technology integration. 2006, Sensors and Actuators B, Vol. 119, pp. 159-166.
[126A] M. Heule, L.J. Gauckler. Miniaturised arrays of tin oxide gas sensors on single microhotplate substrates fabricated by micromolding in capillaries. 2003, Sensors and Actuators B, Vol. 93, pp. 100-106.

[127A] M. Heule, S. Vuillemin, L.J. Gauckler, Patterning colloidal suspensions by selective wetting microcontact-printed surfaces. 15, 2003, Advanced Materials, Vol. 15, pp. 1237-1245.
[128A] Hruby, J, Modal analysis and gain calcualtions for a sheet electron beam in a ridged slow-wave structure. [ed.] B.E. Carlsten. 2002, High-Energy Density and High Power RF: 5th Workshop, pp. 55-60.
[129A] J. Yasaitis, M. Perez-Maher, J. Karam, Micromachining and Microfabriaction Process Technology VIII. 2003. Proceedings of SPIE. pp. 430-439.
[130A] T. Garino, J. Cesarano, A. Morales, Antireflection micropatterning using EB-Lithography. 2003, Mat. Res. Soc. Symp. Proc., Vol. 741, pp. 227-232.
[131A] A.M. Morales, R. Pitchumani, T.J. Garino, A.K Gutmann, L.A. Domeirer, Fabrication of Ceramic Microstructures via Microcasting of Nanoparticulate Slurry. 10, 2005, Journal of American Ceramic Society, Vol. 88, pp. 570-578.
[132A] Masks. M. Heule, L.J. Gauckler, Microfabricatoin of Ceramics based on Colloidal Suspensions and Photoresist 3, 2001, J. Photopolym. Sci. Technol., Vol. 14, pp. 449-452.
[133A] M. Heule, L.J. Gauckler, Gas sensors fabricated from ceramic suspensions by micromolding in capillaries. 23, 2001, Adv. Mater., Vol. 13, pp. 1790-1793.
[134A] S. Akbar, P. Duda, C. Lee, High Temperature Ceramic Gas Sensors (A Review). 4, 2006, Int. J. Appl. Ceram. Technol., Vol. 3, pp. 302-311.
[135A] S.M. Kanan, O.M. El-Kadri, I.A. Abu-Yousef, M.C. Kanan,Semiconducting metal oxide based sensors for selective gas pollutant detection. 2009, Sensors, Vol. 9, pp. 8159-8196.
[136A] Buchanan, R.C. Powder consolidation and forming of ceramics. Ceramic Materials for Electronics. 2nd. New York : CRC Press, 2003, pp. 373-393.
[137A] O.O. Omatete, M.A. Janney, R.A. Strelow, Gelcasting: From laboratory development toward industrial production, 10, 1991, Ceram. Bull., Vol. 70, pp. 1641-1649.
[138A] U. Hoefer, K. Steiner, E. Wagner. s.l., Contact sheet resistances of SnO_2 thin films using transition line measurements. : Sensors and Actuators:B, 1993, Vol. 26, pp. 59-63.
[139A] G.K. Reeves, H.B. Harrison. s.l., Obtaining the specific contact resistance from transmission line model measurements.: IEEE Electronic Device Letters, 1982, Vol. 3, pp. 111-113.
[140A] J. Tamaki, T. Hashishin, Y. Uno, D. Dao, S. Sugiyama. s.l., Ultrahigh-sensitive WO3 nanosensor with interdigitated Au nano-electrode for NO2 detection.: Sensors and Actuators B, 2008, Vol. 132, pp. 234-238.
[141A] Tohey, M. 2, s.l., Electrodes for nano-dot based gas sensors.: Sensors and Actuators B, 2005, Vol. 105, pp. 232-250.
[142A] Korotcenkov, G. Chemical Sensors: Nanostructured Materials. New York : Momentum Press, 2010. Vol. 2.
[143A] The kinetics of ordering in gadolinium zirconate: an unusual oxygen ion conductor. S. Haile, S. Meilicke. s.l. : Materials research society symposia proceedings, 1996.
[144A] Basic physics of semiconductor hydrogen sensors. Gaman, V. 4, s.l. : Russian physics journal, 2008, Vol. 51.

[145A] The kinetic study of temperature-programmed reduction of nickel oxide in hydrogen atmosphere. B. Jankovic, B. Adnadevic, S. Mentus. 2008, Chemical Engineering Science, Vol. 63, pp. 567-575.

[146A] M. Graf, S.K. Muller, D. Barrettino, A. Hierlemann, Transistor heater for microhotplate-based metal-oxide microsensors. 5, 2005, Electron Device Letters, IEEE, Vol. 26, pp. 295-297.

[1B] C. Powell and B. Morreale, "Materials challenges in advanced coal conversion technologies," *MRS Bull,* vol. 33, pp. 309-315, 2008.

[2B] "Annual Energy Outlook 2007 With Projections to 2030," U.S. Department of Energy, Washington, DC, 2007.

[3B] D. L. West, F. C. Montgomery and B. L. Armstrong, "Compact, DC-electrical biased sulfur dioxide sensing elements for use at high temperatures," *Sensors and Actuators B: Chemical,* vol. 162, no. 1, pp. 409-417, 2012.

[4B] M. J. Madou and S. R. Morrison, Chemical sensing with Solid State Devices, San Diego: Academic Press, INC, 1989.

[5B] G. Eranna, B. C. Joshi, D. P. Runthala and R. P. Gupta, "Oxide Materials for Development of Integrated Gas Sensors-A Comprehensive Review," *Critical Reviews in Solid State and Materials Sciences,* vol. 29, no. 3-4, pp. 111-188, 2010.

[6B] A. Mandelis and C. Christofides, Physics, Chemistry and Technolgy of Solid State Gas Sensor Devices, Toronto and Nicosia: Joh Wiley & Sons. Inc., 1993.

[7B] P. A. Cox, Tarnsition Metal Oxides, An Introduction to Their Electronic Structure and Properties, Oxford: Clarendon Press, 1995.

[8B] M. T. Greiner, L. Chai, M. G. Helander, W. M. Tang and Z. H. Lu, "Transition Metal Oxide Work Functions: The Influence of Cation Oxidation State and Oxygen Vacancies," *Advanced Functional Materials,* vol. 7, no. 11, pp. 4557-4568, 2012.

[9B] A. A. Saaman and P. Bergveld, "A Classification of Chemically Sensitivr Semiconductor Devices," *Sensors and Actuators,* vol. 7, pp. 75-87, 1985.

[10B] T. E. Sullivan, R. B. Childs, J. M. Ruths and S. J. Fonash, "Phys. SiO2 and Its Interfaces,," *Proc. Int. Top. Conf.,* p. 454, 1978.

[11B] F. Maximilian and H. Meixner, "Selectivity in High-temperature Operated Semiconductor Gas-sensors," *Sensors and Actuators B: Chemical,* vol. 52, no. 1-2, pp. 179-187, 1998.

[12B] A. M. Azad, S. A. Akbar, S. G. Mhaisalkar, L. D. Birkefeld and K. S. Goto, "Solid State Gas Sensors A review," *J. Electrochem. Soc.,* vol. 139, no. 12, pp. 3690-3701, 1992.

[13B] J. F. Marucco, J. Gautron and P. Lemasson, *J. Phys. Chem. Solids,* vol. 42, p. 363, 1981.

[14B] D. E. Williams, In Solid State Gas Sensors, Chapter 5, Bristol, 1987.

[15B] G. Korotcenkov, "The role of morphology and crystallographic structure of metal oxides in response of conductometric-type gas sensors," *Materials Science and Engineering R: Reports,* vol. 61, pp. 1-39, 2008.

[16B] G. Korotcentov, "Metal oxides for solid-state gas sensors: What determines our choice?," *Material Science and Engineering B,* vol. 139, no. 1, pp. 1-23, 2007.

[17B] C. Wildfire, "Investigation of Gadolinium Based Pyrochlores for their use in High-Temperature Nano Derived H2 Gas Sensors," West Virginia University, Morgantown, 2012.

[18B] D. X, "Understanding and optimization of gas sensors based on metal oxide semiconductors," Chemical Engineering Department, University of Colorado, USA, Ph.D. Thesis Dissertation, 2007.

[19B] E. B. Varhegyi, J. Gerblinger, F. Reti, I. V. Perczel and H. Meixner, "Study of the behaviour of CeO2 in SO2-containing atmosphere," *Sensors and Actuators B,* Vols. 24-25, pp. 631-635, 1995.

[20B] H. Windischmann and P. Mark, "A model for the Operation of a Thin film SnOx Conductance Modulation Carbon Monoxide Sensor," *J. Electrochem Soc.,* vol. 126, 1979.

[21B] P. Mark, *J. Chem. Phys. Solids. ,* vol. 25, no. 911, 1964.

[22B] A. M. Azad, S. G. Mhaisalkar, L. D. Birkefeld, S. A. Akbar and K. S. Goto, "Behaviour of a New ZrO2-MoO3 Sensor for Carbon Monoxide Detection," *J. Electrochern. Soc,* vol. 139, no. 10, pp. 2913-2920, 1992.

[23B] L. D. Birkefeld, A. M. Azad and S. A. Akbar, "Carbon Monoxide and Hydrogen Detection by Anatase Modification of Titanium Dioxide," *J. Am. Ceram. Soc.,* vol. 75, no. 11, p. 2964, 1992.

[24B] B. Chiou, J. Li and J. Duh, "Characteristics of Pd-doped tin oxide ceramics in response to CO gas," *J. Electron. Mater.,* vol. 17, no. 485, 1988.

[25B] V. Aroutiounian, "Metal Oxide hydrogen, oxygen and carbon monoxide sensors for hydrogen setups and cells," *International Journal of Hydrogen Energy,* vol. 32, pp. 1145-1158, 2007.

[26B] P. Soundarrajan and F. Schweighardt, "Hydrogen Sensing and Detection," in *Hydrogen Fuel*, Taylor & Francis Group, LLC, 2009, pp. 496-518.

[27B] G. J. Li and s. Kawi, "High-surface area SnO2: a novel semiconductor oxide gas sensor," *Materials Letters,* vol. 34, pp. 99-102, 1998.

[28B] J. P. Ahn, J. H. Kim, J. k. Park and M. Y. Huh, "Microstructure and gas-sensing properties of thick film sensor using nanophase SnO2 powder," *Sensors and Actuators B: Chemical,* vol. 99, pp. 18-24, 2004.

[29B] N. Yamazoe and N. Miura, "Some basic aspects of semiconductor gas sensors," in *Chemical Sensor Technology, Volume 4*, vol. 4, Tokyo, Chemical Sensor Technology, 1992, p. 19.

[30B] M. Hayashi, T. Hyodo, Y. Shimizu and M. Egashira, "Effects of microstructure of mesoporous SnO2 powders on their H2 sesing properties," *Sensors and Actuators B: Chemical,* vol. 141, no. 2, pp. 465-470, 2009.

[31B] C. Xu, J. Takaki, N. Miura and N. Yamazoe, "Grain size effects on gas sensitivity of porous SnO2-based elements," *Sensors and Actuators B: Chemical,* vol. 3, pp. 147-155, 1991.

[32B] Y. Shimizu, N. Nakamura and M. Egashira, "Effects of diffusivity of hydrogen and oxygen through pores of thick film SnO2-based sensors on their sensing properties," *Sensors and Actuators B: Chemical,* vol. 13/14, pp. 128-131, 1993.

[33B] Y. Shimizu, T. Maekawa, Y. Nakamura and M. Egashira, "Effects of gas diffusivity and reactivity on sensing properties of thick film SnO2-based sensors," *Sensors and Actuators B: Chemical,* vol. 46, pp. 163-168, 1998.

[34B] N. Yamazoe, G. Sakai and K. Shimanoe, "Oxide semiconductor gas sensors," *Catalysis Surveys form Asia,* vol. 7, no. 1, pp. 63-75, 2003.

[35B] D. Davazoglou and K. Georgouleas, "Low Pressure Chemically Vapor Deposited WO3 Thin Films for Integrated Gas Sensor Applications," *J.Electrochemical Society,* vol. 145, pp. 1346-1350, 1998.

[36B] Y. Shimizu, N. Matsunaga, T. Hyodo and M. Egashira, "Improvement of SO2 sensing properties of WO3 by noble metal loading," *Sensors and Actuators B: Chemical,* vol. 77, pp. 35-40, 2001.

[37B] I. Kim, S. Han, J. Gwak, D. Hong, D. Jakhar, K. Singh and J. Wang, "Development of micro hydrogen gas sensor with SnO2-Ag2O-PtOx composite using MEMs process," *Sensors and Actuators B: Chemical,* vol. 127, no. 2, pp. 441-446, 2007.

[38B] Y. Lee, K. Lee, D. Lee, Y. Jeong, H. Lee and Y. Choa, "Preperation and gas sensitivity of SnO2 nanopowder homogenously doped with Pt nanoparticles," *Current Applied Physics, Nano Korea 2007 Symposium,* vol. 9, no. 1, pp. S79-S81, 2009.

[39B] B. Guo, A. Bermak, P. C. Chan and G. Yan, "Characterization of intergrated in oxide gas sensors with metal additives and ion implantations," *IEEE Sensors Journal,* vol. 8, no. 8, pp. 1397-1398, 2008.

[40B] P. Manjula, L. Satyanarayana, Y. Swarnalatha and S. V. Manorama, "Raman and MASNMR studies to support the mechanisms of low temperature hydrogen sensing by Pd doped mesoporous SnO2," *Sensors and Actuators B: Chemical,* vol. 138, no. 1, pp. 28-34, 2009.

[41B] A. Galdikas, V. Jasutis, S. Kaciulis, G. Mattogno, A. Mironas, V. Olevano, D. Senuliena and A. Setkus, "Peculiarities of Surface Doping with Cu in SnO2 Thin Film Gas Sensors," *Sensors and Actuatros B: Chemical,* vol. 43, pp. 140-146, 1997.

[42B] M. Radecka, K. Zakrzewska and M. Rckas, "Solid Solutions for Gas Sensors," *Sensors and Actuators B : Chemical,* vol. 47, pp. 194-204, 1998.

[43B] U. S. Choi, G. Sakai, K. Shimanoe and N. Yamazoe, "Sensing properties of Au-loaded SnO2–Co3O4 composites to CO and H2," *Sensors and Actuators B: Chemical,* vol. 107, no. 1, pp. 397-401, 2005.

[44B] O. Safonova, T. Neisiua, A. Ryzhikov, B. Chenevier, A. Gaaskov and M. Labeau, "Characterization of the H2 sensing mechanism of Pd-promoted SnO2 by XAS in operando conditions," *Chemical Communications,* pp. 5202-5204, 2005.

[45B] I. P. Matusko, V. K. Yatsimirskii, N. P. Maksimovich, N. V. Nikitina, P. M. Silenko, V. P. Ruchko and V. B. Ishchenko, "Sensitivity to hydrogen of sensor

materials based on SnO2 promoted with 3d metals," *Theoretical and Experimental Chemistry,* vol. 442, no. 2, pp. 128-133, 2008.

[46B] N. Yamazoe, Y. Kurokawa and T. Seiyama, "Effects of additives on semiconductor gas sensors," *Sensors and Actuators,* vol. 174, p. 283–289, 1983.

[47B] R. K. Sharma, P. H. Chan, Z. Tang, G. Yan, I. M. Hsing and J. K. Sin, "Sensitive, Selective and Stable Tin Dioxide Thin-films for Carbon Monoxide and Hydrogen Sensing in Integrated Gas Sensor Array Applications," *Sensors and Actuators B : Chemical,* vol. 72, pp. 160-166, 2001.

[48B] A. Salehi and M. Gholizade, "Gas-sensing properties of indium-doped SnO2 thin films with variations in indium concentration," *Sensors and Actuators B: Chemical,* vol. 89, pp. 173-181, 2003.

[49B] J. Xu, Y. Shun, Q. Pan and J. Qin, "Sensing characteristics of double layer film of ZnO," *Sensors Actuators B: Chemical,* vol. 66, pp. 161-163, 2000.

[50B] M. Franke, U. Simon and T. Koplin, "Metal and Metal Oxide Nanoparticles in Chemiresistors: Does the Nanoscale Matter?," *Small,* vol. 2, no. 1, pp. 36-50, 2006.

[51B] H. Zhang, Z. Li, L. Liu, X. Xu, Z. Wang, W. Wang, W. Zheng, C. Wang and B. Dong, "Enhancement of hydrogen monitoring properties based on Pd-SnO2 composite nanofibers," *Sensors and Actuators B: Chemical,* vol. 147, no. 1, pp. 111-115, 2010.

[52B] R. Huck, U. Bottger, D. Kohl and G. Heiland, "Effects in the Detection of H2 and CH4 by Sputtered SnO2 Films with Pd and PdO Deposites," *Sensors and Actuators B: Chemical,* vol. 17, pp. 355-359, 1989.

[53B] Y. Li, W. Wlodarski, K. Galatsis, S. H. Moslih, J. Cole and S. Russo, "Gas sensing properties of p-type semiconducting Cr-doped TiO2 thin films," *Sensors and Actuators B: Chemical,* vol. 83, no. 1-3, pp. 160-163, 2002.

[54B] C. Wildfire, E. Çiftyürek, K. Sabolsky and E. M. Sabolsky, "Fabrication and Testing of High-Temperature Nano-Derived Resistive-Type Microsensors for Hydrogen Sensing," *Journal of The Electrochemical Society,* vol. 161, no. 2, pp. B3094-B3102, 2014.

[55B] S. M. Kanan, O. M. El-Kadri, I. A. Abu-Yousef and M. C. Kanan, "Semiconducting metal oxide based sensors for selective gas pollutant detection," *Sensors,* vol. 9, no. doi:10.3390/s91008158, pp. 8159-8196, 2009.

[56B] D. L. West, F. C. Montgomery and B. L. Armstrong, "Compact, DC-electrical biased sulfur dioxide sensing elements for use at high," *Sensors and Actuators B : Chemical,* vol. 162, pp. 409-417, 2012.

[57B] D. Shin, T. M. Besmann and B. L. Armstrong, "Phase stability of noble metal loaded WO3 for SO2," *Sensors and Actuators B,* 2012.

[58B] D. Morris and R. G. Egdell, "Application of V-doped TiO2 as a sensor for detection of SO2," *Journal of Materials Chemistry,* vol. 11, pp. 3207-3210, 2001.

[59B] X. Liang, T. Zhong, B. Quan, B. Wang and H. Guan, "Solid-state potentiometric SO2 sensor combining NASICON with V2O5-doped TiO2 electrode," *Sensors and Actuators B : Chemical,* vol. 134, pp. 25-30, 2008.

[60B] E. B. Varhegyi, J. Gerblinger, F. Reti, I. V. Perczel and H. Meixner, "Study of the behaviour of Ce02 in S02-containing environment," *Sensors and Actuators B: Chemical,* Vols. 24-25, pp. 631-635, 1995.

[61B] A. Neubecker, T. Pompl, T. Doll, W. Hansch and I. Eisele, "Ozone Enhanced Molecular Beam Deposition of Nickel Oxide (NiO) for Sensor Applications," *Thin Solid Films,* vol. 310, pp. 19-23, 1197.

[62B] C. Fujimoto, Y. Hayakawa and A. Ono, "Evaluation of the efficiency of deodorants by semiconductor gas sensors," *Sensors and Actuators B : Chemical,* pp. 191-194, 1996.

[63B] S. C. Lee, B. W. Hwang, S. J. Lee, H. Y. Choi, S. Y. Kim, S. Y. Jung, D. Ragupathy and D. D. Lee, "A novel tin oxide-based recoverable thick film SO2 gas sensor promoted with magnesium and vanadium oxides," *Sensors and Actuators B: Chemical,* vol. 160, no. 1, pp. 1328-1334, 2011.

[64B] D. Girardin, F. Berger, A. Chambaudet and R. Planade, "Modelling of SO2 detection by tin dioxide gas sensor," *Sensors and Actuators B: Chemical,* vol. 43, p. 147–153, 1997.

[65B] F. Berger, M. Fromm, A. Chambaudet and R. Planade, "Tin dioxide-based gas sensors for SO2 Detection," *Sensor and Actuators B,* vol. 45, pp. 175-181, 1997.

[66B] N. Bukun, A. Vinokurov, M. Vinokurova, L. Derlyukova, Y. Dobrovolsky and A. Levchenko, "Chemisorption and electrochemical reactions of SO2 on modified SnO2 elctrodes," *Sensors and Actuators B: Chemical,* vol. 106, pp. 153-157, 2005.

[67B] M. Egashira , Y. Shimizu and Y. Takao, "Trimethylamine Sensor based on Semiconductive Metal Oxides for Detection of Fish Freshness,," *Sensors and Actuators B : Chemical,* vol. 1, pp. 108-112, 1990.

[68B] T. Akamatsu, T. Itoh, N. Izu and W. Shin, "NO and NO2 Sensing Properties of WO3 and Co3O4 Based Gas Sensors," *Sensors,* vol. 13, pp. 12467-12481, 2013.

[69B] J. Leng, X. Xu, N. Lv, H. Fan and T. Zhang, "Synthesis and gas-sensing characteristics of WO3 nanofibers via electrospinning," *Journal of Colloid and Interface Science,* vol. 356, pp. 54-57, 2011.

[70B] N. Izu, G. Hagen, D. Schonauer, U. Roder-Roith and R. Moos, "Application of V2O5, WO3, TiO2 for Resistive-Type SO2 Sensors," *Sensors,* vol. 11, pp. 2982-2991, 2011.

[71B] M. Stankova, X. Vilanova, J. Calderer, E. Llobet, P. Ivanov, I. Gracia, C. Cane and X. Correig, "Detection of SO2 and H2S in CO2 stream by means of WO3-based micro-hotplate sensors," *Sensors and Actuators B: Chemical,* vol. 102, pp. 219-225, 2004.

[72B] S. Dongwon, T. M. Bessman and B. L. Armstrong, "Phase stability of noble metal loaded WO3 for SO2," *Sensors and Actuators B : Chemical,* vol. 176, pp. 75-80, 2013.

[73B] C. Imawan, H. Steffes, F. Solzbacher and E. Obermeier, "A new preparation method for sputtered MoO3 multilayers for the application in gas sensors," *Sensors and Actuators B: Chemical,* vol. 78, no. 1-3, pp. 119-125, 2001.

[74B] C. Imawan, H. Steffes, F. Solzbacher and E. Obermeir, "Structural and gas-sensing properties of V2O5-MoO3 thin films for H2 detection," *Sensor and Actuators B: Chemical,* vol. 77, no. 1-2, pp. 346-351, 2001.

[75B] M. Ferroni, V. Guidi, G. Martinelli, P. Nelli, M. Sacerdoti and G. Sberveglieri, "Characterization of a molybdenum oxide sputtered thin film as a gas sensor," *Thin Solid Films,* vol. 307, no. 1-2, pp. 148-151, 1997.

[76B] K. Galatsis, Y. X. Li, W. Wlodarski, E. Comini, G. Faglia and G. Sberveglieri, "Semiconductor MoO3–TiO2 thin film gas sensors," *Sensors and Actuators B: Chemical,* vol. 77, no. 1-2, pp. 472-477, 2001.

[77B] A. K. Prasad and P. I. Gouma, "MoO3 and WO3 based thin film conductimetric sensors for automotive applications," *Journal of Material Science,* vol. 38, no. 21, pp. 4347-4352, 2003.

[78B] J. F. Currie, A. Essalik and J. C. Marusic, "Micromachined thin film solid state electrochemical CO2 , NO2 and SO2," *Sensors and Actuators B: Chemical,* vol. 59, no. 2-3, pp. 235-241, 1999.

[79B] C. H. Foulkes, "GAS!" The Story of the Special Brigade, N&M Press, 2001.

[80B] S. K. Pandey, K. H. Kim and K. T. Tang, "A review of sensor-based methods for monitoring hydrogen sulfide," *Trends in Analytical Chemistry,* vol. 32, pp. 87-99, 2012.

[81B] G. Fang, Z. Liu, C. Liu and K. Yao, "Room Temperature H2S Sensing Properties and Mechanism of CeO2-SnO2 Sol-gel Thin Films," *Sensors and Actuators B: Chemical,* vol. 66, no. 1-3, pp. 46-48, 2000.

[82B] S. C. Lee, S. Y. Kim, B. W. Hwang, S. Y. Jung, D. Ragupathy, I. S. Son, D. D. Lee and J. C. Kim, "Improvement of H2S Sensing Properties of SnO2-Based Thick Film Gas Sensors Promoted with MoO3 and NiO," *Sensors,* vol. 13, pp. 3889-3901, 2013.

[83B] Z. Sun, H. Yuan, Z. Liu, B. Han and X. Zhang, "A Highly Efficient Chemical Sensor Material for H2S: Fe2O3 Nanotubes Fabricated Using Carbon Nanotube Templates," *Advanced Materials ,* vol. 17, pp. 2993-2997, 2005.

[84] D. H. Dawson, G. S. Henshaw and D. E. Williams, "Description and characterization of a hydrogen sulfide gas sensor based on Cr2-yTiyO3+x," *Sensor and Actuators B: Chemical,* Vols. 26-27, pp. 76-80, 1995.

[85B] E. P. Barret, G. C. Georgiades and P. A. Sermon, "The mechanism of operation of WO3-based H2S sensors," *Sensors and Actuators B: Chemical,* vol. 1, pp. 116-120, 1990.

[86B] B. Fruhberger, M. Grunze and D. J. Dwyer, "Surface chemistry of H2S sensitive tungsten oxide films," *Sensors and Actuators B: Chemical,* vol. 31, pp. 167-174, 1995.

[87B] R. M. Ferrizz, R. J. Gorte and J. M. Vohs, "TPD and XPS investigation of the interaction of SO2 with model ceria catalysts," *Catalysis Letters,* vol. 82, no. 1-2, pp. 123-129, 2002.

[88B] B. J. Lindberg, K. Hamrin, G. Johansson, U. Gelius, C. Nordling and K. Siegbahn, "Molecular Spectroscopy by Means of ESCA II. Sulfur compounds. Correlation of electron binding energy with structure," *Phys. Scripta 1,* vol. 286, 1970.

[89B] C. D. Wagner and J. A. Taylor, "Contributions to screening in the solid state by electron systems of remote atoms: Effects to photoelectron and Auger transitions," *J. Electron Spectrosc. Relat. Phenom.,* vol. 28, p. 211, 1982.

[90B] M. D. Antonik, J. E. Schneider, E. L. Wittman, K. Snow, J. F. Vetelino and R. J. Lad, "Microstructural effects in WO3 gas sensing films," *Thin Solid Films,* vol. 256, no. 1-2, pp. 247-252, 1995.

[91B] X. Niu, W. Du and W. Du, "Preparation, characterization and gas-sensing properties of rare earth mixed oxides," *Sensors and Actuators B: Chemical,* vol. 99, p. 399–404, 2004.

[92B] C. Liewhiran, N. Tamaekong, A. Wisitsora and S. Phanichphant, "The Monitoring of H2S and SO2 Noxious Gases from Industrial Environment with Sensors Based on Flame-spray-made SnO2 Nanoparticles," *Engineering Journal,* vol. 16, no. 3, pp. 123-134, 2012.

[93B] C. V. Gopal, S. V. Reddy, S. V. Manorama and V. J. Rao, "Preparation and Characterization of Ferrites as Gas Sensor Materials," *Journal of Material Science Letter,* vol. 19, no. 9, pp. 775-778, 200.

[94B] G. N. Chaudhari, M. A. Alvi, H. G. Wankhadea, A. B. Bodade and S. V. Manorama, "Nanocrystalline chemically modified CdIn2O4 thick films for H2S gas sensor," *Thin Solid Films,* vol. 520, no. 11, p. 4057–4062, 2012.

[95B] S. V. Jagtab, V. Kadu A, V. S. Sangawar, s. V. Manorama and G. N. Chaudhari, "H2S sensing characteristics of La0.7Pb0.3Fe0.4Ni0.6O3 based nanocrystalline thick film gas sensor," *Sensors and Actuators B: Chemical,* vol. 131, no. 1, pp. 290-294, 2008.

[96B] U. Kersen and L. Holappa, "Surface Characterization and H2S sensing potential of iron molybdate particles produced by supercritical solvothermal method and subsequent oxidation," *Appl. Phys. A ,* vol. 85, pp. 431-436, 2006.

[97B] E. P. Schneeberg, "Sulfur Fugacity Measurements with the Electrochemical Cell AgAgIAg (sub 2+x) S,f s," *Economic Geology,* vol. 68, pp. 507-517, 1973.

[98B] J. Vangrunderbeek, F. Vandecruys and R. V. Kumar, "Sensing Mechanism of high temperature hydrogen sulphide sensor based on sodium ß-alumina," *Sensors and Actuators B : Chemical,* vol. 56, pp. 129-135, 1999.

[99B] R. S. Falconer, I. F. Vetelino, D. J. Smith and M. J. Osborn, "An Activation Process for Increased Sensitivity of a SAW Gas Microsensor," *IEEE Ultrasonic Sympososium,* 1990.

[100B] W. Luo, q. Fu, D. Zhou, J. Deng, H. Liu and G. Yan, "A surface acoustic wave H2S gas sensor employing nanocrystalline SnO2 thin film," *Sensors and Actuators B: Chemical,* vol. 176, pp. 746-752, 2013.

[101B] G. N. Chaudhari, D. R. Bambole, A. B. Bodade and P. R. Padole, "Characterization of nanosized TiO2 H2S gas sensor," *J. Mater. Sci. ,* vol. 41, pp. 4860-4864, 2006.

[102B] M. D. Shirsat, M. A. Bangar, M. A. Deshusses, N. V. Myung and A. Mulchandani, "Polyaniline nanowires-gold nanoparticles hybrid network based chemiresistive hydrogen sulfide sensor," *Appl. Phys. Lett.,* vol. 94, 2009.

[103B] J. K. Howard and K. V. Srikrishnan, "Thin film capacitor with a dual bottom electrode structure". U.S. Patent, Patent 4 423 087, 27 Dec. 1981.

[104B] S. L. Firebaugh, K. F. Jensen and M. A. Schmidt, "Investigation of high-temperature degradation of platinum thin films with an in situ resistance measurement apparatus," *J. of Microelectromech. Syst., .,* vol. 7, pp. 128-135, 1998.

[105B] D. Briand, F. Beaudin, N. F. de Rooij, R. Desplats and P. Perdu, "Failure analysis of micro-heating elements suspended on thin membranes," *Microelectron. Reliab.,* vol. 45, no. 9-11, p. 1786–1789, 2005.

[106B] M. P. da Cunha, T. Moonlight, R. Lad, D. Frankel and G. Bernhardt, "High Temperature Sensing Technology for Applications Up To 1000°C," in *IEEE SENSORS Conference*, Lecce, 2008.

[107B] S. V. Patel, M. di Battista, J. L. Gland and J. W. Schwank, "Survivability of a silicon-based microelectronic gas-detector structure for high-temperature flow applications," *Sensors and Actuators B: Chemical,* vol. 37, pp. 27-35, 1996.

[108B] S. P. Beeby, A. Blackburn and N. M. White, *J. Micromech. Microeng.,* vol. 9, pp. 218-229, 1999.

[109B] M. N. Hamidon, V. Skarda, N. M. White, F. Krispel, P. Krempl, M. Binhack and W. Buff, "Fabrication of high temperature surface acoustic wave devices for sensor applications," *Sens. Actuator A: Phys,* Vols. 123-124, pp. 403-407, Sep. 2005.

[110B] C. Y. Lee, S. J. Lee and C. L. Hsieh, *Proc. NEMS-IEEE International Conference,* pp. 434-437, 2007.

[111B] S. A. Wright and Y. B. Gianchandani, "Discharge-Based Pressure Sensors for High Temperature Applications Using Three-Dimensional and Planar Microstructures," *in Proc. MEMS, IEEE 20th International Conference,* pp. 115-118, 2007.

[112B] L. C. Martin and R. Holanda, "NASA Technical Memorandum, NASA-IM-106714," National Aeronautics and Space Administration, Cleveland, Ohio, 1994.

[113B] J. D. Wrbanek and K. H. Laster, "NASA/TM-2005-213433,," National Aeronautics and Space Administration, Cleveland, Ohio, Jan. 2005.

[114B] D. Bonfert, H. Gieser, K. Bock, P. Svasta and C. Ionescu, *In Proc. SIITME-IEEE,* pp. 83-88, 2010.

[115B] J.-F. Lei, C. L. Martin and H. A. Will, "NASA Technical Memorandum 107418," National Aeronautics and Space Administration, Lewis Res. Center, Cleveland, Ohio, Jun. 1997.

[116B] R. C. Budhani, S. Prakash, H. J. Doerr and R. F. Bunshah, "Thin-film temperature sensors for gas turbine engines: Problems and prospects," *J. Vac. Sci. Technol., A 4,* vol. 6, p. 3023–3024, Nov/Dec. 1986.

[117B] M. Sreemany, S. Sen, M. Sreemany and S. Sen, *Appl. Surf. Sci,* vol. 253, pp. 2739-2746, Dec. 2006.

[118B] C. C. Mardare, E. Joanni, A. Mardera, J. R. Fernandes, C. M. De sa and P. B. Traves, "Effects of adhesion layer (Ti or Zr) and Pt deposition temperature on the properties of PZT thin films deposited by RF magnetron sputtering," *Appl. Surf. Sci,* vol. 243, pp. 113-124, 2005.

[119B] J. Puigcorbe, D. Vogel, B. Michel, A. Vila, I. Gracia, C. Cane and J. R. Morante, "Thermal and mechanical analysis of micromachined gas sensors," *J. Micromech. Microeng.,* vol. 13, pp. 548-556, 2003.

[120B] H. Esch, G. Huyberechts, G. Maes, J. manca and W. d. Ceuninck, "The stability of Pt heater and temperature sensing elements for silicon integrated tin oxide gas sensors," *Sensors and Actuators B: Chemical,* vol. 65, pp. 190-192, 2000.

[121B] H. C. Kim, N. D. Theodore and T. L. Alford, "Comparison of texture evolution in Ag and Ag(Al) alloy thin films on amorphous SiO2," *J. Appl. Phys,* pp. 5180-5188, May 2004.

[122B] K. Sieraddzki, K. Bailey and T. L. Alford, "Agglomeration and percolation conductivity," *Appl. Phys. Lett.,* vol. 79, pp. 3401-3403, Nov. 2001..

[123B] D. J. Srolovitz and M. G. Goldiner, "The thermodynamics and kinetics of film agglomeration," *JOM-J. Miner. Met. Mater. Soc,* vol. 47, pp. 31-36, Mar. 1995.

[124B] K. Sreenivas, I. Reaney, T. Maeder, N. Setter, C. Jagadish and R. G. Elliman, "Investigation of Pt/Ti bilayer metallization on silicon for ferroelectric thin film integration," *J. Appl. Phys.,* vol. 75, pp. 232-239, 1993.

[125B] K. F. McCarty, J. C. Hamilton, Y. S. Angela, S. R. Stumpf, J. Figuera, K. Thurmer, F. Jones, A. K. Schmid, A. A. Talin and N. C. bartelt, "How metal films de-wet substrates—identifying the kinetic pathways and energetic driving forces," *New J. Phys.,* vol. 11, April 2009.

[126B] C. Dong, J. W. Ha, H. M. Kim, S. D. Lee, Y. D. Park, J. H. Woo and E. J. Yoon, "Method for depositing a platinum layer on a silicon wafer". U.S. Patent Patent 5.736,422, 7 April 1998.

[127B] R. M. Tiggelaar, R. P. Sanders, A. W. Groenland and J. G. Gardeniers, "Stability of thin platinum films implemented in high-temperature microdevices," *Sens. Actuator A: Physical,* vol. 152, pp. 39-47, May 2009.

[128B] T. Maeder, L. Sagalowicz and P. Muralt, "Stabilized Platinum Electrodes for Ferroelectric Film Deposition using Ti, Ta and Zr Adhesion Layers," *Jpn. J. Appl. Phys.,* vol. 37, pp. 2007-2012, 1998.

[129B] M. P. d. Cunha, T. Moonlight, R. Lad, G. Bernhardt and D. J. Frankel, "“Enabling Very High Temperature Acoustic Wave Devices for Sensor & Frequency Control Applications," in *IEEE 2007 International Ultrasonics Symposium Proceedings*, New YorK, 2007.

[130B] G. L. Selman, J. G. Day and A. A. Bourne, "Dispersion Strengthened Platinum," *Platinum Metals Rev,* vol. 18, pp. 46-57, 1974.

[131B] R. B. McGrath and G. C. Badcock, "New Dispersion Strengthened Platinum Alloy," *Platinum Metals Rev.,* vol. 31, no. 1, pp. 8-11, 1987.

[132B] D. J. Frankel, G. P. Bernhardt, B. T. Sturtevant, T. Moonlight, M. P. Cunha and R. J. Lad, "Stable Electrodes and Ultrathin Passivation Coatings for High Temperature Sensors in Harsh Environments," in *Sensors, IEEE*, Lecce, 2008.

[133B] L. J. van der Pauw, "A method of measuring specific resistivity and Hall effect of discs of arbitrary shape," Philip Res. Rep. , Eindhoven, Netherlands, Feb. 1958..

[134B] T. C. Tsone and J. Drobek, "Diffusion in Thin Film Ti–Au, Ti–Pd, and Ti–Pt Couples," *J. Vac. Sci. Technol.,* vol. 9, pp. 271-275, July 1972.

[135B] J. F. Moulder, W. F. Stickle, P. E. Sobol and K. D. Bomben, Handbook of X-Ray Photoelectron Spectroscopy, Chigasaki, Japan: ULVAC-PHI. Inc., 1992-1995.

[136B] P. Ficalora, J. Wu, V. Srikrishnan and J. Carloni, "Department of the Navy," Naval Ordnance Systems Command, Washington, D.C., Mar. 1971..

[137B] L. M. Pecora and P. J. Ficalora, "Some bulk and thin film properties of ZrPt3 and HfPt3," *J. Elec. Mat.,,* vol. 6, pp. 531-540, Feb. 1977..

[138B] E. Çiftyürek, K. Sabolsky and E. M. Sabolsky, "Platinum thin film electrodes for high-temperature chemical sensor applications," *Sensors and Actuators B:Chemical,* vol. 181, p. 702–714, 2013.

[139B] J. Puigcorbe, D. Vogel, B. Michael, A. Vila, I. Gracia, C. Cane and J. R. Morante, "High temperature degradation of Pt/Ti electrodes in micro-hotplate gas sensors," *Journal of Micromechanics and Microengineering,* p. 119–124, 13 (June) (2003.

[140B] J. Courbat, D. Briand and N. F. de Rooij, "Reliability improvement of suspended platinum-based micro-heating elements," *Sensors and Actuators A: Physical,* vol. 142, pp. 284-291, 2008.

[141B] T. Ryll, H. Galinski, L. Schlagenhauf, P. Elser, J. L. Rupp, A. Bieberle-Hutter and L. J. Gauckler, "Thin-Film Electrodes: Microscopic and Nanoscopic Three-Phase-Boundaries of Platinum Thin Film Electrodes on YSZ Electrolyte," *Advanced Functional materials,* vol. 21, no. 3, pp. 565-572, 2011.

[142B] M. Ohring, Material Science of Thin Films, ISBN: 978-0-12-524975-1,.

[143B] G. K. Wertheim and D. N. Buchanan, "Charge transfer in intermetallics: HfPt3," *Physical Review B,* vol. 40, p. 5319–5324., 1989.

[144B] U. Seidel and H. Schmid, "Effect of high temperature annealing on the electrical performance of titanium/platinum thin film," *Thin Solid Films,* vol. 516, pp. 898-906, 2008.

[145B] W. l. Worrell and P. J. Meschter, *Met. Trans. A.,* vol. 8A, pp. 503-509, Mar. 1977.

[146B] P. M. Georgea, M. D. Alvey and R. F. Fisher, *J. Vac. Sci. Technol. A,* vol. 10, pp. 2253-2260, 1991.

[147B] J. M. Lee, S. K. Hong, C. S. Hwang and H. J. Kim, *Journal of the Korean Physical Society,* vol. 33, pp. 148-151, 1998.

[148B] J. B. Goodenough, "Perspective on Engineering Transition-Metal Oxides," *Chemistry of Materials,* vol. 26, pp. 820-829, 20136.

[149B] R. Marschall and L. Wang, "Non-metal doping of transition metal oxides for visible-light photocatalysis," *Catalysis Today,* vol. 225, pp. 111-135, 2014.

[150B] H. Zhenk, J. Z. Ou, M. S. Strona, R. B. Kaner, A. Mitchell and K. Kalantar-zadeh, "Nanostructured Tungsten Oxide properties, Synthesis, and Applications," *Advanced Functional Materials,* vol. 21, pp. 2175-2196, 2011.

[151B] W. T. Yao and S. H. Yu, "Recent advances in hydrothermal synthesis of low dimensional nanoarchitectures," *International Journal of Nanotechnology,* vol. 4, no. 1/2, pp. 129-141, 2007.

[152B] S. Walia, S. Balendhran, H. NILI, S. Zhuiykov, G. Rosengarten, Q. H. Wang, M. Bhaskaran, S. Sriram, M. S. Strano and K. Kalantar-zadeh, "Transition metal oxides – Thermoelectric," *Progress in Materials Science,* vol. 58, pp. 1443-1489, 2013.

[153B] X. Li, Z. Song and B. Qu, "Shape-controlled electrochemical synthesis of SrWO4 crystallites and their optical properties," *Ceramics International,* vol. 40, no. 1, pp. 1205-1208, 2013.

[154B] A. Kuzmin, A. Kalinko and R. A. Evarestov, "First principles LCAO study of phonons in NiWO4," *Central Europian Journal of Physics,* vol. 9, no. 2, pp. 502-509, 2011.

[155B] G. S. Rohrer, Structure and Bonding in Crysatlline Materials, Cambridge: Cambridge University Press, 2004.

[156B] B. Y. Zhang, A. W. Holzwarth and R. T. Williams, "Electronic band structures of the scheelite materials CaMoO4, CaWO4, PbMoO4, and PbWO4," *PHYSICAL REVIEW B ,* vol. 50, no. 20, pp. 57-69, 1998.

[157B] B. J. Macey, "Crystal Chemistry of MTO4 Compounds with the Zircon, Scheelite and Monazite Structure Types," Virginia Polytechnique Institute and State University, Blacksburg, 1995.

[158B] Z. Shan, Y. Wang, D. H. and F. Huang, "Structure-dependent photocatalytic activities of MWO4 (M = Ca, Sr, Ba)," *Journal of Molecular Catalysis A: Chemical,* vol. 302, no. 1-3, pp. 54-58, 2009.

[159B] F. a. Rabuffetti, S. P. Culver, L. Suescun and R. L. Brutchey, "Structural Disorder in AMoO4 (A = Ca, Sr, Ba) Scheelite Nanocrystals," *Inorganic Chemistry,* vol. 53, pp. 1056-1061, 2013.

[160B] W. Oganowskil, J. Hanuza, B. Jezowska, J. Trzebiatowska and J. Wrzyszcz, "Physicochemical properties and structure of MgMoO4-MoO3 catalysis," *Journal of catalysis,* vol. 39, no. 2, pp. 161-172, 1975.

[161B] Y. Hu, Z. Gao, W. Sun and X. Liu, "Anisotropic surface energies and adsorption behaviors of scheelite crystal," *Colloids and Surfaces A: Physicochemical and Engineering Aspects,* vol. 415, pp. 439-448, 2012.

[162B] E. Alan and N. Greenwood, Chemistry of the Elements, 2nd ed., Butterworth-Heinemann, 1997.

[163B] D. A. Spasskii, V. N. Kolobanov, V. V. Mikhailin, L. Y. Berezovskaya, L. I. Ivleva and I. S. Voronina, "Luminescence peculiarities and optical properties of MgMoO4 and MgMoO4:Yb crystals," *Optics and Spectroscopy,* vol. 106, no. 4, pp. 556-563, 2009 , V. N. Kolobanov, V. V. Mikhaĭlin, L. Yu. Berezovskaya, L. I. Ivleva, I. S. Voronina.

[164B] L. Zhou, W. wang, H. Xu and S. Sun, "Template-Free Fabrication of CdMoO4 Hollow Spheres and Their Morphology-Dependent Photocatalytic Property," *Crystal Growth Design,* vol. 8, no. 10, pp. 3595-3601, 2008.

[165B] L. Tang, J. Zhai, H. Zhang and X. Yao, "Microwave dielectric properties of tunable Ba0.5Sr0.5TiO3 and scheelite AMoO4 (A = Ba, Sr) composite ceramics," *Journal of Alloys and Compounds,* vol. 551, pp. 556-561, 2013.

[166B] E. M. Sabolsky, P. Gansor, E. Çiftyürek, K. Sabolsky, C. Xu and J. W. Zondlo, "In-situ formation of a solid oxide fuel cell cermet anode by NiWO4 reduction," *Journal of Power Sources,* 2013.

[167B] M. V. Reddy, G. V. Subba and B. R. Chowdari, "Metal Oxides and Oxysalts as Anode Materials for Li Ion Batteries," *Chemical Rewievs,* vol. 113, no. 7, p. 5364–5457, 2013.

[168B] E. Lassner, W. D. Schuber, E. Lüderitz and H. U. Wolf, "Tungsten, Tungsten Alloys, and Tungsten Compounds," *Ullmann's Encyclopedia of Industrial Chemistry,* 2000.

[169B] S. P. Culver, F. A. Rabuffetti, S. Zhou, M. Mecklenburg, Y. Song, B. C. Melot and R. L. Brutchey, "Low-Temperature Synthesis of AMoO4 (A = Ca, Sr, Ba) Scheelite Nanocrystals," *Chemistry of Materials ,* vol. 25, p. 4129−4134, 2013.

[170B] C. L. Wu, C. K. Waang, C. Lin, S. Wang and J. Huang, "Electrochromic properties of nanostructured tungsten oxide films prepared by surfactant-assisted sol–gel process," *Surface & Coatings Technology,* vol. 231, pp. 403-407, 2013.

[171B] C. S. Cundy and P. A. Cox, "The hydrothermal synthesis of zeolites: Precursors, intermediates and reaction mechanism," *Microporous and Mesoporous Materials,* vol. 82, no. 1-2, pp. 1-78, 2005.

[172B] K. Byrappa and M. Yoshimura, Handbook of Hydrothermal Technology, A Technology for Crystal Growth and Materials Processing, Norwich, NY: William Andrew Publishing, 2001.

[173B] W. J. Dawson and R. J. Riman, "Hydrothermal synthesis of advanced ceramic powders," *Advances in Science and Technology,* vol. 45, pp. 184-193, 2006.

[174B] L. I. Stepenova, L. S. Ivashkevich and G. A. Branitskii, "Hydrothermal Synthesis of Tungsten and Molybdenum Mixed Oxides," *Russian Journal of Inorganic Chemistry,* vol. 54, no. 10, pp. 1553-1558, 2009.

[175B] X. Xing, Q. Xing, R. Yu, J. Meng, J. Chen and G. Liu, "Hydrothermal synthesis of ZrW2O8 nanorods," *Physica B,* vol. 371, pp. 81-82, 2006.

[176B] S. Wannapop, T. Thongtem and S. Thongtem, "Characterization of Donut-Like SrMoO4 Produced by Microwave Hydrothermal Process," National Reserach Univeristy of Thailand, 2012.

[177B] C. J. Mao, J. Geng, X. C. Wu and J. J. Zhu, "Selective synthesis and luminescence properties of self assembled SrMoO4 superstructures via a facile sonochemical Route," *J. Phys. Chem.,* vol. 114, pp. 1982-1988, 2010.

[178B] Y. Mi, Z. Huang, F. Hu, Y. Li and J. Jiang, "Room-Temperature Synthesis and Luminescent Properties of Single-Crystalline SrMoO4 Nanoplates," *J. Phys. Chem.,* vol. 113, pp. 20795-20799, 2009.

[179B] J. P. Liu, X. T. Huang, Y. Y. Li and Z. K. Li, *J. Mater.Chem.,* vol. 17, p. 2754, 2007.

[180B] X. tang, X. Zhu, J. Dai, J. Yang, L. Hu, L. Chen, X. Zhu, X. Li, H. Jiang, R. Zhang and Y. Sun, "c-Axis oriented SrMoO4 thin films by chemical solution deposition: Self-assembled orientation, grain growth and photoluminescence properties," *Acta Materialia,* vol. 65, pp. 287-294, 2014.

[181B] Z. Liu, M. Miyauchi, T. Yamazaki and Y. Shen, "Facile synthesis and NO2 gas sensing of tungsten oxide nanorods assembled microspheres," *Sensors and Actuators B: Chemical,* vol. 140, pp. 514-519, 2009.

[182B] M. Amberg, J. R. Gunter and H. Schmalle, "Preparation, crystal structure, and luminescence of magnesium molybdate and tungstate monohydrates, MgMoO4 · H2O and MgWO4 · H2O," *Journal of Solid State Chemistry,* vol. 77, pp. 162-169, 1988.

[183B] J. Liu, X. Huang, Y. Li and Z. Li, "A general route to thickness-tunable multilayered sheets of sheelite-type metal molybdate and their self-assembled films," *Journal of Materials Chemistry,* vol. 17, pp. 2754-2758, 2007.

[184B] J. C. Sczancoski, L. S. Cavalcante, M. R. Joya, J. A. Varela, P. S. Pizani and E. Longo, "SrMoO4 powders processed in microwave-hydrothermal: Synthesis, characterization and optical properties," *Chemical Engineering Journal,* vol. 140, pp. 632-637, 2008.

[185B] W. Hirschwald, in *In Current Topics In Material Science*, vol. 7, 1981, p. 143.

[186B] Y. Abraham, N. A. Holzwarth, R. T. Williams and G. E. Matthews, "The electronic structure of oxygen related defects in PbWo4 and CaMoO4 crystals," *Physical Review B,* vol. 64, 2001.

[187B] T. Esaka, "Oxide Ion Conduction via Interstitial Sites in the Substituted Scheelite and Spinel-type Oxides," *Electrochemistry,* vol. 78, no. 1, pp. 16-22, 2009.

[188B] W. Chen, C. S. Chen and L. Winnubst, "Ta doped SrCo0.8Fe0.2O3-x membrans Phase Stability and oxygen permeation in CO2 atmosphere," *Solid state Ionics,* vol. 196, pp. 30-33, 2011.

[189B] Q. Zeng, Y. B. Zuo, C. G. Fan and C. S. Chen, "CO2 tolerant oxygen seperation membrans targeting Co2 capture application," *Journal of membrane Science,* vol. 335, pp. 140-144, 2009.

[190B] L. Z. Pei, Y. K. Xie, Y. Q. Pei and C. Z. Yuan, "Synthesis and formation process of zirconium dioxide," *Material Science Poland,* vol. 31, no. 2, pp. 186-192, 2013.

[191B] T. Kinoshita, M. Senna, Y. Doshida and H. Kishi, "Synthesis of size controlled phase pure KNbO3 fine particles via a solid-state route from a core-shell structured precursor," *Ceramics International,* vol. 38, pp. 1897-1904, 2012.

[192B] A. L. Tiano, C. Koenigsmann, A. C. Santullia and S. S. Wong, "Solution-based synthetic strategies for one-dimensional metal-containing nanostructures," *Chemical Communications,* vol. 46, pp. 8093-8130, 2010.

[193B] E. Formo, M. S. Yavuz, E. P. Lee, L. Lane and Y. Xia, "Functionalization of electrospun ceramic nanofibre membranes with noble-metal nanostructures for

catalytic applications," *Journal of Materials Chemistry,* vol. 19, no. 23, pp. 3878-3882, 2009.

[194B] H. Ogihara, M. Sadakane, Y. Nodasaka and W. Ueda, "Shape-controlled synthesis of ZrO2, Al2O3, and SiO2 nanotubes using carbon nanofibers as templates," *Chemistry of Materials,* vol. 18, no. 21, 2006.

[195B] A. A. Al-Ghamdi, F. Al-Hazmi, F. Alnowaiser, R. M. Al-Tuwirqi, A. A. Al-Ghamdi, A. O. Alhartomy, F. El-Tantawy and F. Yakuphanoglu, "A new facile synthesis of ultra fine magnesium oxide nanowires and optical properties," *Journal of J Electroceramics,* vol. 29, pp. 198-203, 2012.

[196B] A. Kato, S. Oishi, T. Shishido, M. Yamazaki and S. Lida, "Evaluation of stoichiometric rare-earth molybdate and tungstate compounds as laser materials," *Journal of Physics and Chemistry of Solids,* vol. 66, no. 11, pp. 2079-2081, 2005.

[197B] R. Adhikari, G. Gyawali, H. T. Kim, T. Sekino and W. S. Lee, "Synthesis of Er3þ loaded barium molybdate nanoparticles: A new approach for harvesting solar energy," *Materials Letters,* vol. 91, p. 294–297, 2013.

[198B] J. Kubo and W. Ueda, "Catalytic behavior of AMoOx (A = Ba, Sr) in oxidation of 2-propanol," *Materials Research Bulletin,* vol. 44, no. 4, pp. 906-912, 2009.

[199B] D. Logvinovich, R. Aguiar, R. Robert, M. Trottmann, S. G. Ebbinghaus, A. Reller and A. Weidenkaff, "Synthesis, Mo-valence state, thermal stability and thermoelectric properties of SrMoO3-xNx (x>1) oxynitride perovskites," *Journal of Solid State Chemistry,* vol. 180, pp. 2649-2654, 2007.

[200B] H. H. Wang, D. F. Cui, Y. L. Zhou, Z. H. Chen, F. Chen , T. Zhao, H. B. Lu, G. Z. Yang, M. C. Xu, Y. C. Lan, X. L. Chen, H. J. Qian and F. Q. Liu, "Growth and characterization of SrMoO3 thin films," *Journal of Crystal Growth,* vol. 226, pp. 261-266, 2001.

[201B] D. Y. Kim, J. S. Kim, B. H. Park, J. K. Lee, J. H. Kim, H. J. Lee, J. Chang, H. J. Kim, I. Kim and Y. D. Park, "SrFeO3 nanoparticles dispersed SrMoO4 insulating thin films deposited from Sr2FeMoO5 target in oxygen atmosphere," *Applied Physics Letters,* vol. 84, no. 24, 2004.

[202B] I. Nagai, S. Ikeda, N. Shirakawa, R. Iwasaki, H. Nishimura and M. Kosaka, "Highest conductivity oxide SrMoO 3 grown by a floating-zone method under ultralow oxygen partial pressure," *Applied Physics Letters,* vol. 87, 2005.

[203B] J. A. Rodriguez, "Electronic and chemical properties of mixed-metal oxides: basic principles for the design of DeNOx and DeSOx catalysts," *Catalysis Today,* vol. 85, no. 2-4, pp. 177-192, 2003.

[204B] D. L. Perry, Handbook of Inorganic Compounds, CRC Press, 2010.

[205B] N. W. Hurst, S. J. Gentry and A. Jones, "Temperature Programmed Rduction," *Catalysis Reviews,* vol. 24, no. 2, pp. 233-309, 1982.

[206B] J. Guo, L. Zhou, H. Wang, T. Shao, Z. M. Qi and X. Yao, "Infrared spectra, Raman spectra, microwave dielectric properties and simulation for effective permittivity of temperature stable ceramics AMoO4–TiO2 (A = Ca, Sr)," *Dalton Transcations,* vol. 42, pp. 1483-1491, 2012.

[207B] A. P. Marques, M. T. Tanaka, E. Longo, E. R. Leite and L. L. Rosa, "The Role of the Eu3+ Concentration on the SrMoO4:Eu Phosphor Properties: Synthesis, Characterization and Photophysical Studies," *Journal of Fluorescence,* vol. 21, no. 3, pp. 893-899, 2011.

[208B] s. Vidya, A. John, S. Solomon and J. K. Thomas, "Optical and dielectric properties of SrMoO4 powders prepared by the combustion synthesis method," *Advances in Materials Research,* vol. 1, no. 3, pp. 191-204, 2012.

[209B] M. Karlsteen, A. Baranzahi, L. A. Spetz, M. Willander and I. Lundstrom, "Electrical Properties of Inhomogeneous SiC MIS Structures," *Join'hal of Electronic Materials,* vol. 24, no. 7, 1995.

[210B] U. Hoefer, J. Frank and M. Fleischer, "High temperature Ga2O3 gas sensor and SnO2 gas sensors a comparison," *Sensors and Actuators B: Chemical,* vol. 78, pp. 6-11, 2001.

[211B] D. Errandonea, L. Gracia, R. Lacomba-Perales, A. Polian and J. C. Chervin, "Compression of scheelite-type SrMoO4 under quasi-hydrostatic conditions: Redefining the high-pressure structural sequence," *Journal of Applied Physics,* vol. 113, 2013.

[212B] R. Merkle and J. Maier, "How Is Oxygen Incorporated into Oxides? A Comprehensive Kinetic Study of a Simple Solid-State Reaction with SrTiO3 as a Model Material," *Angew Chem Int. Ed. Engl.,* vol. 47, no. 21, pp. 3874-3894, 2008.

[213B] E. T. Turkdogan and B. B. Rice, *Metallurgical Transaction,* vol. 5, 1974.

[214B] S. J. Lee, S. Y. Jung, S. C. Lee, H. K. Jun, C. K. Ryu and J. C. Kim, "SO2 Removal and Generation of MgO-Based Sorbents Promoted with Titanium Oxide," *Ind. Eng. Chem. Res. ,* vol. 48, pp. 2691-2696, 2009.

[215B] S. Sugiyama, T. Miyamoto, H. Hayashi and J. B. Moffat, *Bull. Chem. Soc. Jpn. ,* vol. 69, p. 235, 1996.

[216B] J. A. Schwarz, C. I. Contescu and K. Puty, Dekker Encyclopedia of Nanoscience and Nanotechnology.

[217B] M. Kandavel and S. Ramaprabhu, "Hydrogen storage properties of Mg-based composites prepared by reaction ball milling,," *J. Phys.: Condens. Matter,* 2006.

[218B] R. A. Cox-Galhotra and S. McIntosh, "Unreliability of simultaneously determining kchem and Dchem via conductivity relaxation for surface-modified La0.6Sr0.4Co0.2Fe0.8O3−δ," *Solid State Ionics,* vol. 181, pp. 1429-1436, 2010.

[219B] P. Hjalmarsson, M. Søgaard and M. Mogansen, "Oxygen transport properties of dense and porous (La0.8Sr0.2)0.99Co0.8Ni0.2O3-δ," *Solid State Ionics,* vol. 180, pp. 1290-1297, 2009.

[220B] Y. Li, "Oxygen Transport Kinetics in Solid Oxide Fuel Cell Cathode," West Virginia University, Morgantown, 2012.

[221B] J. W. Gardner, "A non linear Diffusion Model of Electrical Conductance in Semiconducting Gas Sensors," *Sensors and Actuators B: Chemical,* pp. 166-170, 1990.

[222B] G. J. Cadena, J. Riu and F. X. Rius, "Gas sensors based on nanostructured materials," *The Analyst,* Vols. i-SECTION: CRITICAL REVIEW, no. 132, pp. 1083-1099, 2007.

[223B] G. Korotcenkov, B. K. Cho, L. Gulina and V. Tolstoy, "Ozone sensors based on SnO2 films modified by SnO2–Au nanocomposites synthesized by the SILD method," *Sensors and Actuators B: Chemical,* vol. 138, no. 2, pp. 512-517, 2009.

[224B] M. A. Andio, "Sensor Array Devices Utilizing Nano-structured Metal-oxides for Hazardous Gas Detection," The Ohio State University , Ohio , 2012.

[225B] K. Arshak and I. Gaidan, "Development of an array of polymer/MnO2/Fe2O3 mixtures for use in gas sensing applications," *Sensors and Actuators B : Chemical,* vol. 118, pp. 386-392, 2006.

[226B] J. Li, Y. Lu, L. Ye, L. Delzeit and M. Meyyappan, "A Gas Sensor Array Using Carbon Nanotubes and Microfabrication Technology," *Electrochemical and Solid-State Letters,* vol. 8, no. 11, pp. H100-H102, 2005.

[227B] S. Semancik, R. E. Cavicchi, M. C. Wheeler, J. E. Tiffany, G. E. Poirier, R. M. Walton, J. S. Suehle, B. Panchapakesan and D. L. DeVoe, "Microhotplate platforms for chemical sensor research," *Sensors and Actuators B: Chemical,* vol. 77, no. 1-2, p. 579–591, 2001.

[228B] "ASM Handbook," *Mechanical grinding and Polishing,* pp. 257-280, 2004.

[229B] W. Chen, C.-s. Chwn and L. Winnubst, "Ta-doped SrCo0.8Fe0.2O3-δ membranes: Phase stability and oxygen permeation in CO2 atmosphere," *Solid State Ionics,* vol. 196, pp. 30-33, 2011.

G. BIBLIOGRAPHY:

Thesis:

The final technical report is based on the work of these two theses, which were supported by this program.

E. Çiftyürek**,** Nano-Derived Sensors for High-Temperature Sensing of H_2, SO_2, and H_2S, WVU Ph.D. thesis (2014).

C. Wildfire, Investigation of Gadolinium Based Pyrochlores for their use in High-Temperature Nano-Derived H_2 Gas Sensors. WVU Ph.D. thesis (2012).

Publications:

E. Çiftyürek, K. Sabolsky, and E.M. Sabolsky, "Evaluation of Molybdates Nanomaterials for High Temperature Sulfur Species within a Resistive-type Sensor Platform," in preparation for submission to *Sens. Actuators B* (2014).

E. Çiftyürek, K. Sabolsky, and E.M. Sabolsky, "Platinum-Zirconium Composite Thin Films for High-Temperature MEMS Electrode Applications," submitted to *Sens. Actuators B* (2014).

E.M. Sabolsky, E. Çiftyürek, C. Wildfire, K. Sabolsky, J. Taub, K. Sierros, and T. Evans, "Nano-derived Microsensors for Monitoring Gas Species in Harsh-Environments," *ECS Transactions* 61 [2], 375-385 (2014).

C. Wildfire, E. Çiftyürek, K. Sabolsky, and E.M. Sabolsky, "Investigation of Doped-Gadolinium Zirconate Nanomaterials for High-Temperature Hydrogen Sensor Applications," *J. Mater. Sci.* 49 [14], 4735-4750 (2014).

C. Wildfire, E. Çiftyürek, K. Sabolsky, and E. M. Sabolsky, "Fabrication and Testing of High-Temperature Nano-Derived Hydrogen Microsensors," *J. Electrochem.* 161 [2], B3094-B3102 (2014).

E.M. Sabolsky, P. Gansor, E. Ciftyürek, K. Sabolsky, C. Xu, and J.W. Zondlo, "In Situ Formation of a Solid Oxide Fuel Cell (SOFC) Cermet Anode by $NiWO_4$ Reduction," *J. Power Sources* 237, 33-40 (2013).

E. Ciftyurek, K. Sabolsky and E.M. Sabolsky, "Platinum Thin Film Electrodes for High-Temperature Chemical Sensor Applications" *Sens. Actuators B* 181, 702-714 (2012).

E.M. Sabolsky, C. Wildfire, E. Çiftyürek, and K. Sabolsky, "Nano-derived, Micro-chemical Sensors for High-temperature Applications," *ECS Transactions* 45 [3], 495-506 (2012).

Presentations:

"High temperature nano-derived hydrogen sensors," Christina Wildfire, Engin Ciftyurek, Katarzyna Sabolsky, Edward M. Sabolsky, European Ceramics Society (ECerS) XII conference in Stockholm, Sweden, June 19-23 2011, Nanomaterials Symposium; INVITED PRESENTATION

"Performance and Stability of High-Temperature Nano-Derived Hydrogen Sensors," Edward M. Sabolsky, Christina Wildfire, Engin Ciftyurek, Katarzyna Sabolsky, 220th Electrochemical Society Meeting, Boston, MA, Oct. 9-14, 2012; PRESENTATION

"High-Temperature Nanomaterials for Electrochemical Micro-Sensors," Edward M. Sabolsky, Christina Wildfire, Engin Ciftyurek, Energy Materials and Applications (EMA) 2012 Conference in Orlando, FL, January 18-20, 2012, S1: New Frontiers in Electronic Ceramic Structures, Advanced Electronic Material Devices and Circuit Integration; PRESENTATION

"Nano-Derived, Micro-Chemical Sensors for High-Temperature Applications," Edward M. Sabolsky, Christina Wildfire, Engin Ciftyurek, Katarzyna Sabolsky, 221st Electrochemical Society Meeting in Seattle, WA, May 6-10, 2012; INVITED PRESENTATION

"High-Temperature Nano-Derived Chemical Micro-Sensors," Edward M. Sabolsky, Christina Wildfire, Engin Ciftyurek, Katarzyna Sabolsky, 10th International Symposium on Ceramic Materials and Components for Energy and Environmental Applications (CMCEE) 2012 in Dresden, Germany, May 20-23, 2012; PRESENTATION

"High-Temperature Compatible Electrodes with Various Microstructural Architectures," E. Çiftyürek, K. Sabolsky, and E.M. Sabolsky, 221st Electrochemical Society Meeting in Seattle, WA, May 6-10, 2012; PRESENTATION.

"Degradation of Platinum Thin Films Electrodes for High-Temperature MEMS Applications", E. Çiftyürek, K. Sabolsky and E. M. Sabolsky, WV Academia Science 2012 Charleston, West Virginia, USA. PRESENTATION.

"High-Temperature Nano-Derived Sensors for Online Monitoring of SO_2 Emissions", E. Çiftyürek, C. Wildfire, and E. M. Sabolsky, Materials Science & Technology 2012, Pittsburgh, Pennsylvania, USA. PRESENTATION.

"High-Temperature Nano-derived Sensor Development for Detection of H_2S and SO_2 Emissions." E. Çiftyürek, K. Sabolsky, and E. M. Sabolsky, Materials Science & Technology 2013, Quebec, Canada. PRESENTATION.

"Nano-Derived Microsenors for Monitoring Gas Species in Harsh-Environments." E.M. Sabolsky, Çiftyürek, C. Wildfire, K. Sabolsky, J. Taub, K. Sierros, and T.H. Evans, 225th Electrochemical Society Meeting in Orlando, FL, May11-14, 2014; INVITED PRESENTATION.

"Nano-derived Tungstate and Molybdate Oxides for the Sensing of H_2, H_2S and SO_2 at High Temperatures," E. M. Sabolsky, E. Ciftyurek, K. Sabolsky, 13th International Ceramics Congress in Montecatini Terme, Italy, June 8-13, 2014; PRESENTATION.

H. LIST OF ACRONYMS AND ABBREVIATIONS:

δ	Oxygen deficiency
E_G	Energy Gap
K	Boltzmann Constant
E_F	Fermi Level
L_D	Debye Length
E	Dielectric Constant
ε_0	Permittivity of Free Space
T	Temperature
e^-	Electron Charge
Φ	Work function
n_d	Carrier Concentration
D	Grain Size
L	Thickness of Sensing Layer
ppm	Parts Per Million
ppb	Parts Per Billion
k	Boltzmann Constant
MOS	Metal Oxide Semiconductor
IDEs	Interdigitated Electrodes
EDS	Energy Dispersive X-ray Spectroscopy
PVD	Physical Vapor Deposition
CVD	Chemical Vapor Deposition
SEM	Scanning Electron Microscope
SMM	Strontium Magnesium Molybdenum Oxide
SMW	Strontium Magnesium Tungsten Oxide
TEM	Transmission Electron Microscope

XRD	X-ray Diffraction
DMM	Digital Multimeter
XPS	X-ray Photoelectron Spectroscopy
AES	Auger Electron Spectroscopy
W_{DL}	Depletion Layer
ECR	Electrochemical Relaxation
Uv-Vis	Ultraviolet–Visible Light Spectroscopy
UPS	Ultraviolet Photoelectron Spectroscopy
FT-IR	Fourier Transformed Infrared
TCE	Coefficient of thermal expansion
TPR	Temperature Programmed Reduction
XANES	X-ray Absorption Near Edge Structure

I. APPENDICES:

None